This electronic thesis or dissertation has been downloaded from the King's Research Portal at https://kclpure.kcl.ac.uk/portal/

Advanced Quantification of Myocardial Perfusion

Zarinabad Nooralipour, Niloufar

Awarding institution:
King's College London

The copyright of this thesis rests with the author and no quotation from it or information derived from it may be published without proper acknowledgement.

END USER LICENCE AGREEMENT

Unless another licence is stated on the immediately following page this work is licensed under a Creative Commons Attribution-NonCommercial-NoDerivatives 4.0 International licence. https://creativecommons.org/licenses/by-nc-nd/4.0/

You are free to copy, distribute and transmit the work

Under the following conditions:

- Attribution: You must attribute the work in the manner specified by the author (but not in any way that suggests that they endorse you or your use of the work).
- Non Commercial: You may not use this work for commercial purposes.
- No Derivative Works - You may not alter, transform, or build upon this work.

Any of these conditions can be waived if you receive permission from the author. Your fair dealings and other rights are in no way affected by the above.

Take down policy

If you believe that this document breaches copyright please contact librarypure@kcl.ac.uk providing details, and we will remove access to the work immediately and investigate your claim.

Download date: 05. May. 2023

Title: Advanced Quantification of Myocardial Perfusion

Author: Niloufar Zarinabad Nouralipour

Advanced Quantification of Myocardial Perfusion

Niloufar Zarinabad Nooralipour

Division of Imaging Sciences and Biomedical Engineering

School of Medicine

King’s College London

A dissertation submitted to graduate school of King’s College London in partial fulfilment of the requirements for the degree

Of

Doctorate of philosophy

In the memory of Dr Philip Batchelor

(30 Dec 1967_30 Aug 2011)

شکر خدا که هر چه طلب کردم از خدا

بر منتهای همت خود کامران شدم

به نام پدر بوسه‌ای باید زد دست‌هایی را

که می‌تابانند نیرو را و محکم می‌کنند استوری پایه‌های زیستن را

به نام مادر بوسه‌ای باید زد دست‌هایی را

که می‌شوید غبار خستگی روزگار را

و سیراب میکند روح تشنه را

به پاس تعبیر عظیم و انسانی شان از کلمه ایثار و از خود گذشتگی به پاس عاطفه سرشار و گرمای امیدبخش وجودشان که در این سردترین روزگاران بهترین پشتیبان است به پاس قلب های بزرگشان که فریاد رس است و سرگردانی و ترس در پناهشان به شجاعت می گراید و به پاس محبت های بی دریغشان که هرگز فروکش نمی کند. این مجموعه را به پدر و مادر عزیزم تقدیم می کنم.

Abstract

Ischemic heart disease remains a major global health concern with significant morbidity and mortality issues. Identifying areas of myocardial tissue at risk early on can help guide clinical management and develop appropriate treatment strategies to prevent myocardial infarction, thus improving patient outcomes. Using the latest cardiac magnetic resonance (CMR) imaging techniques, first-pass perfusion imaging allows for a very high spatial resolution, non-invasive and radiation free quantification of myocardial blood flow (MBF). True quantification of very high resolution perfusion images offers a unique capability to localize and measure subendocardial ischemia.

A common technique for calculating MBF from dynamic contrast-enhanced cardiovascular MR (DCE-CMR) is to track a bolus of contrast agent and measure MBF using fully quantitative methods. These methods which are based on central volume principle deconvolve the changes in the concentration of the injected contrast agent in the tissue with the arterial input function (AIF). However deconvolution is inherently a difficult process and therefore numerically unstable with noise contaminated data.

The purpose of this study is to enable high spatial resolution voxel-wise quantitative analysis of myocardial perfusion in DCE-CMR, in particular by finding the most favourable quantification algorithm in this context. Voxel-wise quantification has the potential to combine the advantage of visual analysis with the objective and reproducible evaluation made possibly by a true quantitative assessment. Four deconvolution algorithms – Fermi function modelling, deconvolution using B-spline basis, deconvolution using exponential basis and Auto-Regressive Moving Average modelling (ARMA) were tested to calculate voxel-wise perfusion estimates. The algorithms were developed on synthetic data and validated against a true gold-standard using a hardware perfusion phantom and an explanted perfused pig heart. The accuracy of each method was assessed for different levels of spatial resolution. Moreover robustness of each deconvolution algorithm to variation in perfusion modelling parameters was evaluated. Finally, voxel-wise analysis was used to generate high resolution perfusion maps on real data acquired from healthy volunteers and patients with coronary artery disease.

Both simulations and maps in the hardware phantom, explanted pig heart data and patient studies showed that voxel-wise quantification of myocardium perfusion is feasible and can be used to detect abnormal regions with high sensitivity in identifying the tissue at risk.

In general ARMA and the exponential method showed to be more accurate, on the other hand, Fermi model was the most robust method to noise with highest precision for voxel-wise analysis. Inevitably the choice of quantification method for data analysis boils down to a trade-off between accuracy and precision of the estimation.

List of abbreviations

AIF	Arterial input function
ANOVA	Analysis of variance
AR	Auto regressive
ARMA	Autoregressive moving average
BIBO	Bounded input bounded output
CA	Contrast agent
CAD	coronary artery diseases
CMR	Cardiovascular magnetic resonance
CNR	Contrast to noise ratio
CV	Coefficient of variation
CVD	Cardiovascular disease
DCE	Dynamic contrast enhanced
ECG	Electrocardiography
FRI	Fraction of residual information
GS	Gold standard
LAD	left anterior descending artery
LCX	left circumflex artery
LV	Left ventricle
MA	Moving average
MBF	Myocardial blood flow
MDCT	Multi-detector computed tomography
MPR	Myocardial perfusion reserve
MR	Magnetic resonance
MTT	Mean transit time
PET	Positron emission tomography
RCA	Right coronary artery
ROC	Region of convergence
ROI	Region of interest
RF	Radio frequency
STD	Standard deviation
SI	Signal intensity
SNR	Signal to noise ratio
SPECT	Single photon emission computed tomography
SVD	Singular value decomposition
TE	Time of echo

Table of Contents

5 EFFECTS OF TRACER ARRIVAL TIME ON THE ACCURACY OF HIGH RESOLUTION (VOXEL-WISE) MYOCARDIAL PERFUSION MAP FROM CONTRAST-ENHANCED FIRST-PASS PERFUSION MAGNETIC RESONANCE. 106

Introduction

This PhD project was collaboratively undertaken from October 2009 to August 2012 between the Division of Imaging Sciences and Biomedical Engineering, King's College London (KCL), UK and MR Clinical Science, Philips Healthcare, Best, Netherlands in response to the need for accurate quantification of myocardium perfusion at voxel level.

Contrast-enhanced first-pass cardiac magnetic resonance (CMR) perfusion offers higher spatial resolution than nuclear-medicine techniques resulting in improved visual detection of subendocardial perfusion abnormalities (1,2).

This feature alone results in improved detection of significant coronary artery disease. Alternatively to visual assessment, quantitative analysis of myocardial blood flow (MBF) provides reproducible and observer-independent measures of myocardial perfusion, with additional advantages in the assessment of patients with multi-vessel disease and balanced ischemia as well as for assessment of the true extent and severity of ischemia.

MBF analysis is usually performed on a segmental basis, thereby neglecting relevant diagnostic information about the extension, localisation and transmurality of ischemia provided by visual assessment using high-resolution CMR.

The primary aim of this thesis is to expand the usage of existing myocardial perfusion deconvolution algorithms in the literature (3-6) for estimation of the cardiac blood flow in voxel level. Here, the focus lies on developing, optimizing and validating quantification methods.

This thesis is a collection of contributions that have been, or will be, published in international scientific journals and conferences proceedings.

Structure of this thesis

The thesis is organised in seven chapters.

Chapter 1 discusses the use of MRI in clinical routine, with specific focus on myocardial perfusion imaging and its use for the assessment of ischemia.

Chapter 2 provides an overview of myocardial perfusion quantification. It describes myocardial perfusion quantification challenges and the logic behind optimization and deconvolution methods used for perfusion assessment. It reviews in detail the existing deconvolution algorithms in the literature and introduces a new optimized ARMA method developed by the author for MBF estimation.

Chapter 3 describes the validation of deconvolution methods using an explanted blood-perfused pig heart. It investigates the effect of variation in the deconvolution modelling parameters on the accuracy of deconvolution methods. Individual correlations with gold-standard fluorescent-labelled coloured microspheres are presented for each method order. Also, different deconvolution methods are compared in terms of their robustness to variation in the modelling parameters.

Chapter 4 describes the validation of voxel-wise quantitative perfusion imaging against simulated synthetic data and a hardware perfusion phantom with known flow values. It investigates the effects of noise on the accuracy of deconvolution methods and compares different deconvolution algorithms in terms of their robustness to noise.

Chapter 5 aims to explore the effects of tracer arrival time (tOnset) on the estimation of MBF in voxel-wise analysis. It describes development of an algorithm that enables automated optimization of analysis parameters in each voxel for a more accurate estimation of MBF.

Chapter 6 explores the relationship between the level of spatial resolution and accuracy of different deconvolution methods. Here, new methods introduced by Bvarly etal. (7) have been used to measure the amount of un-modelled information which remains in the tissue due to resolution reduction.

Chapter 7 summarizes the findings and provides an outlook for future projects.

1 Study background

1.1 Cardiovascular disease

According to the World Health Organization and the American Heart Association 2012 update report, cardiovascular disease (CVD) remains the leading cause of mortality and disability in the world in men and women of every major ethnic group(8). CVD claims more lives each year than the next four leading causes of death combined—cancer, chronic lower respiratory diseases, accidents, and diabetes mellitus.

Cardiovascular disease refers to any disease that involves heart or blood vessel. One of the most common types of CVD is coronary artery disease (CAD) which is the result of the accumulation of atheroma, a fatty plaque, within the walls of the coronary arteries that supply the myocardium with oxygen and nutrients. The filling up of the plaque in the artery causes narrowing of the artery and over time restricting blood flow supply to the myocardium. A reduction of the amount of oxygenated blood reaching the myocardium (ischaemia) can cause cellular hypoxia, and if its severity and duration are enough, it can result in myocardial infarction, reduction in cardiac function (heart failure) and electrical instability of cellular membranes (arrhythmias and sudden cardiac death) (9). The amount of delivered oxygen and nutrition rich blood into myocardium is known as myocardial perfusion.

In addition to genetic factors, obstructive atherosclerosis is often caused by an unhealthy diet, lack of exercise, being overweight and smoking. All of these are major risk factors for developing atherosclerosis of the coronary epicardial vessels and, in turn, myocardial ischaemia and, since ischaemia starts the cascade of events leading to myocardial damage, its detection is considered a sensitive marker for the diagnosis of CAD (10).

Several tests are available to confirm CAD, after an initial physical exam and blood tests are complete. The most common tests to diagnose CAD are the following:

1.1.1 Electrocardiogram (ECG) and echocardiogram (echo)

Electrocardiogram is the most common test for diagnosis of CAD. ECG records electrical signals as they travel through the heart and it can often reveal evidence of a previous heart attack or one that is in progress. However the ECG only gives the indication for the reduction in blood flow during stress and is not very accurate.

An echocardiogram (echo) uses ultrasound waves to produces images of the heart which shows the movement of the heart wall. Parts that move weakly may have been damaged during a heart attack or receiving too little oxygen (abnormality in the blood flow). This may indicate coronary artery disease or various other conditions. .However the analysis of the movement of heart walls as provided is not accurate enough to determine the extension of necrotic tissue and to define myocardial viability. Therefore evaluation of myocardial perfusion is important.

The availability, low cost and non-invasiveness of contrast enhanced echocardiography have fostered an increasing interest in the possibilities of this modality to provide an accurate and quantitative diagnosis of the myocardial state. The intravenous injection of contrast agents (microbubbles) has allowed visualizing flow information and regional perfusion. However, interpretation of the results can be very difficult and recent studies have suggested that stress echocardiography detects significantly less jeopardized viable myocardium than stress nuclear myocardial perfusion imaging. This subsequently translates into fewer patients at risk for cardiac events being detected (11).

1.1.2 X-ray angiography (XA)

X-ray angiography (XA) can be used to visualize the blood flow through the heart and coronary arteries. During XA, streams of contrast agents are injected into the arteries of the heart using catheters to create detailed images of the blood vessels in real time. The contrast agent outlines narrow spots and blockages on the X-ray images which are possibly the cause of a lack of perfusion. Major downsides of this modality are its invasiveness, the high amount of x-ray radiation and injected contrast agent. This method only produces 2D view of a 3D volume, thus to be able to assess the flow in the tissue, multiple views of the heart are need. This is done sequentially, so the machine position can be altered. Also more bolus of contrast agent is needed in order to acquire the information from another position. Moreover damage to blood vessels can occur at the site of puncture/injection, and anywhere along the vessel during passage of the catheter. This modality doesn’t provide any perfusion information and only provides us with information about the anatomy. Cost of performing cardiac XA has been compared with other imaging modalities in figure 1.1-1.

1.1.3 Single photon emission computed tomography (SPECT)

Single photon emission computed tomography (SPECT) allows a non-invasive assessment of directional change in regional tissue perfusion. This technique which produces 3D spatial information collects photons over large time period to construct a single view, so the data set does not give temporal information and the resolution is in the order of a cubic centimetre, which only allows placing approximately one voxel across the thickness of the myocardium. SPECT has been reported to have sensitivity of 0.87 [95% confidence interval (0.86-0.88)] and specificity of 0.73 [95% confidence interval (0.7-076)]. This modality is widely available and most extensively evaluated. However, SPECT is relatively slow and requires prolonged imaging times. Due to its relative nature SPECT frequently fails to identify patients having high risk coronary artery disease, resulting in occasional false –negative studies in patients with balanced reduction of flow due to three-vessel disease(12).

1.1.4 Positron Emission Tomography (PET)

A modality which is very similar to SPECT is positron emission tomography (PET). While radioactive tracer in SPECT emits gamma radiation that is measured directly, the radioactive tracer used in PET emits positrons that annihilates with electrons, emitting two gamma photons in opposite directions. A PET scanner detects these emissions. While several tracers have been used for evaluating myocardial perfusion with PET, the most widely used in clinical practice are rubidium-82 (^{82}Rb), oxygen -15-labled water ($H_2{}^{15}O$) and nitrogen-13-labeled ammonia (^{13}N-ammonia). Significant advantages of this nuclear medicine technique are 3D spatial information, which allow full coverage of the heart to determine the extent and size of ischemic lesions, kinetic modelling of tracer distribution and validation with radiolabeled microspheres in animal models.

PET has the advantage of routine, robust attenuation correction and higher spatial resolution than SPECT and thus is likely to result in higher accuracy for CAD detection compare to SEPCT. PET has been shown to allow non-invasive and accurate quantification of regional MBF if suitable tracers are used and appropriate mathematic models are applied. It has provided a wealth of new information in the field of cardiac physiology and pathophysiology and remains the gold standard against which new techniques should be tested (12,13).

However this modality is burdened by its limited availability and disadvantages such as exposure of the patient to radiation, a low spatial resolution (however better than SPECT) and not being suitable for the detection of subendocardial perfusion defects (13-16).

1.1.5 Multi-detector Computed Tomography (MDCT)

The ability of computed tomography (CT) to identify infarcted myocardium as an enhanced territory after coronary occlusion was described in late 1970s on excised animal hearts (17). This method found a second wind with the arrival of multi-detector computed tomography (MDCT). MDCT is a rapidly evolving technology with growing application in the non-invasive diagnosis of CAD. The rapid advancement of MDCT technology over the past 5 years has greatly improved its spatial and temporal resolution and has expanded its application beyond coronary angiography towards a more comprehensive evaluation of cardiovascular disease, including function, viability, and perfusion (18-25). Recently George et al (26) performed adenosine stress CT perfusion imaging and demonstrated that the combination of CT perfusion and angiography detected perfusion abnormalities with a sensitivity and specificity of 86% and 92%, respectively, as compared with a combination of coronary angiography and SPECT. Cost of performing cardiac MDCT has been compared with other imaging modalities in figure 1.1-1.

1.1.6 Cardiovascular Magnetic Resonance (CMR)

Cardiovascular magnetic resonance imaging (CMR) is a medical imaging technology for the non-invasive assessment of the function and structure of the cardiovascular system with an exogenous contrast agent. It is based on the same principles as magnetic resonance imaging (MRI) with extra optimisations, such as ECG gating and rapid imaging techniques or sequences, for use in the cardiovascular system. Unlike SPECT and PET, MRI benefits from advantages such as the superior temporal and spatial resolution, the absence of any radiation hazards, and the availability of highly stable and inert MR contrast agents of low toxicity(27). MRI is able to obtain serial perfusion images with sub-second resolution after the injection of the contrast agent. The regional variations of signal intensity as a function of time (image number) provide quantitative information about tissue perfusion (28-30). Several clinical studies compared CMR favourably to SPECT and PET for the diagnosis and assessment of myocardial ischaemia (31-33).

Table 1-1 Diagnostic Performance of Perfusion Imaging Techniques (2)

	N	Sensitivity	Spasticity	Radiation	Spatial Resolution	Availability
SPECT	4480	0.87	0.73	Yes	Very low(10-15mm)	Wide
PET	1442	0.85	0.87	Yes	Low (6-4mm)	Limited
CMR	1516	0.91	0.81	No	High (2-1mm)	Wide
MDCT	40	0.86	0.92	Yes	Very high	Variable

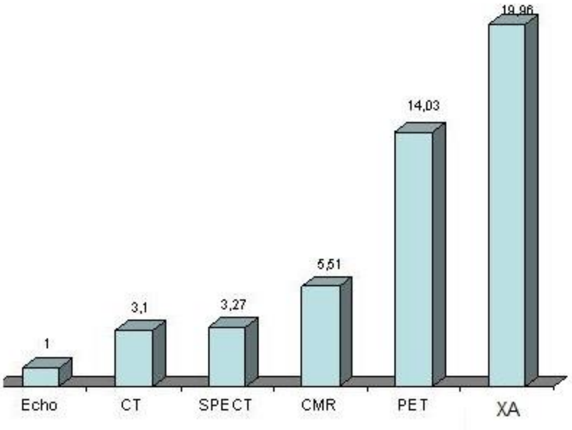

Figure 1.1-1 Estimated average costs of CMR and other common cardiac imaging procedures when compared to 2D echocardiography (Adapted from (34)). Echocardiography is the cost comparator where costs of other modalities are a ratio of x-fold higher costs

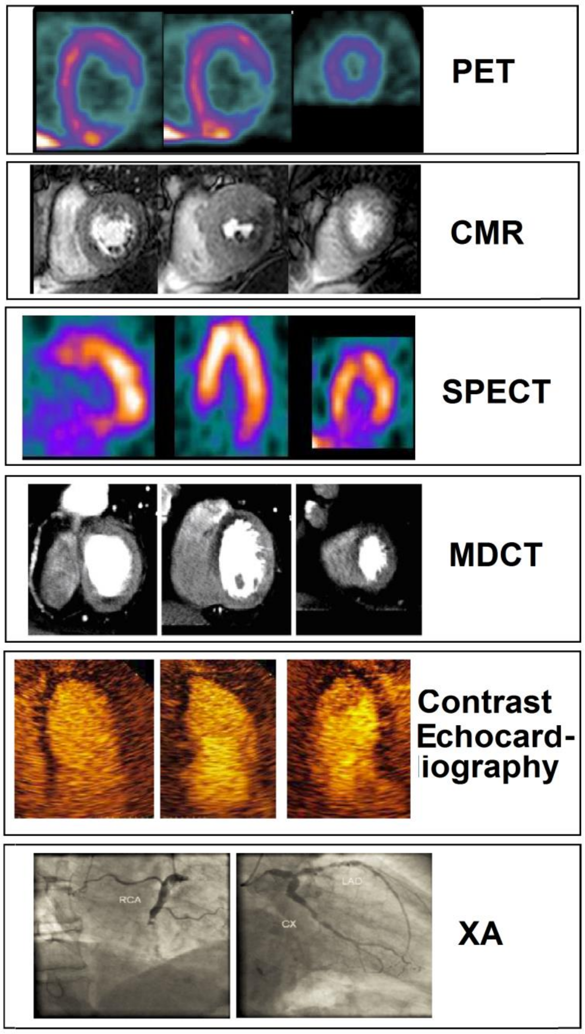

Figure 1.1-2 Example image of each modality (Images are adapted from (35,36)).

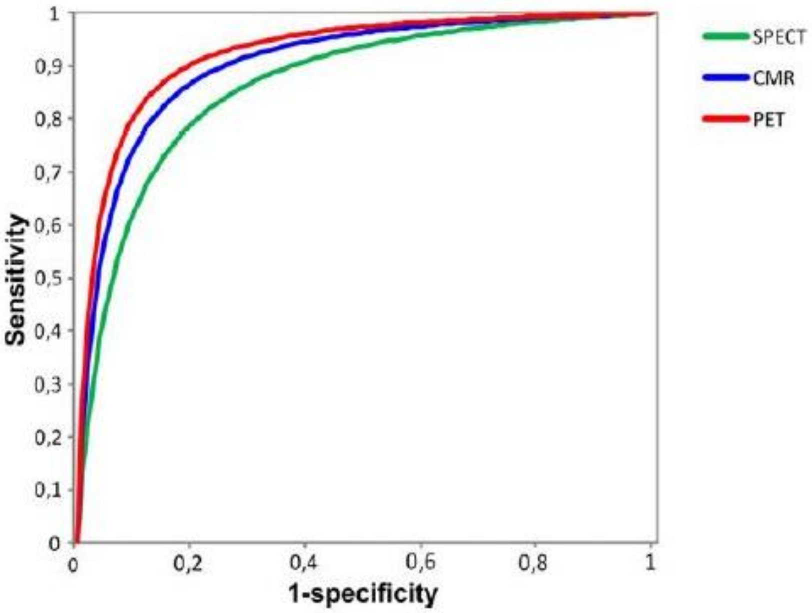

Figure 1.1-3 Comparison between diagnostic performance of PET, SPECT and CMR. Meta-regression analysis demonstrated that CMR and PET have a significantly higher diagnostic accuracy than SPECT. A higher but no significant diagnostic performance was observed for PET in comparison with CMR (Modified from (37)).

.

The continuous development of hardware, acquisition sequences, contrast agents and new post-processing tools, allows expansion of the applications of CMR towards better understanding of pathophysiology and better management of disease (38,39). CMR is now a robust technique which delivers high anatomical detail, good tissue contrast, excellent spatial and temporal resolution, versatility, and lack of ionizing radiation. These, together with the acceptable costs and risks and growing availability in hospitals, makes CMR a current modality of choice for myocardial perfusion imaging (40).

1.2 Cardiovascular magnetic resonance

CMR has become an important and sophisticated tool for non-invasive evaluation of the cardiovascular structures, providing essential information about cardiac function. It uses the same principle as MRI with some optimization. Therefore for a better understanding of CMR, a small introduction on MRI is given, followed by a description of cardiovascular imaging protocols.

1.2.1 Introduction to MRI

The phenomenon of nuclear magnetic resonance was described in the 1940’s independently by both Felix Bloch and Edward Purcell. The nuclear magnetic resonance phenomenon can be described in a nutshell as follows. If a sample is placed in a magnetic field and is subjected to radiofrequency (RF) radiation (energy) at the appropriate frequency, nuclei in the sample can absorb the energy. The frequency of the radiation necessary for absorption of energy depends on the characteristic of the nucleus and spatial location in the magnetic field if that field is not everywhere uniform. The latter variable provides the basis for magnetic resonance imaging (MRI). After absorption of energy by the nuclei, the length of time and the manner in which the nuclei dissipate that energy can also be used to reveal information regarding a variety of dynamic processes.

This was used widely over the subsequent two decades for analysing chemical compounds. It was only in the 1970’s following MR tissue characterisation by Damadian when MRI application entered the clinical arena. Its imaging application began with Lauterbur having the idea of applying magnetic field gradients in three dimensions to derive spatial orientation using MRI. Subsequent introduction of phase and frequency encoding introduced by Ernst alongside the Fourier transformation forms the basis of modern MRI techniques. This was taken a step further with Mansfield developing echo-planar imaging, with improvements in the use of gradients and signal analysis (41).

1.2.1.1 Basic Principles of MRI

The hydrogen atom consists of a positively charged proton and is abundant in the human body. This forms the basis for the use of MRI in medical imaging.

The proton has an inherent spin, which creates a tiny magnetic field (Figure 1.2-1 a). In the tissues of the body, the magnetic fields resulting from each proton are randomly aligned. When the body is placed in a large and powerful magnet, some of these tiny magnetic fields align with the large external magnetic field and some actually align against the field cancelling each other out. A slight excess will align with the field so that the net result (M_0) is an alignment with the external field (Figure 1.2-1 b).

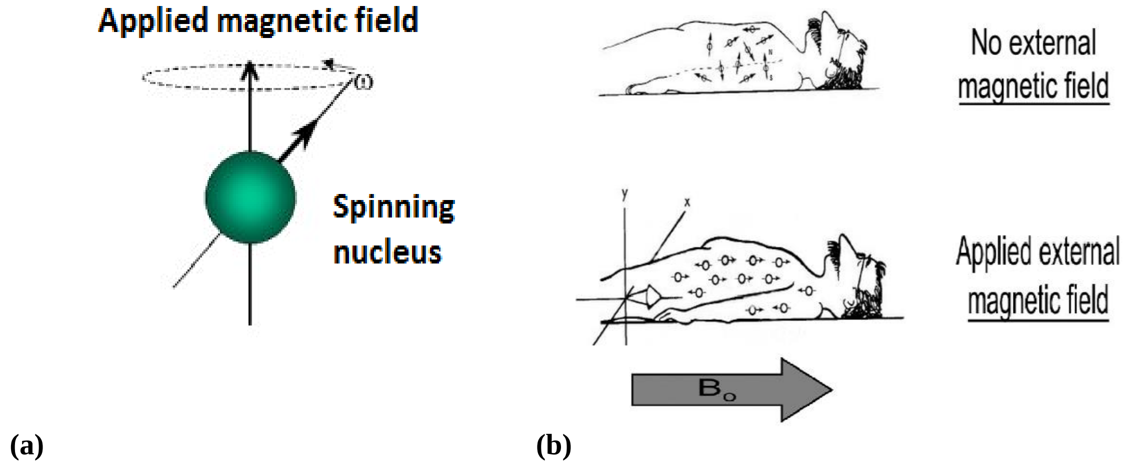

Figure 1.2-1 (a) A spinning charged particle such as proton nuclei generates a magnetic field. (b) Spinning protons with axis of magnetic moments. When placed in a large external magnetic field(B_0), most of the protons tend to align with the field and reach equilibrium. Image is adapted from (mauricewilkinscentre.org).

This equilibrium can be disturbed by applying energy to the to the body's tissues ("excitation"). The latter is achieved by using a radiofrequency (RF) pulse, provided the pulse is of the same or close to the natural frequency of vibration of the protons. This frequency is called resonance frequency and it is directly proportional to the magnetic environment that the proton experiences. An atom will only absorb external energy if that energy is delivered at its resonance frequency.

As a result of the excitation with the RF pulse at the resonance frequency, enough protons absorb energy to jump from the current energy level to the higher level. They will alter their alignment from the direction of the main magnetic field (B_0) to the direction opposite the main magnetic field. The effect of all this is that the net magnetization (M_0) flips θ° from the positive z-axis to transverse plane.

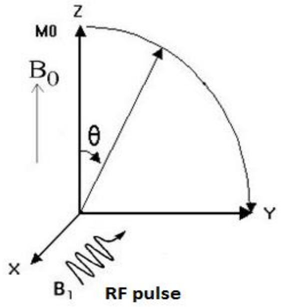

Figure 1.2-2 Rotation of the net magnetization by application of an RF pulse. All nucleuses in a volume of tissue together have a net magnetization M_0 in the magnetic field B_0at Z direction. When a RF-pulse of 90° (in B_1direction) excites the tissue, the net magnetization changes to Z = 0.

The angle of magnetization is moved to an angle away from the main magnetic field depending on the amplitude and duration of the RF pulse. The magnetization rotates around the main axis of the magnetic field, resulting in high frequency alternating magnetic field. This gives rise to an electromagnetic resonance signal, which can be measured in a receiver RF coil as a voltage.

However the signal is only transient, as the nucleus gives off the acquired energy back to its invoiermnet(after RF pulse is switched off) and the net magnetization realigns in the longitudinal plane with the main magnetic field (B_0).. . Some of the energy given off is detectable as an electromagnetic signal. The emission of energy in the form of an electromagnetic resonance signal after excitation is called Free Induction Decay (FID). Some of this energy also goes to heating up the surrounding tissue, referred to as the lattice. Therefore this mechanism can be divided into spins and lattice. This type of spin-lattice interaction is the result of the excited system returning to equilibrium. In the classical description, this emission is the net result of the Z component (M_z) of the magnetization recovering back to M_0 (figure 1.2.3). The time course whereby the system returns to equilibrium, or M_z grows to M_0, is mathematically described by an exponential curve. The time that nuclear spin magnetization takes to return to 63% of its initial position is termed longitudinal (or spin–lattice) relaxation time T1. The rate at which this happens depends on the characteristics of the tissue (if the equilibrium is restored more quickly, the tissue has a short T1) so it can be used to visualize different tissues in the human body.

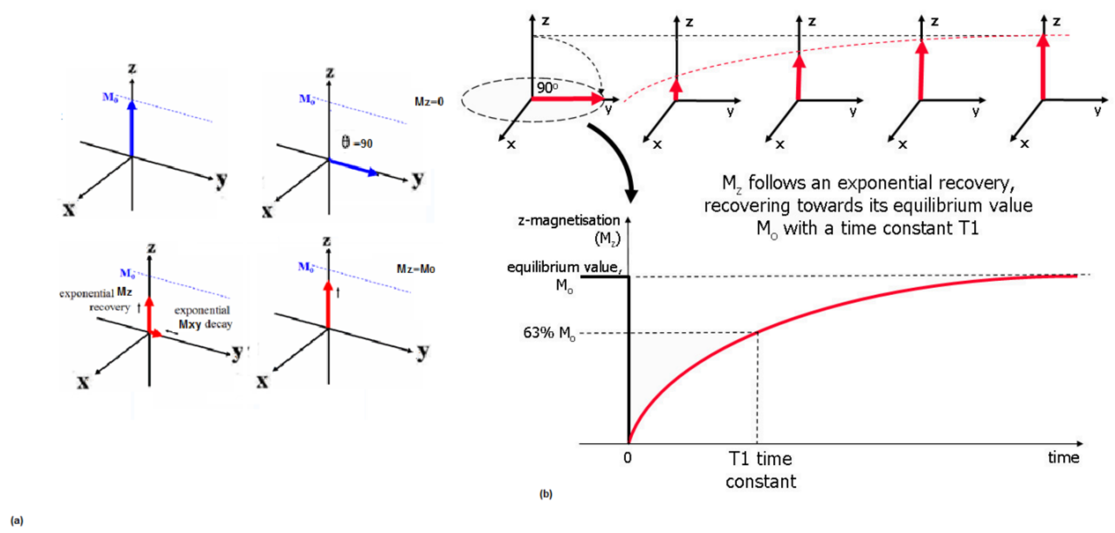

Figure 1.2-3 (a) *M* at equilibrium, followed by a 90° RF excitation pulse, Decay of M_{xy}, and recovery of M_z (time constant T1). (b) Diagram showing the process of T1 relaxation after a 90° rf pulse is applied at equilibrium. The z component of the net magnetisation, M_z is reduced to zero, but then recovers gradually back to its equilibrium value if no further rf pulses are applied (images adapted from (42)).

The second aspect of restoring equilibrium is loss of the transverse component of magnetization (M_{xy}) which is in the plane perpendicular to the axis of the magnetic field. This happens because of the interaction between different protons and inhomogeneities in the magnetic field. Therefore the rotating vector of magnetization moves out of phase (de-phased) such that they are all not pointing in the same direction anymore. However they still remain within the plane perpendicular to the magnetic field. As a result, the sum of these rotating vectors is reduced and so is the signal.

The time that M_{xy}takes to lose 63 % of its original value is known as a transverse (or Spin-Spin) relaxation time T2 or T2* depends on the reason of the de-phasing. T2 includes dephasing of the net magnetisation vectors caused by spin-spin interactions at the atomic and molecular levels. At atomic level spins affect each other by their individual oscillating magnetic fields. This changes their frequency of precession, and they move out of phase. T2* includes dephasing caused by magnetic field inhomogeneities and susceptibility effects as well. These also cause variations in the magnetic field experienced by nuclear spins. This changes their frequency of precession even more, and they move out of phase much faster (a faster loss of signal). Again, the speed at which this occurs is dependent on tissue properties which govern the T2 or T2* value.

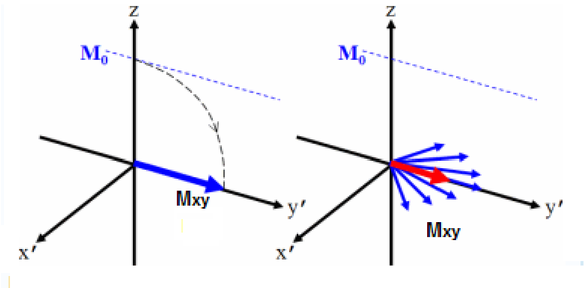

Figure 1.2-4 Dephasing of spins causes M_{xy} to decay away. The rotating frame is shown

Spatial orientation is necessary in order to create an image in MRI. This is made possible using gradient fields. Three orthogonal linear field gradients are used in MRI. In contrast to the static field of the magnet, gradient fields can be altered over time in all 3 dimensions (x,y and z). Gradient fields are used to spatially encode the positions of protons by varying the magnetic field linearly across the imaging volume. In this way, a 2D slice can be selected by applying a gradient in the direction perpendicular to it, whilst the excitation RF pulse is transmitted. Therefore the resonance frequency will vary as a function of position in the *x*, *y* and *z*-axes nd the RF pulse will only have an effect on the slice of tissue in which the protons have the same resonance frequency as the pulse itself. The signal detected in the RF detector coil is described by sine function. The frequency of this function is used to define spatial orientation. The digitized representations of these signals are converted into a data matrix called k-space. Data in the centre of k-space encodes contrast information in the MRI image – as it has low spatial frequency– whereas data in the periphery of k-space provides image sharpness, as it has high spatial frequency. The image can then be calculated using these individual spatial frequency components using Fourier transformation. The MRI images give a representation of the signals in the time domain.

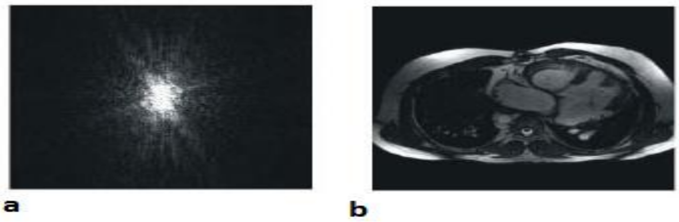

Figure 1.2-5 k-Space (a) and its associated image (b).Image adapted from D Moratal,Biomed Imaging Interv journal 2008; 4(1):e15.

Unfortunately, MRI introduces artifacts into the image as a result of a limitation or malfunction in the hardware or software of the machine. It also can be caused by the human body or a consequence of environmental influences. These artifacts can affect the quality of the images and consequently the diagnostic quality. The knowledge of artifacts and noise producing factors is important for continuing maintenance of high image quality. Correction for MR specific artifacts requires systematic research and is beyond the scope of this thesis. In this study we only have selected patients with good image quality without any artifacts.

1.2.2 How magnetic resonance perfusion works

When the heart is imaged using CMR, its tissue has more or less the same signal intensity (greyscale level) throughout all cardiac phases, therefore the signal intensity is not a good parameter to estimate perfusion. However it would be possible to influence the greyscale locally and temporally by injecting a contrast agent which affects T1 relaxation time.

The contrast agents used are based on Gadolinium. Gadolinium paramagnetic property reduces the T1 relaxation. In the imaging sequences used, a shorter T1 leads to a stronger signal and thus a brighter image (which means change of intensity in the voxels depending on the amount of contrast which is present at the location). Most of these gadolinium based contrast agents are extracellular contrast agents. They diffuse rapidly from the vessels into the extracellular fluid and blood plasma (but not into intact cells). Blood flows from the smallest capillaries through the tissue into the small veins. In healthy tissue this blood flow is unobstructed, and diffusion is assumed to play a very minor role in the perfusion compared to flow. When the blood supply is decreased in myocardium, the perfusion is smaller.

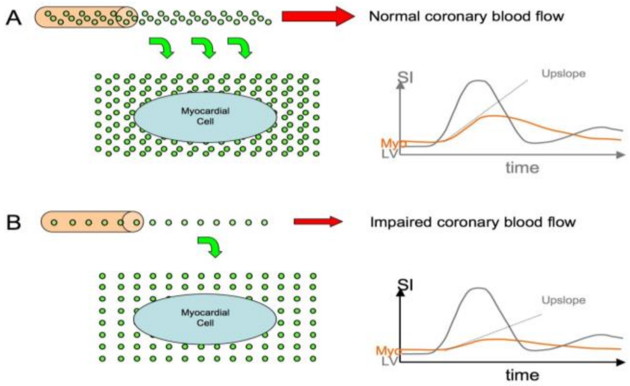

Figure 1.2-6.The extracellular contrast agent reaches the myocardium and passes into the extracellular space with an amount and rate, which is proportional to blood, flow. In normal conditions (A), a certain amount of contrast agent diffuses disperses into the extracellular space, giving a strong myocardial signal (Myo) occurring later than the increment of signal in the left ventricle (LV); when regional coronary blood flow is impaired (B), the amount and rate of wash-in of the contrast agent is reduced (Upslope), and peak signal intensity is lower (43).

1.2.2.1 Dynamic contrast enhanced MR imaging (DCE-MRI)

Dynamic contrast enhanced MR imaging (DCE-MRI) is used to image healthy tissue and beginning ischemia. In this method images are acquired directly after contrast administration to capture first passes of the fast flowing contrast through the highly organized vascular structure.

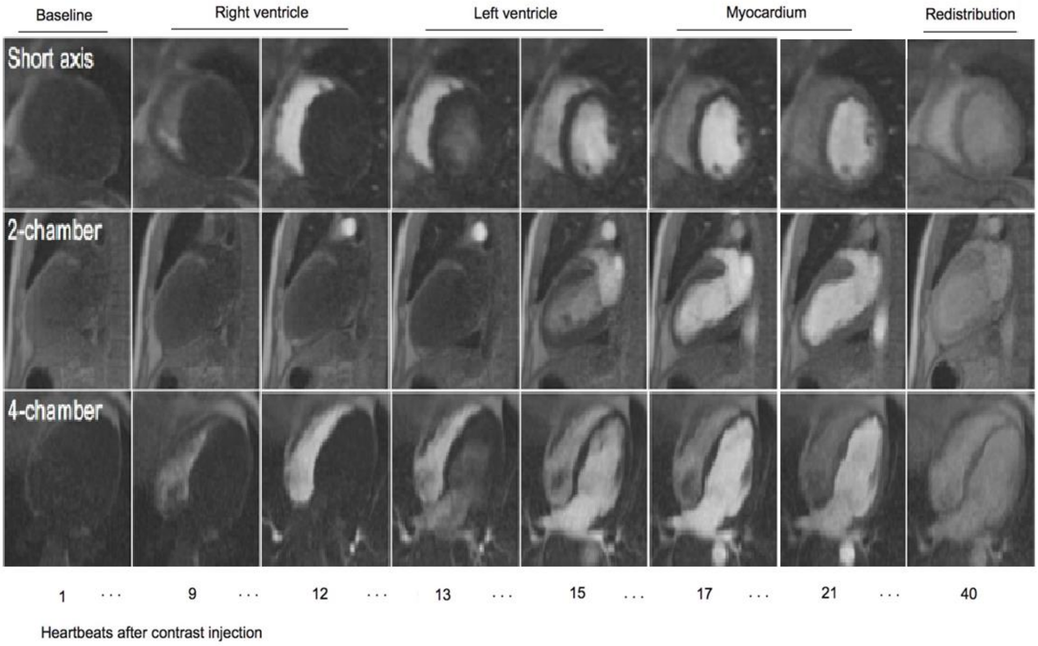

Figure 1.2-7 Example of first pass perfusion images in short axis, 2-chamber, and 4-chamber view. The first image corresponds to the beginning of intravenous injection of the contrast agent (baseline). Then the contrast reaches the right ventricle (9-12 heart beats), the left ventricle (13-15 heart beats), and finally the myocardium (17-21 heart beats). After 40 heartbeats the redistribution of the contrast agent is complete. After 15 minutes most of the contrast agent is washed-out.

1.2.3 CMR data acquisition techniques

1.2.3.1 Spin Echo

In spin echo image acquisition technique, after a 90 degree pulse, the net magnetization M_0 is rotated into transverse plane where it precesses, giving rise to a signal detectable by the FR receiver coli. The magnetization vectors start to de-phase and amplitude of the signal starts to decrease because of field inhomogeneities and spin-spin interactions (see section 1.2.1.1). This sequence uses a 180 degree pulse (refocusing pulse) at a given time after the 90 degree excitation RF pulse to reverse the de-phasing of the transverse magnetization caused by magnetic field inhomogeneitiesand susceptibility effects (removing T2* effects). This magnetization vectors come back into phase once again and the signal will grow in amplitude to form an echo. The echo time (TE) is the time between the initial RF pulse (a 90 degree pulse) and the maximum spin echo signal, so the 180 degree pulse is applied half way through this period.

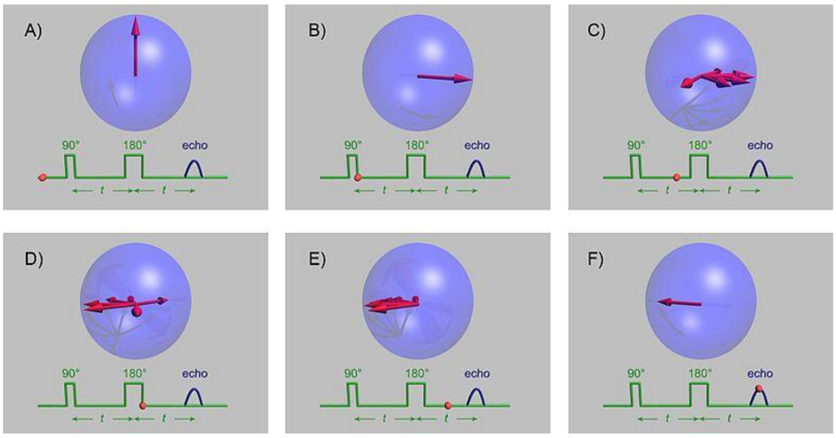

Figure 1.2-8 The spin echo sequence. A) - The vertical red arrow is the average magnetic moment of a group of spins, such as protons. B) A 90 degree pulse has been applied that flips the arrow into the horizontal (x-y) plane. C) Spins affect each other by their individual oscillating magnetic fields. This changes their frequency of precession, and they move out of phase. In addition to the latter, due to local magnetic field inhomogeneities, as the net moment processes, some spins slow down due to lower local field strength (and so begin to progressively trail behind) while some speed up due to higher field strength and start getting ahead of the others. These two together make the signal decay. D) A 180 degree pulse is now applied so that the slower spins lead ahead of the main moment and the fast ones trail behind. E) Progressively, the fast moments catch up with the main moment and the slow moments drift back toward the main moment. F) Complete refocusing has occurred and at this time, an accurate T2 echo can be measured with all T2 * effects removed.

Spin echo sequences are often acquired and are used to study the anatomy of the heart, the thoracic aorta and great vessels. However it is not suitable for dynamic imaging (perfusion imaging)

1.2.3.2 Gradient Echo

Gradient echo sequences are the workhorse of cardiac imaging because of their speed and versatility. Gradient echo imaging is employed in the assessment of ventricular function, blood velocity and flow measurements, and assessment of valvular disease and myocardial perfusion. A gradient echo is generated by using a pair of bipolar gradient pulses. There is no 180° refocusing pulse and the data are sampled during a gradient echo, which is achieved by de-phasing the spins with a negatively pulsed gradient before they are re-phased by an opposite gradient with opposite polarity to generate the echo.

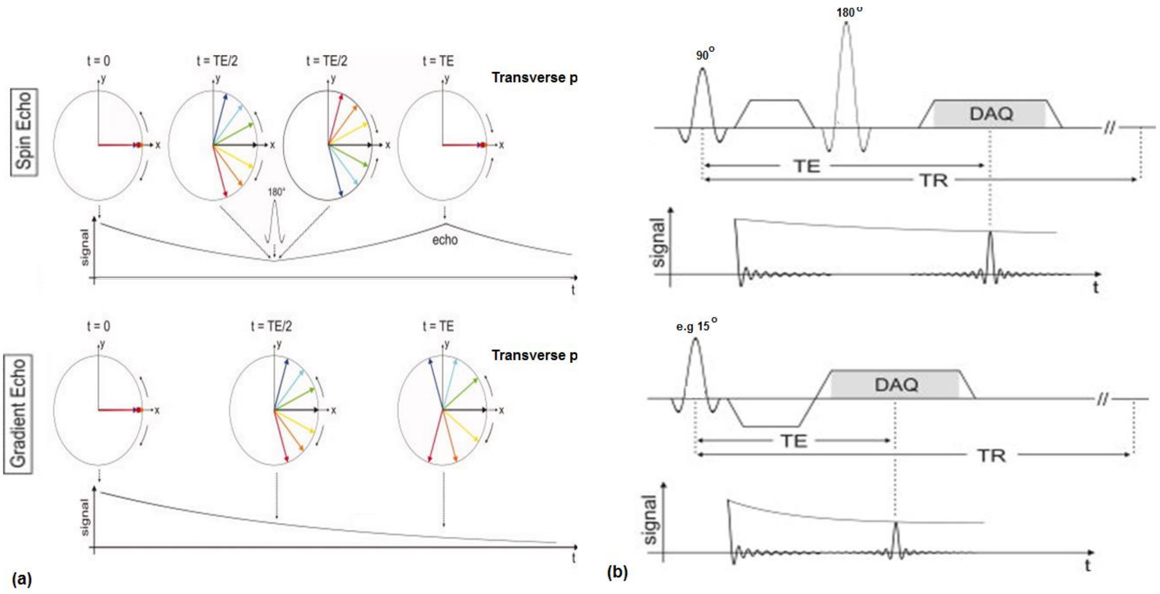

Figure 1.2-9 (a) Signal formation for spin echo (top) and gradient echo (bottom) imaging in transverse plane. Top: The 180° refocusing pulse for spin echo imaging flips over magnetization in transverse plane and reverses the rotation direction of the transverse magnetization and results in a compensation of de-phasing caused by the T2* effect resulting in the re-phasing of the magnetization at echo time TE. The coloured arrows represent exemplary magnetization vectors. Bottom: For gradient echo imaging, the de-phasing is not reversed. Note that shorter echo times are necessary for detectable gradient echo signal intensity. (b)Simplified spin echo (top) and gradient echo (bottom) pulse sequence diagrams. The basic difference between gradient echo and spin echo imaging is related to the fact that echo formation is a result of a single RF pulse and gradient reversal while spin echo imaging uses two RF pulses, i.e., a second 180° pulse, for echo generation. DAQ reflects the period of data acquisition adapted from (44).

Gradient echo sequences allow much shorter acquisition times than spin echo sequences. This is because of the angle of gradient echo the excitation pulse is smaller) so the time needed for longitudinal relaxation is shorter. Therefore shorter repetition times can be used. This permits imaging of multiple phases throughout the cardiac cycle with relatively short period of breath hold. Gradient echo imaging is employed in the assessment of flow measurements, myocardial perfusion.

1.2.4 Motion correction

Despite the progression of MR in cardiac imaging, many MR studies suffer from image degradation due to motion during the acquisition. Motion of the heart is the vector sum of three components: motion caused by the pumping action of the four chambers, motion caused by respiration, and any resulting motion from voluntary or involuntary patient movement. The latter component is usually managed in cardiovascular magnetic resonance (MR) imaging by means of patient cooperation or anesthesia in pediatric patients.

The type and severity of image degradation induced by cardiac motion depends on the imaging sequence and parameters used (45,46). Assessment of cardiac motion effects on the quality of the MR image is beyond scope of this study and hasn’t been systematically addressed in this thesis.

Respiratory motion can be reduced by holding the breath during cardiac perfusion imaging. But even without this large movements (due to breathing), some minor moments will always take place which have to be corrected after the acquisition. This motion correction is applied to all images in this study, but it is beyond the scope of this thesis and will not be discussed further.

Another type of MR artifacts which may influence the accuracy of CMR image assessment is flow-related dephasing artifacts, or dephasing artifacts between myocardium and blood pool. Evaluation of the effect of these artifacts on the accuracy of the assessment requires additional research which is beyond scope of this thesis and is not systematically addressed here.

1.2.4.1 ECG gating

The contraction of the heart muscle is a major determining factor in the image quality of cardiac MR images. The application of the conventional MRI protocol would result in unreadable images due to overwhelming motion artifacts (47). Using the electrical activity of the heart, MRI data acquisition can be synchronized to the corresponding mechanical event. In this way cardiac motion can be frozen and all slices will be acquired when the heart is static in same phase of the heartbeat (ECG gating) (48). The ability to reliably detect ECG is crucially important in order to synchronize perfusion imaging to cardiac cycle. If the heart imaging takes longer than the fraction of heart beat, the heart would be smeared out over the entire image. However in the majority of cardiovascular MR sequences, data are acquired over several cardiac cycles with the assumption that motion is the same between heartbeats. This is an oversimplification, as heart motion and heart rate vary naturally on a beat-to-beat basis with respiration and other factors. In addition, breath holding, often used in cardiovascular MR to eliminate respiratory motion, has also been demonstrated to affect cardiac activity (45).

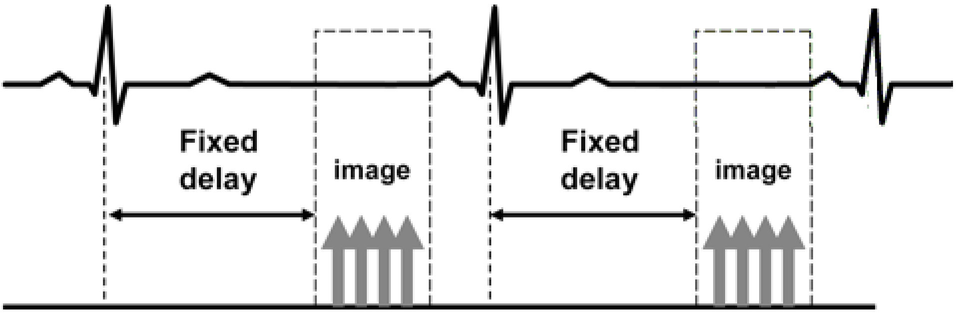

Figure 1.2-10 Diagrams show the timing of image acquisition in segmented cardiac MR imaging in relation to ECG gating. Segmented acquisition requires that k-space be filled over several cardiac cycles.

1.2.5 Cardiac magnetic resonance stress testing

In combination with using vasodilator drugs MR has the capability to diagnose ischemia. Cardiac stress MR is increasingly used for the diagnosis and evaluation of myocardial ischemia and viability, providing a safe and effective evaluation of patients with coronary artery disease (CAD). When compared with other well-established diagnostic techniques, such as SPECT or PET, cardiac stress MR offers an excellent depiction of wall motion, high contrast, and a high spatial resolution without using ionizing radiation (14). Cardiac stress MR perfusion (MR-PERF) tests the presence of inducible myocardial perfusion defects during administration of cardiac stress agents such as adenosine. Adenosine induces maximal vasodilatation in the arterial coronary vessels. Since the microvasculature distal to a coronary artery stenosis is fully dilated at rest, this area will not dilate further with adenosine and resistance to blood flow will be higher in comparison to normal vessels. This mechanism, together with a mild reduction of the coronary perfusion pressure, is responsible for a differential distribution of coronary blood flow and thus of the Gadolinium based contrast agent during first pass perfusion, making possible to visualize areas of myocardium with reduced blood-flow as darker areas.

1.2.6 Segmentation of the heart

In cardiac imaging the orientation of the heart, angle selection for cardiac planes, number of segments, slice display and thickness, organization for segments, and assignment of segments to the coronary arterial territories are important factors that need to be considered during for data acquisition. American Heart Association (AHA) has recommended a standardized model for the heart which divides it into 17 rather large volumetric segments for the regional analysis of left ventricular function or myocardial perfusion.

This model was originally created to compare results between different modalities like SPECT and CMR.The segments are large because of the low resolution of the SPECT. Images resulting from CMR studies should be oriented along the heart axes in order to cleanly depict the ventricles, the atria, and the myocardial regions supplied by the major coronary arteries. It is recommended by the AHA to perform a reorientation of the data and select the image slices so that the long axis of the heart (line apex to the centre of the mitral valve) becomes orthogonal to the image planes, and the selected slice images show short axis cuts (49). This approach maintains the integrity of the cardiac chambers and the distribution of coronary arterial blood flow to the myocardium.

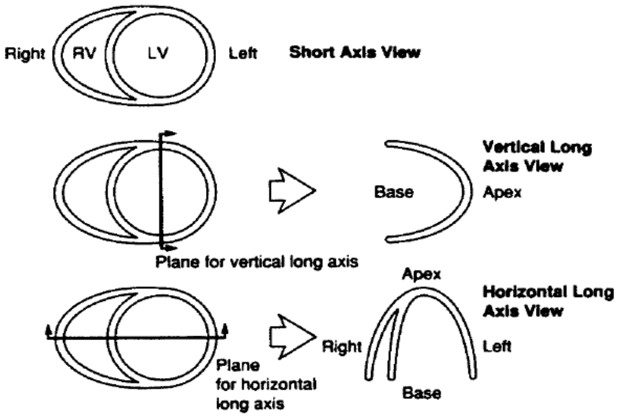

Figure 1.2-11 Cardiac plane definition and display for tomographic imaging modalities. Image adapted from Standardized Myocardial Segmentation (49).

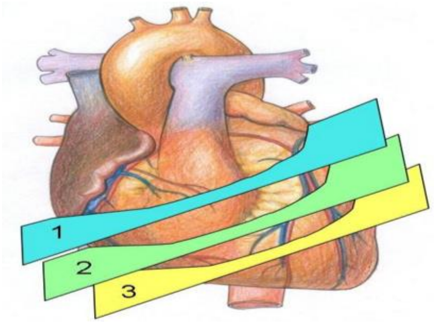

Figure 1.2-12 This figure shows a schematic of the heart. The planes represent the slices which are acquired with the MRI machine. These slices correspond to the slices defined in the AHA model.

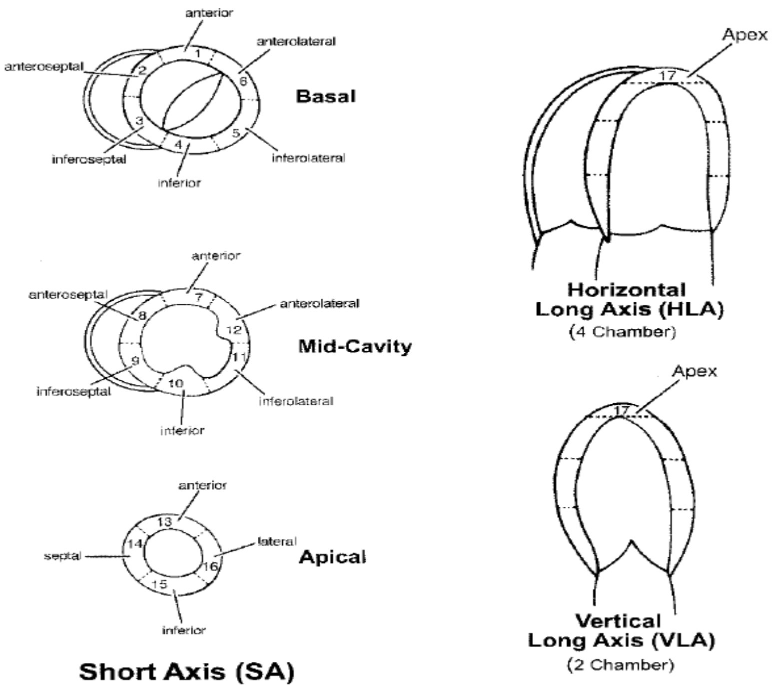

Figure 1.2-13 Diagram indicating how the left ventricle can be divided into 17 segments for 2D echocardiography. One can identify these segments in a series of longitudinal views or a series of short-axis views. Image adapted from Standardized Myocardial Segmentation (49).

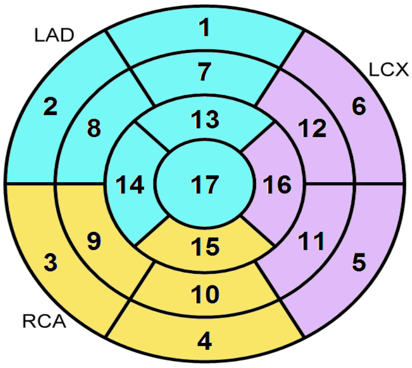

Figure 1.2-14 Display of myocardium segments, on a circumferential polar plot, of the 17 myocardial segments and the recommended nomenclature for imaging of the heart. Modified from Standardized Myocardial Segmentation (49).

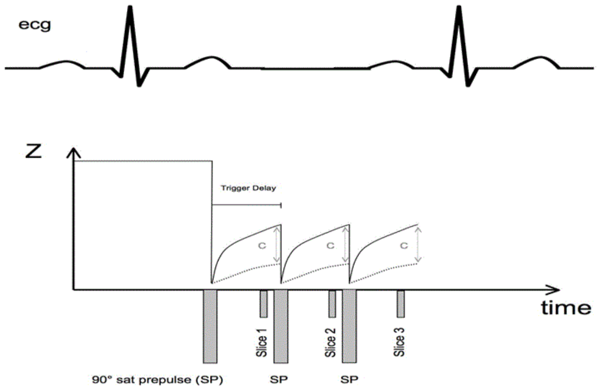

Figure 1.2-15 Regardless of the type of image readout adopted (Turbo-Gradient Echo Imaging or Steady State Free Precession), perfusion sequences are usually built with a 90° saturation prepulse (SP) to generate the T1 image contrast (i.e. signal intensity difference). Triggering on the QRS complex of the ECG, the scanner produces the SP which nulls the longitudinal magnetization of tissues. Immediately after, magnetization starts to recover, at a speed, which is proportional to the T1 of tissues. Left ventricular myocardium perfused by normal coronary arteries receives more blood than ischemic zones, resulting in a higher concentration of the contrast agent and shorter T1. Ischemic myocardium presents with less contrast agent and thus with a longer T1. After a delay (trigger delay) that allows the magnetization to recover dependent on the contrast agent concentration, the scanner starts the image readout. The image contrast (i.e. signal intensity difference) between normally perfused and ischemic myocardium is caused by the differences of T1.

Cardiac perfusion imaging is performed during approximately 40 – 60 heartbeats after injection of the contrast agent (Fig 1.2-8). The contrast agent is administered into an antecubital vein at a speed of 3-5 ml/sec using an automatic MR compatible pump. Higher doses (e.g. 0.1 mmol/kg body weights) are preferred for visual assessment; lower doses (e.g. 0.025 mmol/kg body weight) are more suitable for quantitative and semi-quantitative evaluation. A full dataset (e.g. 3-4 short axis views) is acquired every heart beat to visualize the flow of the contrast agent through the left ventricular cavity and the myocardium. Imaging is usually performed first during adenosine stress (140µg/kg bodyweight/minute for up to 6 minutes) and repeated approximately 10-15 minutes later at rest(10,43,50).

Different imaging sequences can be used. Most centres use Turbo-Gradient Echo Imaging (TGrE, TFE, FLASH). In addition to using an appropriate imaging sequence to visualize the data, a method to generate optimal T1 contrast has to be chosen. Most centres use saturation pre-pulse to null the signal and then wait for signal recovery (Fig 1.2-15).

With such saturation recovery pulse sequences signal depends on the amount of the contrast agent: good perfusion = high concentration of contrast agent = rapid recovery of Mz magnetization = bright tissue; reduced perfusion = low concentration = slow recovery of Mz magnetization = dark tissue. In comparison to inversion-recovery sequences that are used for late gadolinium enhancement, saturation recovery pulse sequences have the advantage that the contrast is independent of heartbeat variations during ECG-triggered image acquisition.

1.3 High resolution CMR

The latest developments of CMR perfusion offer the possibility to acquire very high-resolution images during first pass of the contrast agent, allowing multiple measurements of blood flow across the left ventricular wall (51-55). This high spatial resolution results in an improved visual detection of subendocardial perfusion abnormalities, as ischemia preferentially affects the subendocardial layers of the left ventricle (LV)(56-58), and in an improved detection of hemodynamically significant coronary artery disease (CAD)(59-61) . Furthermore, optimized CMR techniques provide data suitable for true quantification of blood flow in areas of myocardium as small as 17 mm^3 (corresponding to the size of a voxel – 1.3 x 1.3 x 10 mm).

True high resolution quantification of perfusion images offers a unique capability to localize and measure subendocardial ischaemia. It may be useful for detecting ischaemia in patients without significant CAD, while using segmental analysis for CMR imaging will result in loss of spatial information and ignoring a relevant part of the diagnostic information about the extension, localization, and transmurality of ischemia provided on visual assessment by high-resolution CMR.

Up to now, only a few studies have used stress high resolution CMR for detecting subendocardial perfusion deficit (62-64) and CMR has not been validated specifically. We believe that high resolution CMR stress perfusion has the potential to develop into the principal diagnostic technique for the assessment of perfusion deficits.

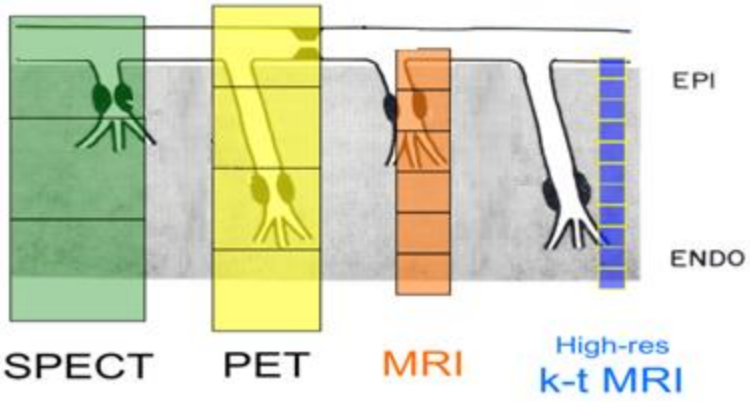

Figure 1.3-1 Schematic comparison of spatial resolution between SPECT, PET, standard MRI and high-resolution k-t MRI (keyhole technique) (65,66). Nuclear medicine techniques are relatively limited in spatial resolution, since SPECT and PET can only offer 2-4 voxels across the left ventricular wall. Standard clinical MRI (nowadays available on all the new scanners installed) can offer up to 6 voxels, while high-resolution k-t perfusion MRI has more than 10 voxels across the wall allowing discrimination of multiple perfusion layers.

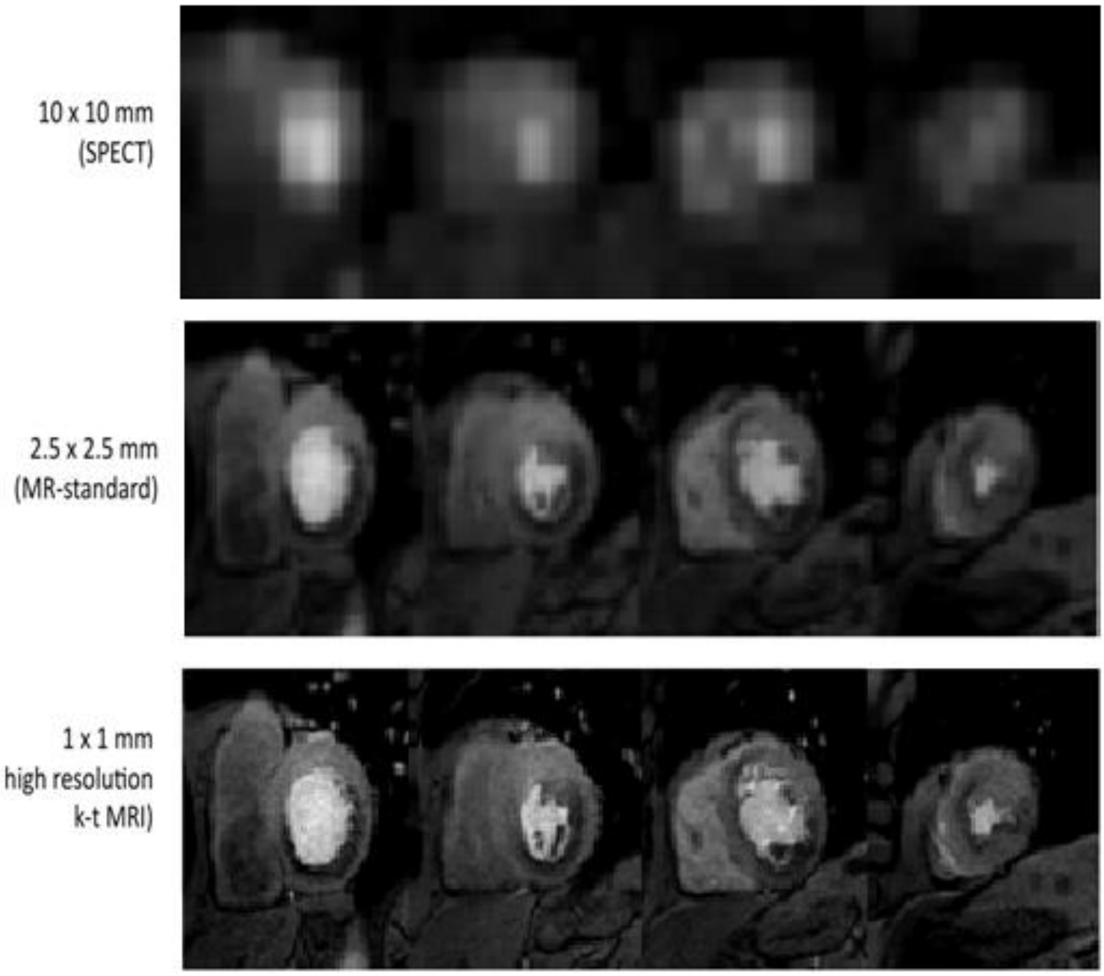

Figure 1.3-2 Comparison between down sampled MR images to simulate SPECT and standard MR resolution, compared with high resolution k-t MRI at 3T microsphere concentration, adapted from (43).

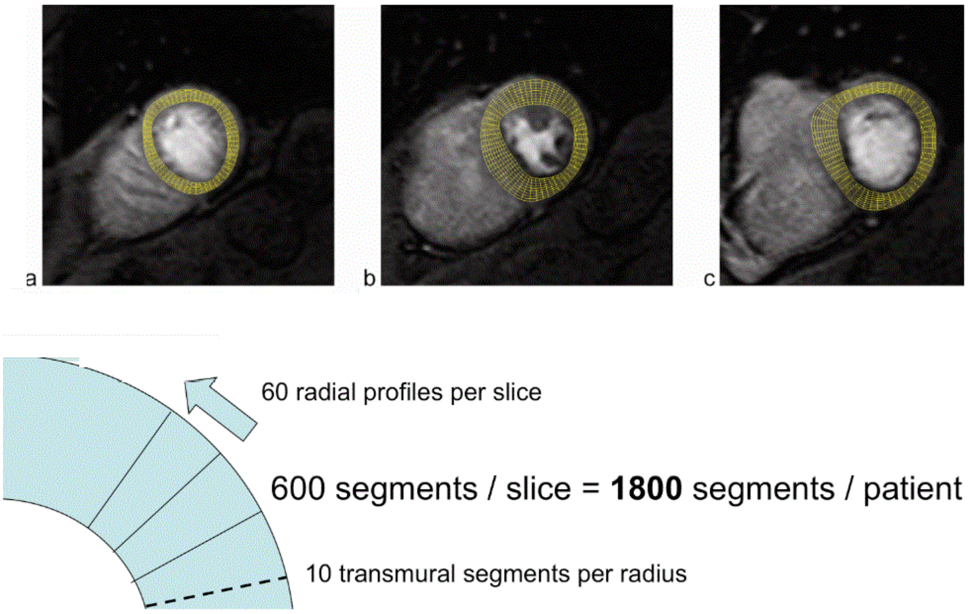

Figure 1.3-3 A high resolution (voxel-wise) segmentation for three slices of myocardium .The amount of segments can easily be increased. Here, 600 segments are shown for each slice, instead of the 6 segments as described by the AHA model.

For the high resolution (voxel-wise) analysis of the myocardium, a sampling grid which divides the LV into 3 slices (basal, mid cavity and apical slice) (49) has been chosen. Each slice is then divided into 10 further transmural positions starting from the sub-endocardium to the sub-epicardium and 60 angular positions resulting in a total of 600 regions of interest (ROI) per slice (Fig 1.3-3). This sampling grid allows us to acquire same number of ROI independent of the thickness of the slice and resolution of the images (or in other words acquisition parameters). With the current available high resolution imaging techniques, average size of ROIs in the sampling grid (sampling grid voxels) is similar to size of an acquisition voxel. However in some cases such as patients with hypertrophic cardiomyopathy, size of the sampling grid voxel can be bigger than size of an acquisition voxel. In this thesis the phrase voxel-wise is referred to the sampling grid voxels and not the acquisition one.

1.4 Assessment of Perfusion

Dynamic MRI following the injection of a bolus of gadolinium contrast medium permits the assessment of first-pass myocardial enhancement, which can yield information concerning regional myocardial blood flow (MBF). The regional variations of signal intensity (SI) in each ROI (one voxel, or a group of voxels) of the MR perfusion image as a function of time provide quantitative information about tissue perfusion. By recording the heart rate or the time at which each image is acquired (images are usually acquired in series with a time increment that equals one or two R-to-R intervals), signal intensity (SI) vs. time curves can be generated. These signal intensity curves can be used to assess the myocardial perfusion using semi quantitative and quantitative methods. A typical time-intensity curve is shown in the below figure.

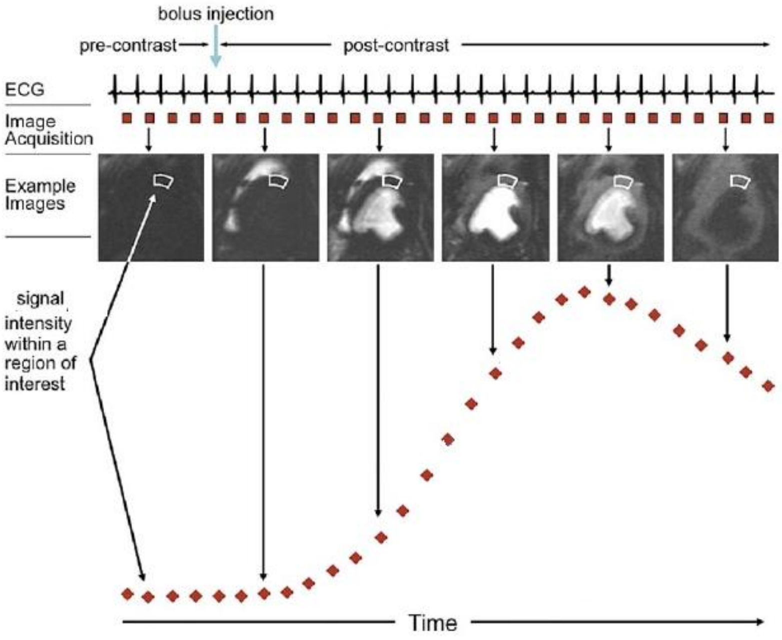

Figure 1.4-1 CMR image acquisition. The myocardial perfusion can be assessed by measuring the mean signal intensity within a region of interest and plotting the signal intensity against time using semi-quantitative and quantitative methods, modified from (67).

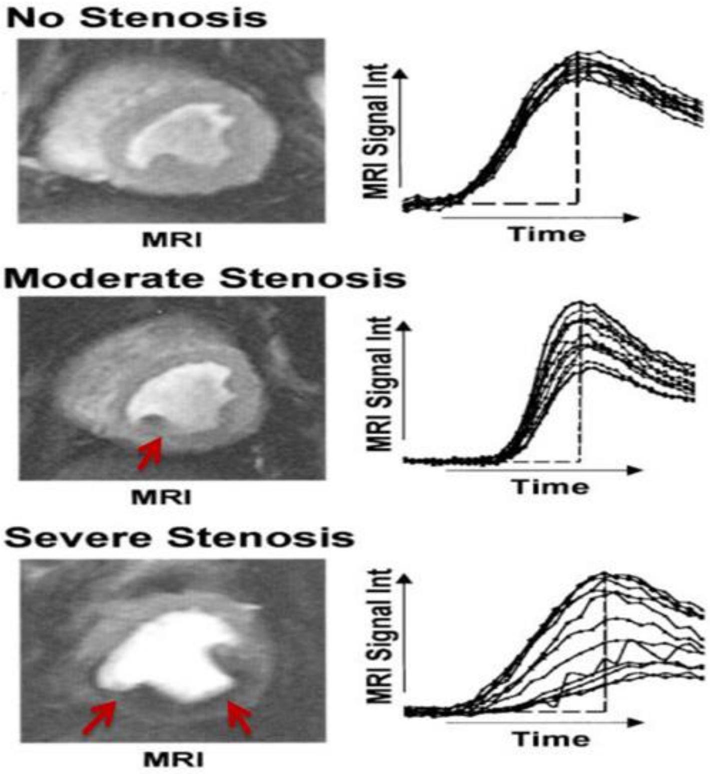

Figure 1.4-2 Magnetic resonance first pass perfusion can identify regional reduction in myocardial blood flow. From top to bottom: a single frame from the magnetic resonance short axis image; the magnetic resonance first pass perfusion signal-intensity curves for 12 myocardial segments; Magnetic resonance first pass perfusion correctly identifies a moderate flow reduction as a mild reduction of enhancement, showing a markedly reduced enhancement with a severe stenosismodified from (67).

First-pass myocardial perfusion magnetic resonance images obtained in patients have been generally evaluated by visual assessment (68-70) and by semi-quantitative approaches such as upslope analysis of the myocardial SI curve (14,68,71). The use of fully quantitative analysis of myocardial first-pass contrast-enhanced MRI allows the absolute quantification of MBF in units of mL/g/min and may permit more accurate and objective assessment of altered myocardial perfusion in patients with heart disease(3,4,15,72-74).

1.4.1 Visual Assessment

Visual assessment is based on the identification of regions with lower intensity in comparison to normal myocardial segments. The observation of the arrival of the contrast agent wash in is the best parameter for visual assessment. Care needs to be taken to not interpret small subendocardial rim-like black areas as ischemia. They are maybe due to strong differences of magnetization within a small area. The artefact can be reduced by using smaller doses of contrast agent and higher spatial resolution (75-77). Visual assessment is usually performed comparing stress and rest images, and viability images obtained with late gadolinium enhancement techniques. CMR visual assessment is reported to have sensitivity and specificity of 95% and 78% respectively (14).

1.4.2 Semi-quantification

Similarly to the visual assessment, the speed of the wash in of the contrast agent is the best parameter for semi-quantification.

The upslope of the contrast agent wash in is used as an index for blood flow. The simplest approach is a linear fit of the time curve of the myocardial signal. To correct for different arrival speeds of the bolus during rest and stress, the myocardial upslope is normalized by the upslope of the signal intensity curve in the left ventricular (LV) blood pool (68). These empirical adjustments were used to define a perfusion index, which could be calculated for rest and stress. Consequently, the parameters obtained from dividing the stress perfusion index by rest value are termed “myocardial perfusion reserve index”. More recently the area under the myocardium signal intensity curve, up to the time where the first pass peak is observed in the blood, was used to estimate myocardial perfusion reserve (78).

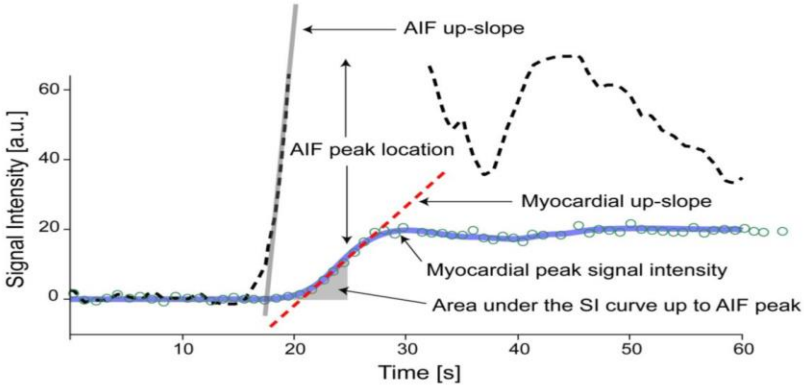

Figure 1.4-3 The signal intensity changes in the LV blood pool (arterial input function AIF dashed line), and in an anterior segment of the left ventricle (blue line). The dashed red line is the up-slope parameter, and gives the initial rate of contrast enhancement. It is often normalized by the up-slope of the AIF. The area under the tissue curve (gray shaded area), up to the location in time where the peak of the AIF is observed, has been proposed as an alternative parameter to assess perfusion. Image adapted from (29).

Even though this approach is not fully quantitative and perfusion indices cannot be compared in magnitude directly to the coronary flow reserve ratio measured in the catheterization laboratory, it is relatively simple to estimate the perfusion index from the signal intensity curves. Moreover the perfusion reserve index calculated from the upslope has been shown to accurately discriminate between ischemic and normal territories (79). Semi quantitative assessment has shown to have sensitivity and specificity of 99% and 83%, respectively(14).

However there are a few studies demonstrating the underestimation of perfusion parameters by semi-quantitative methods (80,81). Moreover semi-quantitative analysis relies on a ratio which introduce a bias on the data itself and the relationship between MBF and the semi quantitative methods parameters such as the curve upslope is not as clear-cut as the relationship between MBF and the impulse response amplitude which we get from quantitative analysis (28,30).

1.4.3 Full quantification

Absolute quantification of myocardial perfusion in (ml/g/min) of tissue is feasible from first pass myocardial perfusion CMR data. The quest to fully quantify myocardial perfusion has been largely motivated by the desire to obtain quantitative, observer-independent, and reproducible measures of the myocardial perfusion status. In order to estimate the MBF, quantification methods deconvolve the signal intensity in the LV blood pool with the signal intensity curve in myocardium. Whether a quantitative approach improves the accuracy of myocardial perfusion imaging, such as for the detection of coronary artery disease, still remains controversial. But in the research area, there is a long line of evidence proving that the measurement of myocardial perfusion leads to new insights in coronary physiology and the etiology of cardiac diseases.

In this thesis we focus on full quantification of myocardial perfusion on the voxel level, and we provide evidence for the feasibility of the high resolution (voxel-wise) quantification of myocardial perfusion for the detection of coronary artery disease.

1.4.4 Contrast to noise ratio

An important parameter for the evaluation of SI curves and perfusion assessment is the contrast to noise ratio (CNR) of the SI curve. CNR is defined as the ratio of the observed SI change from baseline to peak, divided by the standard deviation (STD) of the SI curve before contrast enhancement:

$$CNR = \frac{SI_{peak} - SI_{baseline}}{STD_{baseline}}$$

The CNR depends on many factors including: the contrast agent dosage, the size of the Region of Interest (ROI) used and the used MR pulse sequence parameters (e.g., the flip angle). Improvements of the CNR by the use of higher contrast-agent dosages are limited by the requirement for quantitative perfusion studies to maintain a linear relationship between the SI and the contrast-agent concentration, which is only maintained with low contrast-agent concentrations (this will be explained further in chapter 2).

Although voxel wise analysis takes full advantage of the underlying spatial resolution of the images, it suffers from a poor CNR. To overcome the latter shortcoming issue, we can group voxels and increase the ROI size in the myocardium. Under the assumption that SI noise in each voxel of a myocardial tissue region is additive white Gaussian noise, the CNR is expected to increase in proportion to $N^{1/2}$, where N represents the number of voxels in the given ROI.

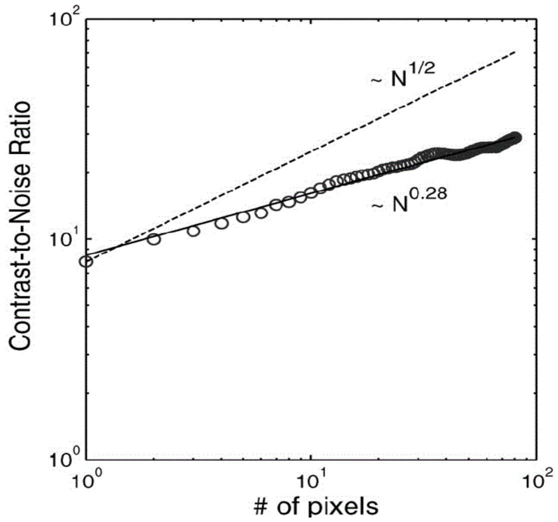

Figure 1.4-4 The CNR was determined for a range of myocardial ROI sizes. CNR is assumed to be proportional to the square root of the number of pixels in the ROI(N). Image adapted from (28).

However, Jerosch-Herold et al.(28) demonstrated that the variation of the CNR as a function of the number of voxels in a user-defined myocardial ROI, fell below the above prediction of an increase proportional to $N^{1/2}$ (Fig 1.4-4) which suggests that noise in adjacent voxels is not uncorrelated, and is not necessarily random (i.e. not white Gaussian noise). The use of SI curves with CNR ratios higher than 10:1 for perfusion analysis was recommended in this study.

1.5 Key points

- Cardiovascular magnetic resonance (CMR) first-pass perfusion provides high spatial resolution images of myocardial ischemia, allowing regional myocardial perfusion assessment and separate visualization of both subendocardial and subepicardial layers.
- The regional variations of signal intensity in MR perfusion images as a function of time (image number) provide quantitative information about tissue perfusion.
- CMR techniques provide data suitable for true quantification of blood flow in areas of myocardium as small as 17 mm^3 (corresponding to the size of a voxel – 1.3 x 1.3 x 10 mm).
- True quantification of very high resolution perfusion images offers a unique capability to localize and measure subendocardial ischaemia and may be useful for detecting ischaemia in patients without significant CAD.

2 Perfusion assessment

In dynamic contrast enhanced cardiovascular magnetic resonance imaging (DCE-CMR) perfusion studies, contrast agents are injected into patients while at stress and rest, to produces local changes of T1 relaxation properties in the tissue and the blood.

Once contrast agent is injected it flows through the heart and temporarily distributes in the myocardium before being washed out of the body. MRI is able to obtain serial images with sub-second resolution after the injection. These perfusion images can be evaluated with three different methods, visual assessment, semi-quantitative assessment and quantitative approach which allow more accurate and objective assessment of myocardial perfusion in comparison to the other methods.

In this chapter, we focus on fully quantitative assessment of myocardial perfusion using MRI. We start with the performance requirements and theoretical background of absolute myocardial blood flow (MBF) quantification by myocardial perfusion MRI, and go on to describe the mathematical models used for quantification.

2.1 Signal intensity vs. contrast agent concentration

Several studies have been performed to investigate the quantitative relationship between the amount of contrast agent and the signal intensity (82-85). The qualitative relationship of the observed behaviour is quite obvious to some extent: a higher tracer concentration gives a higher signal. However accurate full quantification of MBF by myocardial first-pass perfusion MRI is heavily dependent on a linear relationship between signal intensity and the concentration of gadolinium contrast medium (i.e rate of increase in gadolinium concentration = rate of increase in signal intensity).

The characteristic intensity curves in the myocardium are considered as the output of the system. The blood flowing through the myocardium follows directly from the blood in the LV. Therefore there is direct relationship between this myocardial tissue curve (output) and the arterial input function (AIF) taken from the blood pool in LV. Moreover the perfusion is in essence the relationship between these two curves. Thus in order to measure the perfusion precisely, both the signal in the left ventricular (LV) blood pool and signal in the myocardium must behave in the same linear fashion with the concentration of gadolinium contrast medium.

2.1.1 The linearity of left ventricular blood pool and myocardial signal intensity

To maximize the contrast-to-noise ratio (CNR) in the myocardium, a large gadolinium bolus and a long recovery delay (time from saturation pulse to the beginning of the readout) is preferred. However, at high gadolinium concentration full longitudinal magnetization recovery occurs with a long saturation recovery time, which may cause clipping of LV blood signal intensity (nonlinear relationship) (Fig 2.1-1). Further increases in gadolinium concentration may even reduce the signal by T2* effects due to paramagnetic characteristics of the gadolinium This spatial characteristic can produce local field inhomogeneities that cause spin dephasing on gradient-echo images. As a consequence, an accurate estimation of the arterial input function (AIF), which is normally measured from the LV blood pool signal intensity, requires a low gadolinium dose. To meet the competing requirements for a low gadolinium dose (AIF) and a high gadolinium dose (CNR) in a single perfusion scan, various approaches have been proposed.

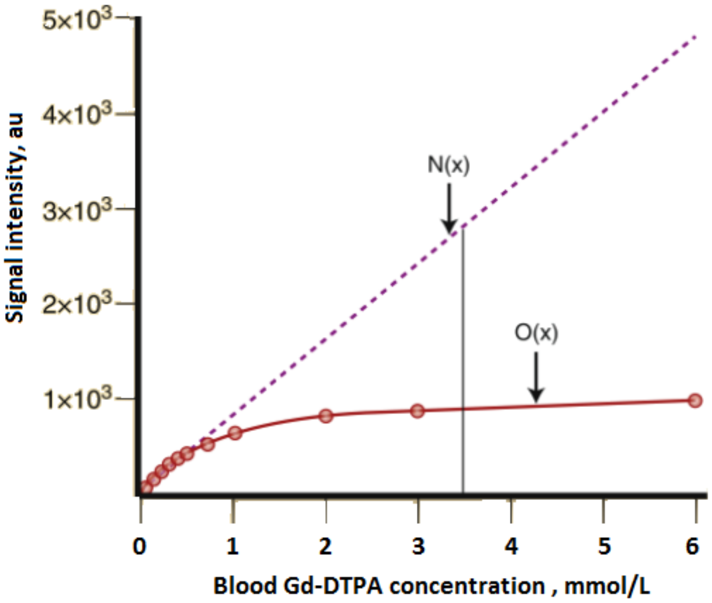

Figure 2.1-1 Relationship between blood signal intensity and Gd-DTPA (gadolinium diethylenetriamine pentaacetic acid) concentration determined in human blood samples by using a saturation recovery myocardial perfusion magnetic resonance sequence (balanced Turbo Field Echo, repetition time = 3.0 ms; echo time = 1.5 ms; flip angle = 40°; saturation recovery time = 200 ms) (O(x)) and the theoretical linear curve of the blood signal intensity versus Gd-DTPA concentration without saturation effects (N(x)). Saturation effect is observed when Gd-DTPA concentration exceeded 0.67 mmol/L. The peak left ventricular concentration was previously estimated as 3.5 ± 1.4 mmol/L (4 mL/s, 0.05 mmoL/kg; vertical line) (86). (modified from Ichihara et al. (74)).

To preserve an accurate AIF, previous studies using quantitative measures have focused on low doses (0.025–0.05 mmol/kg) of contrast agent (3,4,87-89). Low-dose techniques are applied for precise and reproducible absolute quantification of cardiac perfusion (3,4,87-89). This approach is limited by a low CNR in the myocardial tissue as a result of limited myocardial enhancement.

Dual-bolus first-pass perfusion MRI methods were introduced to allow the use of high gadolinium concentration contrast to assess the myocardium with optimum CNR, and a lower gadolinium concentration bolus to maintain the linearity of the LV signal intensity and to accurately determine the AIF (81,90-93). Christian et al. (81) demonstrated in their canine experiment that a dual-bolus method allowed accurate measurement of absolute epicardial and endocardial perfusion across a wide range of blood flow rates (0 to > 5.0 mL/min/g). Recently, the same group compared the dual-bolus to single-bolus quantitative perfusion MRI for estimation of absolute MBF in a canine model (91). Their study demonstrated that both single-bolus (0.025 mmol/kg) and dual-bolus (0.0025 and 0.10 mmol/kg) perfusion methods correlated closely with MBF, but with greater signal and contrast in the dual-bolus images (91). A recent study conducted by Utz et al. (92) has demonstrated that the dual-bolus technique (0.005 and 0.05 mmol/kg) is potentially superior to a standard single-bolus (0.05 mmol/kg) protocol for the assessment of myocardial perfusion reserve (MPR). This study demonstrated that regional MPR can be assessed with a reduced coefficient of variation using a dual-bolus protocol (92). The advantages of dual-bolus technique are currently achieved at the cost of increased complexity in both the imaging protocol and post-processing.

In a third approach, the dual-T1 sensitivity technique or dual inversion time method has been suggested (94). It acquires both low-resolution, low T1-sensitivity blood pool and high-resolution, high T1-sensitivity myocardial data within each RR interval. This technique uses a shorter inversion recovery time (eg, 20 msec) to measure the AIF and a longer recovery time (e.g., 600 msec) to assess the myocardial perfusion response (94).

Finally, an alternative approach is to use post-imaging signal intensity calibration, such as in vitro phantom-based (95) or in vivo image theory–based (96) methods to compensate for signal distortion due to T1 shortening at peak contrast.

Previously, it had been assumed that within the myocardium a nonlinear relationship between signal and concentration of gadolinium contrast medium was not a problem at concentrations required to measure physiologic blood flow. However, a growing body of evidence suggests that myocardial nonlinearity becomes significant in the contrast concentration range necessary for sufficiently high myocardial CNR. A previous healthy volunteer study has shown the signal intensity does not increase proportionally with gadolinium contrast concentrations in the myocardium of more than 0.05 mmol/kg (97). Recently, Hsu et al. (98) demonstrated that nonlinearity between myocardial signal intensity and gadolinium contrast concentration affects the quantification of perfusion when full-dose Gd-DTPA contrast (0.1 mmol/kg) is used in healthy human subjects. However, they also demonstrated that nonlinear correction of myocardial signal intensity is feasible and improves the quantification of perfusion (98). In this thesis a universal dual-bolus injection scheme as described by Ishida et al. (99) has been used to avoid confounding effects due to signal saturation.

2.2 Quantification of high-resolution magnetic resonance perfusion

As mentioned earlier the perfusion is in essence the relationship between the AIF and myocardial tissue signal intensity curve. Several mathematical methods, which all of them are based on indicator–dilution principle, have been used to model this relationship and consequently quantify the MBF. In this section we describe these mathematical methods in detail, however before that we need to explain the theory behind perfusion modelling or in other words, we will answer- How MBF can be calculated from the AIF and tissue signal intensity curves?

2.2.1 Indicator dilution principle

An indicator (contrast agent) is a substance that permits observations of some element of volume of the fluid under study. The indicator shows the position of the element of the volume in the space with respect to time and distinguishes the indicated element from all other elements of volume. In practice a known quantity of indicator is injected into a fluid flowing at unknown rate through a system of unknown volume. Then the fluid is sampled in one or more points downstream from the point of injection and the concentration of the indicator diluted into the fluid is measured as a function of time. The indicator–dilution theory, developed by Zierler et.al.(100) provides a mathematical basis for characterizing the vascular physiology of a tissue based on the changes in the concentration of the indicator. Moreover it allows us to calculate the flow rate of fluid into regions of tissue using the concentration of the fluid.

The indicator may be injected into the system in any of a number of ways, usually only once and as rapid as possible, or continuously at a constant rate. However, in order to calculate the flow based on the Indicator–dilution principle an assumption must be made. It is necessary for flow and volume to be constant during the period of the measurement, it means every unit of fluid entering the system must eventually leave the system or we can say we should consider it as a linear single input single output system.

Based on the indicator–dilution theory, the measured LV signal intensity (tracer concentration), $C_{aif}(t)$ and the measured myocardium tissue signal intensity, $C_{myo}(t)$, under the assumption that the initial concentration in tissue region is zero, are related according to the following convolution:

$$C_{myo}(t) = \int_0^t C_{aif}(t-\tau)h(\tau)d\tau = C_{aif}(t) * h(t) \quad [1]$$

where $h(t)$ is the myocardial impulse response.

Deriving the convolution equation

Let m unite of indicator be injected at time zero into a system, and measure the concentration of the indicator at exit as a function of time, $C_{out}(t)$. The amount of indicator, dm, leaving the system during a small time interval between time t and $t + dt$ is the concentration of indicator leaving the system, $C_{out}(t)$, multiplied by the volume of fluid leaving the system during this time interval, and this is the flow rate , F, (in unite of ml/min) multiplied by time.

$$dm = C_{out}(t) \cdot F \cdot dt \quad [2]$$

Now consider the amount of indicator which leaves the system at time t is made by indicator introduced into the system during the time interval between s and $s + ds$ time unite before t. The amount of indicator introduced during this time interval is $m_{in} \cdot ds$. Of that indicator, the fraction eliminated per unit time at time t is $k(t)$. Therefore, of the indicator, $m_{in} \cdot ds$, introduced between s and $s + ds$ time unites before t, the amount which is leaving per units time at t is $k(s) \cdot m_{in} \cdot ds$.

Summing all such time intervals before, the rate at which indicator leaves the system at time t is:

$$m_{out} = \int_0^t k(s) \cdot m_{in}(t - s) \cdot ds \qquad [3]$$

This is also equal to: $m_{out} = C_{out}(t) \cdot F$.

Therefore:

$$C_{out}(t) = \frac{1}{F} \int_0^t k(s) \cdot m_{in}(t - s) \cdot ds \qquad [4]$$

The amount of indicator at the input to the system is

$$m_{in} = C_{aif}(t) \cdot F.$$

Under assumption that flow is constant and that the system describing the flow into and through the tissue is linear and stationary, the equation [4] can be written as:

$$C_{out}(t) = \int_0^t C_{aif}(t - s) k(s) ds\ . \qquad [5]$$

where $k(t)$ is a transfer function which describes the fraction of injected indicator leaving the system per unit of time.

However CMR allows the detection of the mass of contrast agent residing in the tissue ROI, C_{myo}, instead of measurement of ROI out flow mass. Therefore we need to find a relation between C_{myo} and $C_{aif}(t)$ to be able to estimate the flow from CMR images.

According to indicator–dilution theory, the amount of tracer which remains in the tissue region after injection of the indicator is:

$$C_{myo} = \int_0^t F[C_{aif}(s) - C_{out}(s)] ds. \qquad [6]$$

By inserting equation 5 in the above equation instead of $C_{out}(t)$:

$$C_{myo} = \int_0^t F C_{aif}(s) * [1 - k(s)] ds = C_{aif}(t) * h(t).$$

Here $h(t)$ represents the fraction of contrast agent which has still remained in the ROI at time t and is called the tissue impulse response, the response of a tissue region to an impulse input (delta Dirac function).

The character of $h(t)$ is such that its value is zero until the tracer enters the tissue, at which point the concentration instantaneously achieves its maximum and then remains constant for a time period equal to minimum transit time required for the tracer to began to exit the tissue, finally the tracer concentration returns to zero over a period of time determined by the distribution of the transit time of the tracer molecules. This function can never be less than zero and never be greater than 1, because the quantity of indicator remaining in the system during any time interval can never be less than zero and never be more than all of it that entered the system.

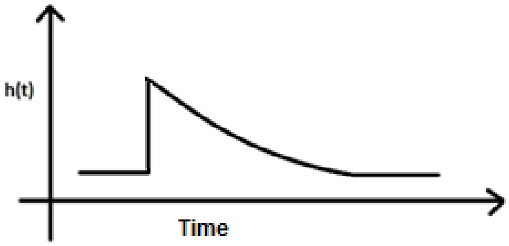

Figure 2.2-1 a graph of the impulse response function, h(t).

As mentioned earlier, the advantage of explicitly determining the tissue impulse response is the ability of deriving information about blood flow rate from it. To derive this, assume a special condition when$C_{aif}(t) = \delta(t)$, where $\delta(t)$ is the delta Dirac function. If we replace the $C_{aif}(t)$ in equation [1] and [6] with the delta function, we will have

$$\int_0^t F[\delta(s) - C_{out}(s)]ds = h(t)\ .$$

For any input function with C_{aif} and for finite flow rates, we have $C_{out}(t = 0) = 0$, as tracer cannot instantaneously pass through a ROI and reach the output after injection. Therefore initial amplitude of the $h(t)$ (tissue impulse response) will be equal to the flow rate, $h(0) = F$ and the perfusion value in the myocardium ROI will be equal to flow divided by density of myocardium, $h(0)/SG_{myo}$. As $SG_{myo} \approx 1$, Myocardium blood flow (MBF) can be considered as myocardial perfusion.

2.2.2 Deconvolution

Most quantitative methods are based on an inverse operation and they deconvolve the tissue and LV signal in order to estimate tissue impulse response function, $h(t)$, from which myocardium perfusion can be computed (4,101-104). This inverse operation is challenging because it consists of inverting the convolution of $h(t)$ with $C_{aif}(t)$, which is in this context an ill-posed noise sensitive inverse problem and it needs regularization.

2.2.2.1 Ill-posed problem

A problem will be ill –posed if it does not fulfil the Hadamard definition of a well-posedness problem. Base on the Hadamard well-posedness definition a problem is well posed if:

1) For all admissible data, a solution exists

2) For all admissible data, the solution is unique

3) The solution depends continuously on the data.

In the Z-domain deconvolution will be simplified to a multiplication and impulse response can be calculated as inverse z transform of:

$$H(Z) = \frac{C_{myo}(z)}{C_{aif}(z)} = C_{myo}(z) \cdot C_{aif}(z)^{-1}.$$

Considering the above violations, recovering $h(t)$ from observed $C_{myo}(z)$ and $C_{aif}(z)$ is an ill-posed problem as the inverse of $C_{aif}(z)$ may not exist due to incomplete data _ $C_{aif}(z)$ matrix is rank deficient (i.e. has zero eigenvalues and it is not invertible) _ or badly conditioned matrix (over determined matrix or non square matrices). Moreover, deconvolution is inherently a difficult process and therefore numerically unstable with noise contaminated data. To illustrate this, suppose that contrast agent is injected impulsively. Then the bolus must travel through the heart, which consists of three major compartments: from the injection position through the right heart, from the right heart through the lungs to the left heart, and from the left heart to the myocardium tissue. Assuming each compartment is well mixed with same mean transit time $\frac{1}{\gamma}$ (thus same kernel $\gamma e^{-\gamma t}$) [18], and the impulsive input travels through n compartments, then the arterial input at the tissue site can be represented as the n-fold convolution of the unit kernel:

$$C_{aif}(t) = \delta(t) * [\gamma e^{-\gamma t}]_1 * \dots\dots\dots * [\gamma e^{-\gamma t}]_n = \gamma \frac{(\gamma t)^n}{n!} e^{-\gamma t} \qquad [7]$$

Now consider a situation in which t the $C_{myo}(t)$ is a noisy data and causes an error in kernel estimation:

$$C_{myo}(t) + N_\varepsilon(t) = \int_0^t C_{aif}(t-s)[h(s) + E_\varepsilon(s)]ds \qquad [8]$$

where N_ε is noise in $C_{myo}(t)$ and $E_\varepsilon(s)$ is the error introduced during deconvolution process.

Based on partial integration relation :

$$\int_0^t f(s)\, D_s^n g(s) ds = \sum_{m=0}^{n-1} D_s^m f(s) D_s^{n-1-m} g(s)|_{s=0}^{s=t} + (-1)^n \int_0^t D_s^n f(s) g(s) ds$$

the convolution of the error, $E_\varepsilon(t)$, with $C_{aif}(t)$ in equation [8] :

$$\int_0^t C_{aif}(t-s) E_\varepsilon(s) ds = \gamma^{n+1}(-1)^n e^{-\gamma t} \int_0^t \frac{(s-t)^n}{n!} e^{\gamma s} E_\varepsilon(s) ds$$

can be simplified by defining function of the form $f(s) = \frac{(s-t)^n}{n!}$ and $e^{\gamma s} E_\varepsilon(s) = D_s^n g(s)$, which:

$\sum_{m=0}^{n-1} D_s^m f(s) D_s^{n-1-m} g(s) = 0, s = 0, t$.

The above sum approximates to zero at $s = t$ as $D_s^m f(s) = \frac{(s-t)^{n-m}}{n-m!}$ vanishes at $s = t$. For the above some to be equal to zero at $s = 0$, we define $g(s)$ with high degree of freedom as :

$g(s) = \sum_{m=0}^{n} \alpha_m e^{(\gamma+\beta_m)s}$, where α_m and β_m are the roots of:

$$D_s^k g(s)_{s=0} = \left[\sum_{m=0}^{n} \alpha_m (\gamma + \beta_m)^k\right] = 0.$$

Therefore $E_\varepsilon(s) = e^{-\gamma s} D_s^n g(s) = \sum_{m=0}^{n} \alpha_m (\gamma + \beta_m)^n e^{\beta_m s}$.

Assuming that $\beta_m \propto \frac{1}{\varepsilon}$, where ε is the transit time of the disturbance, then

$$E_\varepsilon(t) = o(\varepsilon^{-n}). \quad [9]$$

Whereas the measurement of the C_{myo} is corrupted by:

$$N_\varepsilon(t) = \int_0^t C_{aif}(t-s) E_\varepsilon(s) ds =$$

$$\gamma^{n+1} (-1)^n e^{-\gamma t} (-1)^n \int_0^t D_s^n f(s) g(s) ds$$

$$\gamma^{n+1} e^{-\gamma t} \int_0^t \sum_{m=0}^{n} \alpha_m e^{(\gamma+\beta_m)s} ds =$$

$$\gamma^{n+1} \sum_{m=0}^{n} \alpha_m \frac{e^{\beta_m t} - e^{-\gamma t}}{(\gamma+\beta_m)} = o(\varepsilon) \qquad [10]$$

The error is $o(\varepsilon^{-n})$, while the noise is $o(\varepsilon)$. Therefore the even presence of minor noise in $C_{myo}(t)$, $N_\varepsilon(t)$, can correspond to an arbitrary large perturbation, $E_\varepsilon(t)$, in the estimation of the impulse response. When the number of tissue-injected components increases, the deconvolution will be more sensitive to the noise. This susceptibility to noise can be reduced by constraining deconvolution by a minimum of prior information about the solution.

2.2.2.2 Regularization and optimization

In general terms, regularization is the approximation of an ill posed problem by a family of adjacent well posed problems. In simple worlds, regularization involves introducing additional information in order to solve an ill-posed problem or to prevent over fitting. This information is usually of the form of adding restrictions or bounds on the norm of the results.

While a great many regularization methods such as discrete Fourier transform (DFT), singular value decomposition (SVD) have been used for solving the ill-posed inverse problems, the least square minimization methods are considered as simplest form of regularization (105,106).

$$min \left\| C_{myo}(t) - h(t) * C_{aif}(t) \right\|^2 \quad [11]$$

These methods are based on minimizing the Euclidean distance (residual) between observed and estimated data. Different techniques are available which provide numerical solution to the problem of minimizing these residuals. Amongst all methods the most popularized ones include: Tikhonov linear regularization (L^2-norm), L^1-norm, Newtown, Gauss-Newtown method and Levenberg-Marquardt algorithm (for nonlinear least square minimization) (106). In all of these minimization techniques the tissue impulse response is estimated within the span of a given function basis $B = \{h_j\}$ with the span coefficients of ($K = \{k_j\}$). Usually the span coefficients can appear linearly in the convolution equation (it depends on the mathematical function which is used for representation of $h(t)$):

$$C_{myo}(t) = C_{aif}(t) * [\textstyle\sum_j k_j h_j] \ .$$

The above equation can be discretized in the form of

$$\boldsymbol{C}_{myo} = \boldsymbol{M}.K$$

Where $\boldsymbol{C}_{myo} = \{C_{myo}(n_j)\}, j = 1,..,N$ and $\boldsymbol{M} = \{[C_{aif} * h_j](t_j)\}$ **.**

These span coefficients can be calculated by minimizing the mean square error between the observed tissue data and the estimated one (Euclidean distance):

$$\left\|C_{myo}(t) - h(t) * C_{aif}(t)\right\|^2 = \left\|\boldsymbol{C}_{myo} - \boldsymbol{M} \cdot K\right\|^2 \ . [12]$$

However regularization methods in general solve the problem to obtain a feasible result which may not necessary be the optimal one. This drawback has led to the use of a multitude of optimization techniques for determining the optimal results from deconvolution (107).

The optimization techniques add conditions and restrictions to the regularization minimization problem (linear least square minimization) in order to define the acceptable value of the variable, such restrictions termed the constraints. The general formulation of the optimization problem can be mathematically represented as:

$$min_K \ \mathcal{P}(K)$$

$$subject\ to\ g(K) \leq 0\,, r(K) = 0$$

where $\mathcal{P}(K)$ is called optimization objective function. In my work the optimization objective function is the least square minimization problem introduced in equation 12.

The solution of this optimization problem is a set of values for the span coefficients of $h(t)$, i.e $K = \{k_j\}$, for which the objective function assumed an optimal value. Here since the non-increasing and non-negativity are the principle information about the tissue impulse response, constrained decreasing monotonicity is regarded as the most natural starting point of regularization frame work. So the optimization problem can be rewritten as:

$$minimize_{\{k_j\}} \qquad \left\|C_{myo}(t) - h(t) * C_{aif}(t)\right\|^2$$

$$\text{Subject to:} \ \ h(t) \geq 0\,,\ \ h(t)' \leq 0$$

Keeling et.al (104) demonstrated that the above constrained regularization technique performs favourably compared to Tikhonov regularization and widely used regularization methods based on SVD. In this thesis, the above constrained technique has been used to solve the ill-posed deconvolution problem and obtain $h(t)$ (and consequently MBF) from $C_{myo}(t)$ and $C_{aif}(t)$.

In order to accurately calculate absolute MBF using first-pass myocardial perfusion MRI, it is essential to use a model for $h(t)$ which best describes its behaviour and minimize$\mathrm{P}(K)$. The approaches which can be used to model and thus quantify MBF from the observed contrast enhancement can be broadly divided into two categories: model-based deconvolution, and model-independent deconvolution.

2.2.2.3 Model-Dependent deconvolution (Tracer-Kinetic Modelling)

Quantitative assessment of myocardial perfusion with MRI using tracer-Kinetic modelling has been described by several investigators since the early 1990s (83,95,108-112). Tracer-Kinetic modelling specifies the functional spaces in myocardial tissue, how tracer moves through these spaces, and how it traverses permeable barriers between spaces.

A considerable degree of simplification is necessary to arrive at models that can be used for numerical calculations and simulations. As commonly used MR contrast agents, such as Gd-DTPA, are excluded from the intracellular space and cannot penetrate any cell, we can consider a simplified model for the exchange of tracer and comprise only the vascular and interstitial spaces.

2.2.2.3.1 Two compartment modelling

In this model the distribution of tracer in the tissue is separated into two compartments: the plasma (vascular space) and the extra vascular extracellular space (EES).

The tissue is supplied with contrast agent by the arteries. Once it is in the plasma space, the contrast agent is able to diffuse to the EES in the capillary walls. The rate at which transfer of the contrast agent occurs depends on the permeability- surface area product (PS) and flow in the tissue. The contrast agent can then diffuse back from the EES to the plasma and subsequently leaves the plasma.

The mass balance of Gd-DTPA across the EES which follows from the concentration inside the plasma can be described by the following first-order differential equation established by Kety (95,111):

$$\frac{dC_{ess}(t)}{dt} = K_{ep}(C_{aif}(t) - C_{ess}(t)) \quad [13]$$

where $C_{ess}(t)$ is the signal in the EES, $C_{aif}(t)$ the signal in the blood plasma, and K_{ep} the transfer rate [min^{-1}] of tracer from the EES to the blood plasma and vice versa.

Here for the concentration of contrast agent within the plasma compartment to be equal to the concentration in the supplying artery, the plasma mean transit time is assumed to be negligible compare to data sampling interval ($MTT \ll \Delta t$), however there is evidence to suggest that this is not often the case (113,114). The above equation can be solved by convolution.

$$C_{ess}(t) = K_{ep}\int_0^t C_{aif}\,(\tau)e^{-K_{ep}(\mathrm{t}-\tau)}d\tau \qquad [14]$$

This equation explains the exchange of tracer between compartments at cellular level. In a single voxel, all different kinds of compartments are present; therefore the tissue signal in a voxel can be represented as:

$$C_{myo}(t) = v_p C_{aif}(t) + v_e C_{ess}(t) \qquad [15]$$

In which $C_{myo}(t)$ is the tissue signal, v_p is the fraction of plasma in the voxel and v_e is the fraction of EES in the voxel. Equation [15] can be rewritten as

$$C_{myo}(t) = v_p C_{aif}(t) + K_{ep}\int_0^t C_{aif}\,(\tau - \Delta T)e^{-\frac{K_{ep}}{v_e}(\mathrm{t}-\tau)}d\tau$$

$$=C_{aif}(t) * K_{ep}e^{-\frac{K_{ep}}{v_e}(\mathrm{t})} + v_p C_{aif}(t) = C_{aif}(t) * h(t) + v_p C_{aif}(t) \qquad [16]$$

In the kinetic-tracer modelling the tissue impulse response has been modelled as $h(t) = K_{ep}e^{-\frac{K_{ep}}{v_e}(\mathrm{t})}$.

2.2.2.3.2 One compartment modelling

A further simplification of the two-compartment can be done by assuming that v_p is negligible, and therefore the contribution of the contrast agent in the plasma compartment to the total tissue signal is ignored. This results in a one–compartment equation:

$$C_{myo}(t) = K_{ep}\int_0^t C_{aif}\,(\tau - \Delta T)e^{-\frac{K_{ep}}{v_e}(\mathrm{t}-\tau)}d\tau$$

$$=C_{aif}(t) * K_{ep}e^{-\frac{K_{ep}}{v_e}(\mathrm{t})} = C_{aif}(t) * h(t) \; [17]$$

Myocardium blood perfusion MBF (ml/gr/min) in the kinetic-tracer modelling is related to a parameter called K^{trans} through the flowing equation

$$MBF = \frac{K^{trans}}{E(1-H)\rho}. \qquad , \quad K^{trans} = k_{ep}v_{\mathrm{e}} \qquad [18]$$

where E is the fraction of the tracer extracted in its first pass through the capillary (extraction efficiency of the region) and ρ is the myocardial tissue density and H is the haematocrit constant which is proportion of the blood volume that is occupied by red blood cells.

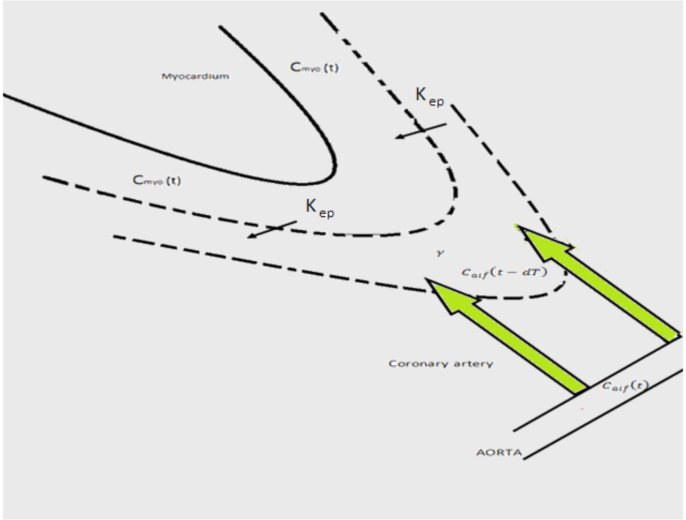

Figure 2.2-2 The model depicted graphically. dT represents the time delay between the appearances of Gd-DTPA in the aorta.. Kep describes the diffusion of Gd-DTPA over the myocardial capillary membranes

Larsson et al. (83,110) quantified myocardial perfusion from contrast-enhanced MR images of the human heart using a two-compartment model analysis. The K_{ep} of Gd-DTPA in human myocardium was quantified by measuring the longitudinal relaxation rate of the myocardium with contrast-enhanced MRI and obtaining the input function with arterial blood sampling (83,110). The K_{ep} value was 0.54 ± 0.10 mL/min/g in their study. Vallée et al. (112,115) modified Larsson's two-compartment model by defining the myocardial capillaries and the extracellular space as a single compartment.

2.2.2.3.3 Patlak plot

Ichihara et al.(74) developed a method for quantifying myocardial blood flow with minimal operator interaction by using a Patlak plot method. The Patlak plot method is based on a one-compartment pharmacokinetic model and it was introduced first by Rutland(116).

The Patlak plot method assumes that the efflux of the contrast agent from the ESS back to plasma is negligible and permits the calculation of K_{ep} by linear least-squares fitting models and significantly simplifying the analytical procedures.
The solution to equation [13] when $C_{ess}(t)$is assumed to be negligibly small compared with C_{aif}, will result in a linear kinetic model :

$$\frac{dC_{ess}}{dt} \cong K_{ep}C_{aif}(t)\ \ ,\ C_{myo}(t) = v_e C_{ess}(t)$$

$$C_{myo}(t) = K_{ep}\int_0^t C_{aif}\,(\tau)d\tau$$

$$K_{ep} = C_{myo}(t)/\int_0^t C_{aif}(\tau)d\tau$$

The plot of $C_{myo}(t)$ against $\int_0^t C_{aif}(\tau)d\tau$ yields a straight line with a slope of K_{ep} and therefore MBF. But this linear relationship is maintained under the assumption $(C_{aif}(t) \gg C_{ess}(t))$ and will be no longer valid after Gd-DTPA transferred back to blood pool.

The major remaining problem of the kinetic–tracer modelling is that the model-based approach does not provide MBF directly but rather the product of E and MBF, i.e., K_{ep} and thus K^{trans} (Eq [18]). If MBF is to be determined from K_{ep}, the value of E for gadolinium contrast agent must be known. This value, which is highly dependent on the permeability surface of the system, can change based on permeability or flow limitation of the system. It may reflect the flow, or it may reflect PS. More generally, it reflects a mixture of the two. To date there are few reports where the E for gadolinium contrast agent has been investigated. All of these studies were conducted in a canine model and estimated the value of the E to be approximately 0.45 (108,109,111). Moreover high temporal resolution DCE-MRI can readily be achieved on modern scanners these days and the error introduced by MTT effects thus have to be considered as the MMT is not negligible any more compare Δt

2.2.2.4 Model independent deconvolution

The main focus of this thesis is model– independent deconvolution of the myocardial perfusion, where no specific functional model of the tissue structure is used.

Model independent deconvolution, which is based on indicator–dilution theory, can be used to estimate the tissue impulse response, $h(t)$, and perfusion without any assumption and it is widely used with intravascular contrast agents and has been applied with extracellular contrast agents to quantify myocardial, renal and tumour perfusion(4-6,29,117). Several models have been introduced and used by the researchers for quantification of MBF. Here we have picked the most favourable methods and have described them in detail. Also we have introduced a novel approach for perfusion assessment which is an optimized version of one of the existing methods.

2.2.2.4.1 B-spline

Jerosch-Herold et.al (4) developed a model-independent deconvolution method that parameterized $h(t)$ as a sum of weighted B-spline functions and stabilized the solution by using Tikhonov regularization.

A spline curve is a sequence of curve segments that are connected together to form a single sufficiently smooth continuous curve. A B-spline function which is similar to Bézier curve is a polynomial piecewise function that has a high degree of smoothness at the places where the polynomial pieces, known as *knots*, are connected.

The equation for k-order B-spline with $p+1$control points $(h_0, h_1, \dots, h_p)$ is (4,118,119):

$$h(t) = \sum_{j=0}^{P} h_j B_j^{(k)}(t) \qquad t_{k-1} \leq t \leq t_{p+1} \; [19]$$

In a B-spline function each control point is associated with a positive definite basis function $B_j^{(k)}$which is given by the recurrence relations:

$$B_j^{(k)}(t) = B_j^{(k-1)}(t)\frac{t-t_j}{t_{j+k-1}-t_j} + B_{j+1}^{(k-1)}(t)\frac{t_{j+k}-t}{t_{j+k}-t_{j+1}} \qquad [20]$$

$$B_j^{(1)}(t) = \begin{cases} 1 & t_j \le t \le t_{j+1} \\ 0 & elsewhere \end{cases}$$

$B_j^{(k)}$ is a polynomial of order *k* (degree *k*-1) which is nonzero at $t_j \le t \le t_{j+k}$. *k* must be at least 2 (first degree-linear) and can be not more, than *p*+1 (the number of control points).

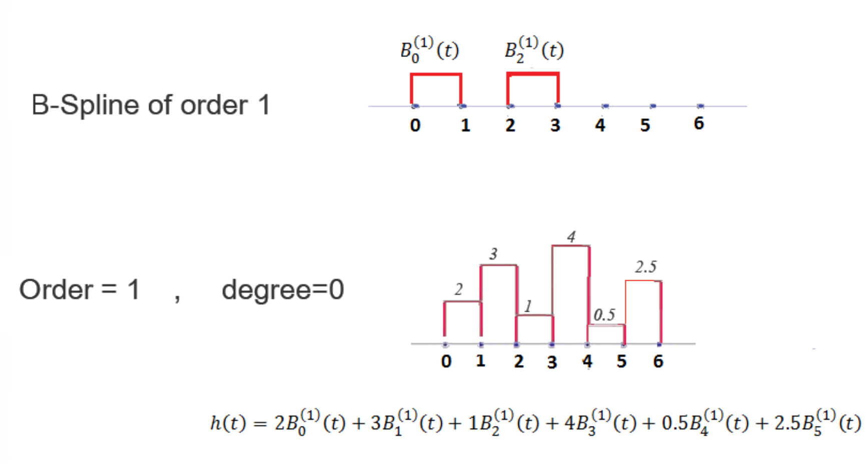

Figure 2.2-3 an example B-spine function of order 1

A knot vector $(t_0, t_1, \dots t_{p+k})$,where $t_0 \le t_1 \le t_2 \le \cdots \le t_{p+k}$, must be specified. Across the knots basis functions are $C^{k\text{-}2}$ continuous. The knots can be considered as division points that subdivide the interval $[t_0, t_{p+k}]$ into knot spans. The half-open interval $[t_j, t_{j+k})$ is the *j*-th knot span. The total number of knot spans for B-spline curve of order *k* with *p* control point is *(p-k+2)*. As since $B_j^{(k)} = 0$ for $t \le t_j$ or $t \ge t_{j+k}$ therefore a control point h_j influences the curve only for $t_j \le t \le t_{j+k}$. The shapes of the $B_j^{(k)}$basis functions are determined entirely by the relative spacing between the knots $(t_0, t_1, \dots t_{p+k})$.

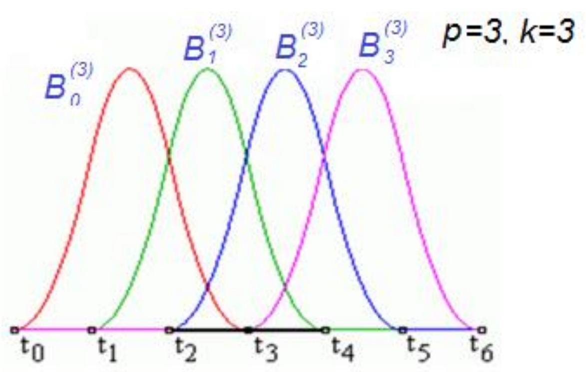

Figure 2.2-4 Iterations scheme for cubic (k = 3) basis functions. Here the total number of knot pans is 3.For a given t value in the knot span$[t_2, t_3)$ and $[t_3, t_4)$, only k=3 basis functions are non zero, therefore B-spline depends on k nearest control points at any point t.

B-spline basis functions are nonnegative, $B_j^{(k)} > 0$, and have "partition of unity" property

$$h(t) = \sum_{j=0}^{P} B_j^{(k)}(t) \quad t_{k-1} \le t \le t_{p+1}$$

therefore $0 \le B_j^{(k)} \le 1$.

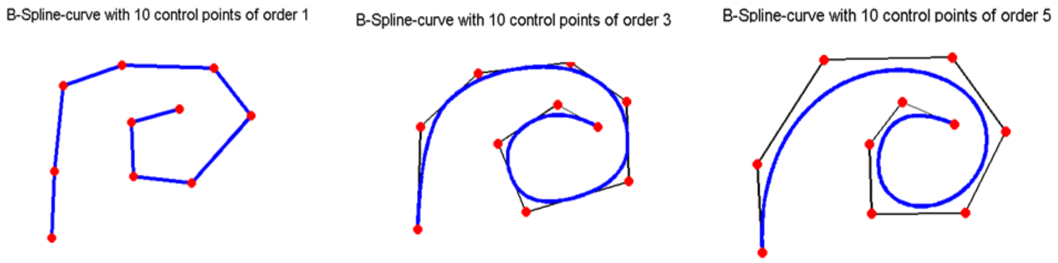

Figure 2.2-5 B-spline curve fitting 4th order with 10 control points. It can be seen that the greater the order, the further the curve can lie from the poles of its control polygon.

Using the above span of basis function for $h(t)$ we can rewrite the equation [1] as:

$$C_{myo}(t) = \sum_{j=1}^{P} h_j \int_0^t C_{aif}(t_i - s) B_j^{(k)}(s) ds$$

This in discrete format will be equal to

$$= \sum_{j=1}^{P} D_{i,j}\, h_j$$

Where D is a P x N design matrix

$$D_{i,j} = \int_0^{t_i} C_{aif}(t_i - s) B_j^{(k)}(s) ds = R_j A_i$$

For more compact notation we introduced $A_{i,j}$, a convolution matrix constructed from the $C_{aif}(t_i)$ for $i = 1 \dots \dots N$ and $R_{i,j}$ is a matrix of spline bases.

$$A = \begin{bmatrix} C_{aif}(0) & 0 & \dots & 0 \\ C_{aif}(1) & C_{aif}(0) & \dots & 0 \\ \vdots & \vdots & \ddots & \vdots \\ C_{aif}(N-1) & C_{aif}(N-2) & \cdots & C_{aif}(0) \end{bmatrix}, R = \begin{bmatrix} B_1^k(1) & B_1^k(2) & \dots & B_1^k(N) \\ B_2^k(1) & B_2^k(2) & \cdots & B_2^k(N) \\ \vdots & \vdots & \ddots & \vdots \\ B_P^k(1) & B_P^k(2) & \cdots & B_P^k(N) \end{bmatrix}$$

$$A = [A_1, A_2 \dots . A_N] \;, R' = [R_1, R_2 \dots \dots R_P].$$

Now we can find the tissue impulse response by solving the least square minimization problem

$$min_{h_j} \left\| C_{myo} - D.\boldsymbol{h} \right\|^2 \;, \boldsymbol{h} \in \boldsymbol{R}^p. \qquad [21]$$

All previous studies using this method (4,28,117,120) have found the tissue impulse response from the above ill posed problem using Tikhonov regularization. Here we have used the regularization technique described in section 2.2.2.2 to calculate $h(t)$ and myocardium blood flow consequently (4,120).

2.2.2.4.2 Fermi function model for deconvolution

The use of Fermi function was motivated by the observed similarity between the simulated impulses response for an intra vascular tracer and shape of the Fermi function. In nature the Fermi function is a probability distribution function and is generally in the form of:

$$H_k(\mu) = \int_0^\infty \frac{x^k dx}{e^{x-\mu}+1} \quad [22]$$

A simplified version of the above equation when $x^k = \delta(t)$, is called Fermi Dirac function and has been used widely in physics to describes the energies of single particles in a system.

As mentioned in the sections 2.2.1, $k(t)$ is the frequency, or probability density function, which describes the fraction of indicator leaving the system at time t and $h(t) = 1 - \int k(t)$ represents the probability that the tracer remains in the system. As Fermi-Dirac function is a probability distribution function, its analytical expression, can be used to represent $h(t)$ in equation [1] :

$$h(t) = F.\left[1 - \int_0^t k(s)ds\right] = F.\left[\frac{1}{e^{[(t-\tau_0-\tau_d).k]+1}}\right] \theta(\tau_d) \; [23]$$

where $\theta(\tau_d)$the unit step is function, τ_d accounts for the delay between the LV signal time course and the input to the region of interest being analyzed.$\tau_0$characterizes the width of the shoulder of the Fermi function during which little or no contrast agent has left the ROI and k is the decay rate of $h(t)$due to contrast agent washout. Initial value of $h(t)$ is proportional to myocardium blood flow, $(h(t=0) = F)$.

We have fitted time curves for tissue to the Fermi function with a Marquardt-Levenberg nonlinear least square algorithm by letting $F, \tau_0 \; and \; k$ vary and maintain τ_d fixed at a user determined value(88,103).

2.2.2.4.3 Exponential basis deconvolution

Keeling et al.(5) proposed decaying exponential functions as basis function of the tissue impulse response. For given M positive constants, $\{\lambda_m\}_{m=1}^M$, let f denote the span of the exponential functions, Then the h(t) takes the form of:

$$h(t) = \sum_{m=1}^M h_m f_m = \sum_{m=1}^M h_m e^{-\lambda_m t} \qquad [24]$$

therefore

$$C_{myo}(t) = \sum_{m=1}^{M} h_m \int_0^t C_{aif}(t_m - s) f_m(s) ds = \sum_{m=1}^{M} h_m \int_0^t C_{aif}(t_m - s) e^{-\lambda_m s} ds$$

and the expansion coefficients $\{h_i\}_{m=1}^M$ will appear linearly in the convolution equation

$$C_{myo}(t) = C_{aif}(t) * ([\sum h_m \, f_m]) \quad [25]$$

The $h(t)$ in discrete format will take the matrix form of:

$$\begin{bmatrix} h(1) \\ h(2) \\ h(3) \\ \vdots \\ h(N) \end{bmatrix} = \begin{bmatrix} e^{-\lambda_1} & e^{-\lambda_2} & e^{-\lambda_3} & \dots & e^{-\lambda_M} \\ e^{-2\lambda_1} & \dots & \dots & \dots & e^{-2\lambda_M} \\ \vdots & \dots & \dots & \dots & \vdots \\ e^{-N\lambda_1} & e^{-N\lambda_2} & e^{-N\lambda_3} & \dots & e^{-N\lambda_M} \end{bmatrix} \begin{bmatrix} h_1 \\ h_2 \\ \vdots \\ h_M \end{bmatrix}$$

Where N is the total number of input and output samples and the convolution equation will be equal to:

$$\begin{bmatrix} C_{myo}(1) \\ C_{myo}(2) \\ C_{myo}(3) \\ \vdots \\ C_{myo}(N) \end{bmatrix} = \begin{bmatrix} C_{aif}(1) & 0 & \cdots & 0 \\ C_{aif}(2) & C_{aif}(1) & \cdots & 0 \\ \vdots & \vdots & \ddots & \vdots \\ C_{aif}(N) & C_{aif}(N-1) & \cdots & C_{aif}(1) \end{bmatrix} \begin{bmatrix} h(1) \\ h(2) \\ h(3) \\ \vdots \\ h(N) \end{bmatrix}$$

Consequently equation [25] can be rewritten as:

$$\begin{bmatrix} C_{myo}(1) \\ C_{myo}(2) \\ C_{myo}(3) \\ \vdots \\ C_{myo}(N) \end{bmatrix} = \begin{bmatrix} C_{aif}(1) & 0 & \cdots & 0 \\ C_{aif}(2) & C_{aif}(1) & \cdots & 0 \\ \vdots & \vdots & \ddots & \vdots \\ C_{aif}(N) & C_{aif}(N-1) & \cdots & C_{aif}(1) \end{bmatrix} \begin{bmatrix} e^{-\lambda_1} & e^{-\lambda_2} & e^{-\lambda_3} & \dots & e^{-\lambda_M} \\ e^{-2\lambda_1} & \dots & \dots & \dots & e^{-2\lambda_M} \\ \vdots & \dots & \dots & \dots & \vdots \\ e^{-N\lambda_1} & e^{-N\lambda_2} & e^{-N\lambda_3} & \dots & e^{-N\lambda_M} \end{bmatrix} \begin{bmatrix} h_1 \\ h_2 \\ \vdots \\ h_M \end{bmatrix}.$$

The tissue impulse response can be estimated from the following linear least square minimization problem using the monotonicity constrained regularization method (as described in section 2.2.2.2),

$$min_{h_m} \left\| \boldsymbol{C}_{myo} - D.\boldsymbol{h} \right\|^2 \ , \boldsymbol{h} \in \boldsymbol{R}^p \qquad h(t) \geq 0\,, \ \ h(t)' \leq 0 \qquad [26]$$

Where $D = \begin{bmatrix} C_{aif}(1) & 0 & \cdots & 0 \\ C_{aif}(2) & C_{aif}(1) & \cdots & 0 \\ \vdots & \vdots & \ddots & \vdots \\ C_{aif}(N) & C_{aif}(N-1) & \cdots & C_{aif}(1) \end{bmatrix} \begin{bmatrix} e^{-\lambda_1} & e^{-\lambda_2} & e^{-\lambda_3} & \dots & e^{-\lambda_M} \\ e^{-2\lambda_1} & \dots & \dots & \dots & e^{-2\lambda_M} \\ \vdots & \dots & \dots & \dots & \vdots \\ e^{-N\lambda_1} & e^{-N\lambda_2} & e^{-N\lambda_3} & \dots & e^{-N\lambda_M} \end{bmatrix}$,

and $\boldsymbol{C}_{myo} = \begin{bmatrix} C_{myo}(1) \\ C_{myo}(2) \\ C_{myo}(3) \\ \vdots \\ C_{myo}(N) \end{bmatrix}$ and $\boldsymbol{h} = [h_1, \dots . h_M]^T$.

The exponential basis time scales, i.e $\{\lambda_m\}_{m=1}^{M}$, are chosen to satisfy the Muntz Theorem.

Muntz Theorem: Suppose $\{\mathrm{\lambda_n}\}_{\mathrm{n=1}}^{\infty}$are positive and satisfy $\mathrm{lim_{n\to\infty}\lambda_n} = +\infty$. Then the Span of $\{\mathrm{e}^{-\lambda_\mathrm{n} \mathrm{t}}\}$ is dense in Lp[0;∞) for 1 <p < ∞ if and only if $\sum_{\mathrm{n=1}}^{\infty} \frac{1}{\lambda_\mathrm{n}} = +\infty$.

These time scales can be distributed uniformly ($\lambda_\mathrm{m} = \frac{\mathrm{M}}{\mathrm{mT}}$), harmonically ($\lambda_\mathrm{m} = \frac{\mathrm{m}}{\mathrm{T}}$,). Harmonic distribution of the time scales provides better approximation compared to uniformly distributed time scales (104).

One of the remaining challenges of the exponential approximation method is setting the order of the approximation, i.e. the number M of the exponentials used. The balance that needs to be reached is that between the accuracy of the deconvolution, which improves as M increases, and its robustness to additive noise, which can be degraded for large M due to over-fitting of physiologically irrelevant detail. Ideally, one needs a method which would provide accurate deconvolution of $h(t)$, and would not be sensitive to noise and selection of parameters. Subsequently myocardium blood flow can be calculated from the amplitude of $h(t)$ at $= 0$.

2.2.2.4.4 Auto regressive moving average model (ARMA)

Autoregressive-moving-average (ARMA) models are mathematical models of the persistence, or autocorrelation, in a time series. ARMA models can also be used to predict behaviour of a time series from past values alone.

One subset of ARMA models are the autoregressive, or AR models. An AR model expresses a time series as a linear function of its past values. The order of the AR model tells how many lagged past values are included.

The other subset is the moving average model which includes lagged terms on the noise or inputs to the system. By including both types of lagged terms, we will have autoregressive-moving-average, or ARMA, models. The order of the ARMA model is included in parentheses as ARMA (*p*, *q*), where *p* is the autoregressive order and *q* the moving-average order. Autoregressive moving average model assumes that the discrete time samples (that are actually acquired in the perfusion MRI, as opposed to continuous-time functions) of myocardial and arterial concentrations of the contrast agent are related according to:

$$C_{myo}(t) = \underbrace{\sum_{i=0}^{Q} b_i C_{aif}(t-i)}_{\text{Moving average}} + \underbrace{\sum_{j=1}^{L} a_j C_{myo}(t-j)}_{\text{Autoregressive}} \quad [27]$$

This model assumes a linear differential relation between C_{aif} andC_{myo}. To identify the a_i and the b_j , the above equation can be written for *t=1 ...N*, where N represents the number of acquisition data points and assuming null initial condition.

$$\begin{bmatrix} C_{aif}(1) & 0 & \cdots & 0 & C_{myo}(0) & 0 & 0 \\ C_{aif}(2) & C_{aif}(1) & \cdots & \cdots & C_{myo}(1) & C_{myo}(1) & \vdots \\ \vdots & \vdots & \vdots & \vdots & \vdots & \vdots & \vdots \\ C_{aif}(N) & C_{aif}(N-1) & \cdots & C_{aif}(N-m) & C_{myo}(N-1) & \cdots & C_{myo}(N-n) \end{bmatrix} \begin{bmatrix} b_0 \\ \vdots \\ b_Q \\ -a_1 \\ \vdots \\ -a_L \end{bmatrix} = \begin{bmatrix} C_{myo}(1) \\ C_{myo}(2) \\ \vdots \\ C_{myo}(N) \end{bmatrix}$$

where N represents the number of acquisition data points and assuming null initial condition. The least squares solution of the above equation, after choosing the best value for L and Q which reduces the degree of freedom of the deconvolution equation and make it more stable, gives the coefficients

a_j, b_i and hence $h(t)$ can be computed by finding the solution of Eq. [27] to the Dirac function ($\delta(t) = 1$ if $t = 0$ and zero if $t \neq 0$) (6,121).

$$min_A \left\| \boldsymbol{C}_{myo} - \boldsymbol{C} \cdot A \right\| \qquad [28]$$

Where $A = \begin{bmatrix} b_0 \\ \vdots \\ b_Q \\ -a_1 \\ \vdots \\ -a_L \end{bmatrix}$ and

$$\boldsymbol{C} = \begin{bmatrix} C_{aif}(1) & 0 & \cdots & 0 & C_{myo}(0) & 0 & 0 \\ C_{aif}(2) & C_{aif}(1) & \cdots & \cdots & C_{myo}(1) & C_{myo}(1) & \vdots \\ \vdots & \vdots & \vdots & \vdots & \vdots & \vdots & \vdots \\ C_{aif}(N) & C_{aif}(N-1) & \cdots & C_{aif}(N-m) & C_{myo}(N-1) & \cdots & C_{myo}(N-n) \end{bmatrix}.$$

Here no further constraints are imposed.

Estimation of the ARMA model order requires that the model to be fitted for many L and Q orders to find the smallest values of L and Q which provide an acceptable fit to the data and reduce the computational burden. A study has been done on the ARMA model to obtain the best order for perfusion quantification previously(121). Finding appropriate orders for the ARMA model can be facilitated by plotting the partial autocorrelation functions for an estimate of L, and similarly using the autocorrelation functions for an estimate of Q (122,123).

In the spatial domain (frequency domain) $h(t)$ will take the form of:

$$\widehat{H}(z) = \frac{C_{tis}(z)}{C_{aif}(z)} = \frac{b_0 - b_1 z^{-1} - \dots - b_Q z^{-Q}}{1 - a_1 z^{-1} - \dots - a_L z^{-L}}. \qquad [29]$$

The inverse Z Transform of such a model, using partial fraction decomposition, yields a solution for $h(t)$ which is a sum of M exponentials.

$$h(t) = \sum_{m=1}^{M} h_m e^{-\lambda_m t}$$

As opposed to the exponential approximation approach, described in the previous section, which models $h(t)$ using a preset exponentials, ARMA modelling goes one step further and finds the exponents λ_m which best describe the available data.

The exponents $\lambda_m = -ln(p_m)$ and p_m are the roots of $1 - \sum_j^L a_j z^{-j}$. More generally, when the ARMA model has $(v+1)$ poles of multiplicity greater than one, terms like $t^v e^{-\lambda_m t}$ also appear in the expansion of $h(t)$ which easily will be neglected when exponential approximation approach have been used. ARMA approach thus achieves required model accuracy with a lower order approximation than the exponential modelling using preset functions, and that would imply additional regularization and a higher robustness to additive noise. Note that the ARMA approach is also justified from the physiological perspective, since it is a discrete-time version of perfusion modelling using linear differential equations with constant coefficients, as studied in a more general context of pharmaco-kinetics by Lindsey (124).

2.2.2.4.5 Optimized ARMA method

In the z-domain, the ARMA model describes the tissue impulse response with the following transfer function: $\widehat{H}(z) = \frac{C_{myo}(z)}{C_{aif}(z)} = \frac{b_0 - b_1 z^{-1} - \cdots - b_Q z^{-Q}}{1 - a_1 z^{-1} - \cdots - a_L z^{-L}}$ and will provide that all its poles ($p_m, m = 1, \cdots, L$), which are the roots of $p(z) = 1 - \sum_{i=1}^{L} a_i z^{-i}$ to be different. In the control system theory, the above transfer function refers to a closed loop transfer function with a following diagram

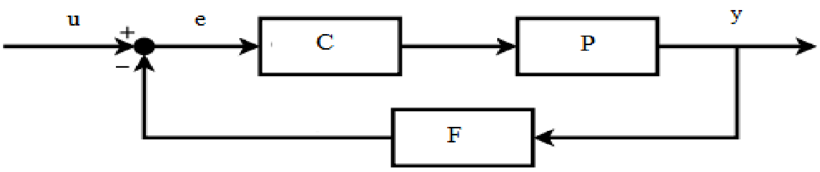

Figure 2.2-6 a simple diagram of a closed loop system transfer function

Where C is the controller module, F is the sensor and P is the main system. So

$$\widehat{H}(z) = \frac{C(Z)P(Z)}{1 - C(Z)P(Z)F(Z)} \qquad [30]$$

Here the performance of the system, or tissue impulse response, can be optimized by controlling the parameters in the controller module.

Theorem: For a linear time invariant system to be asymptotically stable, or Bounded input bonded output (BIBO) stable, it needs all of its transfer function poles, $p_m, m = 1, \cdots, L$, to lie strictly inside the unit circle ($|p_m| < 1$). Or in another words system radius of convergence (ROC) must includes the unit circle ($1 \in$ ROC). Any pole outside or on the unit circle will cause instability.

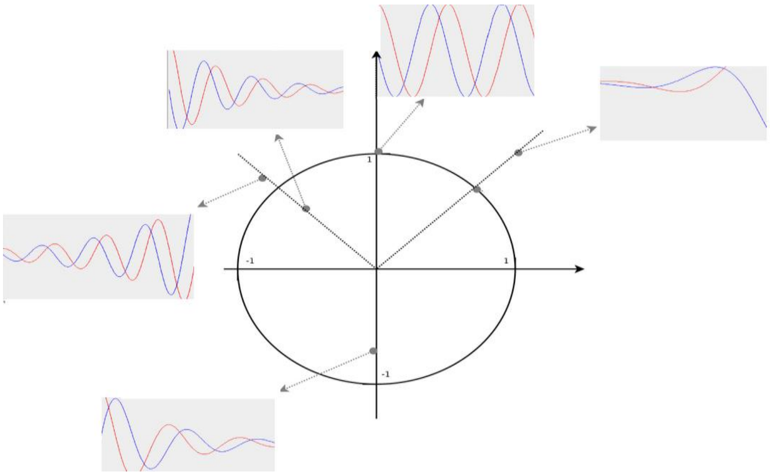

Figure 2.2-7 Different Poles position with their corresponding impulse response. Poles located outside or in the unit circle will result in an unstable impulse response. Unit circle is a circle with a radius of one.

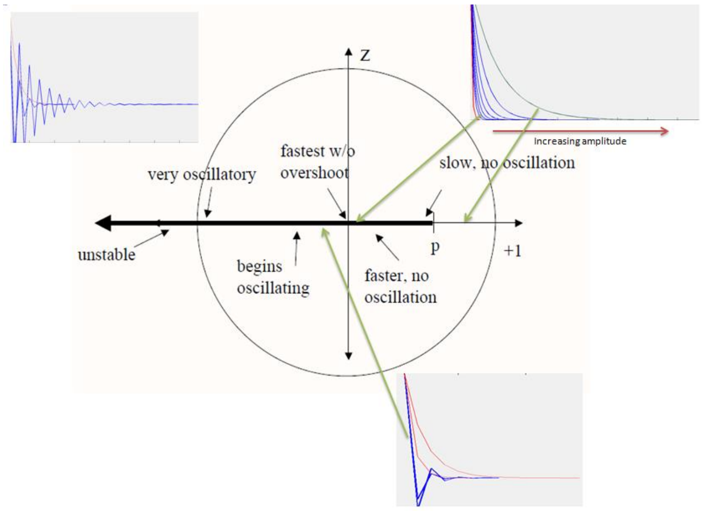

Figure 2.2-8 Even for a stable system, behaviour of the system impulse response is highly dependent on the position of the poles within unit circle. Poles in the left side of z-plane that are close to the unit circle will produce slowly decaying oscillations whereas the ones which are closer to 1 will result in a very oscillating impulse response .

As ARMA does not oblige the tissue impulse response to get a specific mathematical form and the coefficients of the tissue impulse response are obtained without any regularization, there is a possibility for the transfer function poles to lie on or outside of the unit circle $|p_m| > 1$. This will result in a region of convergences (ROC) which doesn't include unit circle and thus instability of the tissue impulse response transfer function. Consequently a control signal will be required in order to guarantee the stability of the system.

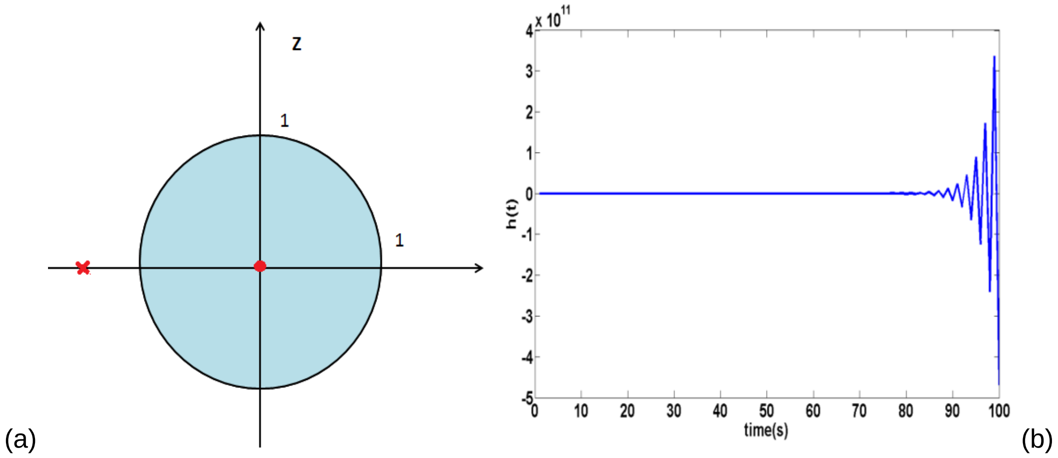

Figure 2.2-9 ROC of a first order AR system with a pole outside unit circle (a). The corresponding tissue impulse response has been shown in (b).

Although the behaviour of the impulse response in a stable system is still dependant on the position of its poles inside the unit circle, the initial value of the impulse response ($h(t = 0)$), remains constant regardless of the position of the poles

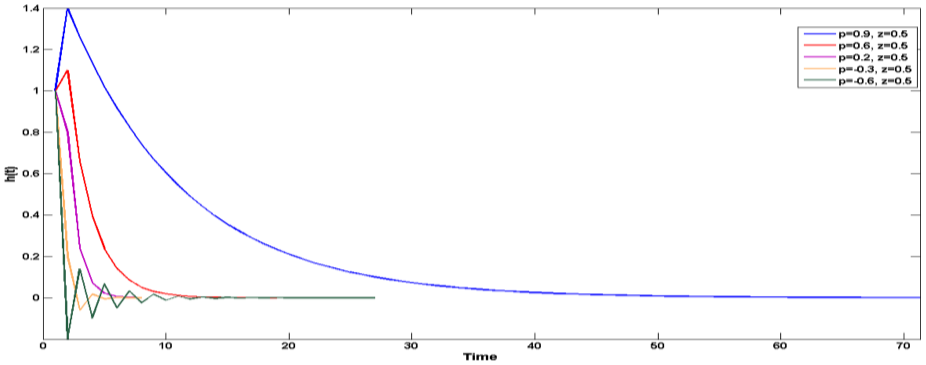

Figure 2.2-10 plot of impulse responses with different pole positions. The amplitude of ($h(t=0)$), remains constant regardless of the position of the poles. For p_m values close to 1, the tissue impulse response has an overshot which decrease as the p_m value falls down. The tissue impulse response starts oscillating as the pole value gets closer to -1.

In the modified controlled ARMA model, the system, which is a controllable system, has been forced into a stable state by using an appropriate control signal which locates all the poles inside the unit circle. This can be done by adding the $|p_m| < 1$ constrain into the linear least square equation [28]

$$min_A\left\|\boldsymbol{C}_{myo} - \boldsymbol{C}\cdot A\right\| \qquad \text{where} \quad |p_m| < 1 \quad , p_m \neq z_f$$

where z_f, $(z_f, f = 1, \cdots, Q)$ are zeroes of $\widehat{H}(z)$, roots of $\sum_i^Q b_i z^{-i}$.

In order to impediment the constrained to the least square equation, we need to take into account the relation between roots and coefficient of the polynomial. Based on the Vieta's formulas, for a polynomial in from of $D(z) = \beta_n z^n + \beta a_{n-1} z^{n-1} + \cdots + \beta_0$, There exist n roots $(x_1, x_2, \dots, x_n)$ in some possibly larger field (for instance if coefficients are in the field of real numbers, the roots will exist in the field of complex numbers), $D(z) = (n - x_1)(n - x_2)..(n - x_n)$, where:

$$\prod_{i=1}^{n} x_i = (-1)^n \frac{\beta_0}{\beta_n}$$

$$\sum_{i=1}^{n} \prod_{i\neq j}^{n} x_j = (-1)^{n-1} \frac{\beta_1}{\beta_n}$$

$$\sum_{1\leq i<j}^{n} x_j x_i = x_1 x_2 + x_1 x_3 + \cdots + x_{n-1} x_n = \frac{\beta_{n-2}}{\beta_n} \qquad [31]$$

$$x_1 + x_2 + \cdots + x_n = -\frac{\beta_{n-1}}{\beta_n} \qquad [32]$$

In the denominator of the transfer function, i.e. $1 - a_1 z^{-1} - \cdots - a_L z^{-L}$, $\beta_n = a_0 = 1$, therefore we can simplify the above equations to:

$$\prod_{m=1}^{L} p_m = (-1)^L a_L, \qquad \sum_{m=1}^{L} \prod_{m\neq j} P_j = (-1)^{L-1} a_{L-1}\,, \qquad p_1 + p_2 + \cdots + p_L = -a_1 \quad [33]$$

Now If $|p_m| < 1$,then the following statements can be made:

- $\left|\prod_{m=1}^{L} p_m\right| < 1$ therefore $|a_L| < 1$.
- $\left|\prod_{m\neq j} P_j\right| < 1$, therefore $\left|\sum_{m=1}^{L} \prod_{m\neq j} P_j\right| = |a_{L-1}| < L$.

- $|a_1| < L$

By limiting the value of coefficients, we can control the positions of the transfer function poles and therefore the behaviour of the tissue impulse response.

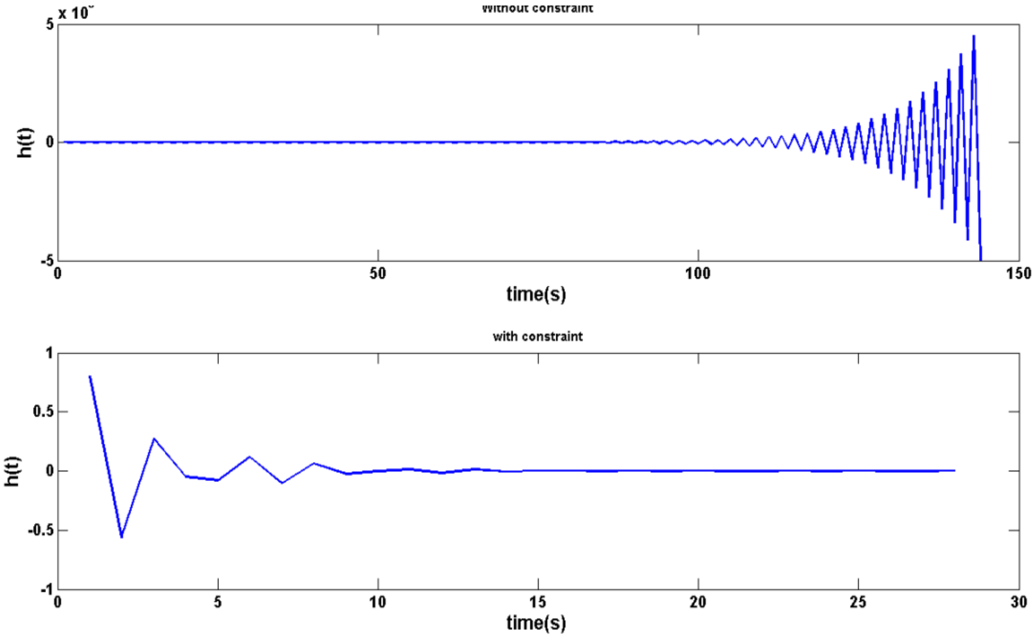

(a)

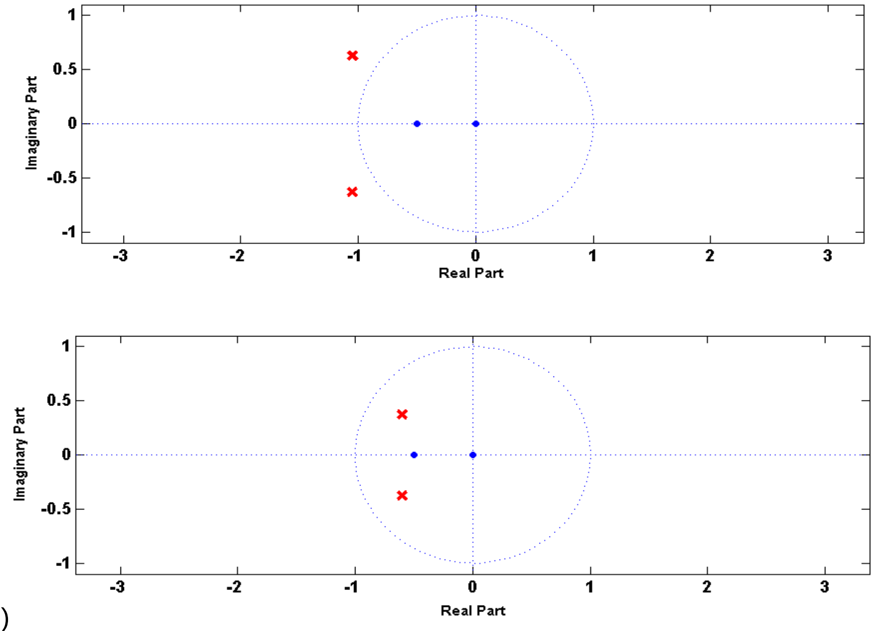

(b)

Figure 2.2-11 (a) An example of a tissue impulse response obtained without (top) and with (bottom) using the optimized ARMA method. Their corresponding Zero-pole plot is shown in figure (b) respectively.

Using Modified ARMA model, the tissue impulse response can be estimated from the following least square minimization problem using the following constrained regularization method:

$$min_A \left\| \boldsymbol{C}_{myo} - \boldsymbol{C} \cdot A \right\| \qquad \text{where} \quad \left| a_{i\,,i\neq L} \right| < L \quad , |a_L| < 1 \quad [34]$$

Myocardium blood flows are calculated from the amplitude of $h(t)$ at t=0 and optimized ARMA model has been used in this thesis for perfusion estimation.

2.3 Key points

- Perfusion in essence is the relationship between the myocardial tissue curve and the arterial input function.
- Accurate full quantification of MBF by myocardial first-pass perfusion MRI is heavily dependent on a linear relationship between signal intensity and the concentration of gadolinium contrast medium.
- Deconvolution, the problem of solving for tissue impulse response $h(t)$, is inherently a difficult process and therefore numerically unstable with noise contaminated data.
- The approaches which can be used to quantifying MBF from the observed contrast enhancement can be divided into two categories: model-based deconvolution, and model-independent deconvolution.
- The major problem of the model-based deconvolution is its dependency to the permeability surface of the system (E) for MBF estimation. This value can change based on permeability or flow limitation of the system.

3 Influence of modelling parameter variation on perfusion quantification

3.1 Introduction

The amount of oxygen delivered to the heart is dependent on blood perfusion, and its reduction may be responsible for symptoms in patients with coronary artery disease. First pass cardiac magnetic resonance (CMR) perfusion, is capable of providing a quantitative measurement of myocardial blood flow (MBF) that could yield functional information allowing for a more accurate diagnosis and for optimization of therapy.

Perfusion CMR measures the level of signal intensity which is assumed to be linearly proportional to concentration of a contrast agent,$C_{myo}(t)$, in a myocardial region of interest (ROI) (74,125). This concentration depends on perfusion rate and arterial concentration of the agent, $C_{aif}(t)$, which is also acquired in the form of signal intensity in the perfusion CMR process, through a convolution integral

$$C_{myo}(t) = C_{aif}(t) \otimes h(t) \quad [1]$$

where $h(t)$ is the response function of the myocardial ROI and characterizes its perfusion properties(i.e. MBF) (29,88,126).

The goal of perfusion MRI post processing is to recover $h(t)$ from observed $C_{aif}(t)$, and $C_{myo}(t)$. The most common technique is to find $h(t)$ through solving a least square minimization problem:

$$min_{h(t)}\left\|C_{myo} - C_{aif}(t) \otimes h(t)\right\|^2 \; [2]$$

However this task is challenging because it amounts an ill-posed inverse problem (5,106,107) and therefore needs regularisation. Several techniques have been used in other studies to solve this ill posed problem and favourable results have been reported (3,4,6,29,117,120,121,127). These techniques use different strategies to represent tissue impulse response, but a common feature of each of these techniques is dependency of perfusion estimate accuracy on the mathematical model. The mathematical models, utilized for $h(t)$ approximation, use varying parameters. Development of these models consists of several logical steps, one of which is the determination of parameters which are exerting the most influence on the model results. These varying parameters specify the model order.

Although estimating MBF values from the available mathematical models have been reported in several studies, rarely have they investigated the influence of model parameter changes on the outcome of deconvolution. We are not aware of any previous study for elucidating model parameter roles on different modelling strategies.

The purpose of this study was to systematically examine how changes in each model's varying parameter (order) will influence the deconvolution outcome and affect its accuracy and precision.

These results are important for the implementation and interpretations of future studies aimed at modelling of the myocardial impulse response and are necessary precursors for the optimization of regularization algorithms in attempts to maintain the integrity of deconvolution results and thus MBF estimate values.

3.2 Theory

The mathematical models used here for representation of the $h(t)$ include series of B-spline functions (4), autoregressive moving average model (ARMA) (128), series of exponential functions (5) and Fermi function modelling (3).

3.2.1 Series of B-spline Functions

Jerosch-Herold et.al (4) developed a model of independent deconvolution approach to estimate myocardial perfusion from tissue impulse response, which parameterized $h(t)$ as a sum of weighted B-spline functions as

$$h(t) = \sum_{j=1}^{P} h_j \, B_j^{(k)}(t)$$

and stabilized the solution of this inverse problem by using Tikhonov regularization method to solve the least square minimization problem in equation [2] (4,129).

$$min_{h_j} \left\| C_{myo} - D.\boldsymbol{h} \right\|^2 \ , \boldsymbol{h} \in \boldsymbol{R}^p$$

$D = RA, \boldsymbol{h} = \{h_j\}_{j=1}^{P}$

$$A = \begin{bmatrix} C_{aif}(0) & 0 & \cdots & 0 \\ C_{aif}(1) & C_{aif}(0) & \cdots & 0 \\ \vdots & \vdots & \ddots & \vdots \\ C_{aif}(N-1) & C_{aif}(N-2) & \cdots & C_{aif}(0) \end{bmatrix}, R = [R_{l,m}]_{NxP} \ \text{where} \ R_{l,m} = B_m^k(l), \ l = 1 \cdots N \ and \ m = 1 \cdots P$$

Here the degree of splines (k), the number of splines (P) and the positions of the break points (control points) (h_j) are the varying parameters in the B-spline functions. In order to keep the inverse problem linear, only the position of control points ($\{h_j\}_{j=1}^{P}$) will be estimated by the least square minimization problem. Therefore k and P will be the predefined parameters in the equation with the high influence on the accuracy of the estimate.

3.2.2 ARMA

The ARMA model assumes that the discrete time samples of measured $C_{myo}(t)$, and $C_{aif}(t)$ are related together according to:

$$C_{myo}(t) = \sum_{i=0}^{Q} b_i C_{aif}(t-i) + \sum_{j=1}^{L} a_j C_{myo}(t-j)$$

In ARMA modelling, no mathematical model has been used for representing the tissue impulse response. Therefore the only factors influencing the model accuracy are the auto-regressive and moving average order ($Q$and L).

Estimation of the ARMA model order requires that the model to be fitted for many L and Q orders to find the smallest values of L and Q which provide an acceptable fit to the data and reduce the computational burden. The value of Q and L should be chosen large enough, not to exclude the efficient model.

3.2.3 Series of Exponential basis

Hautvast et.al (130) recently demonstrated that $h(t)$can be parameterized as sum of exponential decaying function and the regularization of the inverse problem can be

$$h(t) = \sum_{m=1}^{M} h_m f_m = \sum_{m=1}^{M} h_m e^{-\lambda_m t}$$

$$min_{h_m} \left\| \boldsymbol{C}_{myo} - D.\boldsymbol{h} \right\|^2 \ , \boldsymbol{h} \in \boldsymbol{R}^p$$

$$\text{where } D = \begin{bmatrix} C_{aif}(1) & 0 & \cdots & 0 \\ C_{aif}(2) & C_{aif}(1) & \cdots & 0 \\ \vdots & \vdots & \ddots & \vdots \\ C_{aif}(N) & C_{aif}(N-1) & \cdots & C_{aif}(1) \end{bmatrix} \begin{bmatrix} e^{-\lambda_1} & e^{-\lambda_2} & e^{-\lambda_3} & \cdots & e^{-\lambda_M} \\ e^{-2\lambda_1} & \cdots & \cdots & \cdots & e^{-2\lambda_M} \\ \vdots & \cdots & \cdots & \cdots & \vdots \\ e^{-N\lambda_1} & e^{-N\lambda_2} & e^{-N\lambda_3} & \cdots & e^{-N\lambda_M} \end{bmatrix}$$

$$\text{and } \boldsymbol{h} = \{h_m\}_{m=1}^{M}$$

The regularization of this inverse problem can be performed by constraining the estimated kernel to be monotonic.

Same as B-spline function in order to keep the minimization problem in linear range, the total number of exponential functions (M) and the decay rates of the exponential functions (λ_m) is prefixed. Any perturbation in these parameters will have an effect on the accuracy of the regularization outcome.

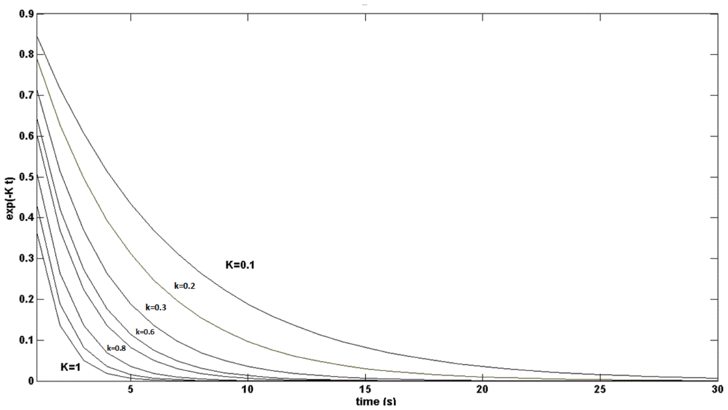

Figure 3.2-1 Series of Exponential functions with different decaying rate (K). Initial amplitude of Exponential increases as decay rate of Exponential decreases.

3.2.4 Fermi

Jerosch- Herold et al. (3) and Wilke et al. (88) fitted time curves for tissue impulse response function to the Fermi function with the following analytical expression:

$$h(t) = F.\left[\frac{1}{\exp[(t-\tau_{onset}).kr]+1}\right]\,\theta(\tau_{onset})$$

using a Marquardt-Levenberg nonlinear least square algorithm by letting kr and F vary and keeping other parameters fixed.

$$\begin{bmatrix} C_{myo}(1) \\ \vdots \\ C_{myo}(N) \end{bmatrix} = F\cdot \begin{bmatrix} C_{aif}(1) & 0 & \cdots & 0 \\ C_{aif}(2) & C_{aif}(1) & \cdots & 0 \\ \vdots & \vdots & \ddots & \vdots \\ C_{aif}(N) & C_{aif}(N-1) & \cdots & C_{aif}(1) \end{bmatrix} \begin{bmatrix} (e^{(1-\tau_0-\tau_d).kr}+1)^{-1} \\ \vdots \\ (e^{(N-\tau_0-\tau_d).kr}+1)^{-1} \end{bmatrix}$$

$$min_{S_i}\left\|\boldsymbol{C}_{myo}-C.\boldsymbol{S}\right\|^2 \;,$$

$$\boldsymbol{S} = F\cdot[\;(e^{(N-\tau_0-\tau_d).kr}+1)^{-1} \quad \cdots \quad (e^{(N-\tau_0-\tau_d).kr}+1)^{-1}]^T$$

As nonlinear least square method has been used for regularization when the Fermi function modelling is used, all of the varying parameters of Fermi function modelling including kr and F will be calculated from the least square minimization problem (3). The only user dependent parameter in Fermi modelling is τ_{onset}, which accounts for the delay between arrival of the constant agent in LV and myocardium ROI and can be calculated for each ROI using its corresponding SI curves (131).Therefore sensitivity of the regularization to changes is varying parameters of the Fermi function is negligible.

3.3 Material and methods

The four approaches (i.e. Fermi function modelling, series of Exponential function, series of B-spline functions and ARMA) are tested on two sets of data. The first set is simulated so that there is a known reference used to assess sensitivity of the models to additive noise. The second test of data is acquired from an MR-compatible blood-perfused pig-heart model.

For each set, we changed the regularization independent parameter of the models such as M in exponential functions or order of ARMA model in a reasonable range to find the best parameter giving the most accurate results.

3.3.1 Simulated data

Simulated data allows for the examination of the influence of variation in quantification-method-orders on perfusion estimates by calculating the absolute error of quantification.

The unit step function was chosen as a noiseless tissue impulse response, $h_{GS}(t)$. $C_{aif}(t)$ used in this experiment is a convolution of many Exponentials as suggested in (5) to model the propagation of an impulsive bolus injection through several compartments of the cardiovascular system. The injected bolus typically travels through at least three major compartments: from the injection site through the right heart, from the right heart through the lungs to the left heart, from the left heart to the coronary arteries and finally to the myocardial tissue. For simplicity, we assumed the same mean transit time ($1/v > 0, v = 0.3897$), and thus the same compartment kernel (ve^{-vt}) for all compartments. The value of v was obtained via a series of sequential deduction performed on the simulated data to produce the $C_{aif}(t)$ similar to the ones obtained from human data. As a result, the arterial input at the tissue site can be formulated as n (n=4) convolution of the unit kernel:

$$C_{aif}(t) = \delta(t) * \left[ve^{-vt}\right]_1 * \left[ve^{-vt}\right]_2 * \ldots * \left[ve^{-vt}\right]_n$$

Initial $C_{myo}(t)$ was then obtained by convolving $h_{GS}(t)$ with the simulated $C_{aif}(t)$ (5). Finally, the constructed $C_{myo}(t)$and $C_{aif}(t)$ were corrupted by additive white Gaussian noise with a selected deviation.

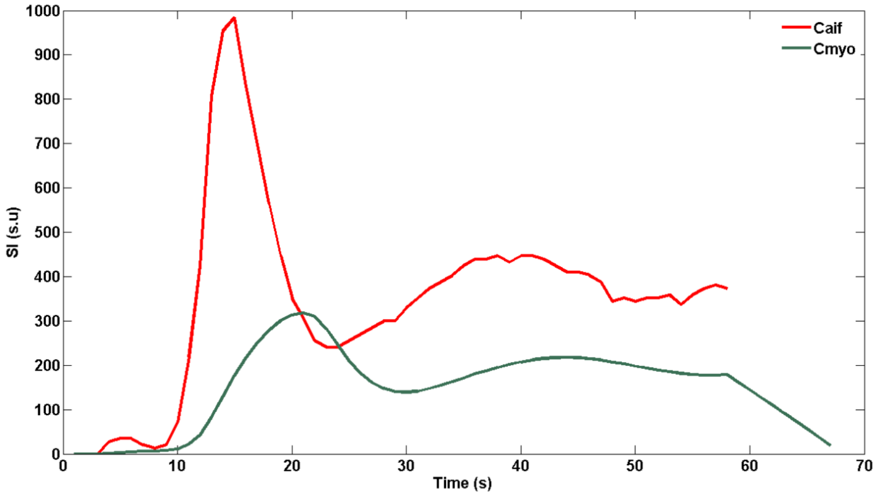

Figure 3.3-1 Simulated tissue and arterial input signal intensity curve in green and red respectively.

3.3.2 Explanted pig heart

3.3.2.1 Experimental design of the study

All animal experiments were conducted after approval from the U.K. Home Office in accordance with the U.K. Animals (Scientific Procedures) Act of 1986 and in compliance with the World Medical Association declaration of Helsinki regarding ethical conduct of research involving animals.

Ten healthy large white cross landrace pigs weighing between 41 and 54 kg were included in this study (Harlan Laboratories, UK). Hearts were harvested as previously described in (132). Sedation was performed with ketamine (10mg /kg i.m.) and xylazine (0.3 mg/kg i.m.) in combination with alphaxolone for general intravenous anaesthesia (1.5 mg/kg i.v.). Heparin was administered (5,000 IU) and exsanguinations started through the superior vena cava. The hearts were removed after transaction of the great heart vessels and intra-coronary infusion of cold (4ºC) cardioplegic solution (Martindale Pharmaceuticals, Romford, Essex, UK) was performed. Catheters were inserted into the coronary arteries for reperfusion. To create left ventricular (LV) preload, a pressure balloon was inserted through the aortic valve into the left ventricle and inflated to a systolic pressure of 50 mmHg. After the hearts were cannulated, pressure-controlled perfusion of the coronary arteries was started at around 50 mmHg. Over approximately five minutes, pressure was slowly increased to a constant perfusion mode of 0.8 ml/min/g. In the event of ventricular fibrillation, electrical defibrillation was performed. After preparation stability was achieved, the left anterior descending (LAD) coronary artery was occluded to create a territory with a perfusion defect. A normally perfused remote territory and CMR imaging were also started.

Perfusion-CMR was performed at rest, with 50% flow reduction and during pharmacological vasodilation with adenosine (Fig 3.3-2). During adenosine infusion, the flow was altered to maintain the same coronary perfusion pressure as during the resting state.

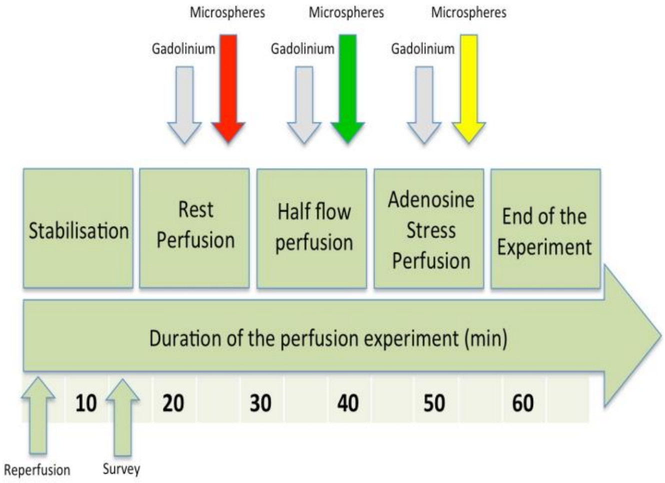

Figure 3.3-2 Figure describes time course of the CMR examination. After preparation stability was achieved CMR imaging was started with the acquisition of rest -perfusion images. Microspheres were injected after gadolinium injection for perfusion imaging. This process was repeated with 50% of the flow and during pharmacological vasodilation with adenosine with coronary perfusion pressure controlled increase in MBF(adapted from (132)

3.3.2.2 Cardiovascular magnetic resonance perfusion imaging

The animal studies (n=5) were performed on a three tesla (Achieva TX, Philips Healthcare, Best, The Netherlands) clinical MR scanner. For signal reception, a clinical interventional L-flex receiver coil array was tightly positioned around the heart chamber, which was then placed in the isocentre of the magnet CMR perfusion. Data were acquired in short axis orientation of the LV following a recognised standard model (133). We used a saturation recovery gradient echo pulse sequence accelerated with k–t BLAST (k-t factor 5 and 11 training profiles) with a repetition time of 2.7 ms, echo time of 0.9 ms, flip angle 20°, spatial resolution at 1.3 x 1.3 x 8 mm. Perfusion CMR was performed using a dual-bolus scheme with 5 ml of neat (0.07 mmol/ml) and 5 ml of dilute (0.007 mmol/ml) gadobutrolum bolus injections (Gadovist, Bayer Healthcare, Leverkusen, Germany) (99).

Dual-bolus method was used here in order to overcome the limitation of T1-induced MR signal saturation in the LV blood pool and low CNR in the myocardial tissue (As described in chapter 2). This technique uses a low dose of dilute contrast agent as a prebolus before the main bolus of neat contrast agent. In the dual-bolus protocol it is essential that both the main-bolus of neat gadolinium contrast agent (CA) and the pre-bolus of diluted gadolinium CA solution, to be of equal volume and administered at the same flow rate. Also each bolus should be followed by a saline flush to maintain a compact CA bolus in the LV chamber. The time delay between each bolus of CA can be controlled to minimize temporal overlap, this delay can be also adjusted to heart rate if required (6-8),

The dual bolus protocol steps are the following:

1) Commence Adenosine infusion and Measure heart rate and blood pressure every two minutes. When criteria (figure 3.3-3) are fulfilled.
2) Instruct the patient to breathe gently until told otherwise.
3) Start image acquisition, start injection. The first CA bolus (dilute) is flushed from the tubing into the patient.
4) End of first contrast agent injection – Patient continuous breathing gently.
5) After the 25s pause flush the main bolus (neat) from the tubing into the patient. Immediately after this the patient is instructed to hold his breath as long as possible and to restart breathing gently when he can’t hold anymore.
6) Adenosine is terminated app. 15 seconds after contrast injection is finished

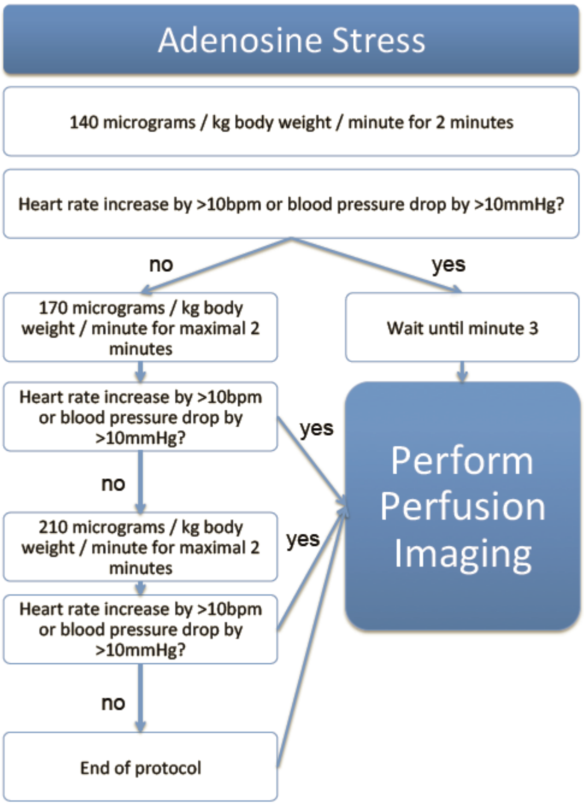

Figure 3.3-3 Stress (adenosine) protocol

3.3.2.3 CMR data extraction

The LV was divided into 16 standard segments (133). Each segment was then divided into 10 further transmural positions starting from the sub-endocardium to the sub-epicardium and 10 angular positions resulting in a total of 100 regions of interest (ROI) per segment. SI-time curves were extracted for each ROI. Extraction of perfusion images was performed with a dedicated software prototype (Philips Healthcare, Best, The Netherlands).

3.3.2.4 Quantitative microsphere analysis

Immediately after the gadolinium injection, a total of approximately 100,000 microspheres were injected into the circulation at the same site used for the gadolinium injection. Up to three different colours of microspheres were used during the experiments. Quantitative analysis of the microtome images was performed in the same standard segments used for perfusion quantification according to previously described methods (134). To assess microsphere deposition cryomicrotome, CMR images were registered to the same coordinate space and microsphere flow quantified in segments as a function of segment volume, arterial flow rate and microsphere count fraction(134). Given that heart geometry was largely unchanged between CMR acquisition and cryomicrotome imaging, it was sufficient to perform accurate rigid registration to align heart geometries, thus bringing the microspheres into the same coordinate space as the CMR images. This was achieved by using a combination of anatomical landmark-based rigid registration (namely identifying the aortic valve, the LV apex and the proximal LAD), as well as fine manual rigid transformation adjustments using the 3D-visualisation software CMGUI (Open CMISS Continuum Mechanics, Imaging, Signal processing and System identification; http://www.cmiss.org/cmgui). Flow was calculated in ml/gr/min of tissue from the following equation:

$$\frac{N_S}{M_S} \times \frac{F_t}{N_t}$$

Where N_s (number of microspheres) is counted in a segment, N_t is the total number of injected microspheres, F_t is the total arterial input flow rate in ml/min and M_S is the mass of a segment in grams. Segment mass was derived from segment volume, which was calculated from a fine binarised left ventricular mesh. To quantify microspheres circumferentially in the same standard segments used for quantitative CMR perfusion analysis, the LV centroid and anterior RV insertion point were identified in each perfusion slice, with circumferential segments then defined every 60 degrees around the centroid allowing for accurate alignment of the perfusion and cryomicrotome slices (Fig 3.3-3).

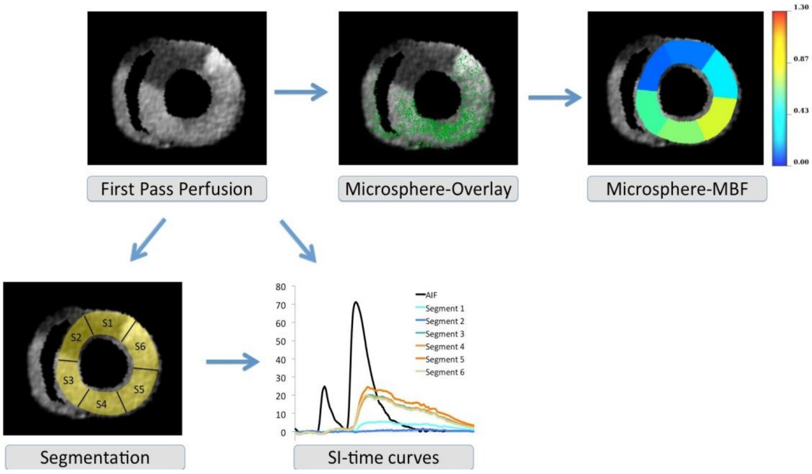

Figure 3.3-4 The figure shows a single time frame of a perfusion study after occlusion of the LAD (upper left). The middle image (top row) shows the overlay with the microsphere distribution after registration of the cryomicrotome images and the MR images. Segmental microsphere quantification reveals the perfusion defect and the normal perfusion in remote myocardium (upper right corner). In the lower row segmentation of the perfusion image is displayed (left), as well as segmental signal intensity (SI) curves during first pass of gadolinium (middle)(Image adapted from (132)) .

3.3.3 Statistical analysis

For synthetic data, numerical considered methods were compared by using absolute perfusion error (e_a), which is defined as:

$$e_a = \left|MBF - MBF_{ref}\right|$$

where MBF_{ref} is the known reference simulated flow value.

Mean ±standard deviation (STD) of e_a was calculated for each different condition tested in the synthetic data to assess the sensitivity of methods to variation in their order. Data analysis for the pig heart was performed with IBM SPSS statistics (SPSS Inc., Chicago, Illinois, USA). Continuous data are expressed as the mean ± standard deviation (STD).

The paired samples T-test was used to compare perfusion measurements between different deconvolution methods. To compare CMR perfusion measurements and microspheres, linear regression analysis was used. Coefficient of variation (CV) is calculated to assess dispersion and variation of each algorithm results due to variation in model order.

3.4 Results

3.4.1 Simulated data

Using the four methods, the respective plots of simulated $C_{aif}(t)$ and $C_{myo}(t)$ curves along with the reconstructed $C_{myo}(t)$ curves from deconvolution is shown on the right hand column of figure 3.4-1. On the left hand side, each methods corresponding extracted tissue impulse response is demonstrated using the following model orders- cubic B-spline with 5 control points(A), second order autoregressive mode (AR) (B), i.e. Q=0 ,L=2, Exponential with 10 time scales (C) and Fermi (D).

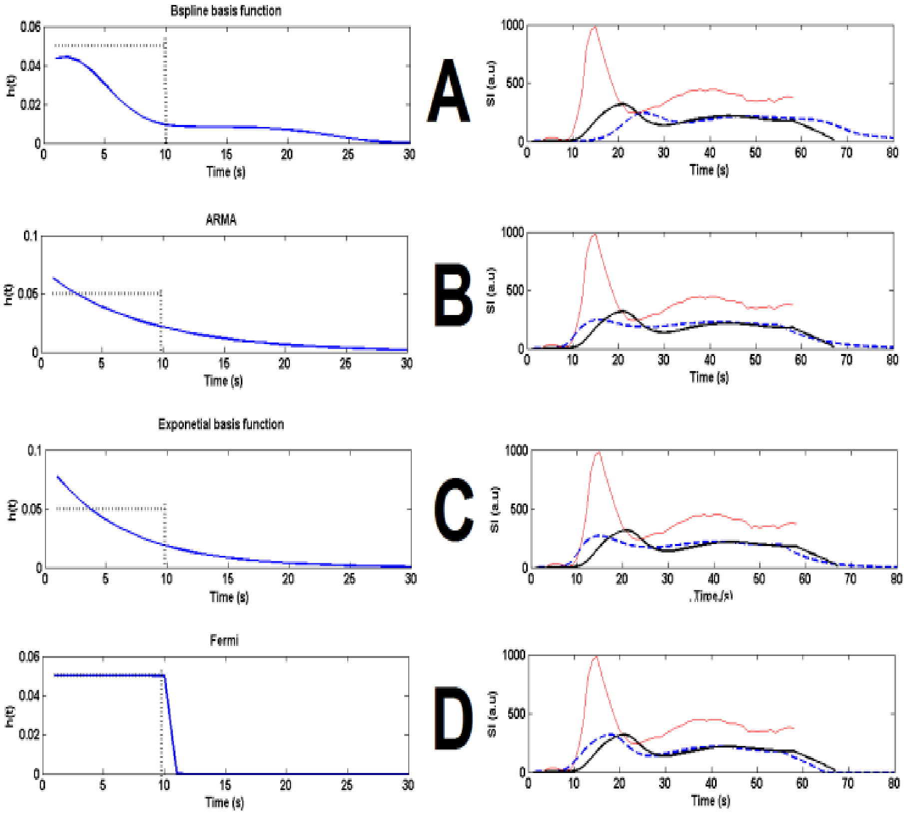

Figure 3.4-1 Results of solving deconvolution for synthetic data using B-spline (A), ARMA (B), exponential basis function (C) and Fermi (D) function modelling are shown. The dashed line in the left column is the step function used as synthetic tissue impulse response, $h_{GS}(t)$. The solid blue curves in the left column are the reconstructed tissue impulse response, $h(t)$, from deconvolution. The solid curves in the right column are simulated tissue, $C_{myo}(t)$, and arterial input intensity curve, $C_{aif}(t)$. Dashed lines in right column are the reconstructed tissue intensity curves (convolution of estimated $h(t)$ and $C_{aif}(t)$). Note that Fermi model provides the closest simulated tissue impulse response to real one. The dashed blue curves in right columns are plotted form zero for illustration proposes.

Table 3-1 represents the modelling parameters of each deconvolution method. These parameters mainly can be divided into two groups: 1) Parameters which will be estimated during deconvolution regularization process (second column), 2) parameters which are independent of the deconvolution process and need to be set (third column). These parameters are defining models order. The range of values assigned to these deconvolution independent parameters for investigation is represented in fourth column.

Table 3-1- Deconvolution methods modelling parameters

Mathematical model	Parameters estimated with deconvolution	Deconvolution independent parameters (order)	Range of values
B-spline	h_j	$P\ and\ k$	$k = 2{:}4$, $P = 3{:}15$
ARMA	$a_i\ and\ b_j$	$Q\ and\ L$	$Q = 0{:}3$, $L = 1{:}4$
Exponential	h_m	M	$M = 5{:}20$
Fermi	k, F	τ_{onset}	Not applicable

The deconvolution independent parameter in Fermi Function modelling, τ_{onset}, is a predefined set parameter which is equal to the delay time between arrival of contrast in LV and myocardium ROI. This parameter is dependent only on each individual ROI and is user independent (131). Effects of tOnset on perfusion quantification accuracy has been studied in more detail in chapter 5.

The bar plots in figure 3.4.2 represents the MBF estimates absolute errors (e_a) for B-spline (a), ARMA (b), exponential (c) –due to changes in their order as mentioned in table 3-1. For B-spline method more accuracy was achieved when a smaller number of control points was used for modelling ($P = 5,\ e_a = 0.004, 8\%$). For the same number of used control points, all degrees of splines had almost similar level of accuracy.

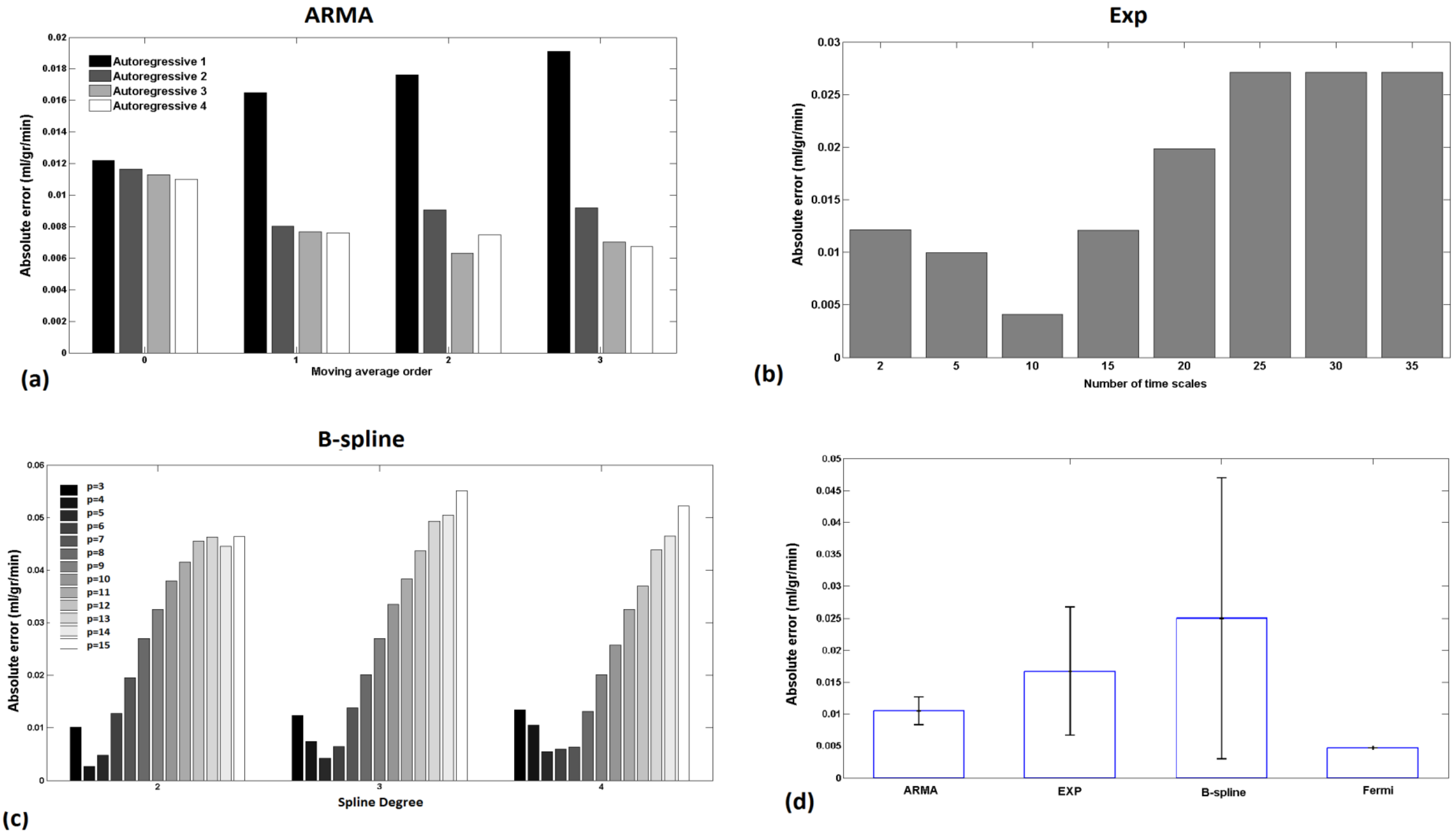

Figure 3.4-2 Bar plots represent the MBF estimates absolute error due to changes in their order for (a) arma, (b) exponential, (c) B-spline. Fermi function method have been compared to mean and SD of all configurations for the synthetic data (d).

For the exponential model the best accuracy was achieved with $M = 10$ ($e_a = 0.004, 9\%$).

All auto regressive model orders in absence of a moving average (MA) model (i.e. $L = 1{:}4$ where $Q = 0$) provided accurate and reliable estimates. However when MA part is added to the model, ARMA with a higher AR order achieved a better accuracy (figure 3.4-2.a). Compared to all models, the Fermi function was most accurate with an absolute error equal to 0.0035 (figures 3.4-2.d).

Table 3-2 represents the coefficient of variation (CV) for each deconvolution model order. For an AR model, CV of L increases proportionally to the order of MA part. The highest CV belongs to Q=3 *(*CV=55%*),* and the lowest belongs to Q=0 *(*CV=4%*).* However for the MA part of ARMA (where AR order (*L)* is constant and MA order (*Q*) varies)*, L*=1 has the highest CV *(*CV=23%*).* In the B-spline model, variation in order of the splines (*k*) had a CV of 5%, whereas the variation in number of nodes *(P)* had higher CV (58% for *k*=3 and 66% for *k*=4). For exponential model time scales (*M*) CV was equal to 40%.

Table 3-2. Coefficient of variation (CV) of deconvolution models order (Synthetic data)

Algorithm	**Order**	**CV % (std/mean)**
B-spline/ P	k=3	58 %
	k=4	66%
B-spline/ k		5 %
AR/L	Q=0	4 %
	Q=1	43 %
	Q=2	50%
	Q=3	55 %
MA/Q	L=1	23 %
	L=2	16 %
	L=3	17 %
	L=4	18 %
EXP/ M		40 %

To determine the number of spline nodes (control points) and exponential basis function time scales, the L-curve approach (135) was adapted from the least square context. A plot of $log\|C_{myo} - h * C_{aif}\|$ versus $log\|h'\|$ is shown in figure 3.4-3.a and 3.4-3.b for varying number of regularly spaced B-spline nodes and Exponential time scales, respectively. Of note, it is important to appreciate that for the examples demonstrated in this work, the number of B-spline nodes which delivers the best match to the exact tissue curve is small. The latter is the same for exponential functions. The higher absolute error demonstrated in fig 3.4-2.b (due to overestimation of the initial value) is typical of results achieved with a large number of time scales. The chosen number of spline nodes or exponential time scales is associated with the vertex located on the corner of the L-curve. This vertex can be detected based on the curvature of the L-curve. And since the number of nodes/time scales is small, the calculation is efficient.

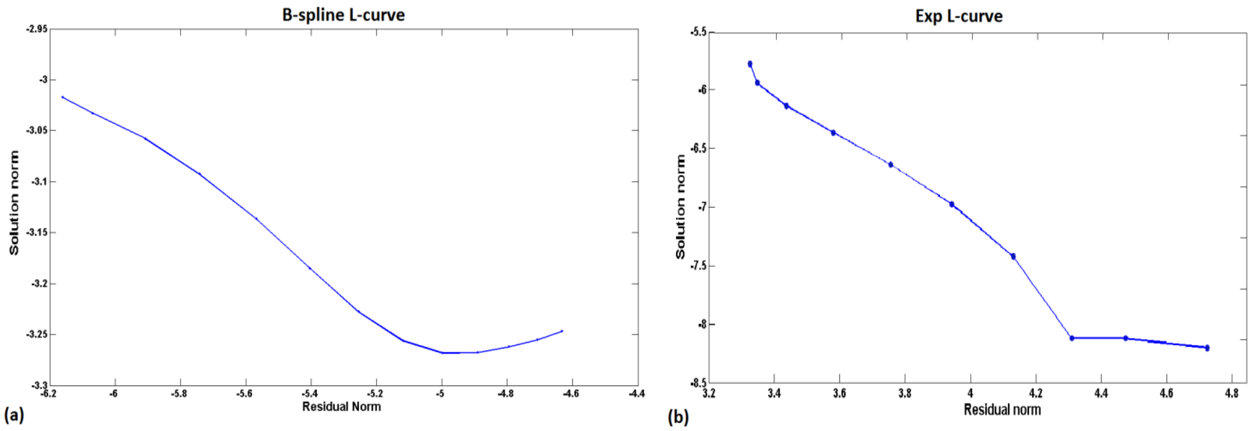

Figure 3.4-3 L-curves are generated by varying the number of spline nodes(control points) for B-spline (a) and number of time scales for Exponential (b) and plotting $log\|C_{myo} - h * C_{aif}\|$ versus $log\|h'\|$. The number for spline nodes and Exponential time scales is associated with the first point where a local minimum is detected in the angle subtended at a vertex in the L- curve.

Sensitivity of the ARMA model to order of AR and MA parts has been tested by keeping the orders of one part (for instance AR part) fixed and varying the other part order. In each stage of the process, MBF has been estimated and absolute error has been calculated. Mean and standard deviation of absolute error is represented in figure 3.4-4.

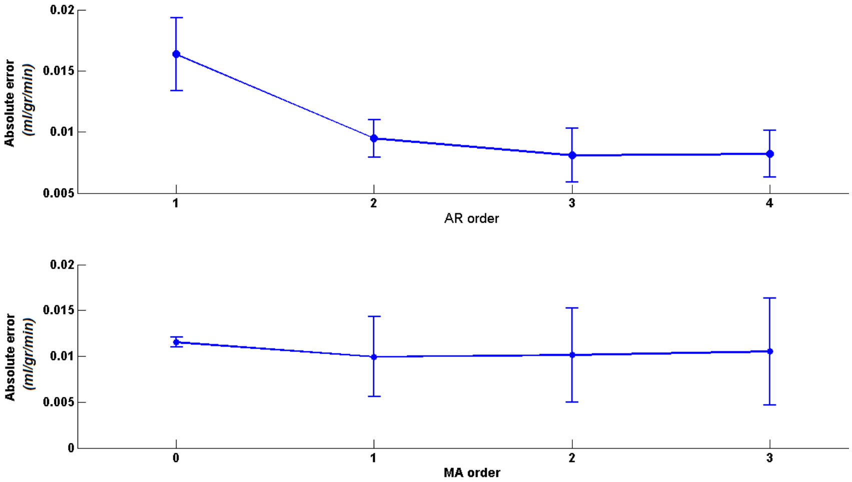

Figure 3.4-4 Error bars represents means and standard deviation of the ARMA method MBF estimates absolute error for (a) fixed auto regressive (AR) orders while moving average (MA) order varies and (b) fixed MA orders while the AR order varies. Note that AR absolute error decreases as the order of AR decreases, whereas for the MA model absolute error remains almost constant.

Error bars in figure 3.4-4.a represent the e_a and STD of different orders of AR model due to variation in Q (order of MA part of ARMA model). First order AR has the highest error and STD amongst all. Second order AR had the lowest STD. Second, third and fourth order AR model had almost similar level of accuracy. In figure (3.4-4.b) the e_a and STD of MA part of ARMA is represented. Whilst all MA orders have similar level of accuracy, MA with Q=0 had the lowest STD. Standard deviation (STD) of e_a increases as MA order increases.

The effect of noise on accuracy of different ARMA model orders has been previously described by the author (121). A correlation between different noise levels and ARMA order is shown in figure 3.4-5 (adapted from the author's Kings College London Master's thesis).

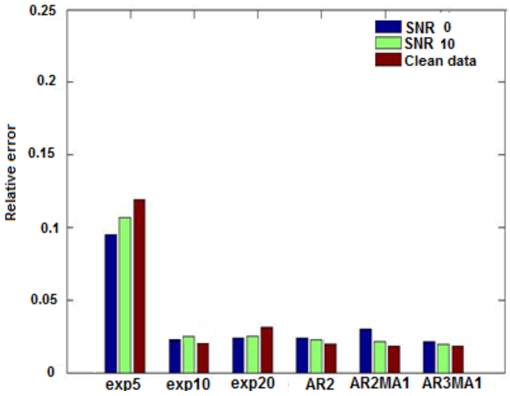

Figure 3.4-5 Bar plots represents the relative error ($\frac{MBF_{GS}-MBF}{MBF_{GS}}$) of the quantification for different order of ARMA and exponential at different noise level. Figure adapted from the author's Kings College London Master's thesis (136). The choice of the order of ARMA model depends of the SNR of the data

3.4.2 Explanted perfused pig heart

In this section, the relationship between microspheres and average perfusion values derived from the four respective techniques based on CMR SI-time curves are examined. The correlation coefficient values (r^2) were obtained from the scatter plots represented in figure 3.4-5. These corresponding data are then summarised in table 3-3.

Table 3-3 Correlation strength of individual algorithm order with microspheres.

Algorithm		r^2
AR	**L=1**	.740
	L=2	.897
	L=3	.926
	L=4	.872
ARMA Q=1	**L=1**	.85
	L=2	.920
	L=3	.890
	L=4	.890
ARMA Q=2	**L=1**	.780
	L=2	.833
	L=3	.903
	L=4	.843
FERMI		.911
EXP	**M=5**	.860
	M=10	.885
	M=15	.539
	M=20	.657
B-spline *k*=3	**P=5**	.836
	P=10	.731
	P=15	.764
B-spline *k*=4	**P=5**	.877
	P=10	.793
	P=15	.748

.

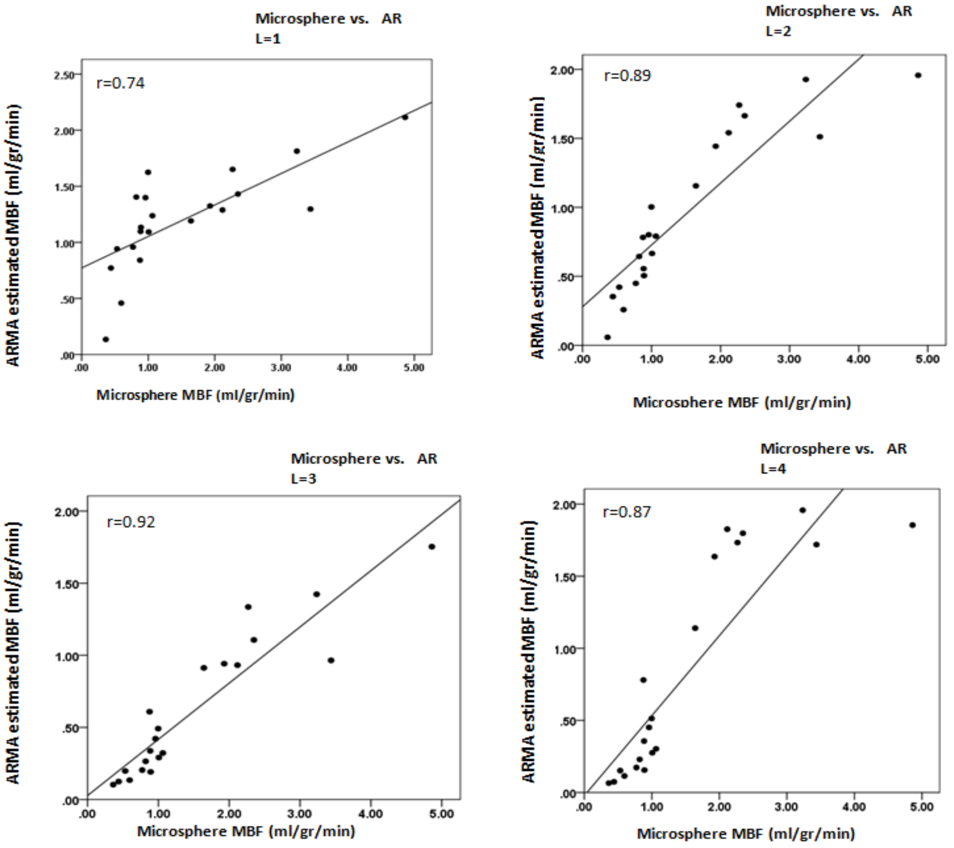
Microsphere vs. AR
L=1
r=0.74
Microsphere vs. AR
L=2
r=0.89
Microsphere vs. AR
L=3
r=0.92
Microsphere vs. AR
L=4
r=0.87
ARMA estimated MBF (ml/gr/min)
Microsphere MBF (ml/gr/min)
.00
.50
1.00
1.50
2.00
2.50
3.00
4.00
5.00

(a)

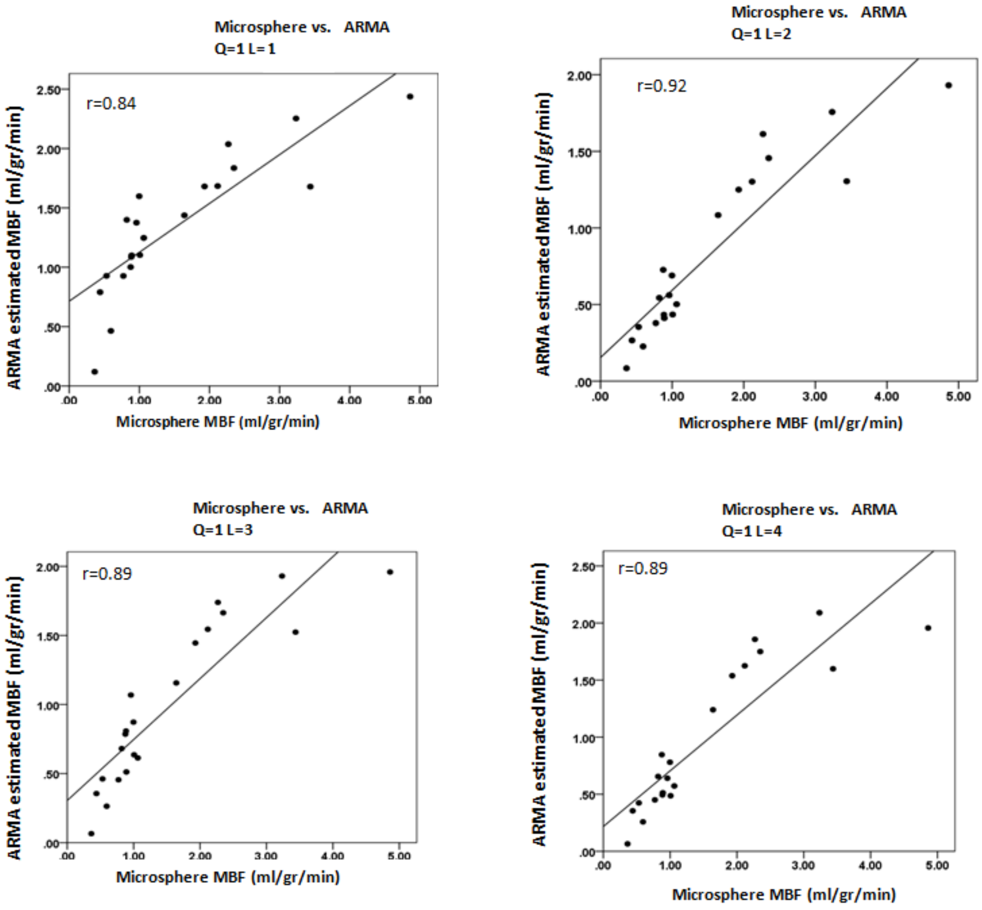
Microsphere vs. ARMA
Q=1 L=1
r=0.84
Microsphere vs. ARMA
Q=1 L=2
r=0.92
Microsphere vs. ARMA
Q=1 L=3
r=0.89
Microsphere vs. ARMA
Q=1 L=4
r=0.89
ARMA estimated MBF (ml/gr/min)
Microsphere MBF (ml/gr/min)
.00
.50
1.00
1.50
2.00
2.50
3.00
4.00
5.00

(b)

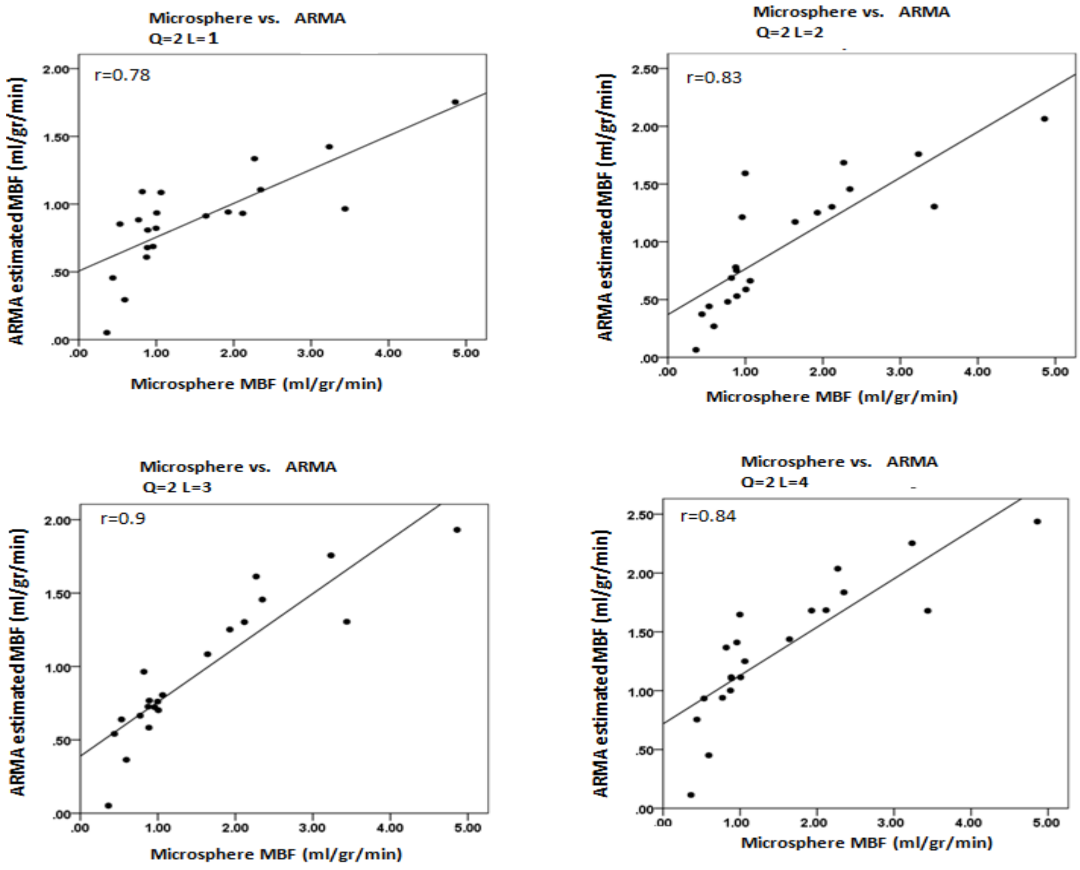
Microsphere vs. ARMA
Q=2 L=1
r=0.78
ARMA estimated MBF (ml/gr/min)
Microsphere MBF (ml/gr/min)
Microsphere vs. ARMA
Q=2 L=2
r=0.83
ARMA estimated MBF (ml/gr/min)
Microsphere MBF (ml/gr/min)
Microsphere vs. ARMA
Q=2 L=3
r=0.9
ARMA estimated MBF (ml/gr/min)
Microsphere MBF (ml/gr/min)
Microsphere vs. ARMA
Q=2 L=4
r=0.84
ARMA estimated MBF (ml/gr/min)
Microsphere MBF (ml/gr/min)
.00
1.00
2.00
3.00
4.00
5.00
.50
1.50
2.00
2.50

(c)

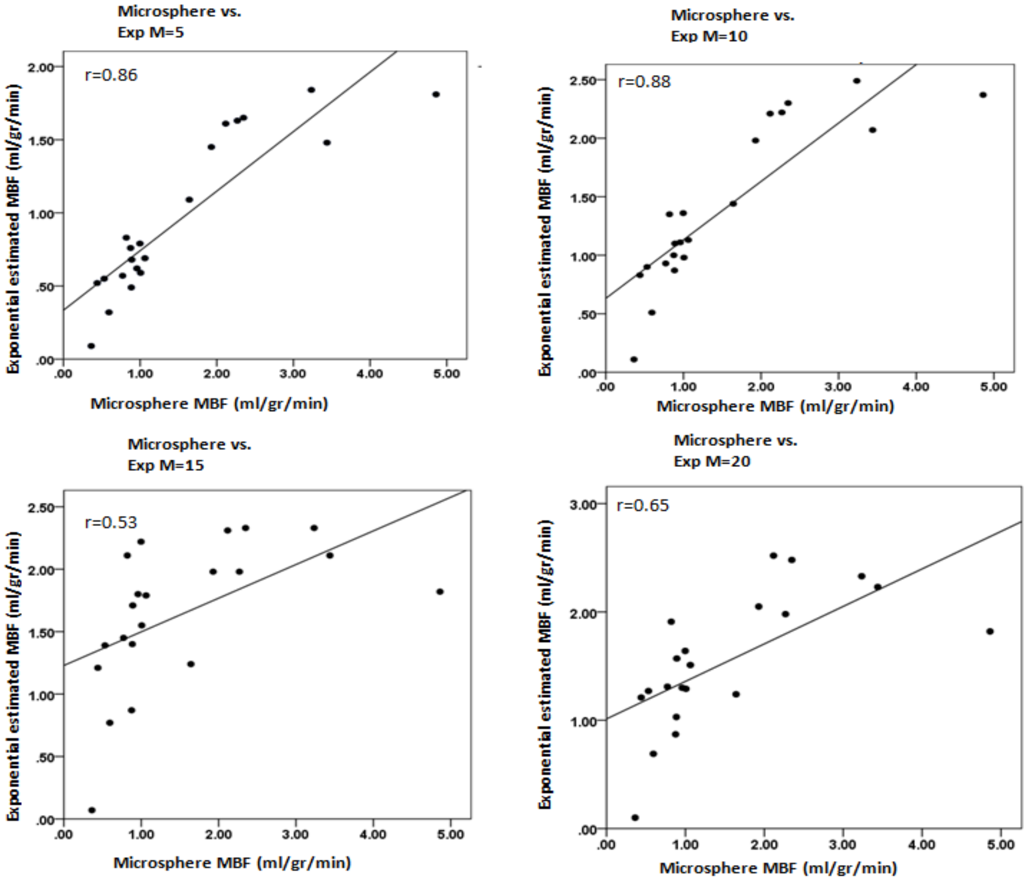
Microsphere vs.
Exp M=5
r=0.86
Exponential estimated MBF (ml/gr/min)
Microsphere MBF (ml/gr/min)
Microsphere vs.
Exp M=10
r=0.88
Exponential estimated MBF (ml/gr/min)
Microsphere MBF (ml/gr/min)
Microsphere vs.
Exp M=15
r=0.53
Exponential estimated MBF (ml/gr/min)
Microsphere MBF (ml/gr/min)
Microsphere vs.
Exp M=20
r=0.65
Exponential estimated MBF (ml/gr/min)
Microsphere MBF (ml/gr/min)
.00
1.00
2.00
3.00
4.00
5.00
.50
1.50
2.50
3.00

(d)

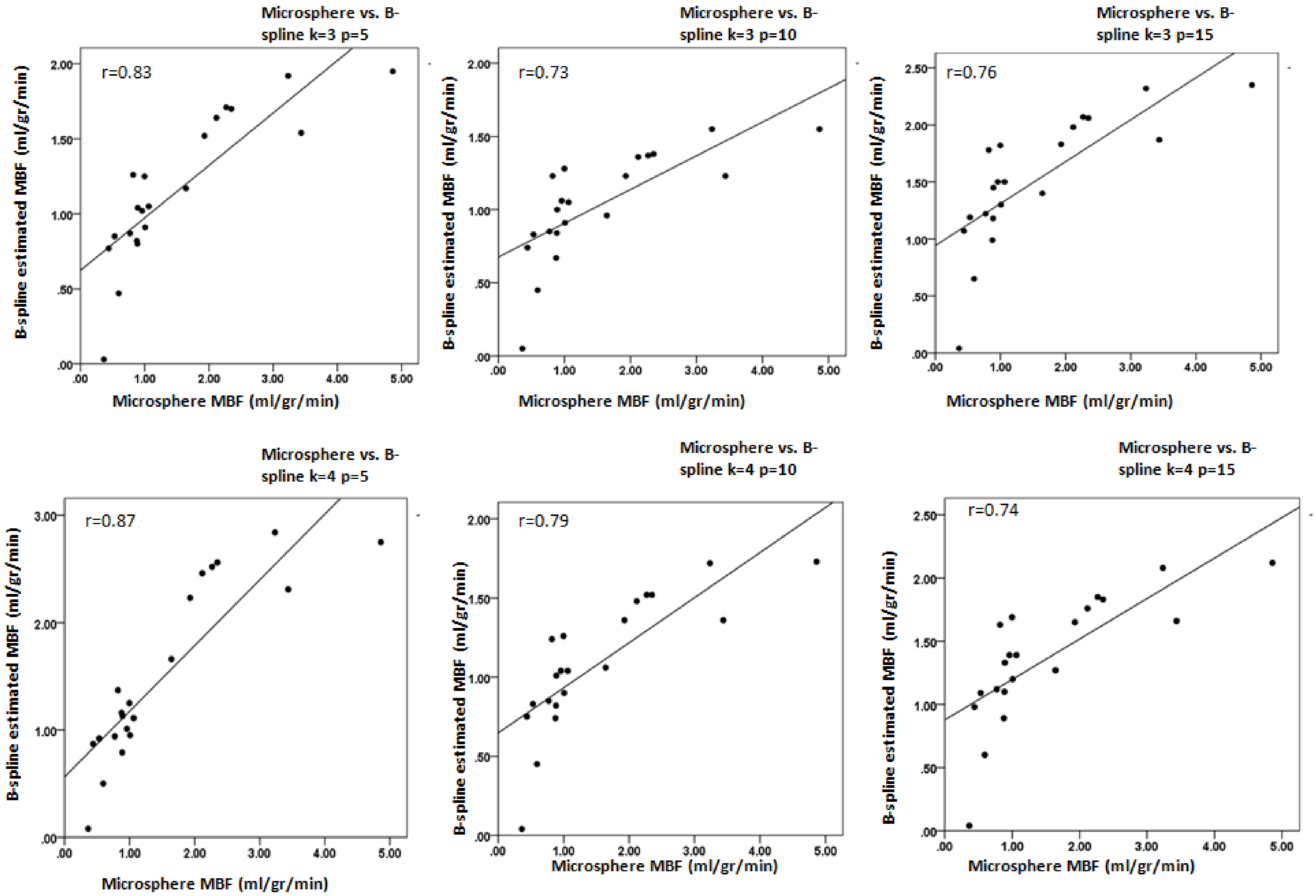
Microsphere vs. B-spline k=3 p=5
r=0.83
Microsphere vs. B-spline k=3 p=10
r=0.73
Microsphere vs. B-spline k=3 p=15
r=0.76
Microsphere vs. B-spline k=4 p=5
r=0.87
Microsphere vs. B-spline k=4 p=10
r=0.79
Microsphere vs. B-spline k=4 p=15
r=0.74
B-spline estimated MBF (ml/gr/min)
Microsphere MBF (ml/gr/min)
.00
1.00
2.00
3.00
4.00
5.00
.50
1.50
2.50

(e)

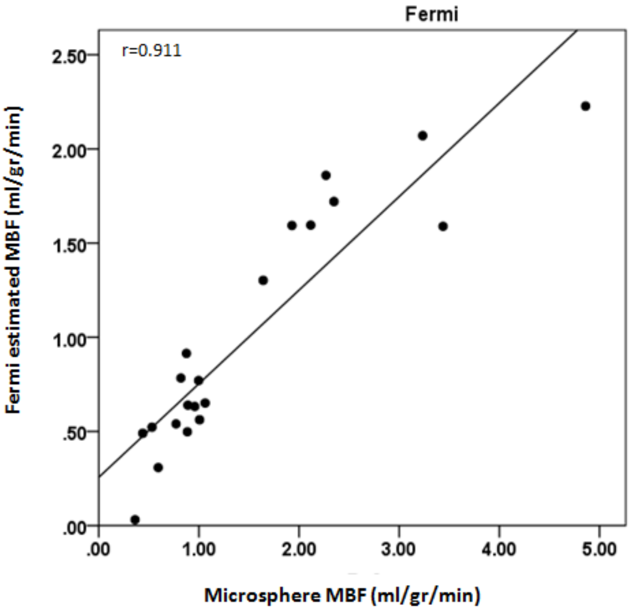

(f)

Figure 3.4-6 Correlation of quantitative perfusion analysis using (a) AR (L=1:4), (b) ARMA (Q=1, L=1:4), (c) ARMA (Q=2, L=1:4),(d) Exponential (M=5:20), (e)B-spline (k=3,4,p=5,10,15) and (f) Fermi with the gold standard of microsphere derived quantitative perfusion. There was good correlation between CMR-derived quantitative perfusion analysis and microspheres. Best correlation was achieved with Fermi function constrained deconvolution and ARMA model (Q=1 L=2) and (Q=2, L=3).

From the latter scatter plots, the following four interpretations can be derived: Firstly, the high r^2 values close to 1 suggest that there is a good correlation between all CMR-derived MBF estimates and the microspheres. Secondly, the third order AR model with constrained deconvolution achieved the best correlation ($r^2 = 0.926, \mathrm{p} < 0.001$) whilst the Exponential basis function deconvolution with $M = 15$ resulted in the weakest correlation ($r^2 = 0.539, \mathrm{p} < 0.001$). Thirdly, ARMA model correlation with microspheres was stronger when the order of the AR part was stronger than the MA part ($r^2 = 0.833$ to 0.926). Fourthly, correlation was stronger for Fermi ($r^2 = 0.911$) and ARMA models compared to the B-spline and Exponential basis models.

The pig heart relative MBF error, which is defined as:

$$e_{rel} = \frac{|CMR\ delivered\ perfusion\ values - microspheres|}{|microspheres|}$$

is represented in figure 3.4-6 as bar plots. Analysis shows excellent results for Fermi deconvolution with small error in estimation of perfusion ($e_{rel} = 0.15$). AR model with ($L = 2$, 3) and ARMA with ($L = 2$, $Q = 1$) had an almost similar level of accuracy as the Fermi model. Exponential deconvolution showed excellent results at M=5 ($e_{rel} = 0.15$) and M=10 ($e_{rel} = 0.14$). B-spline deconvolution showed high accuracy in flow estimation for P=5 and 10 ($e_{rel} = 0.15$ and $e_{rel} = 0.13$ respectively). In general, all methods achieved higher accuracy when lower order was chosen.

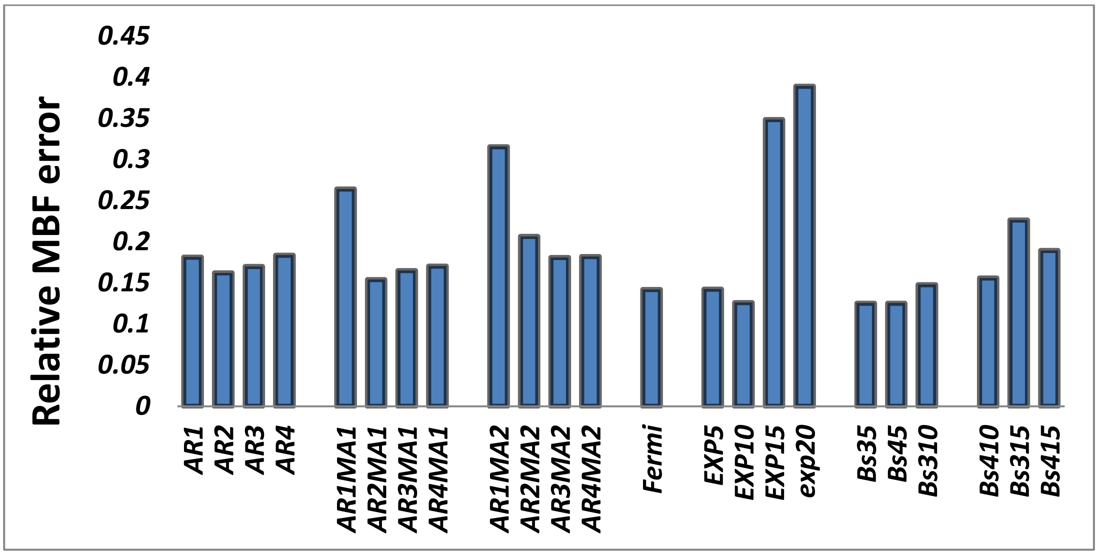

Figure 3.4-7 Bar plot represents the relative MBF error for all methods obtained from explanted Pig heart data.

Table 3-4 Coefficient of variation (CV) of deconvolution methods order (the explanted perfused pig heart).

Algorithm	**order**	**CV % (std/mean)**
B-spline/ *P*	*k*=3	50%
	k=4	48%
B-spline/ *k*		9%
AR/*L*	*Q=0*	4.2 %
	Q=1	48%
	Q=2	55%
MA/*Q*	*L=1*	41 %
	L=2	34 %
	L=3	32.4 %
	L=4	32.1%
EXP/ *M*		20 %

The sensitivity of the models to their order was different between algorithms. B-spline showed minimal sensitivity and variability for changes in degree of B-spline function, *k*, (CV=9), whereas it shows high sensitivity to variation in the total number of control points, *P*, (CV=50% for fourth degree B-spline and CV=48% for thirds degree B-spline). For an AR model CV was minimal at *Q=0*. Exponential deconvolution showed little sensitivity and variability (CV=20 %) to changes in number of time scales (3-4).

3.5 Discussion

Modelling of systems typically proceeds by adopting a class of systems capable of producing the observed outputs and having a structure compatible with our prior knowledge of the nature of the system or source. The problem of model order estimation is one of determining the number and value of the real parameters required to characterize a system.

In this chapter we have addressed the issue of the determination of the dimension of the parameters characterizing the myocardial tissue impulse response.

This study has two points of strength. First of these is utilisation of simulated synthetic data with known tissue impulse response, which has allowed us to examine the accuracy and precision of different model orders.

The second is the existence of a very controlled animal environment where myocardial blood flow to the heart is known and its distribution over time within the myocardium is quantified with CMR and validated versus microspheres. The availability of these gold standards allows the identification of a robust and accurate CMR quantification algorithm.

In this study, the relationship between the estimated perfusion values and the true perfusion values for all four fully quantitative methods with different orders are reported.

In general , the low perfusion estimation absolute error in both synthetic simulated data and pig heart and the good correlation between the CMR derived perfusion estimates assessed with either Fermi, ARMA, Exponential basis or B-spline basis deconvolution and the fluorescent-labelled microspheres demonstrate the reliability of the quantification methods for MBF estimation.

While, Fermi function modelling had the lowest average absolute error amongst all methods, B-spline model with 5 control points ($P=5$), second and third order AR, ARMA with ($L=2,Q=1$) and exponential basis with $M=10$ showed to have similar or better accuracy compare to Fermi function modelling.

Amongst all four deconvolution algorithms, Fermi function modelling is favourable for its rigidity and independency from modelling parameter determination, whereas all other methods accuracy and precision showed to be very dependent on the modelling parameter (order).

The high value of coefficient of variation for B-spline total number of control points (P) in both synthetic data and the explanted pig heart shows its sensitivity to total number of break points (Table 3-2 and 3-4). While the degree of piecewise linear spline functions seems not to be very important factor in accuracy of the deconvolution results.

L-curve approach, statistical analysis and the correlation results in both synthetic data and explanted pig heart recommend that the total numbers of nodes which deliver the best match to the exact kernel and give the most accurate results For B-spline basis deconvolution are rather small.

The dependency of the exponential basis deconvolution to the variation in the number of time scales is moderate. However exponential basis deconvolution showed to have very good correlation with the real perfusion values for $M=5,10$ where the highest accuracy have been achieved as well.

The sensitivity for exponential basis deconvolution to variation in its order in synthetic data was an inverted bell shape with the local minimum at M=10 (Fig 3.4-2). This value can be determined by using the L-curve approach which plots a measure of mismatch of the data versus a measure of ill-posedness. Choosing a value large or smaller than this value will lead to over estimation or under estimation of the initial value of the tissue impulse response, respectively.

Our investigation on both explanted pig heart and simulated data demonstrated that the accuracy of the ARMA models it highly depend on the order of moving average (MA) part of the ARMA (i.e. Q). For Q =0, all AR orders (L) showed to have almost similar accuracy. When $Q>0$, the impact of the AR order on perfusion estimation accuracy increases. For noiseless clean data and when $Q>0$, higher AR orders archived better accuracy compare to low order AR models. Whereas for noisy data (which is the case for CMR perfusion assessment), the lower AR orders showed to be more accurate.

An explanation, in the simplest sense, for this behaviour of ARMA model would the number of poles used for the system transfer function characterization (AR order). In fact by using smaller AR orders, we are using less exponential function to model the tissue impulse response and thus we increase the system degree of the freedom and smoothness. As a result ARMA model will be able to model the system more accurately.

Furthermore the values of the poles and the zeros of a system determine how well the system performs. Physically realisable proper systems must have a number of poles greater than or equal to the number of zeros $(L \geq Q)$. Any system with number of zeros greater than pole would deliver output signals of arbitrary high amplitude for input signals of arbitrary high frequency, which are physically not realisable. (i.e. $H(z) \rightarrow \infty \ as \ z \rightarrow \infty$). A *proper* transfer function always follows $H(z) \rightarrow \lambda \ as \ z \rightarrow \infty$. Therefore for ARMA model to be realisable and accurate, the order of AR should be greater than the order of MA part. Our investigations demonstrated that for ARMA Model, a strictly proper transfer function ($L>Q$) will result in more accurate estimation of MBF. The best results have been achieved with second and third order autoregressive ($L=2, 3$) and with ($L=2, Q=1$).

This study demonstrated that, upon a correct choice of order for the deconvolution algorithms, the four methods have almost similar accuracy in perfusion estimation. The choice of method and its order depends on several factors including signal to noise ratio of the data, computational burden and desired accuracy of the results.

The Fermi model is clearly most favourable as all of the modelling parameters are either fixed or they will be determined during deconvolution process. Moreover it has shown to have good correlation with the real perfusion value.

With reference to given evidences above, we believe that ARMA model with the correct choice of order is clearly superior to other methods with higher correlation coefficients, better accuracy and less computational burden. The choice of the order of ARMA model depends of the SNR of the data (previously shown by the author (121)).

3.5.1 Limitations

The fact that explanted hearts are less physiological and free from external influences such as heart rate and cardiac output make them an ideal validation platform for quantitative perfusion. However, this model oversimplifies in-vivo physiological conditions with complex nervous cardiac regulation, breathing motion during stress and dilution of contrast in the LV and aorta. This is an important consideration when translating results to a more realistic scenario such as living animals or patients.

3.6 Conclusions

Variation in the modeling parameters of deconvolution method influences its accuracy and introduces possible variation in the output of the process. This work has demonstrated that the use of an appropriate order for quantification algorithm is essential to allow CMR perfusion quantification to develop into a useful clinical tool. B-spline and ARMA were the most sensitive method to variation in their modelling order. Fermi model was the most favourable method amongst all.

This chapter has been adapted from, N zarinabad, A Chiribiri, G Hautvast, A Shuster, M Sinclair, J P.H.M. van den Wijngaard, N Smith, J A.E. Spaan, M Siebes, M Breeuwer, E Nagel, ***Modelling parameter role on accuracy of cardiac perfusion modelling;*** *published in Lecture notes for computer science . LNCS 7945, pp. 370–382, 2013.)*

NZ: implemented the post-processing and quantification methods. Data analysis and simulations experiments and preparation of the manuscript.GH: implemented the pre-processing methods. AS: performed pig experiment, AC: performed pig experiment, J W: performed pig experiment, MS: performed microspheres quantification, NS: supervised the project. JS: supervised the project. MS: supervised the project, MB: supervised the project. EN: arrange funding and supervised the project.

4 Method Validation: Voxel-wise quantification of myocardial perfusion by cardiac magnetic resonance. Feasibility and methods comparison

4.1 Introduction

Detection of myocardial ischemia is the key to the diagnosis of coronary artery disease (68). Several invasive techniques, including Doppler catheterization and coronary sinus thermo dilution are available for measuring myocardial blood flow (MBF) in humans. These methods, which are variations of indicator dilution methods, are invasive and can only assess average perfusion of whole coronary artery territories. Amongst non-invasive imaging techniques, positron emission tomography (PET) is currently regarded as a gold standard for the quantification of absolute MBF. However, this technique has several drawbacks including low spatial resolution (making it unsuitable for the detection of subtle subendocardial perfusion defects), patient radiation exposure and high cost (13,14).

Compared with PET, dynamic contrast-enhanced cardiovascular magnetic resonance (DCE-CMR) imaging has several potential advantages: superior spatial resolution, absence of ionizing radiation and availability of stable and inert contrast agents of low toxicity. Estimation of MBF from DCE-CMR studies has been reported using a number of different analysis techniques including quantitative and semi-quantitative methods (3-6,28,29,74,83,117,120,137).

Although favourable results with semi quantitative techniques such as upslope analysis of the myocardial time-intensity curve have been reported, these methods have been shown to underestimate the perfusion parameters (80,81). Moreover semi quantitative analysis relies on a ratio which introduce a bias on the data itself and the relationship between MBF and the semi quantitative methods parameters such as the curve upslope is not as clear-cut as the relationship between MBF and the impulse response amplitude which we get from quantitative analysis (28,30). Whereas using fully quantitative analysis allows the absolute quantification of MBF in units of ml/min/g and may permit more accurate and objective assessment of altered myocardial perfusion in patients with heart disease. Quantitative methods can be further divided into two groups: model-based and model independent analysis.

Model independent quantitative analysis, based on the central volume principle established by Zierler et al.(126), has been applied to DCE-CMR acquired data to determine myocardial perfusion (3,4,6,29,117,120). It is widely used with intravascular contrast agents and has been applied with extracellular contrast agents to quantify renal and tumour perfusion (5,138,139).

Model independent methods require that the measured blood, $C_{aif}(t)$ and tissue, $C_{myo}(t)$, enhancement data, which are related together through the following equation:

$$C_{myo}(t) = \int_0^t C_{aif}(t-\tau)h(\tau)d\tau = C_{aif}(t) * h(t) \quad [1]$$

are mathematically deconvolved to estimate tissue impulse response function, $h(t)$, and myocardium perfusion consequently. (4,6,117,120,126),

This task is challenging because it amounts to inverting the convolution of $h(t)$ with $C_{aif}(t)$ which is in this context an ill-posed noise sensitive inverse problem and needs regularization (106,107).

To the best of our knowledge, myocardial perfusion estimates have only been calculated for segmental quantification of myocardial perfusion, i.e. time curves averaged over groups of voxels, while voxel-wise analysis, although previously used on an experimental isolated pig heart model (6), has not been developed for clinical practice.

Voxel-wise myocardial perfusion analysis allows the quantification of MBF with the potential to preserve the information about extension, localization and transmurality of ischaemia. This technique produces higher resolution images of MBF and thus has the potential to allow a more accurate diagnosis of coronary artery disease. However, the lower contrast to noise ratio (CNR) of single voxel curves may reduce the accuracy and reliability of the measurement.

The objective of this study is to demonstrate the feasibility of voxel-wise perfusion analysis on high-resolution k-t perfusion data, by comparing the main regularized deconvolution methods in terms of accuracy and robustness to noise.

While many regularization methods have been used for deconvolution (as described in chapter 2), the most popular methods for kernel estimation in DCE-CMR include: Fermi function modelling (3,88), deconvolution using a B-spline basis (4,120) and deconvolution using an exponential approximation (5). More recently, Auto Regressive Moving Average (ARMA) has also been used to measure the tissue impulse response (6,121).

4.2 Material and Methods

4.2.1 Synthetic data

A first experiment was performed by using simulated data with known perfusion values and by calculating the absolute error of the MBF quantification.

This experiment was undertaken to verify the reliability of the perfusion estimates at different simulated levels of CNR and flow for each quantification method.

Noiseless gold standard tissue impulse response, $h_{GS}(t)$, was constructed by using the following pharmaco-kinetic model, described by Lindsey et al. (124):

$$h_{GS}(t) = \frac{e^{\lambda_1 t} - e^{\lambda_2 t}}{\lambda_1 - \lambda_2} u(t) - \frac{e^{\lambda_1 t} - e^{\lambda_3 t}}{\lambda_1 - \lambda_3} u(t) \quad [2]$$

where $u(t)$ is the unit step function. The physiological parameters, i.e. $\lambda_n, n = 1,2,3$, were chosen to generate tissue responses of the same order as those obtained by the fitting of real series of DCE-CMR acquisitions. λ_2 and $\lambda_3$and have been kept fixed on 0.21 and 0.36 respectively and the $\lambda_1$value has been changed to simulate a series of perfusion values between 0.5 to 5 ml/g/min. Table 4-1 represents the chosen λ_1 values for each simulated MBF level.

Table 4-1. λ_1 values for generating synthetic data

Simulated Flow (ml/g/min)	λ_1
0.5	**1.5**
1	**2.4**
1.5	**2.85**
2	**3.2**
2.5	**3.5**
3	**3.68**
3.5	**3.79**
4	**3.94**
4.5	**4.06**
5	**4.16**

$C_{aif}(t)$ used in this experiment is a convolution of many exponentials as suggested in (5) to model the propagation of an impulsive bolus injection through several compartments of the cardiovascular system. The injected bolus typically travels through at least three major compartments: from the injection site through the right heart, from the right heart through the lungs to the left heart and finally from the left heart to the myocardium tissue. For simplicity, we assumed the same mean transit time ($1/v > 0, v = 0.3897$), and thus the same compartment kernel ve^{-vt} for all compartments. As a result the arterial input at the tissue site can be formulated as n (n=4) convolution of the unit kernel:

$$C_{aif}(t) = \delta(t) * \left[ve^{-vt}\right]_1 * \left[ve^{-vt}\right]_2 * \ldots * \left[ve^{-vt}\right]_n$$

Initial $C_{myo}(t)$ was then obtained by convolving $h_{GS}(t)$ with the simulated $C_{aif}(t)$ (5). Rician noise of variable amplitudes were added to both $C_{aif}(t)$ and $C_{myo}(t)$ (140,141). The range of noise amplitude was chosen so that CNR in the both $C_{aif}(t)$ and $C_{myo}(t)$ would be between 1 and 40 in to include the CNR range of clinical data. Equal noise amplitudes were added to both $C_{aif}(t)$ and $C_{myo}(t)$ at each CNR level. CNR is defined as the ratio of the signal change from baseline to peak of enhancement data, divided by the standard deviation of the signal intensity curves before contrast.

4.2.2 MRI image acquisition

Image data (phantom and patient) were acquired on a Philips Achieva 3T (TX) system, equipped with a 32-channel cardiac phased array receiver coil (Philips Health Care, Best, Netherlands).

To avoid any confounding effects due to signal saturation, a universal dual-bolus injection scheme was performed in patients and the perfusion phantom as described by Ishida et al. (99). We used 0.001 mEq/kg of body weight as a pre-bolus and 0.01 mEq/kg of body weight as bolus (Gadobutrol Gadovist®, Bayer Schering, Germany). The boluses were injected at 4 ml/second followed by a 20 ml saline flush.

4.2.2.1 Hardware perfusion phantom

A second experiment was performed on a hardware perfusion phantom, which was recently developed by our group (142,143).The perfusion phantom resembles the anatomy of a 60 kg patient. It allows an efficient and reproducible simulation of myocardial perfusion acquisition, providing data suitable for quantification and with the possibility of a validation of the perfusion quantification results with a true gold standard.

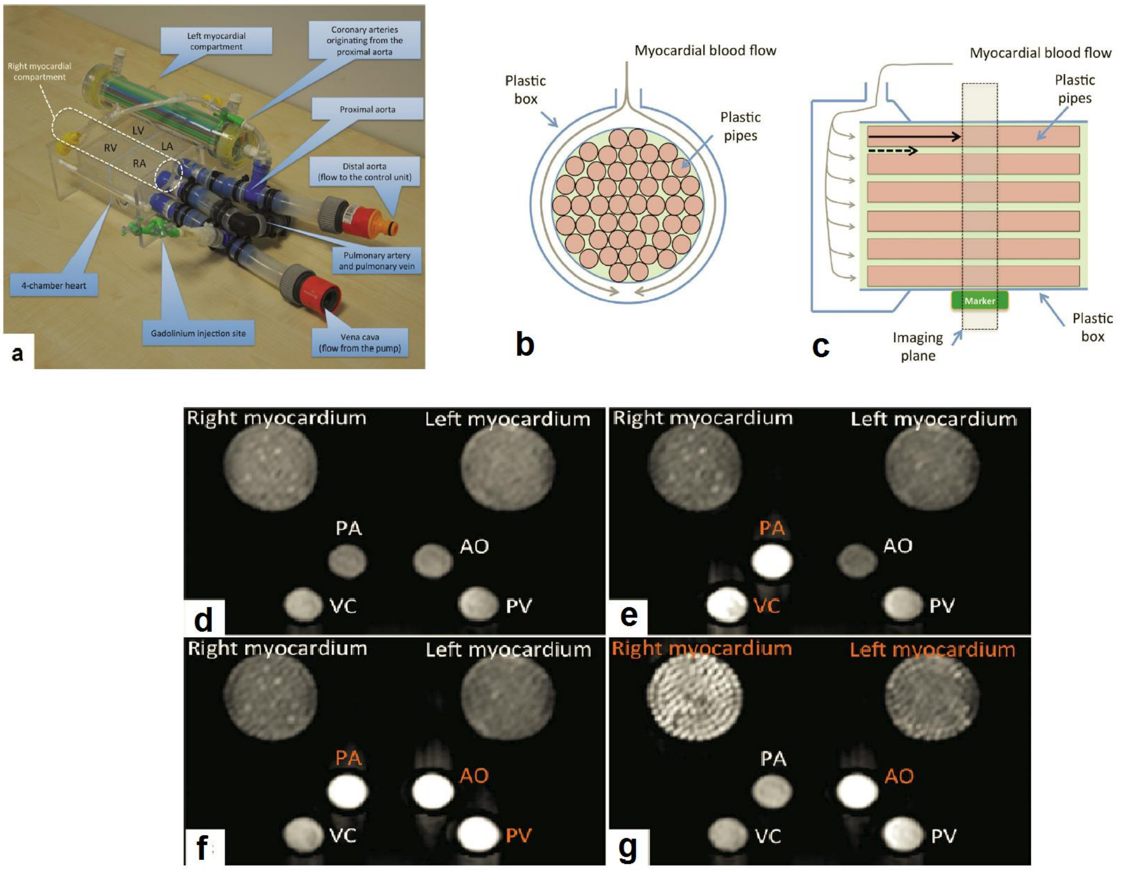

Figure 4.2-1 a: Picture of the perfusion phantom. The right myocardial compartment was removed and replaced with the dotted graph to allow visualization of the four-chamber heart located below. B. Schematic representation of the myocardial compartments. Short-axis view at the level of the myocardial flow inlet, represented by a lateral opening in the compartment. The simulated myocardial blood flow distributes to a circular space surrounding the inlet of the pipes first and then (C) enters the pipes. These are 124 parallel polypropylene pipes (48 shown in this scheme). Myocardial SI curves are generated in the imaging plane during first pass of the bolus of contrast agent, which follows two different pathways: inside the pipes (solid black arrow) and with slower speed in the space between one pipe and the others (dotted arrow). Both components generate the dynamic first-pass signal intensity upslope. The imaging plane is located at the level of a marker that identifies a myocardial distribution volume of 45 mL. This value allows the calculation of the gold standard perfusion rate from perfusion flow measurements. Representation not to scale. (d-g) Example of consecutive dynamics obtained from the perfusion phantom. d: Baseline image, before contrast injection.e: Early image, with SI increase in the VCand pulmonary artery. f: SI increase in the pulmonary artery, pulmonary vein, and aorta. g: SI increase in the aorta, right myocardial compartment (perfusion rate 10 mL/mL/min) and initial signal increase in the left myocardial compartment (5 mL/mL/min) (adapted from(143)).

Phantom data were acquired in one slice in a transverse geometry, visualizing the progression of the bolus of contrast agent in the large thoracic vessels and the myocardial compartments in the same image, with a saturation recovery gradient echo method (repetition time/echo time 3.0ms/1.0ms, flip angle 15°; effective k-t SENSE acceleration 3.8 fold, spatial resolution 1.2x1.2x10 mm, saturation delay 120 ms, Matrix size 132x132 , BW 2137 Hz ,FOV 24x24) (52,144,145).

Myocardial perfusion was simulated for the following experimental conditions. The perfusion phantom has two compartments. Average flow in the reference compartment was kept constant at perfusion rate equal to 5 ml/g/min. Average perfusion rate in the variable compartment ranging across the following values: 1, 2, 3, 4, and 5 ml/g/min. CNR was manipulated by varying the distance of the anterior surface coil from the phantom (high-CNR acquisitions with the coil as close as possible to the phantom; low-CNR acquisitions with the coil 10 cm from the phantom).

4.2.2.2 Patient study

In this study, we present preliminary data obtained for voxel-wise quantification of DCE-CMR data from five patients with angina symptoms referred to evaluate the presence and extension of inducible abnormalities of MBF during stress with adenosine and two healthy volunteers. The study was prospectively performed at Guy's and St Thomas' Hospital London (UK). The institutional review board approved the study and all patients signed an informed consent to be included.

Patients perfusion data were acquired in three slices (apical, mid cavity and basal) in a short axis geometry, visualizing the progression of the bolus of contrast agent in the large thoracic vessels and the myocardial compartments in the same image, with a saturation recovery gradient echo method (repetition time/echo time 3.0ms/1.0ms, flip angle 15°; effective k-t SENSE acceleration 3.8 fold, spatial resolution 1.2x1.2x10 mm, saturation delay 120 ms, Matrix size 251x251 , BW 724 Hz ,FOV 31x31) (52,144,145).

4.2.3 MR image processing

Accurate voxel-based MBF estimation requires respiratory motion correction and myocardial contour delineation. We developed an automated approach based on (146,147), in which respiratory motion was removed using affine image registration by maximization of the joint correlation between consecutive dynamics within an automatically determined region of interest. Then, a temporal maximum intensity projection was calculated to serve as a feature image for an automatic contour delineation method based on active contour models (146,147). Signal intensities were then sampled using bilinear interpolation at a grid of 60 angular positions and 10 transmural positions (or layers). The transmural positions were located on chords perpendicular to the myocardial centre-line.

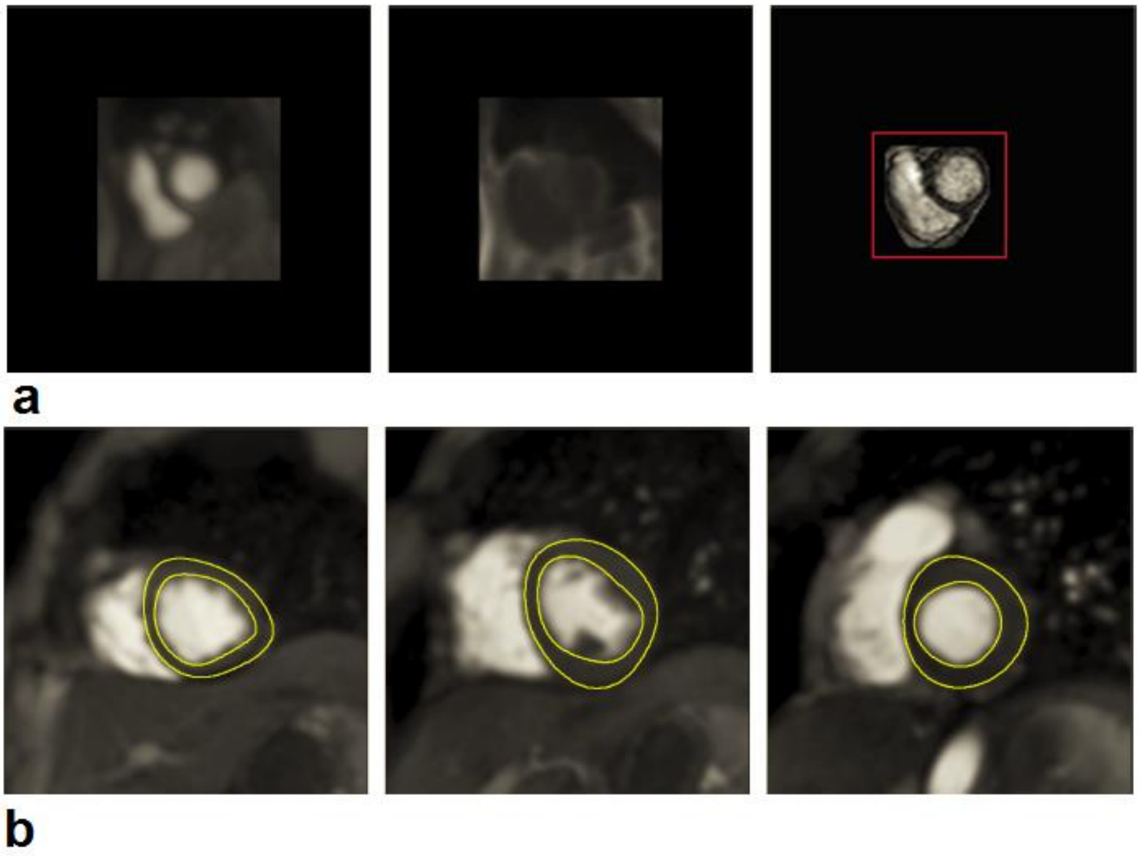

Figure 4.2-2 a) Coarse temporal maximum intensity projection and minimum intensity projection from perfusion CMR images and derived ROI (red box). b) Examples of resultingmyocardial contours at the apical, mid, and basal level displayed at the temporal MIP used during template deformation (Images are adapted from (148)).

To maximize reproducibility of MBF quantification, care was taken to obtain $C_{aif}(t)$ in a robust and reproducible way. $C_{aif}(t)$ was obtained by sampling the trimmed mean intensity within a region of interest in the blood pool of the basal slice. To be robust against the present of papillary muscles, the region of interest was obtained by down scaling the endocardium contours. Furthermore, the trimmed mean operator ignores 15% of outlier samples. The trimmed mean is the mean computed by excluding the 15% of smallest and largest data from the samples and taking the arithmetic mean of the remaining 70 %of the samples. The resulting signal is smooth and represents the AIF closest to the Ostia, (the true location of the input to the coronary system). Prior to deconvolution analysis, baseline correction that includes scaling of the signal intensities proportional to coil sensitivity and correcting for an offset to shift the baseline signal to zero has been performed. Moreover spatial filtering, Gaussian filter of size 5, and temporal filtering, a 30th order Hamming-window based low pass finite impulse response filter with normalized cut-off frequency of 0.23(149), was performed on the extracted signal intensity curves. For all models, the perfusion estimates were computed by deconvolving the measured blood and tissue enhancement data during the first pass of contrast agent in myocardium.

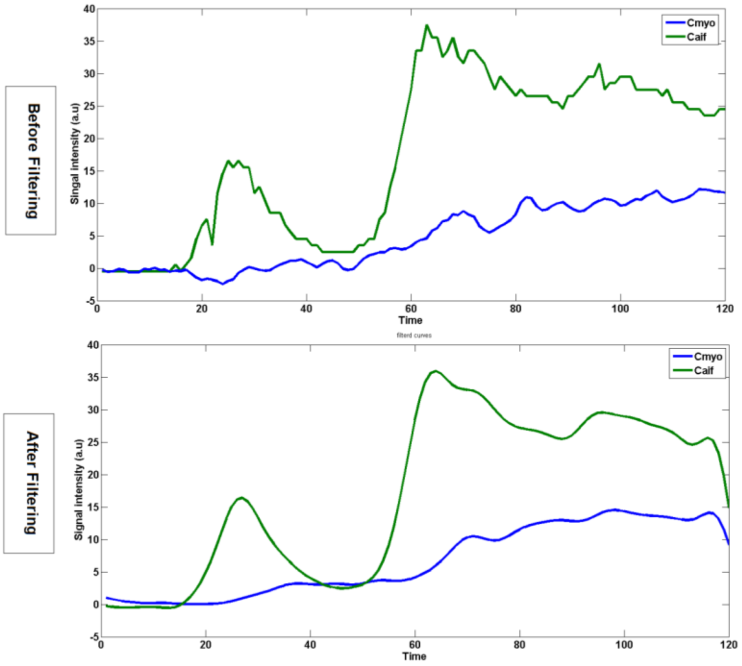

Figure 4.2-3 An example of temporal filtering, a 30th order Hamming-window based low pass finite impulse response filter with normalized cut-off frequency of 0.23, performed on a random voxel. The SNR of the data has been increased after filtering.

The constrained least square problems were solved using *lsqlin* for solving ARMA, B-spline and exponential equations and *lsqnonlin* for Fermi in MATLAB (Mathworks, Natick, Massachusetts, USA, version R2010b) (5,107). We used fourth-degree B-spline polynomial with 15 equally spaced break points (4) and 10 time scale (M=10) for exponential bases deconvolution (5) for the representation of impulse response in this study. To render the deconvolution process more stable and reduce the computational burden, second-order autoregressive model, i.e. AR (Q=0,L=2), (121), was chosen for quantification. It is important to note that this study was undertaken before the one represented in chapter 3. Therefore the order of ARMA model was chosen based on published available studies and not the results obtained subsequently as described in chapter 3.

4.2.4 Statistical analysis

In synthetic numerical and hardware perfusion phantom experiments, considered methods were compared by using the curve fit relative error:

$$x = \frac{\left\| C_{myo}(t) - h(t) * C_{aif}(t) \right\|}{\left\| C_{myo}(t) \right\|} \qquad [3]$$

and absolute perfusion error (e_a), which is defined when the reference perfusion value (gold standard), MBF_{GS} is available as:

$$e_a = \left| MBF - MBF_{GS} \right|$$

Mean ± standard deviation (STD) of e_a was calculated for each different condition tested in the perfusion phantom and synthetic data.

4.3 Results

4.3.1 Synthetic data

Figure 4.3-1 shows plots of simulated $C_{myo}(t)$ and $C_{aif}(t)$ curves for different level of CNR and perfusion rates (a). $C_{myo}(t)$ for a synthetic myocardium voxel along with the estimated $C_{myo}(t)$ curves, which have been obtained using ARMA, exponential, B-spline and Fermi method, at CNR=40 and CNR=5 are shown in Figure 4.3-1(b) and (c), respectively.

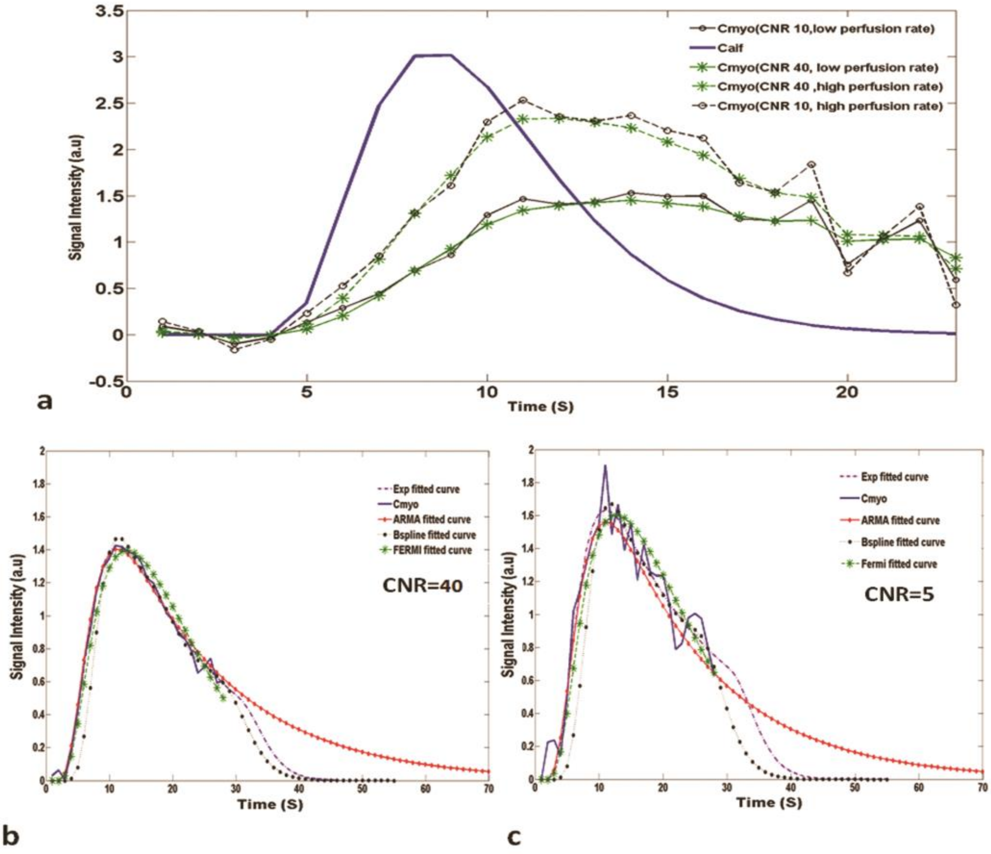

Figure 4.3-1 In a, the synthetic input and output signal intensity (in arbitrary units: a.u.) curves at high simulated perfusion rate and low simulated perfusion rate at different CNR levels. The solid line corresponds to the synthetic $C_{aif}(t)$ and the dotted lines correspond to synthetic $C_{myo}(t)$. In b and c $C_{myo}(t)$ for a synthetic myocardium voxel along with the estimated curves using ARMA, exponential, B-spline and Fermi method are shown at CNR=40 and CNR=5 (MBF_{GS}= 1ml/gr/min), respectively. In general, all methods give good results in terms of fit (x<0.9% for high CNR x< 2% for low CNR).

Figure 4.3-2 shows the absolute errors (e_a) of the synthetic data MBF estimates obtained with the four methods – ARMA (a), exponential (b), B-spline (c) and Fermi (d) – at different levels of flow and CNR. e_a is averaged over all voxels at each CNR level and perfusion rate.

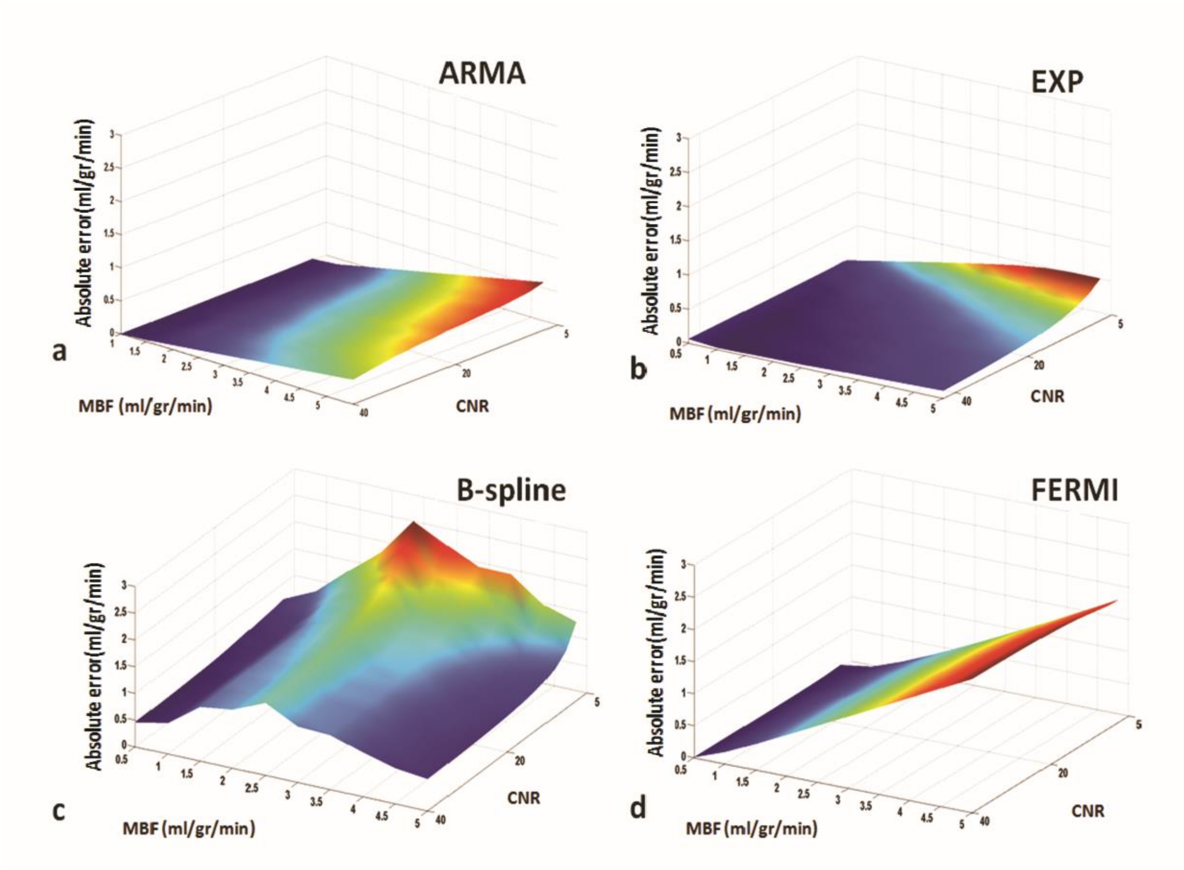

Figure 4.3-2 Surface plot of simulated flow rates (0.5 to 5 ml/gr/min) absolute error(e_a) at different CNR levels (5 to 40 with 15 steps) for the ARMA, exponential, B-spline and Fermi model is represented in figures a, b, c and d, respectively.e_a is averaged over all voxels at each flow and CNR level. In general, the ARMA and the exponential model are more accurate at all flow levels. ARMA is more accurate at flow levels less than 3 ml/gr/min and at high flow levels (MBF>3.5 ml/gr/min) when CNR is high (CNR >20). B-spline is as accurate as exponential method (absolute error<0.5) at flow level equal to 5ml/gr/min, when CNR is high (CNR>25). Absolute error increased as the perfusion level increased with the Fermi model. CNR increases from right to left in the plots.

Table 4-2 represents the mean ±STD of e_a over different CNR levels at each perfusion rate for synthetic data. ARMA and exponential methods provided the most accurate and reliable estimates. When MBF is below 1 ml/gr/min, the Fermi model is as accurate as ARMA. A possible explanation for this behaviour of Fermi model is its natural shape. Femi function has a shape close to unit step function with a plateau portion dependant on the equation parameters. Whereas (as explained previously in chapter 2) shape of $h(t)$ is more similar to a second order impulse response with an overshoot at the beginning of the curve. This overshoot is most probably happening at high flow values. Since Fermi function is not capable of simulating this overshoot, it will result in underestimation and consequently error in the analysis of MBF.

As seen in Figure 4.3-2 and Table 4-2 at a constant MBF absolute error was inversely related to CNR for ARMA, exponential and B-spline but relatively constant for Fermi. For comparable CNR levels, error increased proportionally to MBF with ARMA (a), exponential (b), Fermi (d). The B-spline (c) method shows a bell-shaped error curve with error increasing for flow levels between 0.5-3.5 ml/gr/min and decreasing thereafter. In general, the lowest error was obtained by ARMA and the exponential method. In terms of noise sensitivity, the Fermi model conferred the flattest slope suggesting that this method is more robust to noise compared to other methods.

Table 4-2 Mean and standard deviation (mean±STD) of perfusion estimates absolute error (e_a) in ml/gr/min, over different CNR levels at different perfusion rates for synthetic data.

MBF_{GS}	**ARMA**	**Exponential**	**Fermi**‡	$\mathbf{B-spline}^{*}$
0.5	0.007±0.002	0.06±0.003	0.01±0.008	0.5±0.07
1	0.03±0.028	0.05±0.037	0.1±0.02	0.6±0.11
1.5	0.06±0.054	0.07±0.05	0.231±0.035	1.03±0.13
2	0.09±0.082	0.1±0.077	0.37±0.045	1.25±0.25
2.5	0.11±0.11	0.12±0.09	0.58±0.05	1.6±0.39
3	0.16±0.15	0.15±0.11	0.78±0.053	1.26±0.38
3.5	0.18±0.16	0.2±0.13	1.1±0.056	1.2±0.33
4	0.21±0.19	0.22±0.14	1.4±0.058	1.01±0.34
4.5	0.22±0.21	0.23±0.15	1.6±0.059	0.8±0.26
5	0.23±0.26	0.24±0.17	1.9±0.06	0.7±0.23

All values are in ml/gr/min.

* B-spline method is more sensitive to noise level as the difference between the absolute errors at high and low CNR is significant at all perfusion rates (high STD).

‡ The absolute error is high with Fermi model at perfusion rates greater than 1.5 ml/gr/min; however, it is more robust to noise (low STD).

4.3.2 Hardware perfusion phantom

Using first-pass images acquired on the hardware perfusion phantom, perfusion estimates were computed for different perfusion rates on voxel-wise basis and incrementing levels of spatial averaging , i.e. averaging between a group of 10 voxels, 100 voxels and 600 voxels (the whole slice). Voxel-wise perfusion estimates and results obtained from segmental analysis for different levels of spatial averaging for all four quantification methods is shown in Figure 4.3-3.

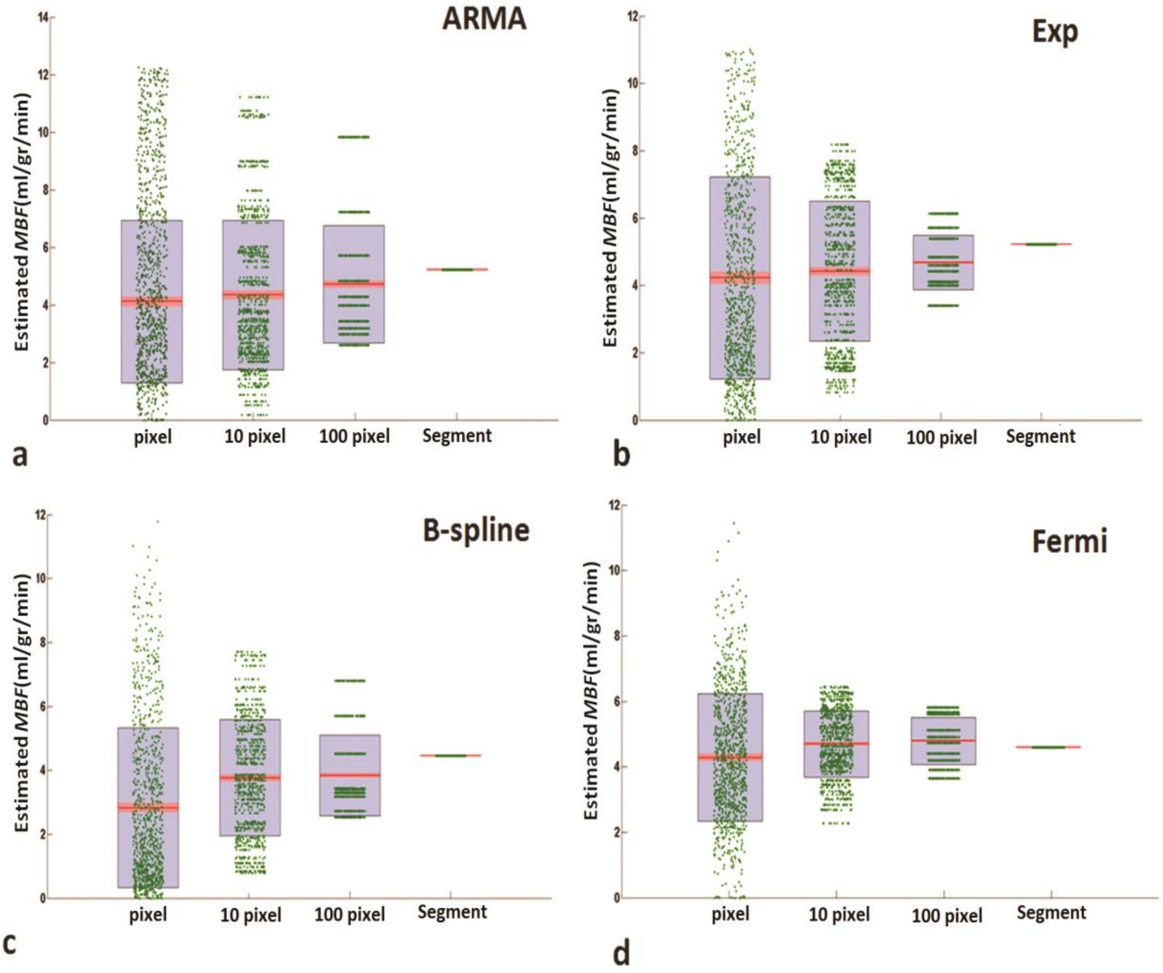

Figure 4.3-3 Scatter-Box plot of estimated MBF in the perfusion phantom experiment, with MBF_{GS} =5 ml/gr/min at high CNR (CNR=32) comparing voxel-wise with segmental analysis, using (a) ARMA, (b) exponential, (c) B-spline and (d) Fermi method. Each individual green dot shows the estimated MBF at each ROI for different levels of spatial averaging (1 voxel, 10 voxel, 100 voxel and whole segment) and they have been spread for visualization reasons and clarity. On each blue box, the central red mark is the median; the edges of the box are the 25th and 75th percentiles. The red area around the median shows the points, which are laid over 95 % of the confidence interval (the points with less than 5% difference from the median).

The average estimated perfusion values obtained from the analysis was compared with the true average perfusion rates. Table 4-3 represents the perfusion estimates relative error (e_{prl}) – defined as absolute error divided by the true average perfusion value, for voxel-wise analysis and segmental analysis.

Table 4-3 Perfusion estimates relative error, e_{prl}, for different levels of spatial averaging at MBF_{GS}=5 ml/gr/min, (comparison between voxel-wise and segmental analysis on perfusion phantom data).

Level of spatial averaging	ARMA	Exponential	Fermi	B-spline
Voxel-wise (610 ROI)	15.4%	15.6%	18%	43%
Segment(one ROI)	6%	6.3%	13%*	12%

*note that this value shows the e_{prl} at MBF_{GS} equal to 5 ml/gr/min (high perfusion rate). We expect that the Fermi model to be as accurate as ARMA and exponential at low perfusion values.

With the ARMA, Fermi and exponential methods, reducing the Region of Interest (ROI) size from a segment, in which time curves averaged over 610 voxels, to one voxel did not have a significant effect on the estimation accuracy but altered the variability of error.

Figure 4.3-4 shows MR images of the hardware perfusion phantom and the corresponding perfusion maps using ARMA, exponential, B-spline and Fermi. The inhomogeneities of flow that are evident in the MR pictures have been captured by voxel-wise perfusion maps.

Figure 4.3-5.a shows a comparison between the mean of estimated perfusion values, averaged over all voxels at each MBF level at high CNR, and true average MBF values from the hardware perfusion phantom. Figure 4.3-5.b represents the mean of e_a averaged over all voxels, at high and low CNR levels and different MBF rates in the perfusion phantom. The difference between e_a at high and low CNR for each perfusion level was not significant for ARMA (STD=0.031 ml/gr/min), exponential (STD=0.028 ml/gr/min) and Fermi (STD=0.014 ml/gr/min), whereas it was significant for B-spline (STD=0.35 ml/gr/min). It implies that ARMA, exponential and Fermi methods are more reliable and robust to noise compared to the B-spline method.

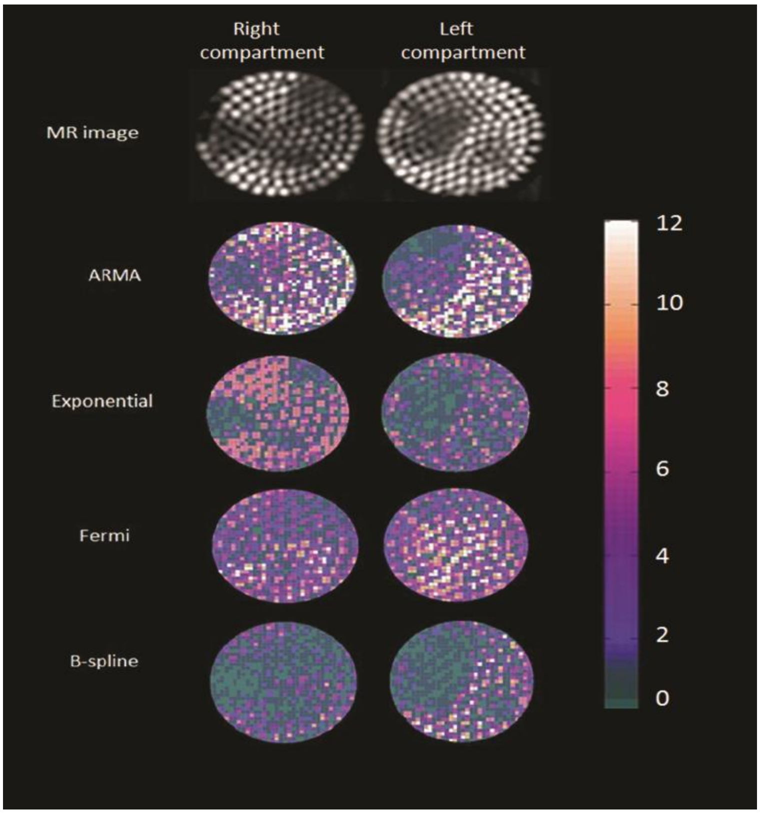

Figure 4.3-4 Maps of estimated MBF in perfusion phantom at high input flow rate (5 ml/gr/min) and high CNR (CNR=32) with exponential, ARMA, Fermi and d B-spline method along with the phantom MR image, which is obtained by calculating maximum intensity projection (MIP) over time of the 10 upslope dynamics. The perfusion inhomogeneity is well depicted with exponential, ARMA and B-spline model. However, perfusion values are underestimated with B-spline method. Average perfusion value in the reference compartment (left compartment) has been used for calibration.

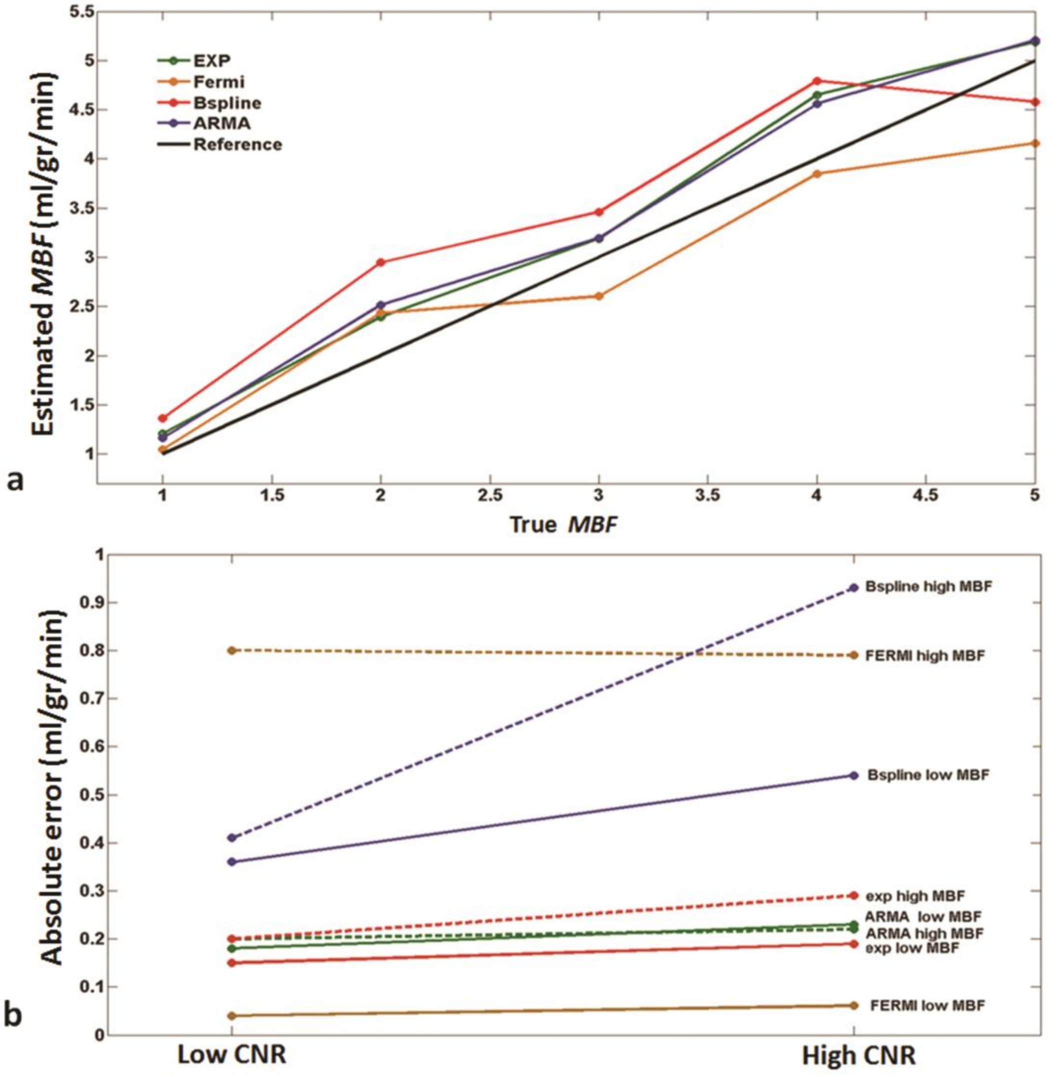

Figure 4.3-5 Plot of mean of estimated perfusion phantom MBF, averaged over all voxels at each flow level vs. true average flow values at high CNR (CNR=32) obtained with ARMA, exponential, Fermi and B-spline method. For flow levels less than 2.5 ml/gr/min, the MBF is overestimated with Fermi method and underestimated thereafter. ARMA and exponential method overestimate MBF at all flow levels. At flow levels higher than 4.5 (ml/gr/min) MBF is underestimated with B-spline method. True flow values were measured by means of precision flow-meters in the perfusion phantom. b: Perfusion estimates absolute error (e_a)in phantom at high CNR (CNR=32) and low CNR (CNR=18) obtained with ARMA, exponential, Fermi and B-spline method using segmental analysis at true average perfusion equal to 1 ml/gr/min (dotted lines) and 5 ml/gr/min is represented. ARMA, exponential and Fermi are the least sensitive methods to noise, while B-spline results vary significantly with CNR level. Absolute error was relatively constant between different MBF levels for all methods except Fermi (absolute error is high with Fermi model at high flow values). ARMA and exponential methods are more accurate at high perfusion rates compared with Fermi model.

4.3.3 Patient Study

The results obtained from patient studies are shown in Figure 4.3-6, Figure 4.3-7 and Figure 4.3-8. The voxel wise SI curves obtained from the images for all cases had a CNR of 14.6±7.4 before filtering and 27.7±8.4 after temporal and spatial filtering, which are of sufficient quality for accurate analysis (28).

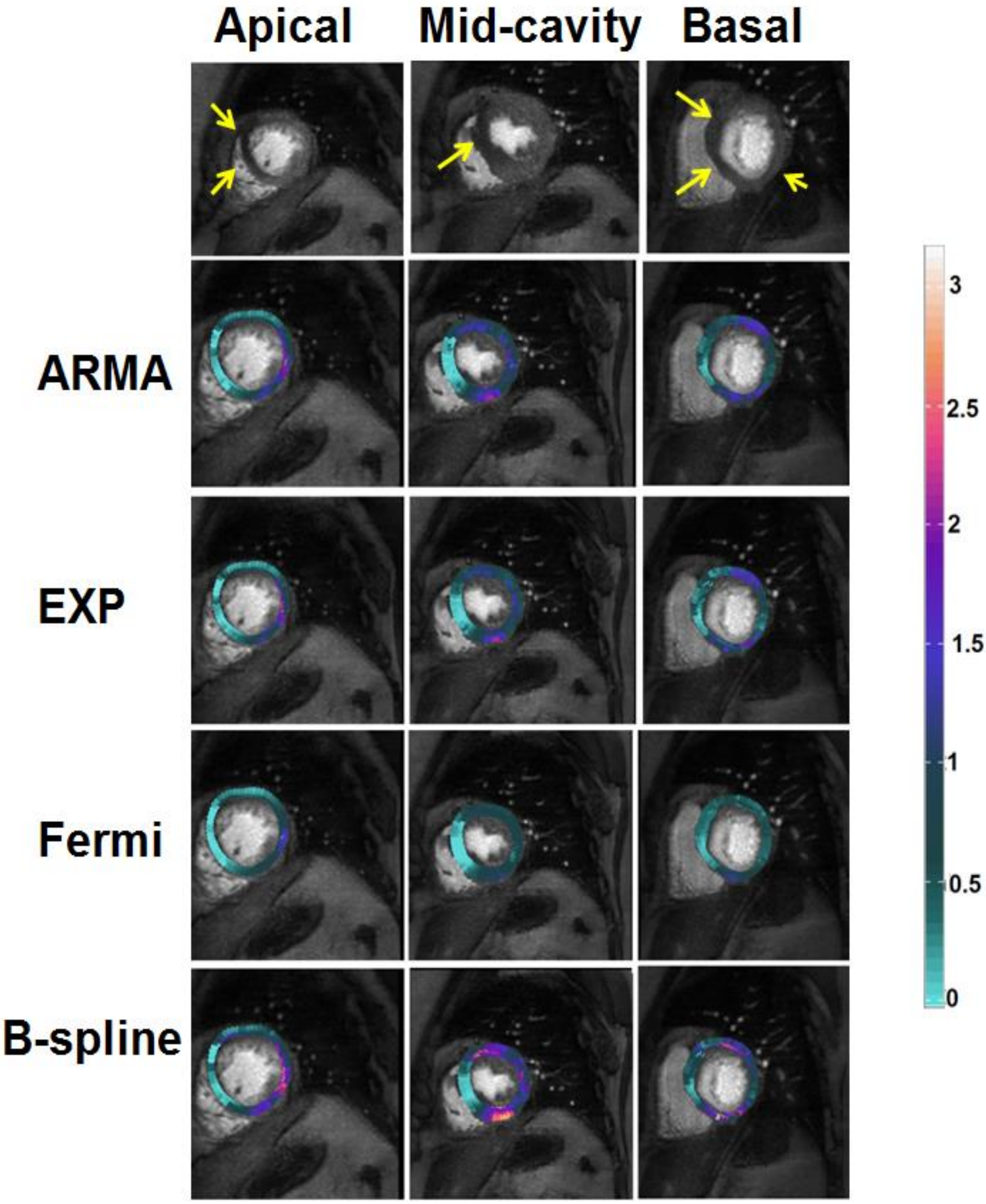

Figure 4.3-6 Results of voxel-wise perfusion quantification for a 67-year-old female with chronic total occlusion of the LAD collateralized by the LCx. The LCx itself presents a 75% stenosis. The first column from leftcorresponds to apical layer, the middle-column corresponds to mid-cavity and the last column corresponds to basal layer in myocardium. In the maps, the light green is the worst. The sensitivity of detection of ischaemia at the edge of the ischemic area has shown a strict dependency on the used method.

Voxel-wise perfusion maps were generated following MBF analysis using the four models and overlaid over the CMR images from a patient dataset with angina (Figure 4.3-6). Diseased areas are represented as light green and correlate well with the perfusion defects seen in the raw CMR images in the first row. Coronary angiographic findings in this patient demonstrated a chronic total occlusion of the LAD which was collateralized by a 75% stenosed LCx.

Figure 4.3-7.a and Figure **4.3-7**.b represents a histogram comparison of estimated perfusion distribution values in two regions of interest obtained from two patients with proven angiographic coronary artery disease. These graphs demonstrate that voxel-wise analysis allows clear discrimination between normal and ischemic region of myocardium. The ability to correctly distinguish between these regions was different depending on the method employed. Figure 4.3-7.c on the other hand is a histogram example in a healthy volunteer. The volunteer graph (Figure 4.3-7.c) yields a single Gaussian-shaped graph for the healthy volunteer in comparison to a double Gaussian-shaped graph in the patient series.

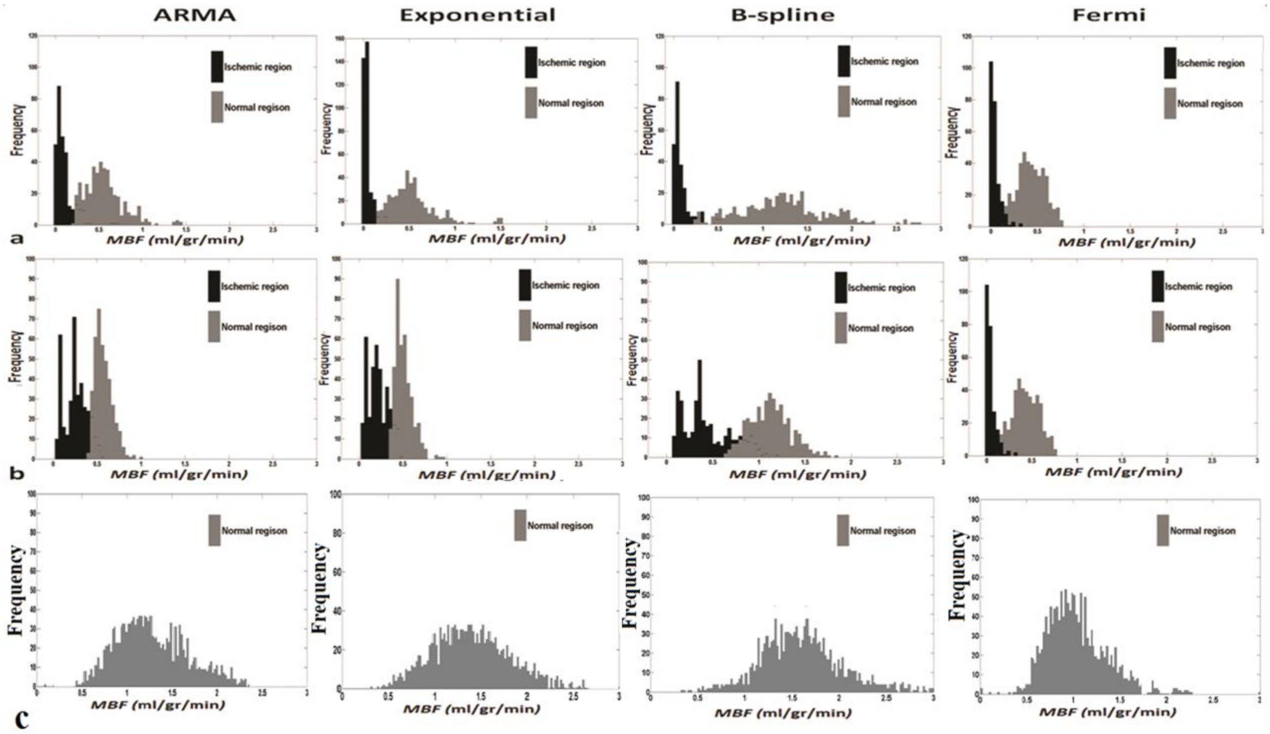

Figure 4.3-7 Histogram of estimated MBF comparing distribution of perfusion values obtained by voxel-wise analysis in two regions of interest in (a) 67-year-old male with 2-vessel coronary artery disease and (b) 48-year-old male with one vessel disease affecting the LAD and (c) a healthy volunteer.

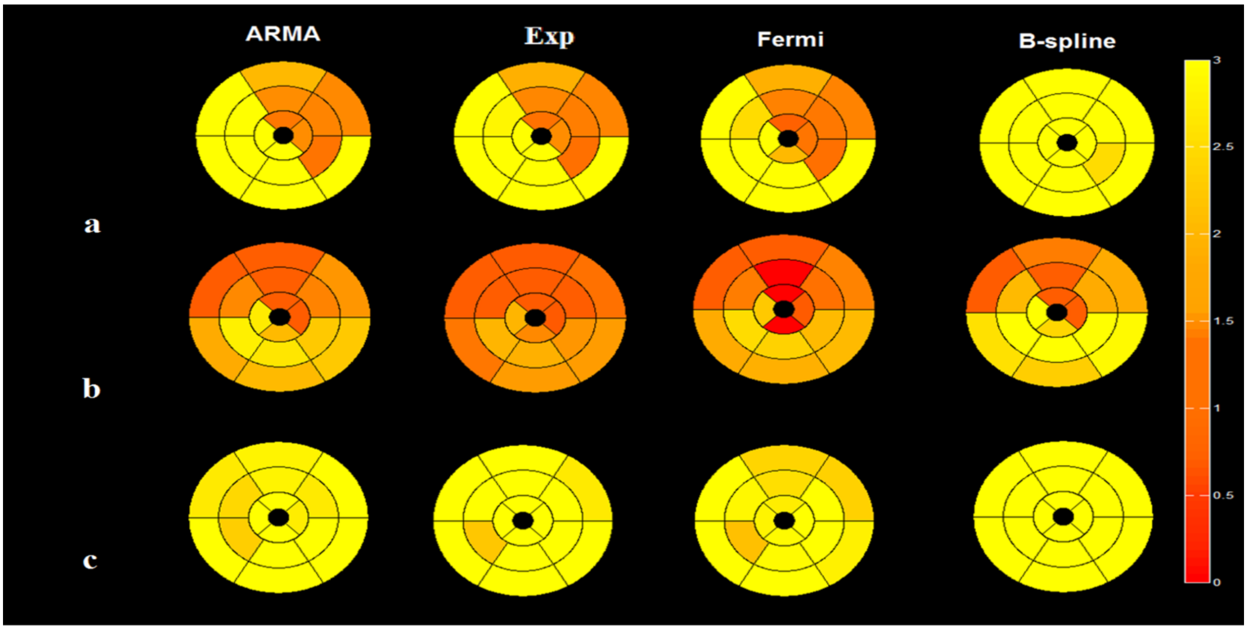

Figure 4.3-8: bull's-eye map of two patients one with (a) LCx disease,(b) LAD disease and (c) a healthy volunteer (same patients nad volunteer as figure 4.3-7) comparing the four different methods using American heart association 16 segments representation. MBF values are averaged over all voxels in each segment. . It can be seen that there is not a significant variation between different regions of myocardium in the healthy volunteer. The perfusion values are presented in ml/gr/min

It is important to note that the clear delineation of ischemic regions qualitatively illustrated in the perfusion maps achieved statistical significance on quantitative analysis of the differences between the estimated MBF.

Table 4-4 represents the respective p-value comparison of mean estimated MBF between normal regions and ischemic regions using the four methods. All p values were <0.05 suggesting the presence of significant difference between normal and ischemic regions in abnormal myocardium. The largest discrimination was provided by both ARMA (p<0.001) and the exponential method (p<0.005).In contrast, the p-values in healthy volunteers represented in table 4-5 are all greater than 0.05 indicating the absence of significant difference between compared regions of interests.

Table 4-4 The respective p-value comparison of mean estimated MBF between normal regions and ischemic regions using the four methods

	ARMA	EXP	BSPLINE	FERMI
Patient 1	0.000118423	6.64E-05	0.000112	0.025928
Patient 2	0.000500101	0.001971	0.011765	0.008551
Patient 3	0.00103014	0.005226	0.012634	0.02299
Patient 4	0.004675219	0.003722	0.001875	0.001999

Table 4-5 The respective p-value comparison of mean estimated MBF within different regions of myocardium in healthy volunteers using different methods.

	ARMA	EXP	BSPLINE	FERMI
Volunteer 1	0.703168828	0.819582	0.5072	0.654329
Volunteer 2	0.782779685	0.897111	0.915155	0.89487

P value for each volunteer is averaged over three p values which compare LCX segments with RCA segments and LAD segments.

In order to facilitate clinical utility of these data, the 16 segment American Heart Association model was used to represent the quantified perfusion values. Figure 4.5-8 represents the bull's-eye map of two coronary artery disease patients - (a) with LCx disease and (b) with LAD disease - and a healthy volunteer –(c). MBF values are averaged over all voxels in each segment.

4.4 Discussion

We believe that this is the first study to demonstrate the feasibility of voxel-wise analysis in detecting underlying ischaemia and compare the differences in perfusion estimates, sensitivity to noise and different levels of spatial averaging between four different deconvolution methods.

Firstly, methods were evaluated with simulated synthetic data. They were then validated with the perfusion phantom, which serves an ideal bridge between synthetic data and patient data. Finally, the validated methods were applied to patient data to show the feasibility of voxel-wise perfusion maps.

The major strength of this study is that we were able to use a phantom as a reference for the different models, flows and noise levels. This is more realistic than synthetic data and thus allows a comparison of the estimated MBF with the true MBF, which is not possible in patients. Here, using the results obtained from phantom experiments, the performance of each method on patients and estimate the accuracy of each method can be predicted.

Based on the more horizontal slope and the low standard deviation displayed in Table 4-2 and 4-3, Figure 4.3-2 and Figure 4.3-5.b, Fermi, ARMA and exponential model are the least sensitive methods to noise. This characteristic enables a more robust analysis of MBF. However among those three methods, a higher variability of error is observed in ARMA and exponential model compared to Fermi (Figure 4.3-3). This makes Fermi the more favourable method in terms of noise sensitivity for voxel-wise analysis.

ARMA and the exponential method provide the most accurate estimates of MBF among the four methods (e_{prl} <6.5%) at all MBF levels on an experimental analysis. This is most pronounced at high perfusion rates (Table 4-2 and Figure 4.3-2 and Figure 4.3-5.a).

In general ARMA and the exponential method are more accurate at all flow rates (Figure 4.3-4 and Figure 4.3-5), On the other hand, Fermi model is the most robust method to noise with highest precision for voxel-wise analysis. Inevitably the choice of quantification method for data analysis boils down to a trade off between accuracy and precision of the estimation.

Perfusion maps and histogram graphs indicate that the difference between accuracy of perfusion estimates depend on the selected method. We conjecture that because $C_{aif}(t)$ and $C_{myo}(t)$ curves appear to be approximately bi-exponential, the exponential bases deconvolution and ARMA method, which can be considered as a generalization of the exponential method (121), provide more accurate and natural tissue kernel and therefore better MBF estimation.

Since voxel-wise analysis offers additional information on the heterogeneity of myocardial perfusion, these results provide a strong case for a voxel-wise approach in clinical applications of DCE-CMR.

4.4.1 Limitations

It is important to note that whilst PET is regarded as the gold standard for the quantification of absolute MBF, we were unable to obtain PET information for this study and compare our results with PET results. The aim of this study was to demonstrate feasibility of a voxel-wise analysis in patients. However, the sample size used here was small and a larger study examining the correlation between voxel-wise analysis and angiographic findings is currently underway. In addition, a cut-off value for MBF between ischemic and normal regions needs to be addressed by further studies validating the results against appropriate functional tests alongside obtaining histological evidence from animal work.

Further studies are required to investigate the correlation between perfusion estimates in the phantom and patient datasets. In addition further optimization of the deconvolution methods, including finding the optimal order of considered methods such as ARMA should be performed.

In this study we have only used model independent analysis to quantify MBF. A direct comparison of model independent and model-dependent analysis will need to be addressed in further studies to define the most appropriate quantitative methods for voxel-wise analysis. Finally as only one filtering method has been used in the study to remove the noise from signal intensity curves, a further study is needed to analyze the interaction between signal intensities sampling resolutions, temporal and spatial filtering methods and MBF results obtained from deconvolution analysis.

4.5 Conclusions

This study demonstrates the feasibility of voxel-wise quantification of myocardial perfusion on high-resolution MR perfusion data sets. Moreover, it compares different algorithms to determine the most

accurate and precise method for voxel-wise myocardial blood flow quantification. Simulations and maps in patients and hardware phantom showed that voxel-wise quantification of myocardium perfusion is feasible and can be used to detect abnormal regions. The exponential and ARMA methods were more accurate than other methods whilst Fermi was the most precise and robust method to noise in the voxel-wise analysis of myocardial perfusion.

This chapter has been adapted from N Zarinabad, A Chiribiri, G. Hautvast, M Ishida, A Schuster, Z Cvetkovic, P. Batchelor, E Nagel, ***Voxel-wise quantification of myocardial perfusion by cardiac magnetic resonance. Feasibility and methods comparison;*** *Magnetic Resonance in Medicine 68:1994–2004 (2012)*

NZ: implemented the post-processing and quantification methods. Data analysis and simulations experiments and preparation of the manuscript.GH: implemented the pre-processing methods. MI: performed phantom experiment, AS: performed phantom experiment, AC: performed phantom experiment, acquired patients data, ZC: supervised the project. PB: supervised the project. EN: arrange funding and supervised the project.

5 Effects of tracer arrival time on the accuracy of high resolution (voxel-wise) myocardial perfusion map from Contrast-Enhanced First-Pass perfusion magnetic resonance.

5.1 Introduction

First-pass perfusion cardiac magnetic resonance (CMR) allows the non-invasive and radiation-free assessment of myocardial blood flow (MBF) and enables a far better spatial resolution than nuclear medicine techniques(125). Recently, the feasibility of quantitative voxel-wise analysis has been demonstrated by us and by others using a hardware perfusion phantom and microspheres in dogs and pigs, respectively (127,150,151).

Voxel-wise quantification has the potential to combine the advantages of visual analysis with the objective and reproducible evaluation made possible by true quantitative assessment. However, before voxel-wise quantification becomes a robust clinical tool, there are several technical challenges to overcome. Voxel-wise quantitative analysis involves lower signal-to-noise ratio (SNR) levels which affect the accuracy of the MBF estimation(127).

Another source of error is the sensitivity of quantification methods such as Fermi function modelling to the delay between tracer arrival time into the arterial input and the tissue (*tAIF* and tOnset, respectively) (152). This issue, which has been demonstrated previously for segmental analysis is likely to be even more important on a voxel-wise analysis firstly due to the reduced SNR, which makes the selection of the real tOnset for each voxel even more difficult and secondly due to significant variation of tOnset amongst different voxels within the same or different segments due to anatomical and physiological factors. Therefore an optimization of the analysis parameters could potentially improve the accuracy of voxel wise quantification. However the individual optimization of tOnset for voxel wise analysis can be time consuming and warrants an automated method.

In the present study we aimed to explore the latter issue systematically. In particular, we sought to demonstrate the importance of tOnset on voxel wise MBF analysis and to develop an algorithm that enables the automated detection of the optimal tOnset in each voxel for a more accurate estimation of MBF.

5.2 Theory

Prevalent available quantitative techniques for estimating MBF use the central volume principle and deconvolve the tissue signal during the first pass of a bolus of contrast agent with the arterial input function sampled from the LV or aorta. According to the central volume principle the concentration of the contrast agent in the tissue region $C_{tiss}(t)$ is related to the concentration of the contrast agent in the arterial input $C_{aif}(t)$ via the following convolution formula(126):

$$C_{myo}(t) = C_{aif}(t) * h(t) \qquad [1]$$

where $h(t)$ is the unknown tissue impulse response. Eq.1 needs to be deconvolved to estimate h(t) and therefore quantify the myocardial blood flow (MBF) according to $h(t = 0)$.

The intensity values after arrival of the contrast agent into the blood pool and tissue will be used for quantification.

Assuming that the tissue residual curve, $C_{tiss}(t)$, has been delayed by t_d second then equation [1] would be rewritten as:

$$C_{myo}{}^{*}(t) = C_{myo}(t - t_d) = C_{aif}(t) \otimes h^{*}(t) \qquad [2]$$

This implies that the delayed tissue residue curve can be represented as convolution of the arterial input curve and a new impulse response ($h^{*}(t)$) which is not equal to $h(t)$ and thus results in a wrong estimation of MBF. This delay will disappear if we align the points in which the onset of contrast agent occurs in the left ventricular blood pool (*tAIF*) and tissue (tOnset).

Well known widely used Fermi function modelling (3) has been used for quantification in this study.

Jerosch-Herold et al. (3) and Wilke et al. (88) fitted time curves for the tissue impulse response function, $h(t)$, to the Fermi function with the following analytical expression:

$$h(t) = R\ \left[\frac{1}{\mathrm{e}^{(t-\tau_0-\tau_d)k}+1}\right]\ u(t-\tau_d) \qquad [3]$$

using a Marquardt-Levenberg nonlinear least square algorithm by letting k, R and τ_0 vary and keeping τ_d fixed. In Eq. [3] $u(t-\tau_d)$ is the unit step function. The τ_d accounts for the delay time between the appearance of the signal in the LV blood pool and myocardial region of interest (ROI) ($\tau_d = T_{onset} - T_{AIF}$). τ_0 characterizes the width of the shoulder of the Fermi function during which little or no contrast agent has left the ROI. R is the index of contrast agent influx parameter and k represents the decay rate of $h(t)$ due to contrast agent wash out. From Eq. [3], MBF is calculated as $h(t)$ at $t = 0$.

In our previous study in chapter 4 (127) for the purpose of MBF estimation using Fermi function modelling, a fixed τ_d , which was selected by the operator based on a random single voxel $C_{aif}(t)$ and $C_{myo}(t)$, has been used as the delay time for all voxels in the myocardium

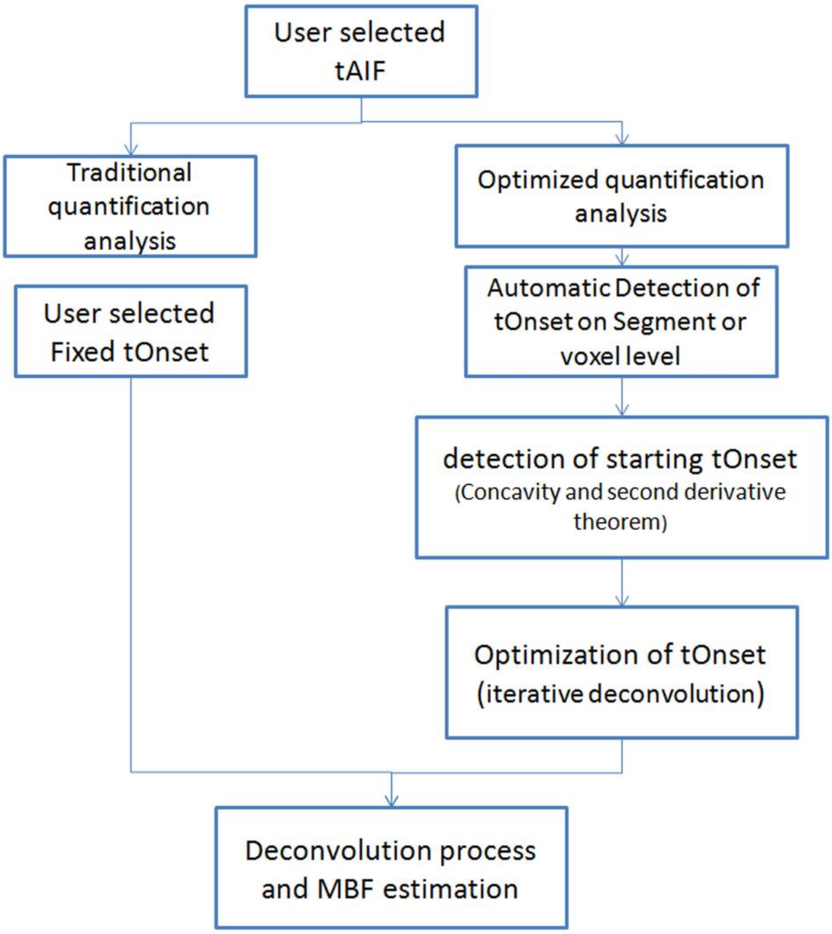

Figure 5.2-1 A flow chart comparing the traditional and optimized quantification analysis.

5.3 Tracer arrival time detection and optimization

We developed an algorithm for detection of individual tOnset for each voxel and examined the effects of both forward and backward shifting of tissue signal on MBF estimation.

The algorithm performs a second derivative test on each individual voxel signal intensity curve, to detect the closest tOnset to the real uptake point of the curve (starting tOnset), followed by an iterative deconvolution to determine the dynamic with the smallest curve fit error (optimized tOnset).

Based on the concavity theorem, if the function $f(x)$ is twice differentiable at x =s, the graph of f in concave upwards at $(s, f(s))$ if $f''(s) > 0$ and concave downwards if $f''(s) < 0$. The points where the concavity changes from up to down are called inflection points of the curve.

The implemented algorithm searches for the inflection point in the tissue signal intensity curve, starting from the dynamic in which the contrast agent appears in the LV (tAIF, selected by the user based on the $C_{aif}(t)$) until when it reached its maximum value in the tissue (before washing out). Now suppose that $f'(s) = 0$ ($f'(s)$is the first derivative) in$[s - \partial, s + \partial]$, then c, $[s - \partial < c < s +$

$\partial]$, will be assumed as the point at which the f has started concaving upward if $f''(c) > 0$ and $f''(c)$ is the maximum of f'' in $[s - \partial, s + \partial]$ ($f''(s)$is the second derivative), (Figure 5.3-1.a).

In the implemented method, the dynamic which obeys the above rule between the user selected AIF arrival time and the estimated inflection time of $C_{myo}(t)$ has been assumed as the starting tOnset and $C_{myo}(t)$ and $C_{aif}(t)$ have been aligned in time.

The iterative deconvolution algorithm begins by using the starting tOnset. Then, the residual error between $C_{myo}(t)$ and the $C_{myo}(t)$ is calculated after shifting the tOnset up to the 4 neighbour dynamics in both temporal directions. The algorithm then selects the dynamic with the smallest residual curve fit error as the optimized tOnset, which is used for quantitative analysis (Figure 5.3-1.b).

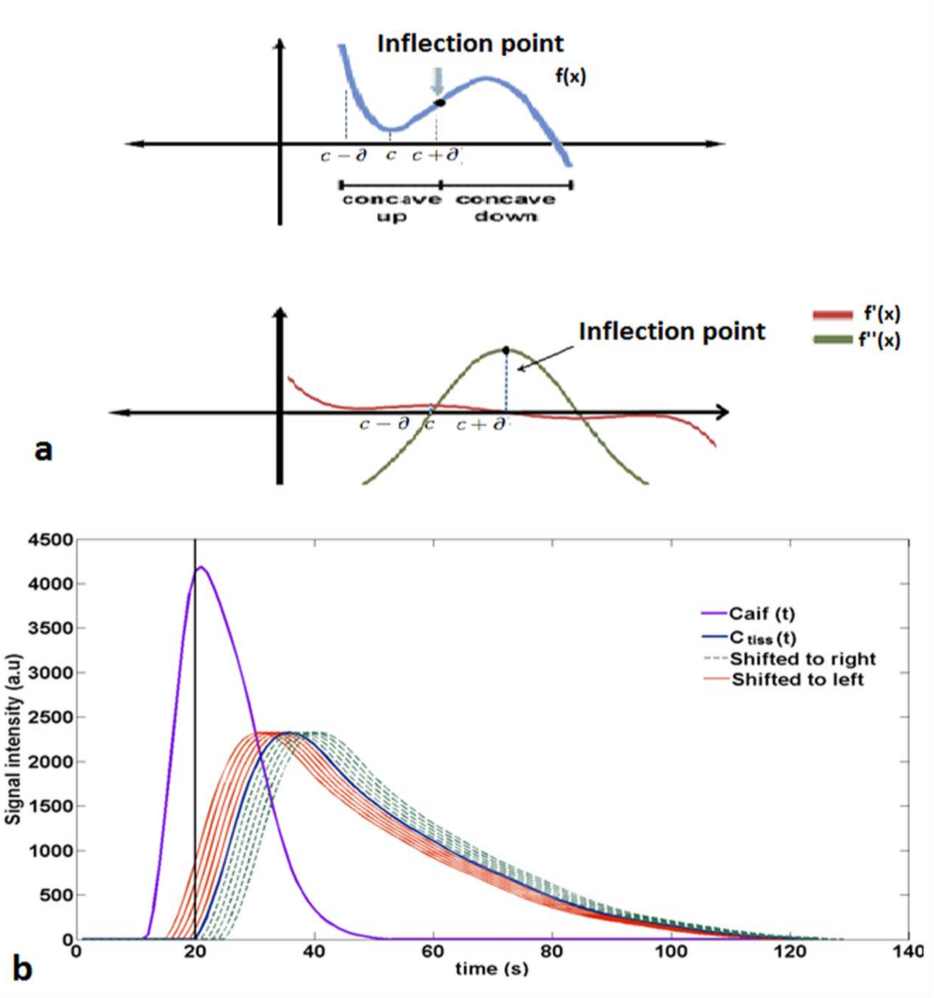

Figure 5.3-1(a) Example of a curve with inflection point along with its first and second derevative curves. **(b)** Series of tissue residue curves $\boldsymbol{C_{tiss}(t)}$and arterial input curve$\boldsymbol{C_{aif}(t)}$. The main tissue residue curve (blue solid line) has been shifted backward (red solid line) and forward (green dotted line) 5 samples in time to examine the effect of tracer arrival delay on the estimation of myocardial blood flow. The black vertical line shows the dynamic in which the real onset of the curve has happened. Similar concept has been used in iterative deconvolution where the algorithm looks for the smallest fit error in the neighbouring area of the starting tOnset by shifting the starting tOnset 5 dynamic in both temporal directions.

5.4 Material and Methods

In a first set of experiments, we used noiseless synthetic data to demonstrate the sensitivity of deconvolution and MBF estimation to the delay time between tAIF and tOnset. Then we tested the accuracy of the automated tOnset detection algorithm and validated it against the true gold standard using a MR compatible perfusion phantom. Finally we used the validated algorithm to compare the results of voxel wise and segmental analysis performed with optimized tOnset with the results obtained from a fixed user selected global tOnset in phantom and patients data.

All the analyses described in this study were performed using automated made in house Software programmed with MATLAB (Mathworks, Natick, Massachusetts, USA, version R2010b). All data (phantom and patient) were acquired on a Philips Achieva 3T (TX) system, equipped with a 32-channel cardiac phased array receiver coil (Philips Health care, Best, The Netherlands).

5.4.1 Simulated Data

Simulated data with known perfusion values has been generated using approaches based on previously published studies(127), avoiding addition of noise in order to examine the effects of timing shifts alone on flow estimates and to evaluate the sensitivity of deconvolution algorithm to tOnset. Effects of noise on the accuracy of MBF estimation has been assessed previously in chapter 4. In this chapter the objective was outlined to validate the automated T_{onset} detection algorithm based on noiseless pure synthetic data.

For this propose a simulated synthetic $C_{myo}(t)$ with known perfusion values (MBF_{GS}= 1 ml/g/min) was shifted up to ± 4 ($C_{myo}(t \pm 4)$) samples in time with respect to $C_{aif}(t)$ in increments of one sample (Figure 5.3-1.b).

Noiseless gold standard tissue impulse response, $h_{GS}(t)$, were constructed by using the following pharmaco-kinetic model, described by Lindsey et al. (124):

$$h_{GS}(t) = \frac{e^{\lambda_1 t} - e^{\lambda_2 t}}{\lambda_1 - \lambda_2} u(t) - \frac{e^{\lambda_1 t} - e^{\lambda_3 t}}{\lambda_1 - \lambda_3} u(t) \quad [4]$$

where $u(t)$ is the unit step function. The physiological parameters, i.e., λ_1, λ_2 and λ_3 were chosen to generate tissue responses of the same order as those obtained by the fitting of real series of DCE-CMR acquisitions. (λ_1 = 2 .4**,** λ_3 =0.21 and λ_3 =0.36 to simulate a perfusion value of 1 ml/g/min).

$C_{aif}(t)$ used in this experiment is a convolution of many exponentials as suggested in (5) to model the propagation of an impulsive bolus injection through several compartments of the cardiovascular system.

$$C_{aif}(t) = \delta(t) * \left[ve^{-vt}\right]_1 * \left[ve^{-vt}\right]_2 * \ldots * \left[ve^{-vt}\right]_n$$

For simplicity, we assumed same mean transit time ($1/v > 0, v = 0.3897$), and thus same compartment kernel ve^{-vt} for all compartments(127). Initial $C_{myo}(t)$ was then obtained by convolving $h_{GS}(t)$ with the simulated $C_{aif}(t)$ (5).

For each time shift an absolute error of quantification (e_a) and fit relative error (x) were calculated as:

$$e_a = |MBF - MBF_{GS}|$$

$$x = \frac{\left\|C_{myo}(t) - h(t) * C_{myo}(t)\right\|}{\left\|C_{myo}(t)\right\|}$$

where MBF_{GS} is the reference standard perfusion value . The absolute error of the perfusion estimates for each time shifts of tOnset was used to demonstrate the importance of time difference.

5.4.2 Hardware perfusion phantom

The second experiment was performed on validated perfusion phantom data (127,142,153). The perfusion phantom allows an efficient and reproducible simulation of myocardial perfusion acquisition, providing validated data suitable for quantification. Unlike the noiseless synthetic data, the phantom datasets are acquired using the same hardware ,software (i.e. MR scanners and acquisition protocols) and similar sequence to those used in patients and therefore contain realistic levels of noise (153). The perfusion phantom data were used to validate the iterative deconvolution algorithms in realistic conditions of SNR and perfusion rates and also to examine the sensitivity of different deconvolution methods to the selection of tOnset.

Phantom data were acquired in one slice in a transverse geometry, visualizing the progression of the bolus of contrast agent in the large thoracic vessels and the myocardial compartments in the same image, with a saturation recovery gradient echo method (typical parameters: repetition time/echo time 3.0ms/1.0ms, flip angle 15°; effective k-t SENSE acceleration 3.8 fold, spatial resolution 1.2x1.2x10 mm, saturation delay 120 ms, matrix size 132x132, Band width 2137 Hz, FOV 24x24 mm^2) (52,144,145).

To avoid any confounding effects due to signal saturation, a universal dual-bolus injection scheme was performed in the perfusion phantom as described by Ishida et al. (99). In the phantom experiments, we used a dosage of Gadolinium of 0.001 mEq/kg of body weight as a pre-bolus and 0.01 mEq/kg of body weight as bolus (Gadobutrol Gadovist®, Bayer Schering, Germany). The boluses were injected at 4 ml/second followed by a 20 ml saline flush. Here the search for the inflection point in $C_{tiss}(t)$ starts from the dynamic in which the main bolus of contrast agent appears in the LV.

5.4.3 Clinical MR data

The feasibility of automated tOnset detection and a comparison with visually selected tOnset values were performed in a small group of patients (n=3) with angina symptoms and definite coronary artery disease on invasive coronary angiography referred to evaluate the presence and extension of inducible abnormalities of MBF during stress with adenosine-induced hyperaemia (140µg/kg/min). The study was performed at Guy's and St Thomas' Hospital London (UK). The institutional review board approved the study and all subjects signed an informed consent to be included.

Patient's perfusion data were acquired in three slices (apical, mid cavity and basal) in a short axis geometry, with imaging methods similar to the methods used in perfusion phantom experiment. Typical parameters for the saturation recovery gradient echo method were: repetition time/echo time 3.0ms/1.0ms, flip angle 15°; effective k-t SENSE acceleration 3.8 fold, spatial resolution 1.2x1.2x10 mm, saturation delay 120 ms, matrix size 251x251, Band width724 Hz, FOV 31 x 31 mm^2 (52,144,145).

Also in the human studies, a universal dual-bolus injection scheme was performed. we used a dosage of Gadolinium of 0.0075 mEq/kg of body weight as a pre-bolus and 0.075 mEq/kg of body weight as bolus (Gadobutrol Gadovist®, Bayer Schering, Germany). The boluses were injected at 4 ml/second followed by a 20 ml saline flush.

5.4.4 MR Image Processing

Accurate voxel-based MBF estimation requires respiratory motion correction and myocardial contour delineation. We developed an automated approach based on published methods (146,147), in which respiratory motion was removed using affine image registration by maximization of the joint correlation between consecutive dynamics within an automatically determined region of interest. Then, a temporal maximum intensity projection was calculated to serve as a feature image for an automatic contour delineation method based on active contour models (see figure 4.2-2) (146,147,154,155). Signal intensities were then sampled using bilinear interpolation at a grid of 60 angular positions and 10 transmural positions (or layers). The transmural positions were located on chords perpendicular to the myocardial centre-line (155). To maximize reproducibility of MBF quantification, care was taken to obtain $C_{aif}(t)$ in a robust and reproducible way. $C_{aif}(t)$ was obtained by sampling the trimmed median intensity within a region of interest in the blood pool of the basal slice. To be robust against the present of papillary muscles, the region of interest was obtained by down scaling the endocardium contours. Furthermore, the trimmed median operator ignores 15% of outlier samples.

Prior to deconvolution analysis, baseline correction that includes scaling of the signal intensities proportional to coil sensitivity and correcting for an offset to shift the baseline signal to zero has been performed. The constrained least square problems were solved using *lsqnonlin* in MATLAB (5,107). Moreover spatial filtering, Gaussian filter of size 5, and temporal filtering, a 30th order Hamming-window based low pass finite impulse response filter with normalized cut-off frequency of 0.23(149), was performed on the extracted signal intensity curves. For all models, the perfusion estimates were computed by deconvolving the measured blood and tissue enhancement data during the first pass of contrast agent in myocardium. For quantification, 20 dynamics from the arrival of the contrast agent (TOnset) were used in both phantom and patients.

In all experiments, the considered methods were compared by using the curve fit relative error and the absolute error (e_a) has been used to compare the method in synthetic and phantom data where a standard reference was available.

Analysis of variance (ANOVA) has been used in patients and phantom to compare the methods using optimized tOnset with using user selected global value for tOnset.

5.5 Results

5.5.1 Simulated Data

Figure 5.5-1.a shows the simulated tissue residue curve, $C_{myo}(t)$, (MBF_{GS}= 1 ml/g/min) along with estimated tissue residue curves obtained from the deconvolution of the original $C_{myo}(t)$ and $C_{myo}(t \pm 4)$. Using the true tOnset (i.e. original $C_{myo}(t)$) for quantification yielded to the best fit of reconstructed $C_{myo}(t)$ to real data (x=0.103).

Figure 5.5-1.b illustrates sensitivity of quantification to tracer arrival time delay. It represents the absolute error (e_a) in estimation of MBF when the $C_{myo}(t)$ has been shifted 4 steps forward and backward in time ($C_{myo}(t \pm 4)$). As the delay time between the real onset of curve and the used one for deconvolution increases, absolute error increases as well. The lowest absolute error has been achieved when the real onset of the curve has been used for quantification ($e_a = 0.15$ ml/gr/min 15%).

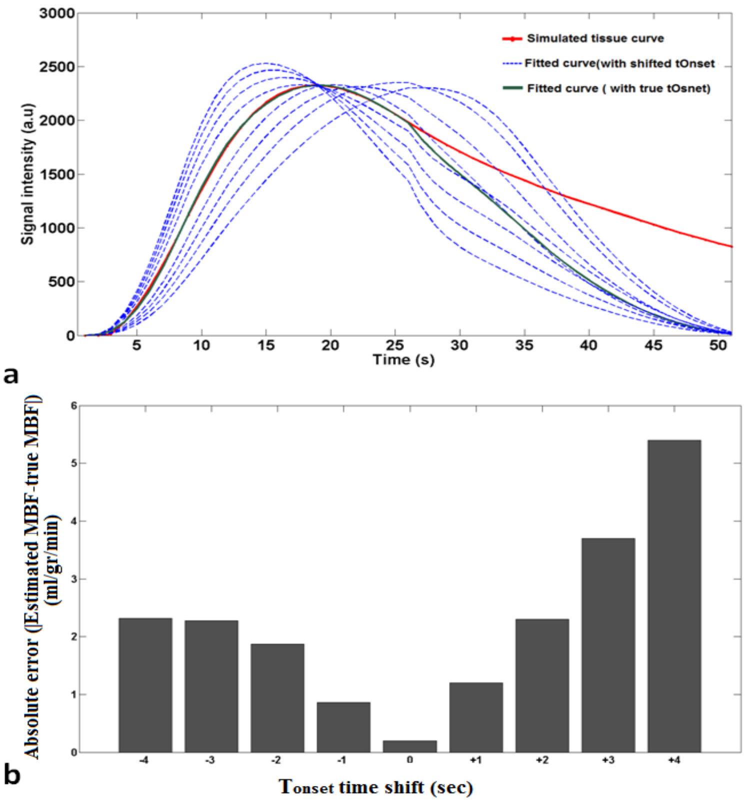

Figure 5.5-1 Shows a simulated tissue residue curve,$C_{tiss}(t)$, (MBF_{GS}= 1 ml/g/min) along with estimated tissue residue curves obtained using original $C_{tiss}(t)$ and $C_{tiss}(t \pm 4)$.The green curve is the reconstructed tissue curve using the true tOnset. The best fit to the real $C_{tiss}(t)$ has been achieved when the real tOnset has been used for quantification.**(b)** 3D bar plot compares the sensitivity of deconvolution to tOnset delay. Vertical axis is the absolute error ($e_a = Estimated\ MBF - True\ MBF$) in estimation of MBF.

5.5.2 Hardware perfusion phantom

To examine the accuracy of tracer arrival time detection algorithm in the validated perfusion phantom with MBF_{GS}= 5 ml/g/min, the starting tOnset, obtained from first stage of the tOnset detection algorithm, has been shifted forward and backward and the deconvolution procedure has been repeated for every shift step. The estimated MBF with its corresponding curve fit error for each step of the procedure in a random voxel has been shown for in figure 5.5-2. For the Fermi model, the dynamic with the smallest curve fit error corresponded to the smallest absolute error ($\frac{e_a}{x}$ =0.4/0.15). This dynamic was the optimal tOnset selected by the automatic tOnset detection algorithm.

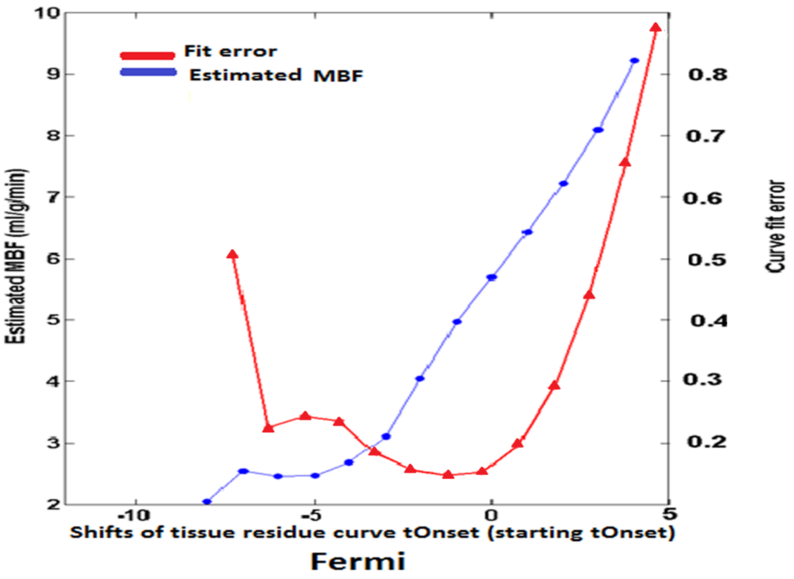

Figure 5.5-2 The estimated MBF (blue- circle) with its corresponding curve fit error (red-triangle) for forward and backward shifts of tOnset in time in a random voxel in perfusion phantom. The horizontal axis shows the shift of the assumed tOnset obtained from second derivative test. The dynamic that gives the smallest curve fit error corresponds to the smallest absolute error. These results validate the iterative deconvolution algorithm for detecting the optimized tOnset.

Figure 5.5-3 a shows a scatter-box plot of the estimated MBF values in the phantom with MBF_{GS}=5ml/g/min, comparing the results obtained using an optimized tOnset for voxel-wise quantification with those obtained with a user selected global fixed tOnset. A significant difference between the MBF values obtained from using a user selected fixed tOnset and optimized tOnset for voxel-wise analysis was seen (P-values =1.3E-98). It demonstrates the sensitivity of voxel-wise analysis to the delay time between tAIF and tOnset. Figure 5.5-3.b compares the estimated MBF absolute errors (e_a) in voxel wise and segmental analysis in the hardware perfusion phantom. The latter figure demonstrates that Using fixed tOnset for deconvolution yielded a higher absolute error compared to when an optimized tOnset has been used in both segmental and voxel-wise analysis. Furthermore this difference between the results obtained from user selected fixed tOnset and optimal tOnset is more apparent in voxel-wise analysis than segmental analysis.

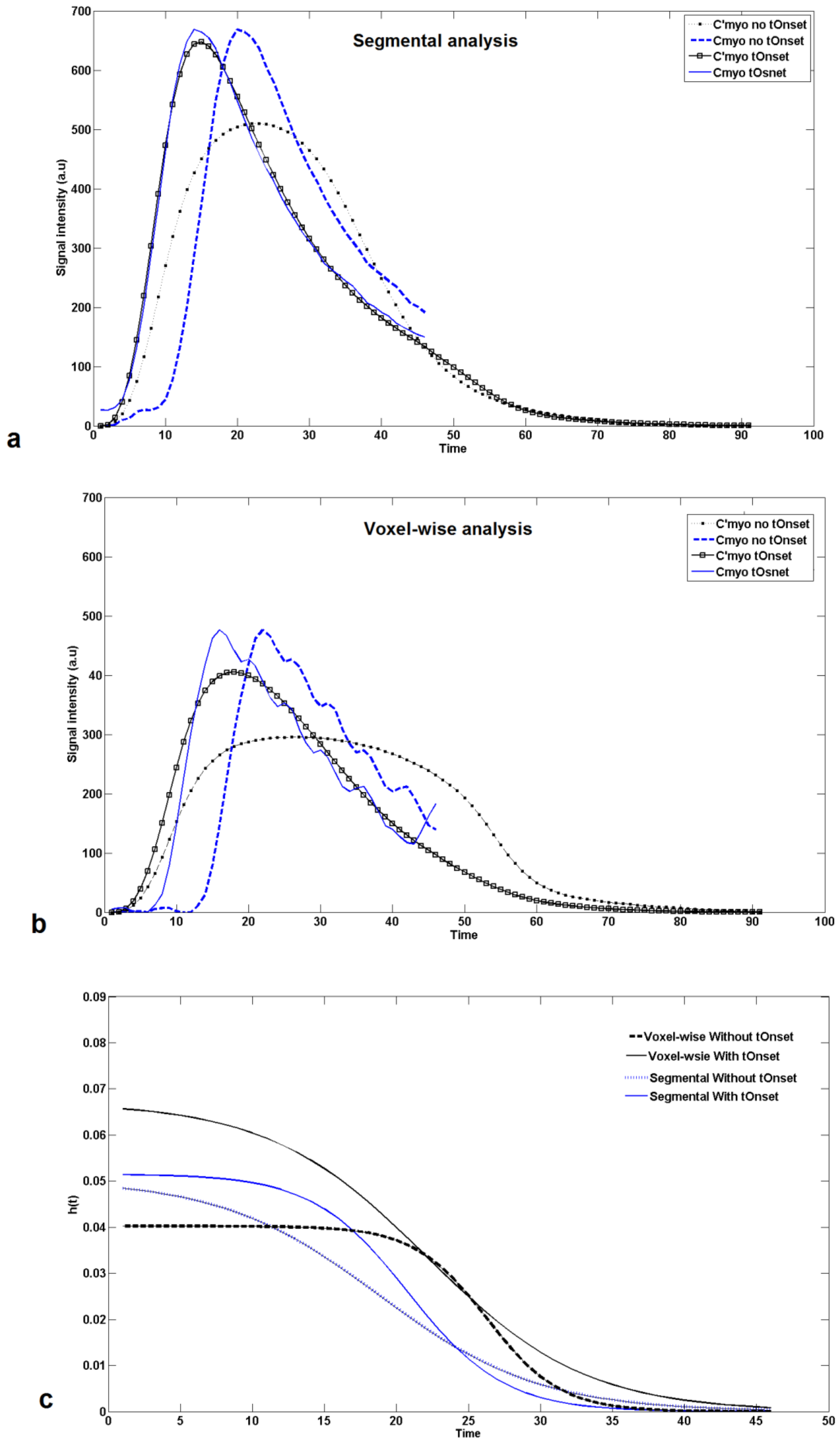

Figure 5.5-3 This figure describes both (a) segmental and (b) voxel-wise comparison between the result of deconvolution with and without tOnset in phantom data (MBF_{GS}=5ml/gr/min). Dashed lines in figure a and b correspond to analysis without tOnset. Solid lines in figure a and b correspond to analysis with tOnset. The black curves in figure a and b are the reconstructed C_{myo} after deconvolution and blue curve are the original myocardium signal intensity curves. Figure (C) represents the corresponding tissue impulse responses, $h(t)$, obtained from deconvolution.

Table 5-1 Mean of estimated voxel-wise perfusion values in phantom with the known perfusion value (MBF_{GS}= 5 ml/g/min).

Estimated voxel-wise perfusion values (ml/g/min) in phantom	
With fixed tOnset	4.4
With optimized tOnset	4.7
Estimated segmental perfusion values (ml/g/min) in phantom	
With fixed tOnset	4.6
With optimized tOnset	4.62

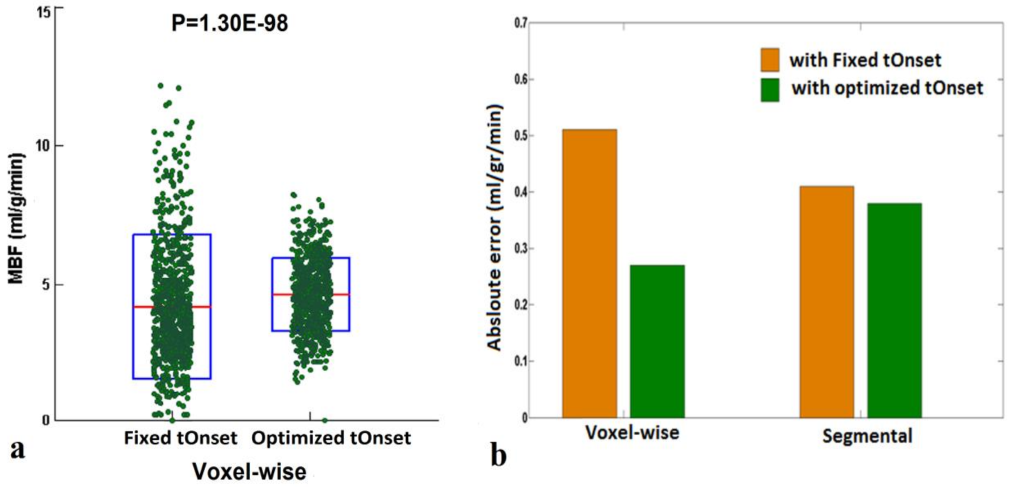

Figure 5.5-4 (a) Scatter-box plot represents the estimated voxel wise MBF values in the phantom ($\boldsymbol{MBF_{GS}}$=5ml/g/min), comparing results obtained using an optimized tOnset with re using a user selected global tOnset. Each individual green dot shows the estimated MBF at each voxel and they have been spread for visualization reasons and clarity. On each blue box, the central red mark is the median; the edges of the box are the 25th and 75th percentiles. (b) Bar plot represents the absolute MBF error in the perfusion phantom. Absolute error have been averaged over all voxels for voxel-wise analysis. Green bar corresponds to absolute with fix tOnset and orange bar corresponds to error when optimal tOnset has been used for quantification. Using the optimized tOnset has resulted in higher accuracy. The greater difference between the optimized tOnset and fixed tOnset error in voxel-wise analysis implies its higher sensitive to tracer arrival time compares to segmental analysis.

Also an error ratio defined as:

$$R_e = \frac{\left(e_{a_{fixed}}/e_{a_{optimzed}}\right)\ voxelwise}{(e_{a_{fixed}}/e_{a_{optimzed}})\ segmental}$$

has been calculated to specify the sensitivity of the deconvolution to the tOnset in both segment and voxel-wise analysis. R_e was 1.9 (2/1.05) for Fermi model. The R_e ratios of greater than one clearly proves that voxel wise analysis is more sensitive to tOnset compares to segmental analysis.

In chapter 4 we demonstrated that Fermi function modelling results in underestimation and considerable amount error at high flow values. Here we have shown (figure 5.5-3) that the utility of tOnset for perfusion estimation improves the accuracy of Fermi method, especially at voxel level.

5.5.3 Clinical MR data

In order to demonstrate the importance of tracer arrival time detection for myocardial perfusion estimation in clinical MR data, firstly we have examined the myocardial segmental analysis sensitivity to tracer arrival time. Then the automated tOnset detection algorithm has been applied to voxel-wise analysis and sensitivity of voxel-wise analysis to tracer arrival time has been tested. Finally voxel-wise results have been compared with the results obtained from segmental analysis.

Figure 5.5-4 compares $(MBF_{optmizd} - MBF_{fixed})$ obtained using segmental analysis with voxel-wise analysis in normal and ischemic regions of a patient with LCX stenosis. As it can be seen there is high discrepancy between the $(MBF_{optmizd} - MBF_{fixed})$ at normal and ischemic regions in voxel –wise analysis compared to segmental analysis. This difference is more apparent in ischemic regions of the voxel- wise analysis. The huge difference between the errors in voxel-wise and segmental analysis in both abnormal and normal regions of myocardium is a result of neglecting individual onset time of each voxel and assuming same onset time for all of them. The variation of tOnset amongst different voxels within the same or different segments is greater in comparison to the variation of the tOnset amongst region of interest in segmental analysis.

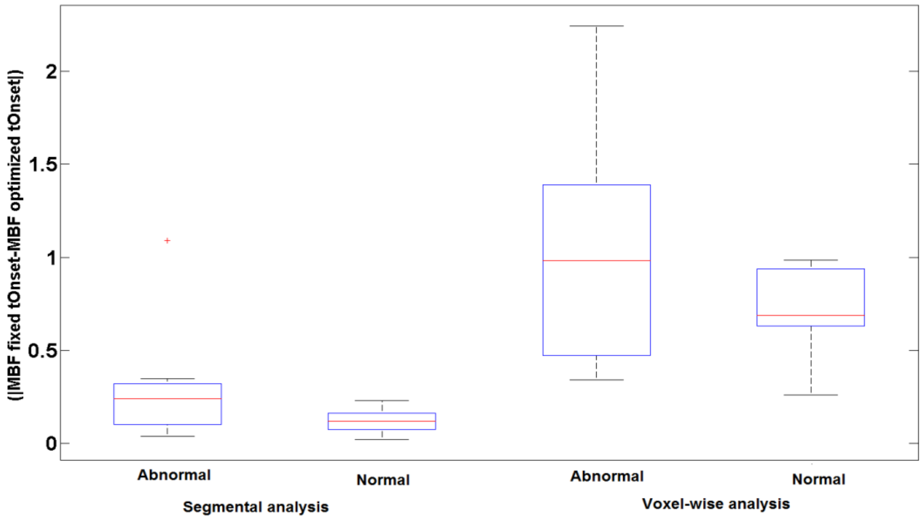

Figure 5.5-5 Box plot represents the difference between obtained MBF values obtained using fixed tOnset and optimized tOnset form quantification in segmental and voxel-wise analysis in a patient with LCX disease. The difference between the obtained MBF values in both normal and ischemic regions of myocardium in voxel-wise analysis is higher than found in segmental analysis. This higher difference proves the sensitivity of voxel-wise analysis to tracer arrival times whereas there is not a significant difference between the results obtained in segmental analysis with and without using optimized tOnset. Moreover the difference between the obtained MBF

in ischemic regions in voxel-wise analysis shows the impotence of the tOnset detection for accurate estimation of MBF in ischemic regions.

Table 5-2.1 represents the mean±STD of the estimated MBF values in the group of three patients with angina in normal and abnormal segments. As it can be seen there is not a significant difference between the obtained values using fixed tOnset and optimized tOnset in segmental analysis ($P<0.05$) proving that segmental analysis is not very sensitive to time delay between tAIF and tOnset. However the significant difference between the estimated MBF values obtained from optimized tOnset and fixed tOnset voxel-wise analysis ($P<0.05$) proves the sensitivity of the voxel-wise analysis to tracer arrival time in patient's data (Table 5-2.2)

Table 5-2 Estimated perfusion values (ml/g/min) in a group of three patients comparing the MBF values in normal and abnormal segments obtained using a fixed tOnset and the optimized tOnset in voxel-wise and segmental analysis.

5-2.1 segmental analysis

	Abnormal segment (N=6)	**Normal segment (N=10)**
fixed tOnset (ml/g/min)	1.69±0.4	2.2±0.56
Optimized tOnset (ml/g/min)	1.87±0.38	2.26±0.59
p Value	0.142173	0.12165

*MBF values have been averaged over all voxels in its corresponding segment

5-2.2 Voxel-wise analysis

	Abnormal segment* (N=6)	**Normal segment (N=10)**
fixed tOnset (ml/g/min)	0.62±0.2	1.43±0.69
Optimized tOnset (ml/g/min)	1.73±0.67	2.1±0.518
p Value	0.002837	0.000129

The box plot in figure 5.5-5 compares the Curve fit relative errors obtained from using fixed tOnset with those obtained from using an optimized tOnset in a patient with chronic total occlusion of the left anterior descending (LAD) coronary artery collateralized by the left circumflex (LCX) coronary artery, the LCX itself presents a 75% stenosis (fractional flow reserve, FFR 0.65), respectively. In the analysis with optimized tOnset a lower curve fit error has been obtained which proves the feasibility of the automated algorithm and accuracy of the results.

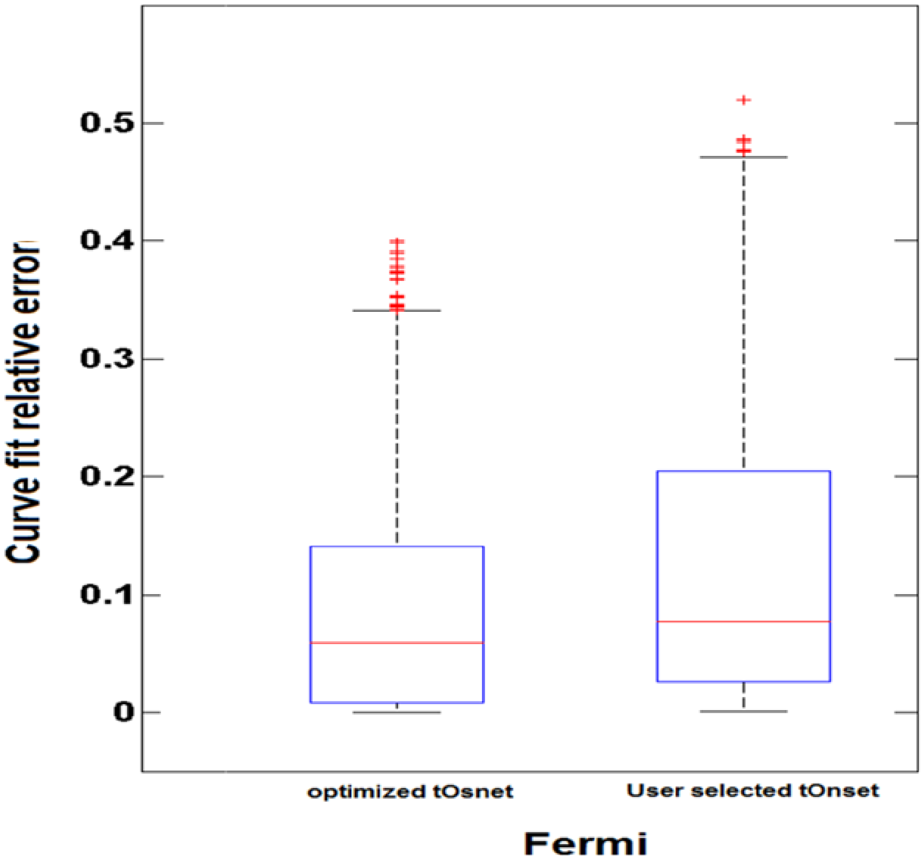

Figure 5.5-6 The comparison between the Curve fit relative errors (x) obtained when a fixed tOnset has been used for analysis and when an optimized tOnset has been used for voxel-wise analysis in a patient with chronic total occlusion of the left anterior descending (LAD) coronary artery collateralized by the left circumflex (LCX) coronary artery. The analysis with optimized tOnset has lower curve fit error compare with when fixed tOnset has been used, validating the iterative deconvolution algorithm.

The temporal delay between tOnset and TAIF (relative tOnset) in myocardial basal, mid-cavity and apical layers in the same patient as above is represented as a delay map in figure 5.5-6.a . These maps show the inhomogeneities of the tracer arrival time into myocardial tissue. A histogram of these relative tOnset values is represented in figure 5.5-6.b. As it can be seen the distribution of the values are divided into two groups: first group is between 0 to 4s, second group is between 4s to 10s. More than 80% of the values, which are related to normal voxels, are distributed between 0s and 3s. Those voxels which are between 4s to 10s are corresponded to the ischemic area in the bull's-eye relative tOnset map.

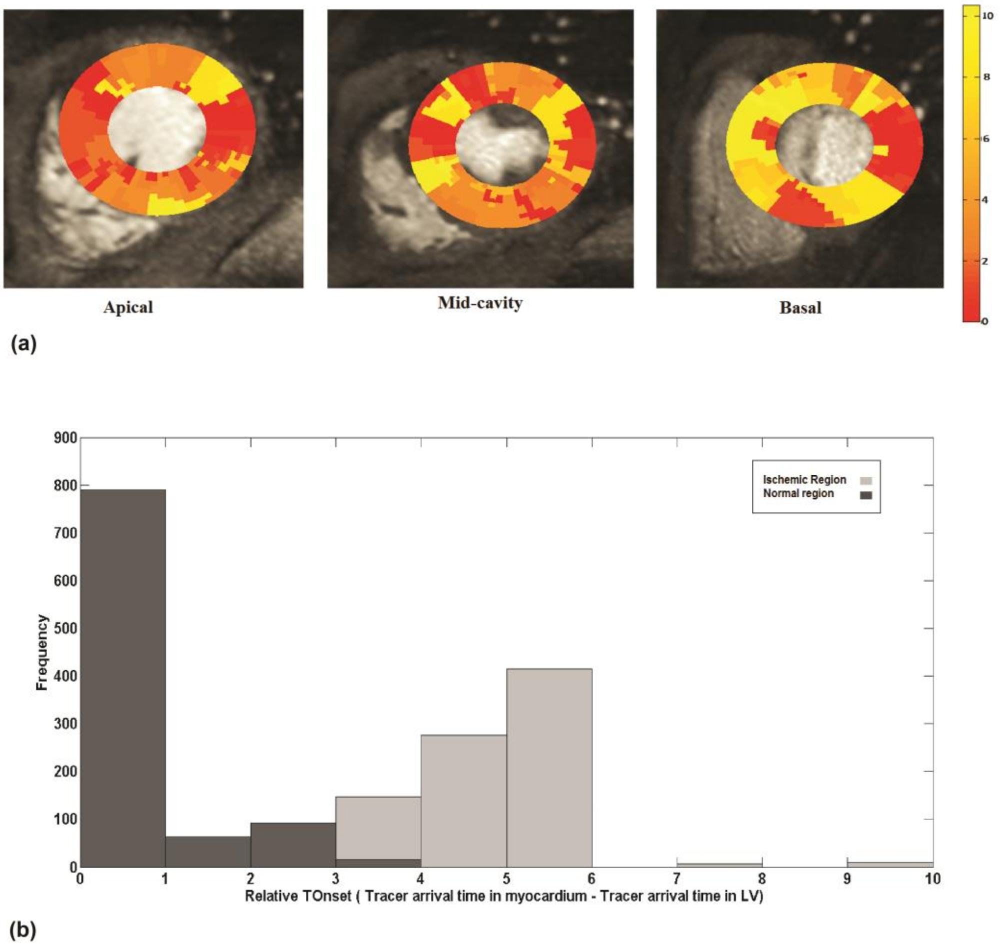

Figure 5.5-7 (a) Delay maps illustrating the relative tOnset (optimized tracer arrival time in myocardium – tracer arrival time in LV) in a patient with chronic total occlusion of the LAD collateralized by the LCX, the LCX itself presents a 75% stenosis (FFR 0.65), respectively. The inhomogeneity of the tOnset in the tissue is apparent here. The difference between tOnset in voxels makes voxel-wise quantification of MBF without using their real onset time inadequate. For the purpose of demining the optimized tOnset, the iterative deconvolution shifts the starting tOnset obtained from concavity theorem ±4 dynamics in time. (b) Represents the histogram of the relative TOnset data in normal and ischemic regions of myocardium shown in the delay map in figure (a).

5.6 Discussion

In the present study we have shown that quantification of myocardial perfusion is sensitive to the delay between the arrival of contrast agent into the LV blood pool and myocardial tissue and consequently an inaccurate selection of tracer arrival time can cause a significant error in estimation of MBF. Therefore the use of an optimized tOnset for deconvolution is needed to improve the accuracy of MBF estimations.

This issue becomes even more important in voxel-wise analysis as it is more sensitive to delay time compared with a segmental analysis due to its higher spatial detail and lower SNR level. It will be more helpful if this problem can be solved on a computational level, as for voxel-wise perfusion maps the number of voxels is too high to select the tOnset for each voxel manually.

This work proposed to improve flow estimates in voxel-wise analysis by automatically finding the delay between *tAIF* and tOnset in each voxel and use it for quantification of MBF.

In this study the assessment of reconstructed tissue curve goodness of fit as a function of the time shift was the basis for determining the optimized tOnset. The algorithm introduced here considers the interaction between the delay time and the fit error to obtain an optimal estimate of the tOnset. It is fast and fully automatic requiring no expert user interaction. On a 2.8 GHz PC, TOnset estimation takes less than 1 minute.

While using the optimized tOnset does not have a significant impact on accuracy of segmental analysis (Figure 5.5-3), using the optimized tOnset for voxel-wise analysis results in higher accuracy compared with when a fixed tOnset has been used for quantification.

Similar results were reflected in our experiments on clinical data, where the use of optimized tOnset allowed a significant improvement in the accuracy of the voxel-wise perfusion maps. Moreover, our results show that the use of a fixed tOnset in voxel-wise analysis amplifies the MBF estimation error particularly in the ischemic segments.

The difference between the delay times in arrival of contrast agent in myocardium normal and ischemic voxels allows for the evaluation of diseased areas of by estimating the time point of tracer arrival at particular voxel. This approach, which is less complex compare to deconvolution analysis, can be used as a novel method for detection of ischemia.

5.6.1 Limitations

The clinical findings presented here are preliminary and meant to demonstrate the feasibility of tOnset optimization on patients' data. Additional studies involving a larger cohort of patients are necessary to better determine the diagnostic power of MBF maps.

To determine the impact of tOnset estimation on accurate quantitative flow estimation in patients, future studies validating the results of voxel-wise MBF analysis in patients versus microspheres in animal studies will be required.

Finally as only one filtering method has been used in the study to remove the noise from signal intensity curves in patients and phantom, a further study is needed to analyze the interaction between signal intensities sampling resolutions, temporal and spatial filtering methods and MBF results obtained from deconvolution analysis.

5.7 Conclusions

Voxel-wise perfusion estimates based on DCE-CMR have many desirable characteristics including high sensitivity in identifying the tissue at risk. However MBF estimates are biased by several factors including the tracer arrival time into myocardium tissue. Therefore attempts to quantify MBF without using the $tOnset$ may be premature. An accurate estimation of myocardial blood flow and thus clearer delineation of the ischemic region in the perfusion maps relies on the precise identification of tOnset. This has to be automatic on voxel–wise level due to the high number of voxels.

This chapter has been adapted from N Zarinabad, , G. Hautvast, M Breeuwer, Eike Nagel, A Chiribiri, ***Effects of tracer arrival time on the accuracy of high resolution (voxel-wise) myocardial perfusion map from Contrast-Enhanced First-Pass perfusion magnetic resonance****; submitted to Magnetic Resonance in Medicine*

NZ: implemented the post-processing and quantification methods. Data analysis and simulations experiments and preparation of the manuscript.GH: implemented the pre-processing methods. MB: supervised the project. EN: arrange funding and supervised the project. AC: performed phantom experiment, acquired patients data, supervised the project.

6 The relationship between first pass perfusion MR spatial resolution level and quantitative myocardial perfusion

6.1 Introduction

Dynamic contrast enhanced cardiovascular magnetic resonance (DCE-CMR) is increasingly becoming a promising clinical tool to explore the presence and extent of myocardial ischemia (14,68,156).

DCE-CMR permits tracking of temporal variations in contrast agent concentrations and deriving physiological parameters of tissue, such as myocardium blood flow (MBF) by using deconvolution methods (29). In addition, the high spatial resolution conferred by CMR permits voxel-wise myocardial perfusion quantification and allows for the detection of subendocardial perfusion abnormalities. The voxel-wise quantitative perfusion analysis has the potential to improve the clinical diagnostic accuracy (157,158).

It is imperative to take into account the poor SNR of voxel based data which results in more inaccuracies in flow measurements compared to segmental analysis. This precludes voxel-wise CMR myocardial perfusion from being as accurate as the current clinical preference, PET.

In order to address the latter issue and obtain higher accuracy myocardium voxels can be grouped to increase the region of interest (ROI) size. However the downside of this approach will be the reduction of spatial resolution and potential information loss on tissue ischaemia localization, extension and transmurality.

In this study we aimed to assess the relationship between the level of spatial resolution of DCE-CMR data and accuracy, of perfusion quantification on different methods including Fermi function modelling(3), ARMA(127), B-spline basis deconvolution(4) and exponential basis deconvolution(5). In addition we used a new method introduced by Bavley et.al (7) to measure the quality of the fit and the ratio of the error that occurs in the results due to SNR reduction.

6.2 Theory

6.2.1 Quantitative perfusion voxel-wise analysis

Accurate voxel-based *MBF* estimation requires respiratory motion correction and myocardial contour delineation. We developed an automated approach based on (146,147), in which respiratory motion was removed using affine image registration through maximisation of the joint correlation between consecutive dynamics within an automatically determined region of interest. Then, a temporal maximum intensity projection was calculated to serve as a feature image for an automatic contour delineation method based on active contour models (146,147). Signal intensities were then sampled using bilinear interpolation on a grid of 60 angular positions and 10 transmural positions (or layers). The transmural positions were located on chords perpendicular to the myocardial centre-line.

Extracted signal intensity (SI) curves were then imported into made-in-house software in MATLAB (Mathworks, Natick, Massachusetts, USA, version R2010b) (5,107) which computes perfusion by deconvolving the measured blood, $C_{aif}(t)$, and tissue enhancement data, $C_{myo}(t)$, during the first pass of contrast agent in myocardium. $C_{aif}(t)$ and $C_{myo}(t)$ are related through the following equation:

$$C_{myo}(t) = C_{aif}(t) * h(t)$$

where $h(t)$ is the tissue impulse response. Tissue characterises such as perfusion and blood volume can be estimated from $h(t)$.

Four deconvolution algorithms – Fermi function modelling, ARMA, B-spline basis deconvolution and Exponential basis deconvolution – were used here to estimate tissue parameters.

Prior to deconvolution analysis, baseline correction that includes scaling of signal intensities proportional to coil sensitivity and correcting for an offset to shift the baseline signal to zero was performed. In addition, spatial filtering, Gaussian filter of size 5, and temporal filtering, a 30th order Hamming-window based low pass finite impulse response filter with normalised cut-off frequency of 0.23(149), were performed on the extracted signal intensity curves. We used fourth-degree B-spline polynomial with five equally spaced break points (4) and 10 time scale (M=10) for Exponential basis deconvolution (5) for the representation of impulse response. To render the deconvolution process more stable and reduce computational burden, ARMA (Q=1,L=2) (121) was chosen for quantification.

6.2.2 Fit quality assessment

The parameters of the chosen deconvolution model for the tissue impulse response, $h(t)$, are adjusted to obtain modelled tissue dynamics as faithful as possible to the observed myocardial curves, generally based on least-square regularisation. When the analysis is applied to each pixel, it generates maps of estimated MBF.

However, nothing guarantees that the modelled myocardial dynamic will effectively match the observed myocardial curves. Furthermore, since for patient data there is no reference value available to assess accuracy of results, quality of fit must be determined to avoid erroneous interpretation of MBF.

So far, visual analysis and correlation coefficient (R2) (159,160) have been commonly used to verify quality of fit. However, these criteria, based on measuring the difference between modelled tissue curve and measured data, depend not only on quality of fit but also on the random noise contained in the data set.

If the correlation coefficient is to be a reliable confidence indicator, noise should be negligible or at least of constant amplitude. Yet both the amplitude of noise and SNR depend on experimental conditions and can vary from one pixel to another, depending on the concentration of contrast agent used. Thus, correlation coefficient is not well suited to studying quality of fit in DCE-CMR.

In this work, we used a new numerical criterion to assess quality of fit of a given model using the properties of the autocorrelation function to overcome the random noise issue (7).

It can be assumed that the observed myocardium concentration of contrast agent data, $C_{myo}(t)$ derived from a series of DCE-CMR acquisitions, is the sum of a deterministic phenomenon of interest and random noise $\theta(t)$. For each pixel, with *i* and *j* being indices of the position within the MR image, it is assumed that:

$$C_{i,j_{myo}}(t) = C'_{i,j_{myo}}(t) + \theta_{i,j}(t) \quad [1]$$

In practice, deconvolution decomposes these data into the sum of a modelled signal ($C^{m}{}_{myo}(t)$) and a residual (r):

$$C_{i,j_{myo}}(t) = C^{m}{}_{i,j_{myo}}(t,k) + r_{i,j} \quad [2]$$

where

$$C^{m}{}_{myo}(t,k) = C_{aif}(t) * h_k(t) \; .$$

$C_{aif}(t)$ is the measured arterial input concentration of contrast agent data from LV and *k* = {*k1*,…,*kn*} are the *n* parameters of the model used to represent $h(t)$. The deconvolution process searches for the parameters of impulse response (k_i) which minimise the following mean square error problem*:*

$$Q = \left\| C_{i,j_{myo}}(t) - C^{m}{}_{i,j_{myo}}(t,k) \right\|^{2} = \left\| r_{i,j} \right\|^{2} . \qquad [3]$$

Using equation [2], Q can then be expressed as:

$$\left\| C'_{myo}(t) + \theta(t) - C^{m}{}_{myo}(t,k) \right\|^{2} = \| e_a + \theta(t) \|^2 \quad [4]$$

Where e_a is the modelling error defined as the difference between $C'_{myo}(t)$ and $C^{m}{}_{myo}(t)$:

$$e_a = C'_{myo}(t) - C^{m}{}_{myo}(t) = r(t) - \theta(t) \quad [5]$$

Equation [4], shows that, the mean square error depends on both the modelling error (e_a) and noise amplitude (θ) and does not perfectly reflect quality of fit as this is dependent on noise amplitude, which is not known beforehand. Moreover, noise amplitude is not constant and this makes the error vary; therefore, it cannot be used to compare different fits. However, if the model is assumed to be robust to noise, then the modelling error is also relatively independent of noise, and Q can be approximated as $\|e_a\|^2 + \|\theta\|^2$.

The aim of this study is to model $C'_{myo}(t)$as well as possible with $C^{m}{}_{myo}(t)$ by rejecting the noise in r.

To determine how well this objective is reached, we used the modelling mean square error (*Q*′) defined as:

$$Q' = \|e_a\|^2 = \|r - \theta\|^{2} \quad [6]$$

The quality of fit improves as Q' decreases, and is perfect when $Q' = 0$. Therefore, to improve the quality of fit, we need to decrease e_a.

e_a can arise from three sources:

1) Statistical modeling error (e') due to accidental modeling of some of the random noise
2) Regression error ($\mathrm{e_r}$) due to failure of the regularization method
3) Deterministic modeling error (e_m) which arises from a poor model adaption to the observed data and yields a poor fit regardless of the parameters used.

If we assume that deconvolution models are robust and $e_a$is noise-independent, then $e_m + e_r \gg$ $e'$and the modelling error are equivalent to $e_a \approx e_m + e_r$.

To represent the non-modelled information (e_a) relative to the total residual, the Fraction of Residual Information (FRI) is defined as follows:

$$FRI = \frac{\|e_a\|^2}{\|r\|^2} = \frac{Q'}{Q} = \frac{\|e_a\|^2}{\|e_a + \theta(t)\|^2}. \quad [7]$$

The FRI ratio is associated with the ability to extract the modelling error from the residual which contains the error due to noise $\theta(t)$.It shows how much modelling information still remains in the residual. This new fit quality assessment is not random-noise-dependent and in an ideal modelling process it will reach its maxima and minima: $FRI = 0$.

However, $C'_{myo}(t)$ is unknown when dealing with observed data from DCE-CMR ($C_{myo}(t)$). To overcome this issue an estimation of FRI based on autocorrelation can be used. However, the postulation has to be made that the modelling error (e_a) is strongly correlated in time. In contrast, by nature, random noise is poorly time-correlated. The autocorrelation function is thus used to distinguish the respective contributions of the modelling error and noise within the residual.

Assuming that $r = e_a + \theta$, for each time lag *l:*

$$\mathrm{R_{rr}(l) = R_{ee}(l) + R_{e\theta}(l) + R_{\theta e}(l) + R_{\theta\theta}(l)}$$

Where R is the autocorrelation function and for $l = 0$, $\mathrm{R_{rr}}(0) = \frac{\|\mathrm{r}\|^2}{\mathrm{M}}$, M is the total number of signal samples. If e_a is deterministic and θ is white noise, then, when *l* > 0, $E\{\mathrm{R_{\theta\theta}(l)}\} = E\{\mathrm{R_{e\theta}(l)}\} = E\{\mathrm{R_{\theta e}(l)}\} = 0$ and $E\{\mathrm{R_{rr}(l)}\} = E\{\mathrm{R_{ee}(l)}\} = \mathrm{R_{ee}(l)}$. $\mathrm{R_{rr}}$is therefore an unbiased estimator of $\mathrm{R_{ee}}$ when *l* > 0. This is no longer true when *l* = 0, as $\mathrm{R_{\theta\theta}}(0)$, which corresponds to the mean noise amplitude, is no longer negligible. However, if e_a is deterministic and the sampling frequency is adequate, $C_{myo}(t)$, $C^m{}_{myo}(t)$ and therefore e_a vary only moderately with time. Thus, $e_a(t + \varepsilon)$ approximates $e_a(t)$ for low values of l and, as a result, $\mathrm{R_{ee}}(0) = \frac{\|\mathrm{e}\|^2}{\mathrm{M}}$ can be approximated by using $\mathrm{R_{ee}}$ (*l*) for low values of *l*. The term $\mathrm{R_{ee}}$ (*l* > 0) is fitted by a polynomial function $\mathrm{P_{ee}}$ (*l* > 0), and then $\mathrm{P_{ee}}$ is extrapolated by continuity to zero in order to estimate $\|\mathrm{e}\|^2$.Therefore:

$$FRI = \frac{\mathrm{M \cdot P_{ee}(0)}}{\|r\|^2} \approx \frac{\mathrm{M \cdot P_{rr}(0)}}{\|r\|^2}.$$

6.3 Material and Methods

Perfusion data were analyzed from scans acquired from patients referred for contrast-enhanced first-pass CMR due to suspicion of symptomatic CAD. Five patients with significant coronary artery disease participated in this study. All participants gave written informed consent, in accordance and with the approval of the local ethics committee.

6.3.1 Data acquisition - CMR protocol

CMR was performed on a 3T system (Achieva TX, Philips Healthcare, Best, Netherlands) using a 32-channel cardiac phased array receiver coil. Perfusion data were acquired in 3 LV (apical, mid-cavity and basal) short-axis slices at end-inspiration with a saturation recovery gradient echo method (repetition time/echo time 3.0 ms/1.0 ms, flip angle 15°, saturation-recovery delay 120 msec, 5-fold k-t sensitivity encoding (k-t SENSE) acceleration with 11 training profiles, giving a net acceleration of 3.8-fold, spatial resolution 1.2 * 1.2 * 10 mm^3). Data were acquired during adenosine-induced hyperemia (140 µg/kg/min) and 15 minutes later at rest using 0.075 mmol/kg of body weight Gadolinium (Gd) extracellular contrast agent (gadobutrol, Gadovist®, Schering, Germany) injected at 4 ml/s followed by a 20-ml saline flush. Each bolus of gadobutrol was preceded by a diluted pre-bolus with 10% of the dose to allow quantification of myocardial blood flow, according to published methods (161-163). To avoid any overlap between the first and second injection of the contrast agent, a long pause (25 seconds) was programmed on the contrast injector (163). Late Gd enhancement images were used to exclude previous myocardial infarction and were acquired 15 minutes after a top-up dose of contrast agent to reach a total dose of 0.2 mmol of Gd/kg of body weight, according to standard practice.

6.3.2 Spatial resolution variation

To test the relation between level of spatial resolution and deconvolution method accuracy (in other words, information loss), we used the following protocol.

First we assigned one voxel to each ROI (600 ROI per slice- in total 1800 ROI per patient) and performed quality of fit analysis on voxel level (100 % resolution). We then incremented the number of voxels assigned to a perfusion ROI in both transmural and angular direction until the resolution fell to 10 % of the original the voxel-wise resolution. Quality of fit analysis was performed on each stage of the process and results obtained from all stages were compared. Coefficient of variation (CV) was calculated to assess dispersion and variation of each deconvolution method's quality of fit due to variation in spatial resolution level.

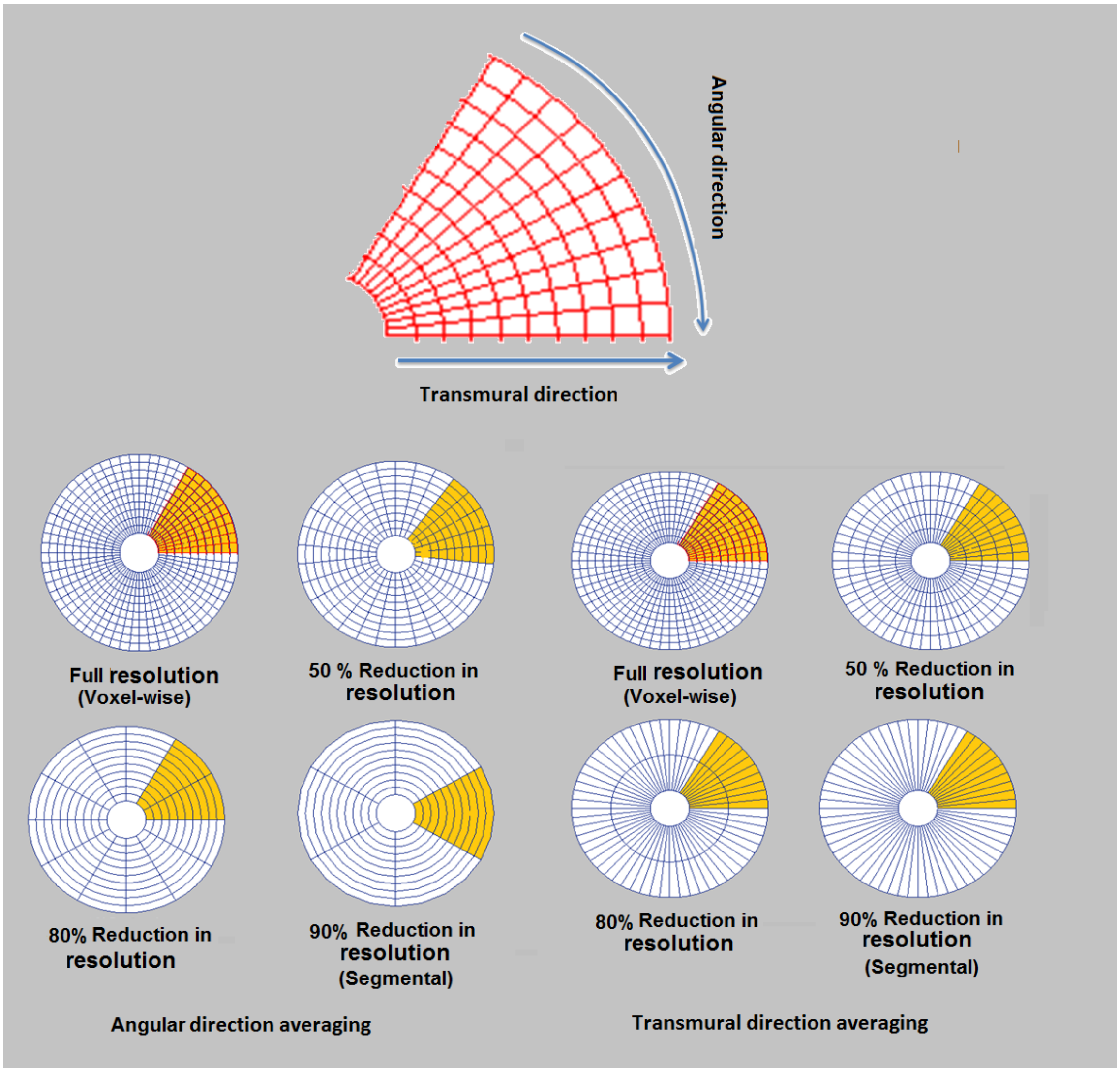

Figure 6.3-1 Bull's-eye plots illustrating the number of ROI used in one slice of myocardium for different levels of spatial resolution. Plots (a) and (b) show the number of ROI in one segment while resolution falls from 100% to 10% in angular and transmural directions, respectively.

6.4 Results

As shown in figure 6.4-1, for a given set of patient's data, both average and standard deviation of the Fraction of residual information (FRI) increased as the resolution decreases for all deconvolution methods. This indicates that the amount of true modelling error which contains un-modelled physiological information increases as the resolution falls down for all deconvolution methods compare to the amount of noise. The increase of standard deviation value as resolution decreases implies that the probability to lose modelling information during quantification of the myocardial perfusion using low resolution data sets is higher.

All deconvolution methods were showen to be more sensitive to changes in spatial resolution level in the transmural direction compared to radial direction. However each different deconvolution method behaved differently. As shown in figures 6.4-1.a and 6.4-1.b, ARMA and exponential had smaller standard deviation at all resolution levels compared to the standard deviation of the Fermi And B-spline methods. Moreover the average amount of un-modelled information (FRI) remained almost constant as resolution falls down in both transmural and radial direction for Fermi and b-spline, whereas the FRI increased for ARMA and exponential as resolution decreased. This increase in amount of un-modelled information is more visible in the transmural direction.

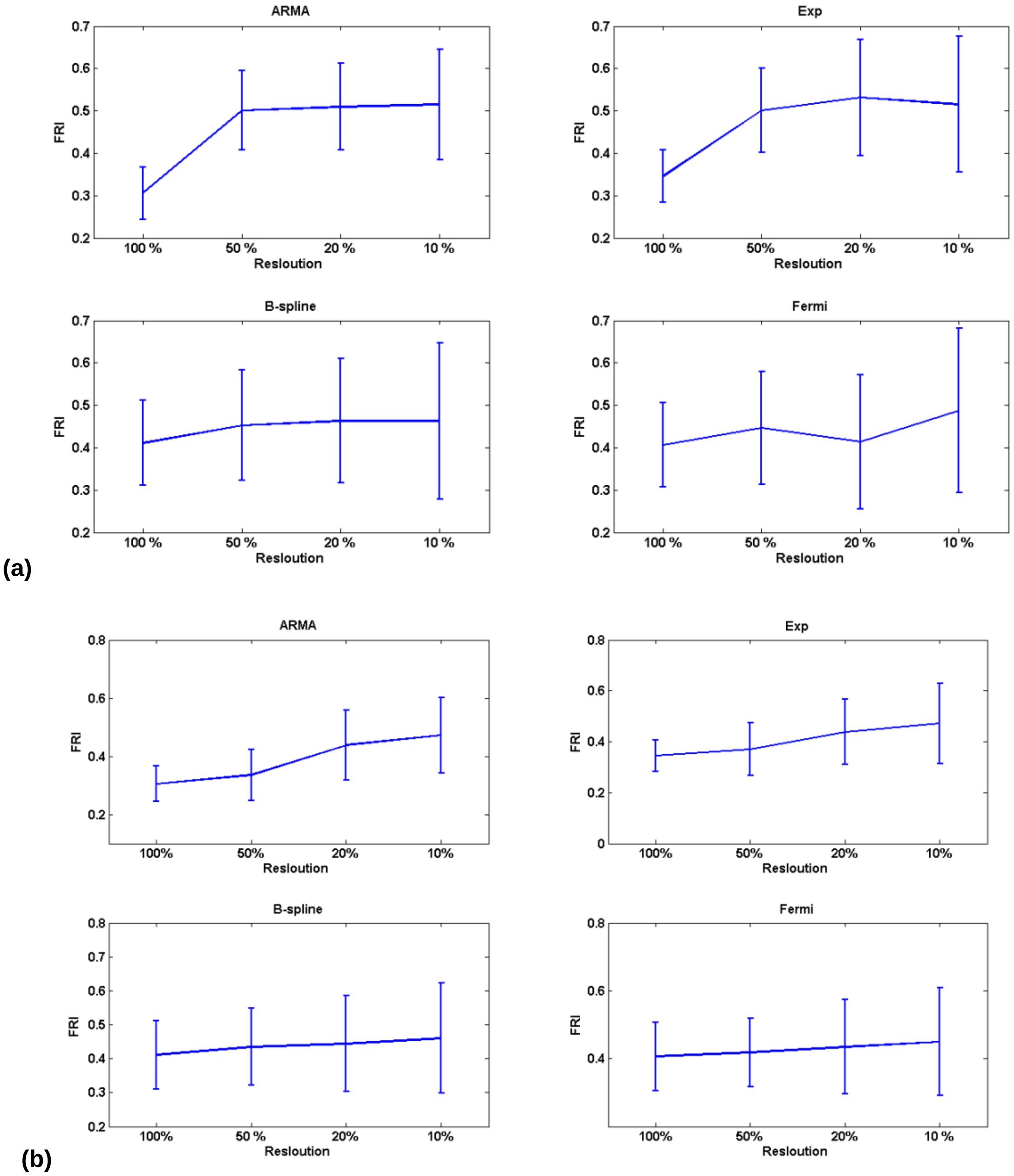

Figure 6.4-1 Bars represent mean and standard deviation of FRI at different levels of spatial resolution. Figures (a) and (b) correspond to reduction of resolution in transmural and angular directions, respectively. Mean FRI value increased as resolution fell for all methods. This is more obvious for ARMA and Exponential methods and transmural direction averaging. STD increased as resolution fell for all methods.

The bar plots in figure 6.4-2 represent the coefficient of variation of FRI for each deconvolution method, respectively. It compares the sensitivity of each method to direction of spatial resolution reduction.

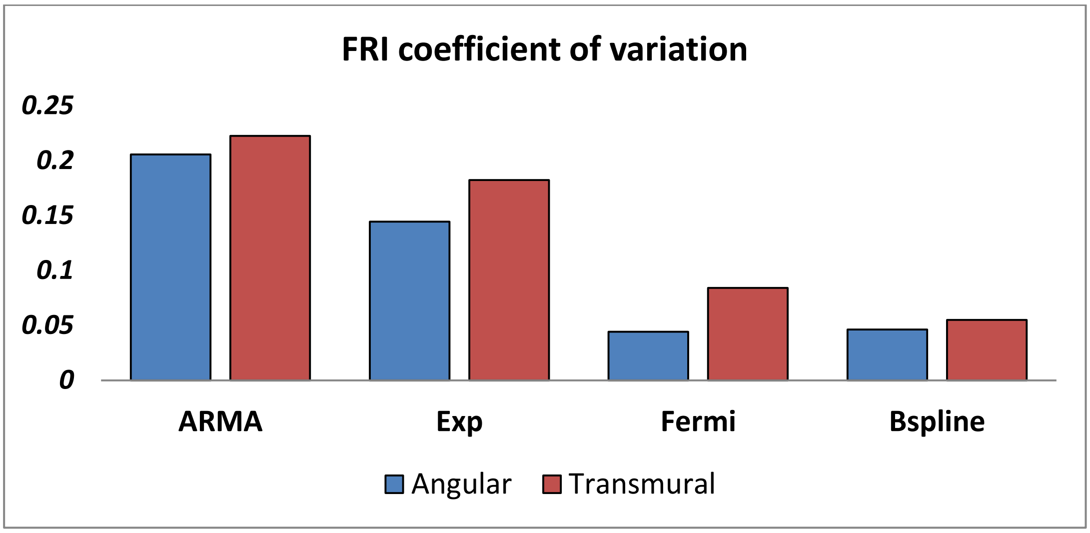

Figure 6.4-2 Bar plot represent FRI coefficient of variation (CV) for all four deconvolution methods in both transmural and angular direction averaging. All methods are more sensitive to changes in level of spatial resolution in transmural direction.

FRI coefficient of variation (CV) is higher at transmural direction for all methods implying the fact that all methods are more sensitive to changes in level of spatial resolution at transmural direction. In general ARMA method has the highest CV and the smallest CV belongs to Fermi and Bspline model at radial direction. The least sensitive method to direction of spatial averaging is Bspline method.

6.5 Discussion

High resolution (voxel-wise) analysis of myocardial perfusion allows for preserving important spatial information and is a superior sensitive method for subendocardial ischaemia detection. However it suffers from low SNR of the signal intensity curves which is one of the major cause of inaccuracies in estimation of myocardial blood flow. Previously spatial averaging has been used to increase the signal-to-noise ratio (SNR) of the signal intensity curves but it potentially results in losing information about the extension, localization, and transmurality of ischemia.

In the present study we have investigated the effect of spatial averaging on the accuracy of the deconvolution methods. We have used a new quality assessment method introduced by Balvay (7) to estimate the amount of un-modeled data at each spatial resolution level.

Our results confirmed that the reduction of spatial resolution will increase the amount of un-modeled information. This information loss is more severe when the spatial resolution reduction is in transmural direction.

Amongst the four deconvolution methods ARMA model showed to be the most sensitive model to changes in spatial resolution level in both directions. This sensitivity was more at transmural direction. Exponential model was the second most sensitive method to level of spatial resolution in transmural direction. Both Fermi and B-spline method were the least sensitive methods to changes in level of spatial resolution.

At high spatial resolution, ARMA model was able to model the most amount of information in the tissue (i.e. low FRI value, FRI=0.305).Whereas at low spatial resolution the amount of modeled information was almost equal for all four methods.

In general, although Fermi showed to be the most robust model to changes in resolution level at both directions, it remains 40±20 % of the information un-modeled at all resolutions. In contrast, ARMA and exponential showed to be more sensitive to spatial resolution level of the data, but they were able to retain only 30± 5% of the data un-modeled at high spatial resolution (low SNR) which is far better that the results obtained with Fermi model at low resolution level.

6.5.1 Limitation

Here we have assumed that noise which has contaminated the data is an additive white Gaussian noise with zero-mean and normal distribution. However the MRI data are normally is degraded by Rician noise with potentially non-zero mean. This assumption will have an effect on FRI estimation. Moreover assumption on the anatomically fixed coronaries within each segment of the myocardium will affect the accuracy of perfusion estimation especially in the angular direction. A further study that analyzes the accuracy of perfusion estimation at different resolution levels at the transition of tissue supplied by one coronary and another is required.

6.6 Conclusion

In this study we have demonstrated that decreasing the resolution level to improve the SNR of the data will result in losing a considerable amount of physiological information which can be possibly used for arriving at a clinical diagnosis.

All deconvolution methods were more sensitive to spatial-resolution averaging in the transmural direction. ARMA and Exponential model showed to be most favorable methods at high spatial resolution levels for MBF assessment. Fermi and B-spline models were the least sensitive methods to both changes in spatial resolution levels and direction of averaging.

This chapter has been adapted from N Zarinabad, , G. Hautvast, M Breeuwer, A Chiribiri , E Nagel, ***The relationship between spatial resolution levels and quantitative myocardial perfusion;*** *submitted to Magnetic Resonance in Medicine*

NZ: implemented the post-processing and quantification methods. Data analysis and simulations experiments and preparation of the manuscript. AC: acquired patients data, GH: implemented the pre-processing methods. MB: supervised the project. EN: arrange funding and supervised the project.

7 Conclusion and further work

In this thesis, we have demonstrated that high resolution quantification of myocardial blood flow from CMR is feasible. Here, quantification of MBF was performed by several methods on four types of data set: simulated synthetic data, hardware perfusion phantom, explanted pig hearts, and patient data.

One of the major facilitators for this thesis was the existence of the perfusion hardware phantom and the blood-perfused pig hearts as these allowed us to fully investigate the reliability of estimated parameters and obtain a ground truth.
In this work, the most favourable deconvolution methods in the literature (i.e. Fermi function modelling, deconvolution using B-spline basis, deconvolution using Exponential basis, autoregressive moving average model) were compared to find the suitable method for voxel-wise quantitative analysis of myocardial perfusion.

The results obtained from simulations and the perfusion maps in the hardware phantom, explanted pig heart data and patient studies showed that voxel-wise quantification of myocardium perfusion is feasible and can be used to detect abnormal regions with high sensitivity in identifying the tissue at risk.

The ARMA method with a proper choice of model order were shown to be more accurate in general. Low order ARMA model (i.e. ($L>Q$)) will result in an accurate estimation of MBF. The best results for ARMA can been achieved with second and third order autoregressive ($L=2$, 3) and with ARMA ($L=2$, $Q=1$).

) On the other hand, the Fermi model was the most robust method to noise conferring the highest precision for voxel-wise analysis. In addition the Femi model is more user friendly as this method is free from any operator dependent varying parameter.

Inevitably the choice of the quantification method for data analysis boils down to a trade off between accuracy and precision of the perfusion estimation. An accurate estimation can be obtained by combining the interpretation of Fermi model and a low order ARMA method.

It is important to note that perfusion estimates are biased by many factors including contrast-to-noise ratio of the data, delay between arrival of contrast into myocardium and LV blood pool (152), non-linear relationship between signal intensity level and concentration of contrast agent (99,125). Some of these issues are even more difficult to address at the voxel level. In the previous chapters, we discussed the effects of each of these issues on the accuracy of perfusion estimates.

In addition to the above shortcomings, the absence of absolute units for the measured concentration of contrast agent and also neglecting water exchange effects in myocardium (164) result in measurement of MBF in arbitrary units and perfusion underestimation, respectively.

Therefore, quantitative measurement of MBF in absolute units (e.g. in ml/gr/min) using DCE-MRI requires calibration. Consequently, the next step after validation of the voxel-wise perfusion analysis and quantification methods is calibration of perfusion estimates.

There are a few proposed methods that can be used to obtain absolute quantification values such as (a) calibration of the maps using a common scaling factor obtained from a previous cross-calibration study, e.g. from a PET-MRI calibration study and (b) quantification of MBF with a subject-to-subject calibration (165-167). One such approach is the bookend-technique, which is based on calibrating DCE-MRI measurements using an extra myocardial blood volume (MBV) map calculated from steady-state T_1 measurements. The use of these subject-specific calibration methods is highly recommended when absolute quantification is required.

In the bookend technique (165,166), T1 weighted images are acquired before and after passage of the bolus of contrast to perform steady-state measurement of MBV. During the passage of contrast, a dynamic contrast enhanced scan is performed. Dynamic measurements can be used to quantify MBV and MBF. This technique calibrates DCE MBF measurements by using a calibration factor obtained from an extra MBV map calculated from steady-state T_1 measurements.

Further work is required to address the need for calibration of perfusion values. Whether or not the addition of T1 steady state to DCE measurements of MBF improves perfusion estimate accuracy remains to be seen.

8 Bibliography

1. Plein S, Kozerke S, Suerder D, Luescher TF, Greenwood JP, Boesiger P, Schwitter J. High spatial resolution myocardial perfusion cardiac magnetic resonance for the detection of coronary artery disease. Eur Heart J 2008;29(17):2148-2155.
2. Salerno M, Beller GA. Noninvasive assessment of myocardial perfusion. Circulation Cardiovascular imaging 2009;2(5):412-424.
3. Jerosch-Herold M, Wilke N, Stillman AE. Magnetic resonance quantification of the myocardial perfusion reserve with a Fermi function model for constrained deconvolution. Med Phys 1998;25(1):73-84.
4. Jerosch-Herold M, Swingen C, Seethamraju RT. Myocardial blood flow quantification with MRI by model-independent deconvolution. Med Phys 2002;29(5):886-897.
5. Keeling SL, Kogler T, Stollberger R. Deconvolution for DCE-MRI using an exponential approximation basis. Medical Image Analysis 2009;13(1):80-90.
6. Neyran B, Janier MF, Casali C, Revel D, Canet Soulas EP. Mapping myocardial perfusion with an intravascular MR contrast agent: robustness of deconvolution methods at various blood flows. Magn Reson Med 2002;48(1):166-179.
7. Balvay D, Frouin F, Calmon G, Bessoud B, Kahn E, Siauve N, Clement O, Cuenod CA. New criteria for assessing fit quality in dynamic contrast-enhanced T1-weighted MRI for perfusion and permeability imaging. Magnetic resonance in medicine : official journal of the Society of Magnetic Resonance in Medicine / Society of Magnetic Resonance in Medicine 2005;54(4):868-877.
8. MEMBERS WG, Lloyd-Jones D, Adams RJ, Brown TM, Carnethon M, Dai S, De Simone G, Ferguson TB, Ford E, Furie K, Gillespie C, Go A, Greenlund K, Haase N, Hailpern S, Ho PM, Howard V, Kissela B, Kittner S, Lackland D, Lisabeth L, Marelli A, McDermott MM, Meigs J, Mozaffarian D, Mussolino M, Nichol G, Roger VL, Rosamond W, Sacco R, Sorlie P, Roger VL, Stafford R, Thom T, Wasserthiel-Smoller S, Wong ND, Wylie-Rosett J, Subcommittee AHASCaSS. Heart disease and stroke statistics--2010 update: a report from the American Heart Association. Circulation 2010;121(7):e46-e215.
9. Spaan J, Kolyva C, van den Wijngaard J, ter Wee R, van Horssen P, Piek J, Siebes M. Coronary structure and perfusion in health and disease. Philosophical transactions Series A, Mathematical, physical, and engineering sciences 2008;366(1878):3137-3153.
10. Chiribiri A, Bettencourt N, Nagel E. Cardiac magnetic resonance stress testing: results and prognosis. Current cardiology reports 2009;11(1):54-60.
11. Brown KA, Rosman DR, Dave RM. Stress nuclear myocardial perfusion imaging versus stress echocardiography: prognostic comparisons. Prog Cardiovasc Dis 2000;43(3):231-244.
12. Schulthess GKv. Molecular anatomic imaging : PET-CT and SPECT-CT integrated modality. Philadelphia, PA: Lippincott Williams & Wilkins; 2007. p. p.
13. Kaufmann PA, Camici PG. Myocardial blood flow measurement by PET: technical aspects and clinical applications. J Nucl Med 2005;46(1):75-88.
14. Al-Saadi N, Nagel E, Gross M, Bornstedt A, Schnackenburg B, Klein C, Klimek W, Oswald H, Fleck E. Noninvasive detection of myocardial ischemia from perfusion reserve based on cardiovascular magnetic resonance. Circulation 2000;101(12):1379-1383.
15. Parkka JP, Niemi P, Saraste A, Koskenvuo JW, Komu M, Oikonen V, Toikka JO, Kiviniemi TO, Knuuti J, Sakuma H, Hartiala JJ. Comparison of MRI and positron emission tomography for measuring myocardial perfusion reserve in healthy humans. Magn Reson Med 2006;55(4):772-779.
16. Bache RJ, Schwartz JS. Effect of perfusion pressure distal to a coronary stenosis on transmural myocardial blood flow. Circulation 1982;65(5):928-935.
17. Higgins CB, Sovak M, Schmidt W, Siemers PT. Uptake of contrast materials by experimental acute myocardial infarctions: a preliminary report. Investigative radiology 1978;13(4):337-339.
18. Hoffmann U, Millea R, Enzweiler C, Ferencik M, Gulick S, Titus J, Achenbach S, Kwait D, Sosnovik D, Brady TJ. Acute myocardial infarction: contrast-enhanced multi-detector row CT in a porcine model. Radiology 2004;231(3):697-701.
19. Mahnken AH, Koos R, Katoh M, Wildberger JE, Spuentrup E, Buecker A, Gunther RW, Kuhl HP. Assessment of myocardial viability in reperfused acute myocardial infarction

using 16-slice computed tomography in comparison to magnetic resonance imaging. Journal of the American College of Cardiology 2005;45(12):2042-2047.

20. Lardo AC, Cordeiro MA, Silva C, Amado LC, George RT, Saliaris AP, Schuleri KH, Fernandes VR, Zviman M, Nazarian S, Halperin HR, Wu KC, Hare JM, Lima JA. Contrast-enhanced multidetector computed tomography viability imaging after myocardial infarction: characterization of myocyte death, microvascular obstruction, and chronic scar. Circulation 2006;113(3):394-404.
21. Gerber BL, Belge B, Legros GJ, Lim P, Poncelet A, Pasquet A, Gisellu G, Coche E, Vanoverschelde JL. Characterization of acute and chronic myocardial infarcts by multidetector computed tomography: comparison with contrast-enhanced magnetic resonance. Circulation 2006;113(6):823-833.
22. Paul JF, Wartski M, Caussin C, Sigal-Cinqualbre A, Lancelin B, Angel C, Dambrin G. Late defect on delayed contrast-enhanced multi-detector row CT scans in the prediction of SPECT infarct size after reperfused acute myocardial infarction: initial experience. Radiology 2005;236(2):485-489.
23. Koyama Y, Matsuoka H, Mochizuki T, Higashino H, Kawakami H, Nakata S, Aono J, Ito T, Naka M, Ohashi Y, Higaki J. Assessment of reperfused acute myocardial infarction with two-phase contrast-enhanced helical CT: prediction of left ventricular function and wall thickness. Radiology 2005;235(3):804-811.
24. Jacquier A, Boussel L, Amabile N, Bartoli JM, Douek P, Moulin G, Paganelli F, Saeed M, Revel D, Croisille P. Multidetector computed tomography in reperfused acute myocardial infarction. Assessment of infarct size and no-reflow in comparison with cardiac magnetic resonance imaging. Investigative radiology 2008;43(11):773-781.
25. George RT, Silva C, Cordeiro MA, DiPaula A, Thompson DR, McCarthy WF, Ichihara T, Lima JA, Lardo AC. Multidetector computed tomography myocardial perfusion imaging during adenosine stress. Journal of the American College of Cardiology 2006;48(1):153-160.
26. George RT, Arbab-Zadeh A, Miller JM, Kitagawa K, Chang HJ, Bluemke DA, Becker L, Yousuf O, Texter J, Lardo AC, Lima JA. Adenosine stress 64- and 256-row detector computed tomography angiography and perfusion imaging: a pilot study evaluating the transmural extent of perfusion abnormalities to predict atherosclerosis causing myocardial ischemia. Circulation Cardiovascular imaging 2009;2(3):174-182.
27. Lee DC, Klocke FJ. Magnetic resonance approaches and recent advances in myocardial perfusion imaging. Curr Cardiol Rep 2006;8(1):59-64.
28. Jerosch-Herold M, Seethamraju RT, Swingen CM, Wilke NM, Stillman AE. Analysis of myocardial perfusion MRI. J Magn Reson Imaging 2004;19(6):758-770.
29. Jerosch-Herold M. Quantification of myocardial perfusion by cardiovascular magnetic resonance. J Cardiovasc Magn Reson 2010;12:57.
30. Lee DC, Johnson NP. Quantification of absolute myocardial blood flow by magnetic resonance perfusion imaging. JACC Cardiovascular imaging 2009;2(6):761-770.
31. Schwitter J, Wacker CM, van Rossum AC, Lombardi M, Al-Saadi N, Ahlstrom H, Dill T, Larsson HBW, Flamm SD, Marquardt M, Johansson L. MR-IMPACT: comparison of perfusion-cardiac magnetic resonance with single-photon emission computed tomography for the detection of coronary artery disease in a multicentre, multivendor, randomized trial. European Heart Journal 2008;29(4):480-489.
32. Sakuma H, Suzawa N, Ichikawa Y, Makino K, Hirano T, Kitagawa K, Takeda K. Diagnostic accuracy of stress first-pass contrast-enhanced myocardial perfusion MRI compared with stress myocardial perfusion scintigraphy. AJR American journal of roentgenology 2005;185(1):95-102.
33. Nagel E, Lehmkuhl HB, Bocksch W, Klein C, Vogel U, Frantz E, Ellmer A, Dreysse S, Fleck E. Noninvasive diagnosis of ischemia-induced wall motion abnormalities with the use of high-dose dobutamine stress MRI: comparison with dobutamine stress echocardiography. Circulation 1999;99(6):763-770.
34. Pennell DJ, Sechtem UP, Higgins CB, Manning WJ, Pohost GM, Rademakers FE, van Rossum AC, Shaw LJ, Yucel EK, Resonance SfCM, Cardiology WGoCMRotESo. Clinical indications for cardiovascular magnetic resonance (CMR): Consensus Panel report. Eur Heart J 2004;25(21):1940-1965.
35. Bettencourt N, Rocha J, Ferreira N, Pires-Morais G, Carvalho M, Leite D, Melica B, Santos L, Rodrigues A, Braga P, Teixeira M, Simoes L, Leite-Moreira A, Cardoso S, Nagel E, Gama V. Incremental value of an integrated adenosine stress-rest MDCT perfusion protocol for detection of obstructive coronary artery disease. J Cardiovasc Comput Tomogr 2011;5(6):392-405.

36. Lonnebakken MT, Bleie O, Strand E, Staal EM, Nygard OK, Gerdts E. Myocardial contrast echocardiography in assessment of stable coronary artery disease at intermediate dobutamine-induced stress level. Echocardiography 2009;26(1):52-60.
37. Jaarsma C, Leiner T, Bekkers SC, Crijns HJ, Wildberger JE, Nagel E, Nelemans PJ, Schalla S. Diagnostic performance of noninvasive myocardial perfusion imaging using single-photon emission computed tomography, cardiac magnetic resonance, and positron emission tomography imaging for the detection of obstructive coronary artery disease: a meta-analysis. Journal of the American College of Cardiology 2012;59(19):1719-1728.
38. Tomlinson DR, Becher H, Selvanayagam JB. Assessment of myocardial viability: comparison of echocardiography versus cardiac magnetic resonance imaging in the current era. Heart Lung Circ 2008;17(3):173-185.
39. Wieben O, Francois C, Reeder SB. Cardiac MRI of ischemic heart disease at 3 T: potential and challenges. Eur J Radiol 2008;65(1):15-28.
40. Hundley WG, Bluemke DA, Finn JP, Flamm SD, Fogel MA, Friedrich MG, Ho VB, Jerosch-Herold M, Kramer CM, Manning WJ, Patel M, Pohost GM, Stillman AE, White RD, Woodard PK. ACCF/ACR/AHA/NASCI/SCMR 2010 expert consensus document on cardiovascular magnetic resonance: a report of the American College of Cardiology Foundation Task Force on Expert Consensus Documents. Circulation 2010;121(22):2462-2508.
41. Geva T. Magnetic resonance imaging: historical perspective. Journal of cardiovascular magnetic resonance : official journal of the Society for Cardiovascular Magnetic Resonance 2006;8(4):573-580.
42. Ridgway JP. Cardiovascular magnetic resonance physics for clinicians: part I. Journal of cardiovascular magnetic resonance : official journal of the Society for Cardiovascular Magnetic Resonance 2010;12:71.
43. Nagel E, Rossum ACV, Fleck E. Cardiovascular Magnetic Resonance: Springer; 2004. 302 p.
44. Markl M, Leupold J. Gradient echo imaging. Journal of magnetic resonance imaging : JMRI 2012;35(6):1274-1289.
45. Scott AD, Keegan J, Firmin DN. Motion in cardiovascular MR imaging. Radiology 2009;250(2):331-351.
46. Nehrke K, Bornert P, Manke D, Bock JC. Free-breathing cardiac MR imaging: study of implications of respiratory motion--initial results. Radiology 2001;220(3):810-815.
47. Lanzer P, Botvinick EH, Schiller NB, Crooks LE, Arakawa M, Kaufman L, Davis PL, Herfkens R, Lipton MJ, Higgins CB. Cardiac imaging using gated magnetic resonance. Radiology 1984;150(1):121-127.
48. Bogaert J, Dymarkowski S, Taylor A. Clinical Cardiac MRI: Springer; 2005.
49. Cerqueira MD, Weissman NJ, Dilsizian V, Jacobs AK, Kaul S, Laskey WK, Pennell DJ, Rumberger JA, Ryan T, Verani MS, Imaging AHAWGoMSaRfC. Standardized myocardial segmentation and nomenclature for tomographic imaging of the heart: a statement for healthcare professionals from the Cardiac Imaging Committee of the Council on Clinical Cardiology of the American Heart Association. Circulation 2002;105(4):539-542.
50. Hussain ST, Paul M, Plein S, Shah AM, McCann G, Marber MS, Maccarthy P, Redwood S, Chiribiri A, Morton G, Schuster A, Ishida M, Westwood MA, Perera D, Nagel E. Design and rationale of the MR-INFORM study: stress perfusion cardiovascular magnetic resonance imaging to guide the management of patients with stable coronary artery disease. Journal of cardiovascular magnetic resonance : official journal of the Society for Cardiovascular Magnetic Resonance 2012;14(1):65.
51. Gebker R, Jahnke C, Paetsch I, Kelle S, Schnackenburg B, Fleck E, Nagel E. Diagnostic performance of myocardial perfusion MR at 3 T in patients with coronary artery disease. Radiology 2008;247(1):57-63.
52. Gebker R, Jahnke C, Paetsch I, Schnackenburg B, Kozerke S, Bornstedt A, Fleck E, Nagel E. MR myocardial perfusion imaging with k-space and time broad-use linear acquisition speed-up technique: feasibility study. Radiology 2007;245(3):863-871.
53. Gerber BL, Raman SV, Nayak K, Epstein FH, Ferreira P, Axel L, Kraitchman DL. Myocardial first-pass perfusion cardiovascular magnetic resonance: history, theory, and current state of the art. Journal of cardiovascular magnetic resonance : official journal of the Society for Cardiovascular Magnetic Resonance 2008;10(1):18.
54. Plein S, Kozerke S, Suerder D, Luescher T, Greenwood J, Boesiger P, Schwitter J. High spatial resolution myocardial perfusion cardiac magnetic resonance for the detection of coronary artery disease. Eur Heart J 2008.

55. Plein S, Ryf S, Schwitter J, Radjenovic A, Boesiger P, Kozerke S. Dynamic contrast-enhanced myocardial perfusion MRI accelerated withk-t sense. Magn Reson Med 2007;58(4):777-785.
56. Algranati D, Kassab GS, Lanir Y. Mechanisms of myocardium-coronary vessel interaction. American journal of physiology Heart and circulatory physiology 2010;298(3):H861-873.
57. Algranati D, Kassab GS, Lanir Y. Why is the subendocardium more vulnerable to ischemia? A new paradigm. American journal of physiology Heart and circulatory physiology 2011;300(3):H1090-1100.
58. Panting JR, Gatehouse PD, Yang G-Z, Grothues F, Firmin DN, Collins P, Pennell DJ. Abnormal subendocardial perfusion in cardiac syndrome X detected by cardiovascular magnetic resonance imaging. The New England journal of medicine 2002;346(25):1948-1953.
59. Greenwood JP, Maredia N, Younger JF, Brown JM, Nixon J, Everett CC, Bijsterveld P, Ridgway JP, Radjenovic A, Dickinson CJ, Ball SG, Plein S. Cardiovascular magnetic resonance and single-photon emission computed tomography for diagnosis of coronary heart disease (CE-MARC): a prospective trial. Lancet 2012;379(9814):453-460.
60. Schwitter J, Wacker CM, van Rossum AC, Lombardi M, Al-Saadi N, Ahlstrom H, Dill T, Larsson HBW, Flamm SD, Marquardt M, Johansson L. MR-IMPACT: comparison of perfusion-cardiac magnetic resonance with single-photon emission computed tomography for the detection of coronary artery disease in a multicentre, multivendor, randomized trial. European heart journal 2008;29(4):480-489.
61. Schwitter J, Wacker CM, Wilke N, Al-Saadi N, Sauer E, Huettle K, Schönberg SO, Luchner A, Strohm O, Ahlstrom H, Dill T, Hoebel N, Simor T, Investigators ftM-I. MR-IMPACT II: Magnetic Resonance Imaging for Myocardial Perfusion Assessment in Coronary artery disease Trial: perfusion-cardiac magnetic resonance vs. single-photon emission computed tomography for the detection of coronary artery disease: a comparative multicentre, multivendor trial. European heart journal 2012.
62. Panting JR, Gatehouse PD, Yang G-Z, Grothues F, Firmin DN, Collins P, Pennell DJ. Abnormal subendocardial perfusion in cardiac syndrome X detected by cardiovascular magnetic resonance imaging. N Engl J Med 2002;346(25):1948-1953.
63. Pilz G, Klos M, Ali E, Hoefling B, Scheck R, Bernhardt P. Angiographic correlations of patients with small vessel disease diagnosed by adenosine-stress cardiac magnetic resonance imaging. Journal of cardiovascular magnetic resonance : official journal of the Society for Cardiovascular Magnetic Resonance 2008;10(1):8.
64. Vermeltfoort IAC, Bondarenko O, Raijmakers PGHM, Odekerken DAM, Kuijper AFM, Zwijnenburg A, van der Vis-Melsen MJE, Twisk JWR, Beek AM, Teule GJJ, van Rossum AC. Is subendocardial ischaemia present in patients with chest pain and normal coronary angiograms? A cardiovascular MR study. European Heart Journal 2007;28(13):1554-1558.
65. van Vaals JJ, Brummer ME, Dixon WT, Tuithof HH, Engels H, Nelson RC, Gerety BM, Chezmar JL, den Boer JA. "Keyhole" method for accelerating imaging of contrast agent uptake. Journal of magnetic resonance imaging : JMRI 1993;3(4):671-675.
66. Jones RA, Haraldseth O, Muller TB, Rinck PA, Oksendal AN. K-space substitution: a novel dynamic imaging technique. Magnetic resonance in medicine : official journal of the Society of Magnetic Resonance in Medicine / Society of Magnetic Resonance in Medicine 1993;29(6):830-834.
67. Lee DC, Simonetti OP, Harris KR, Holly TA, Judd RM, Wu E, Klocke FJ. Magnetic resonance versus radionuclide pharmacological stress perfusion imaging for flow-limiting stenoses of varying severity. Circulation 2004;110(1):58-65.
68. Nagel E, Klein C, Paetsch I, Hettwer S, Schnackenburg B, Wegscheider K, Fleck E. Magnetic resonance perfusion measurements for the noninvasive detection of coronary artery disease. Circulation 2003;108(4):432-437.
69. Ishida N, Sakuma H, Motoyasu M, Okinaka T, Isaka N, Nakano T, Takeda K. Noninfarcted myocardium: correlation between dynamic first-pass contrast-enhanced myocardial MR imaging and quantitative coronary angiography. Radiology 2003;229(1):209-216.
70. Ishida M, Sakuma H, Kato N, Ishida N, Kitagawa K, Shimono T, Yada I, Takeda K. Contrast-enhanced MR imaging for evaluation of coronary artery disease before elective repair of aortic aneurysm. Radiology 2005;237(2):458-464.
71. Al-Saadi N, Nagel E, Gross M, Schnackenburg B, Paetsch I, Klein C, Fleck E. Improvement of myocardial perfusion reserve early after coronary intervention:

assessment with cardiac magnetic resonance imaging. J Am Coll Cardiol 2000;36(5):1557-1564.

72. Pack NA, DiBella EV, Rust TC, Kadrmas DJ, McGann CJ, Butterfield R, Christian PE, Hoffman JM. Estimating myocardial perfusion from dynamic contrast-enhanced CMR with a model-independent deconvolution method. J Cardiovasc Magn Reson 2008;10(1):52.

73. Fritz-Hansen T, Hove JD, Kofoed KF, Kelbaek H, Larsson HB. Quantification of MRI measured myocardial perfusion reserve in healthy humans: a comparison with positron emission tomography. J Magn Reson Imaging 2008;27(4):818-824.

74. Ichihara T, Ishida M, Kitagawa K, Ichikawa Y, Natsume T, Yamaki N, Maeda H, Takeda K, Sakuma H. Quantitative analysis of first-pass contrast-enhanced myocardial perfusion MRI using a Patlak plot method and blood saturation correction. Magn Reson Med 2009;62(2):373-383.

75. Di Bella EV, Parker DL, Sinusas AJ. On the dark rim artifact in dynamic contrast-enhanced MRI myocardial perfusion studies. Magnetic resonance in medicine : official journal of the Society of Magnetic Resonance in Medicine / Society of Magnetic Resonance in Medicine 2005;54(5):1295-1299.

76. Ferreira P, Gatehouse P, Kellman P, Bucciarelli-Ducci C, Firmin D. Variability of myocardial perfusion dark rim Gibbs artifacts due to sub-pixel shifts. Journal of cardiovascular magnetic resonance : official journal of the Society for Cardiovascular Magnetic Resonance 2009;11:17.

77. Meloni A, Al-Saadi N, Torheim G, Hoebel N, Reynolds HG, De Marchi D, Positano V, Burchielli S, Lombardi M. Myocardial first-pass perfusion: influence of spatial resolution and heart rate on the dark rim artifact. Magnetic resonance in medicine : official journal of the Society of Magnetic Resonance in Medicine / Society of Magnetic Resonance in Medicine 2011;66(6):1731-1738.

78. Klocke FJ, Simonetti OP, Judd RM, Kim RJ, Harris KR, Hedjbeli S, Fieno DS, Miller S, Chen V, Parker MA. Limits of detection of regional differences in vasodilated flow in viable myocardium by first-pass magnetic resonance perfusion imaging. Circulation 2001;104(20):2412-2416.

79. al-Saadi N, Gross M, Bornstedt A, Schnackenburg B, Klein C, Fleck E, Nagel E. [Comparison of various parameters for determining an index of myocardial perfusion reserve in detecting coronary stenosis with cardiovascular magnetic resonance tomography]. Z Kardiol 2001;90(11):824-834.

80. Hsu LY, Rhoads KL, Holly JE, Kellman P, Aletras AH, Arai AE. Quantitative myocardial perfusion analysis with a dual-bolus contrast-enhanced first-pass MRI technique in humans. Journal of magnetic resonance imaging : JMRI 2006;23(3):315-322.

81. Christian TF, Rettmann DW, Aletras AH, Liao SL, Taylor JL, Balaban RS, Arai AE. Absolute myocardial perfusion in canines measured by using dual-bolus first-pass MR imaging. Radiology 2004;232(3):677-684.

82. Fritz-Hansen T, Hove JD, Kofoed KF, Kelbaek H, Larsson HB. Quantification of MRI measured myocardial perfusion reserve in healthy humans: a comparison with positron emission tomography. Journal of magnetic resonance imaging : JMRI 2008;27(4):818-824.

83. Larsson HB, Fritz-Hansen T, Rostrup E, Sondergaard L, Ring P, Henriksen O. Myocardial perfusion modeling using MRI. Magn Reson Med 1996;35(5):716-726.

84. Walker-Samuel S, Leach MO, Collins DJ. Reference tissue quantification of DCE-MRI data without a contrast agent calibration. Physics in Medicine and Biology 2007;52(3):589-601.

85. Evelhoch JL. Key factors in the acquisition of contrast kinetic data for oncology. Journal of magnetic resonance imaging : JMRI 1999;10(3):254-259.

86. Ishida M, Sakuma H, Murashima S, Nishida J, Senga M, Kobayasi S, Takeda K, Kato N. Absolute blood contrast concentration and blood signal saturation on myocardial perfusion MRI: estimation from CT data. J Magn Reson Imaging 2009;29(1):205-210.

87. Muehling OM, Huber A, Cyran C, Schoenberg SO, Reiser M, Steinbeck G, Nabauer M, Jerosch-Herold M. The delay of contrast arrival in magnetic resonance first-pass perfusion imaging: a novel non-invasive parameter detecting collateral-dependent myocardium. Heart 2007;93(7):842-847.

88. Wilke N, Jerosch-Herold M, Wang Y, Huang Y, Christensen BV, Stillman AE, Ugurbil K, McDonald K, Wilson RF. Myocardial perfusion reserve: assessment with multisection, quantitative, first-pass MR imaging. Radiology 1997;204(2):373-384.

89. Futamatsu H, Wilke N, Klassen C, Shoemaker S, Angiolillo DJ, Siuciak A, Morikawa-Futamatsu K, Suzuki N, von Ziegler F, Bass TA, Costa MA. Evaluation of cardiac

magnetic resonance imaging parameters to detect anatomically and hemodynamically significant coronary artery disease. Am Heart J 2007;154(2):298-305.

90. Hsu LY, Rhoads KL, Holly JE, Kellman P, Aletras AH, Arai AE. Quantitative myocardial perfusion analysis with a dual-bolus contrast-enhanced first-pass MRI technique in humans. J Magn Reson Imaging 2006;23(3):315-322.

91. Christian TF, Aletras AH, Arai AE. Estimation of absolute myocardial blood flow during first-pass MR perfusion imaging using a dual-bolus injection technique: comparison to single-bolus injection method. J Magn Reson Imaging 2008;27(6):1271-1277.

92. Utz W, Greiser A, Niendorf T, Dietz R, Schulz-Menger J. Single- or dual-bolus approach for the assessment of myocardial perfusion reserve in quantitative MR perfusion imaging. Magn Reson Med 2008;59(6):1373-1377.

93. Kostler H, Ritter C, Lipp M, Beer M, Hahn D, Sandstede J. Prebolus quantitative MR heart perfusion imaging. Magn Reson Med 2004;52(2):296-299.

94. Gatehouse PD, Elkington AG, Ablitt NA, Yang GZ, Pennell DJ, Firmin DN. Accurate assessment of the arterial input function during high-dose myocardial perfusion cardiovascular magnetic resonance. J Magn Reson Imaging 2004;20(1):39-45.

95. Vallee JP, Lazeyras F, Kasuboski L, Chatelain P, Howarth N, Righetti A, Didier D. Quantification of myocardial perfusion with FAST sequence and Gd bolus in patients with normal cardiac function. J Magn Reson Imaging 1999;9(2):197-203.

96. Cernicanu A, Axel L. Theory-based signal calibration with single-point T1 measurements for first-pass quantitative perfusion MRI studies. Acad Radiol 2006;13(6):686-693.

97. Utz W, Niendorf T, Wassmuth R, Messroghli D, Dietz R, Schulz-Menger J. Contrast-dose relation in first-pass myocardial MR perfusion imaging. J Magn Reson Imaging 2007;25(6):1131-1135.

98. Hsu LY, Kellman P, Arai AE. Nonlinear myocardial signal intensity correction improves quantification of contrast-enhanced first-pass MR perfusion in humans. J Magn Reson Imaging 2008;27(4):793-801.

99. Ishida M, Schuster A, Morton G, Chiribiri A, Hussain S, Paul M, Merkle N, Steen H, Lossnitzer D, Schnackenburg B, Alfakih K, Plein S, Nagel E. Development of a universal dual-bolus injection scheme for the quantitative assessment of myocardial perfusion cardiovascular magnetic resonance. J Cardiovasc Magn Reson 2011;13(1):28.

100. Zierler KL. Tracer-dilution techniques in the study of microvascular behavior. Fed Proc 1965;24(5):1085-1091.

101. Pack NA, DiBella EVR, Rust TC, Kadrmas DJ, McGann CJ, Butterfield R, Christian PE, Hoffman JM. Estimating myocardial perfusion from dynamic contrast-enhanced CMR with a model-independent deconvolution method. Journal of cardiovascular magnetic resonance : official journal of the Society for Cardiovascular Magnetic Resonance 2008;10(1):52.

102. Pack NA, DiBella EVR. Comparison of myocardial perfusion estimates from dynamic contrast-enhanced magnetic resonance imaging with four quantitative analysis methods. Magn Reson Med 2010;64(1):125-137.

103. Jerosch-Herold M, Wilke N, Stillman… A. Magnetic resonance quantification of the myocardial perfusion reserve with a Fermi function model for constrained deconvolution. Medical physics 1998.

104. Keeling S, Bammer R, Kogler… T. On the convolution model of dynamic contrast enhanced magnetic resonance imaging and nonparametric deconvolution approaches. kfunigrazacat 2004.

105. Ostergaard L, Weisskoff RM, Chesler DA, Gyldensted C, Rosen BR. High resolution measurement of cerebral blood flow using intravascular tracer bolus passages. Part I: Mathematical approach and statistical analysis. Magnetic resonance in medicine : official journal of the Society of Magnetic Resonance in Medicine / Society of Magnetic Resonance in Medicine 1996;36(5):715-725.

106. Engl HW, Hanke M, Neubauer A. Regularization of inverse problems. Dordrecht ; Boston: Kluwer Academic Publishers; 1996. viii, 321 p. p.

107. Gill PE, Murray W, Wright MH. Practical optimization. London ; New York: Academic Press; 1981. xvi, 401 p. p.

108. Tong CY, Prato FS, Wisenberg G, Lee TY, Carroll E, Sandler D, Wills J. Techniques for the measurement of the local myocardial extraction efficiency for inert diffusible contrast agents such as gadopentate dimeglumine. Magn Reson Med 1993;30(3):332-336.

109. Tong CY, Prato FS, Wisenberg G, Lee TY, Carroll E, Sandler D, Wills J, Drost D. Measurement of the extraction efficiency and distribution volume for Gd-DTPA in normal and diseased canine myocardium. Magn Reson Med 1993;30(3):337-346.
110. Larsson HB, Stubgaard M, Sondergaard L, Henriksen O. In vivo quantification of the unidirectional influx constant for Gd-DTPA diffusion across the myocardial capillaries with MR imaging. J Magn Reson Imaging 1994;4(3):433-440.
111. Diesbourg LD, Prato FS, Wisenberg G, Drost DJ, Marshall TP, Carroll SE, O'Neill B. Quantification of myocardial blood flow and extracellular volumes using a bolus injection of Gd-DTPA: kinetic modeling in canine ischemic disease. Magn Reson Med 1992;23(2):239-253.
112. Vallee JP, Sostman HD, MacFall JR, DeGrado TR, Zhang J, Sebbag L, Cobb FR, Wheeler T, Hedlund LW, Turkington TG, Spritzer CE, Coleman RE. Quantification of myocardial perfusion by MRI after coronary occlusion. Magn Reson Med 1998;40(2):287-297.
113. Kershaw LE, Buckley DL. Precision in measurements of perfusion and microvascular permeability with T1-weighted dynamic contrast-enhanced MRI. Magnetic resonance in medicine : official journal of the Society of Magnetic Resonance in Medicine / Society of Magnetic Resonance in Medicine 2006;56(5):986-992.
114. Donaldson SB, West CM, Davidson SE, Carrington BM, Hutchison G, Jones AP, Sourbron SP, Buckley DL. A comparison of tracer kinetic models for T1-weighted dynamic contrast-enhanced MRI: application in carcinoma of the cervix. Magnetic resonance in medicine : official journal of the Society of Magnetic Resonance in Medicine / Society of Magnetic Resonance in Medicine 2010;63(3):691-700.
115. Vallee JP, Lazeyras F, Kasuboski L, Chatelain P, Howarth N, Righetti A, Didier D. Quantification of myocardial perfusion with FAST sequence and Gd bolus in patients with normal cardiac function. Journal of magnetic resonance imaging : JMRI 1999;9(2):197-203.
116. Rutland MD. Origin of the Patlak-Rutland plot. Nucl Med Commun 1996;17(5):441.
117. Pack NA, DiBella EV, Rust TC, Kadrmas DJ, McGann CJ, Butterfield R, Christian PE, Hoffman JM. Estimating myocardial perfusion from dynamic contrast-enhanced CMR with a model-independent deconvolution method. J Cardiovasc Magn Reson 2008;10:52.
118. Schumaker LL. Spline functions : basic theory. New York: Cambridge University Press; 2007. 582 p. p.
119. De Boor C. A practical guide to splines. New York: Springer; 2000.
120. Pack NA, DiBella EV. Comparison of myocardial perfusion estimates from dynamic contrast-enhanced magnetic resonance imaging with four quantitative analysis methods. Magn Reson Med 2010;64(1):125-137.
121. Batchelor P, Chiribiri A, Nooralipour NZ, Cvetkovic Z. Arma Regularization of Cardiac Perfusion Modeling. International Conference on Acoustics, Speech and Signal Processing, ICASSP 2010 2010:642-645.
122. Kashyap RL. Optimal Choice of AR and MA Parts in Autoregressive Moving Average Models. IEEE Trans Pattern Anal Mach Intell 1982;4(2):99-104.
123. Degooijer JG, Abraham B, Gould A, Robinson L. Methods for Determining the Order of an Autoregressive-Moving Average Process - a Survey. Int Stat Rev 1985;53(3):301-329.
124. Lindsey JK, Byrom WD, Wang J, Jarvis P, Jones B. Generalized nonlinear models for pharmacokinetic data. Biometrics 2000;56(1):81-88.
125. Ishida M, Morton G, Schuster A, Nagel E, Chiribiri A. Quantitative Assessment of Myocardial Perfusion MRI. Curr Cardiovasc Imaging Rep 2010; 3:8.
126. Zierler K. Indicator dilution methods for measuring blood flow, volume, and other properties of biological systems: a brief history and memoir. Annals of Biomedical Engineering 2000;28(8):836-848.
127. Zarinabad N, Chiribiri A, Hautvast GL, Ishida M, Schuster A, Cvetkovic Z, Batchelor PG, Nagel E. Voxel-wise quantification of myocardial perfusion by cardiac magnetic resonance. Feasibility and methods comparison. Magnetic resonance in medicine : official journal of the Society of Magnetic Resonance in Medicine / Society of Magnetic Resonance in Medicine 2012.
128. Neyran B, Janier MF, Casali C, Revel D, Canet Soulas EP. Mapping myocardial perfusion with an intravascular MR contrast agent: robustness of deconvolution methods at various blood flows. Magnetic resonance in medicine : official journal of the Society of Magnetic Resonance in Medicine / Society of Magnetic Resonance in Medicine 2002;48(1):166-179.

129. Wang L, Jerosch-Herold M, Jacobs DR, Jr., Shahar E, Folsom AR. Coronary risk factors and myocardial perfusion in asymptomatic adults: the Multi-Ethnic Study of Atherosclerosis (MESA). J Am Coll Cardiol 2006;47(3):565-572.
130. Hautvast G, Chiribiri A, Zarinabad N, Schuster A, Breeuwer M, Nagel E. Myocardial blood flow quantification from MRI by deconvolution using an exponential approximation basis. IEEE transactions on bio-medical engineering 2012.
131. Zarinabad N, Hautvast G, Breeuwer M, Nagel E, Chiribiri A. Effect of tracer arrival time on the estimation of the myocardial perfusion in DCE-CMR. Journal of Cardiovascular Magnetic Resonance 2012;14:16.
132. Schuster A. Validation of Quantitative Myocardial Perfusion Magnetic Resonance Imaging. London: kings college london; 2012.
133. Cerqueira MD, Weissman NJ, Dilsizian V, Jacobs AK, Kaul S, Laskey WK, Pennell DJ, Rumberger JA, Ryan T, Verani MS. Standardized myocardial segmentation and nomenclature for tomographic imaging of the heart: a statement for healthcare professionals from the Cardiac Imaging Committee of the Council on Clinical Cardiology of the American Heart Association. Circulation 2002;105(4):539-542.
134. van Horssen P, Siebes M, Hoefer I, Spaan JA, van den Wijngaard JP. Improved detection of fluorescently labeled microspheres and vessel architecture with an imaging cryomicrotome. Med Biol Eng Comput 2010;48(8):735-744.
135. Hansen PC. Analysis of Discrete Ill-Posed Problems by Means of the L-Curve. Siam Rev 1992;34(4):561-580.
136. Zarinabad N. Advanced quantification methods for blood flow from first pass myocardial perfusion MRI [Master Thesis]. London: Kings College London; 2009.
137. Chen H, Li F, Zhao X, Yuan C, Rutt B, Kerwin WS. Extended graphical model for analysis of dynamic contrast-enhanced MRI. Magnetic resonance in medicine : official journal of the Society of Magnetic Resonance in Medicine / Society of Magnetic Resonance in Medicine 2011;66(3):868-878.
138. Sourbron S, Dujardin M, Makkat S, Luypaert R. Pixel-by-pixel deconvolution of bolus-tracking data: optimization and implementation. Physics in Medicine and Biology 2007;52(2):429-447.
139. Makkat S, Luypaert R, Sourbron S, Stadnik T, De Mey J. Quantification of perfusion and permeability in breast tumors with a deconvolution-based analysis of second-bolus T1-DCE data. J Magn Reson Imaging 2007;25(6):1159-1167.
140. Gudbjartsson H, Patz S. The Rician distribution of noisy MRI data. Magn Reson Med 1995;34(6):910-914.
141. Rajan J, Poot D, Juntu J, Sijbers J. Noise measurement from magnitude MRI using local estimates of variance and skewness. Physics in Medicine and Biology 2010;55(16):N441-449.
142. Chiribiri A, Schuster A, Ishida M, Hautvast G, Zarinabadnooralipour N, Paul M, Hussain S, Batchelor P, Breeuwer M, Schaeffter T, Nagel E. Dynamic simulation of first pass myocardial perfusion MR with a novel perfusion phantom. J Cardiovasc Magn Reson 2011;13:46.
143. Chiribiri A, Schuster A, Ishida M, Hautvast G, Zarinabad N, Morton G, Otton J, Plein S, Breeuwer M, Batchelor P, Schaeffter T, Nagel E. Perfusion phantom: An efficient and reproducible method to simulate myocardial first-pass perfusion measurements with cardiovascular magnetic resonance. Magnetic resonance in medicine 2012.
144. Plein S, Ryf S, Schwitter J, Radjenovic A, Boesiger P, Kozerke S. Dynamic contrast-enhanced myocardial perfusion MRI accelerated with k-t sense. Magn Reson Med 2007;58(4):777-785.
145. Plein S, Schwitter J, Suerder D, Greenwood JP, Boesiger P, Kozerke S. k-Space and time sensitivity encoding-accelerated myocardial perfusion MR imaging at 3.0 T: comparison with 1.5 T. Radiology 2008;249(2):493-500.
146. Breeuwer M, Quist M, Spreeuwers L. Automatic quantitative analysis of cardiac MR perfusion images. Proceedings of SPIE Medical Imaging ,San Diego, CA, USA 2001;4322:733-742.
147. Spreeuwers L, Breeuwer M. Automatic detection of myocardial boundaries in MR cardio perfusion images. Proceedings of Medical Image Computing and Computer-Assisted Intervention, Utrecht, Netherlands 2001:1228-1231.
148. Hautvast G, Chiribiri A, Zarinabad N, Schuster A, Breeuwer M, Nagel E. Myocardial blood flow quantification from MRI by deconvolution using an exponential approximation basis. IEEE transactions on bio-medical engineering 2012;59(7):2060-2067.
149. Di Bella EV, Wu YJ, Alexander AL, Parker DL, Green D, McGann CJ. Comparison of temporal filtering methods for dynamic contrast MRI myocardial perfusion studies.

Magnetic resonance in medicine : official journal of the Society of Magnetic Resonance in Medicine / Society of Magnetic Resonance in Medicine 2003;49(5):895-902.

150. Hsu LY, Groves DW, Aletras AH, Kellman P, Arai AE. A quantitative pixel-wise measurement of myocardial blood flow by contrast-enhanced first-pass CMR perfusion imaging: microsphere validation in dogs and feasibility study in humans. JACC Cardiovascular imaging 2012;5(2):154-166.

151. Zarinabad N, Chiribiri A, Hautvast G, Shuster A, Sinclair M, Wijngaard JPHMvd, Smith N, Spaan JAE, Siebes M, Breeuwer M, Nagel E. Modelling Parameter Role on Accuracy of Cardiac Perfusion Quantification. Lecture Notes in Computer Science 2013;7945:13.

152. Jerosch-Herold M, Hu X, Murthy NS, Seethamraju RT. Time delay for arrival of MR contrast agent in collateral-dependent myocardium. IEEE transactions on medical imaging 2004;23(7):881-890.

153. Chiribiri A, Schuster A, Ishida M, Hautvast G, Zarinabad N, Morton G, Otton J, Plein S, Breeuwer M, Batchelor P, Schaeffter T, Nagel E. Perfusion phantom: an efficient and reproducible method to simulate myocardial first pass perfusion measurements with cardiovascular magnetic resonance. Magnetic resonance in medicine 2012.

154. Hautvast G, Chiribiri A, Zarinabad N, Schuster A, Breeuwer M, Nagel E. Myocardial blood flow quantification from MRI by deconvolution using an exponential approximation basis. Transaction on biomedical engineering 2012.

155. Hautvast GL, Chiribiri A, Lockie T, Breeuwer M, Nagel E, Plein S. Quantitative analysis of transmural gradients in myocardial perfusion magnetic resonance images. Magn Reson Med 2011.

156. Nandalur KR, Dwamena BA, Choudhri AF, Nandalur MR, Carlos RC. Diagnostic performance of stress cardiac magnetic resonance imaging in the detection of coronary artery disease: a meta-analysis. Journal of the American College of Cardiology 2007;50(14):1343-1353.

157. Parkka JP, Niemi P, Saraste A, Koskenvuo JW, Komu M, Oikonen V, Toikka JO, Kiviniemi TO, Knuuti J, Sakuma H, Hartiala JJ. Comparison of MRI and positron emission tomography for measuring myocardial perfusion reserve in healthy humans. Magnetic resonance in medicine : official journal of the Society of Magnetic Resonance in Medicine / Society of Magnetic Resonance in Medicine 2006;55(4):772-779.

158. Pennell DJ, Sechtem UP, Higgins CB, Manning WJ, Pohost GM, Rademakers FE, van Rossum AC, Shaw LJ, Yucel EK. Clinical indications for cardiovascular magnetic resonance (CMR): Consensus Panel report. Eur Heart J 2004;25(21):1940-1965.

159. Su MY, Jao JC, Nalcioglu O. Measurement of vascular volume fraction and blood-tissue permeability constants with a pharmacokinetic model: studies in rat muscle tumors with dynamic Gd-DTPA enhanced MRI. Magnetic resonance in medicine : official journal of the Society of Magnetic Resonance in Medicine / Society of Magnetic Resonance in Medicine 1994;32(6):714-724.

160. Bogin L, Margalit R, Mispelter J, Degani H. Parametric imaging of tumor perfusion using flow- and permeability-limited tracers. Journal of magnetic resonance imaging : JMRI 2002;16(3):289-299.

161. Christian TF, Aletras AH, Arai AE. Estimation of absolute myocardial blood flow during first-pass MR perfusion imaging using a dual-bolus injection technique: comparison to single-bolus injection method. Journal of magnetic resonance imaging : JMRI 2008;27(6):1271-1277.

162. Christian TF, Rettmann DW, Aletras AH, Liao SL, Taylor JL, Balaban RS, Arai AE. Absolute myocardial perfusion in canines measured by using dual-bolus first-pass MR imaging. Radiology 2004;232(3):677-684.

163. Ishida M, Schuster A, Morton G, Chiribiri A, Hussain S, Paul M, Merkle N, Steen H, Lossnitzer D, Schnackenburg B, Alfakih K, Plein S, Nagel E. Development of a universal dual-bolus injection scheme for the quantitative assessment of myocardial perfusion cardiovascular magnetic resonance. Journal of cardiovascular magnetic resonance : official journal of the Society for Cardiovascular Magnetic Resonance 2011;13:28.

164. Judd RM, Reeder SB, May-Newman K. Effects of water exchange on the measurement of myocardial perfusion using paramagnetic contrast agents. Magnetic resonance in medicine : official journal of the Society of Magnetic Resonance in Medicine / Society of Magnetic Resonance in Medicine 1999;41(2):334-342.

165. Sakaie KE, Shin W, Curtin KR, McCarthy RM, Cashen TA, Carroll TJ. Method for improving the accuracy of quantitative cerebral perfusion imaging. Journal of magnetic resonance imaging : JMRI 2005;21(5):512-519.

166. Shin W, Cashen TA, Horowitz SW, Sawlani R, Carroll TJ. Quantitative CBV measurement from static T1 changes in tissue and correction for intravascular water exchange. Magnetic resonance in medicine : official journal of the Society of Magnetic Resonance in Medicine / Society of Magnetic Resonance in Medicine 2006;56(1):138-145.
167. Shin W, Horowitz S, Ragin A, Chen Y, Walker M, Carroll TJ. Quantitative cerebral perfusion using dynamic susceptibility contrast MRI: evaluation of reproducibility and age- and gender-dependence with fully automatic image postprocessing algorithm. Magnetic resonance in medicine : official journal of the Society of Magnetic Resonance in Medicine / Society of Magnetic Resonance in Medicine 2007;58(6):1232-1241.

9 Table of Figures and tables

10 Acknowledgment

Life has thrown me many curve balls over the years and I would like to give special thanks to my parents for tirelessly supporting me through all the life changing events. Thanks to my mum for being my rock and helping keep me in touch with reality throughout my studies. Thanks to my dad for letting me do it ‘my way’ and for encouraging and inspiring me to reach for my dreams.

This thesis is the end of my journey in obtaining my Ph.D. I have not travelled in a vacuum in this journey. This thesis has been kept on track and been seen through to completion with the support and encouragement of numerous people including my well-wishers, my friends and my colleagues. At the end of my thesis, it is a pleasant task to express my thanks to all those who contributed in many ways to the success of this study and made it an unforgettable experience for me.

I am also extremely indebted to my guide Prof. Eike Nagel for providing necessary infrastructure and resources to accomplish my research work. He has paved the way for me to have very productive research.

I warmly thank Prof Marcel Breeuwer, for his valuable advice, constructive criticism and his extensive discussions around my work. I am very much thankful to him for picking me up as a student at the critical stage of my Ph.D.

At this moment of accomplishment, I pay homage to my guide, Late. Dr. Philip Batchlor. This work would not have been possible without his guidance, support and encouragement. Under his guidance I successfully overcame many difficulties and learned a lot. His unflinching courage and conviction will always inspire me, and I hope to continue to work with his noble thoughts. I wish his soul roots in peace and solace in the heaven. I can only say a proper thanks to his through my future work. It is to him that I dedicate this work.

Although I was the principal author of the publications in this thesis, all the work was done jointly with my co-authors and it is impossible to disentangle each individual contribution. I would like to thank the co-authors of my conference abstracts and journal publication Dr Amedeo Chiribiri, Dr Andreas Schuster and Dr Gilion Hautvast for the pleasure for working with them and for their permission to use our joint work in this thesis.

I gratefully acknowledge the funding received towards my PhD from the Biomedical Research Centre (BRC).

A special thanks goes to the supervisor of my master Degree Prof Zoran Cvetkovic who introduced me to the field of MR research and who helped me to obtain this PhD position at King’s College London.

I would like to pay high regards to my mother, my father for their sincere encouragement and inspiration throughout my research work and lifting me uphill this phase of life. I owe everything to them.

Last but not least, I thank my family and friend who have kept me sane and reminded me that there is more to life than a PhD.

11 Curriculum vitae

Niloufar Zarinabad was born on 19 Sep 1985 in Tehran, Iran. After finishing her bachelor degree in electrical/control engineering in 2007, she spent 5 months working for Iranian national Oil and Gas Company. Then she pursued an advanced degree in Signal Processing at King's College London and completed her Master's Degree winning a fully funded scholarship to pursue a PhD in Imaging Science and Biomedical Engineering in the fall of 2009, of which the results are presented in this dissertation. This position was in the Rayne institute at the division of imaging sciences, King's College London.

Publication

Journal Papers:

- Voxel-wise quantification of myocardial perfusion by cardiac magnetic resonance. Feasibility and methods comparison. **Zarinabad N**, Chiribiri A, Hautvast GL, Ishida M, Schuster A, Cvetkovic Z, Batchelor PG, Nagel E.Magn Reson Med. 2012 Feb 21. doi: 10.1002/mrm.24195.

- Perfusion phantom: An efficient and reproducible method to simulate myocardial first-pass perfusion measurements with cardiovascular magnetic resonance. Chiribiri A, Schuster A, Ishida M, Hautvast G, **Zarinabad N**, Morton G, Otton J, Plein S, Breeuwer M, Batchelor P, Schaeffter T, Nagel E. Magn Reson Med. 2012 Apr 24. doi: 10.1002/mrm.24299.

- Myocardial blood flow quantification from MRI by deconvolution using an exponential approximation basis. Hautvast G, Chiribiri A, **Zarinabad N**, Schuster A, Breeuwer M, Nagel E. IEEE Trans Biomed Eng. 2012 Jul;59(7):2060-7.

Conference papers:

- ARMA regularization of cardiac perfusion modelling, Philip Batchelor, Amedeo Chiribiri, **Zarinabad N**, Zoran Cvetkovic. IEEE, ICASSP 2010: 642-645.

Conference abstracts:

- Comparison of different deconvolution algorithms for voxel-wise quantitative MR perfusion assessment. **Zarinabad N**, Chiribiri A**,** Hautvast G**,** Batchelor P, Plein S, Nagel E**.** J Cardiovasc Magn Reson. 2011; 13(Suppl 1)

- Voxel-Wise Quantitative Assessment of Myocardial Perfusion: A Comparison of Four Different Deconvolution Algorithms using Real Flow Values. **Zarinabad N**, Chiribiri A**,** Hautvast G**,** Nagel E, Batchelor P**.**. ISMRM 19th Annual Meeting Proceedings, 9-13 May 2011, Montréal, Québec.

- Effect of tracer arrival time on the estimation of the myocardial perfusion in DCE-CMR. **Zarinabad N**, Hautvast G , Breeuwer M, Nagel E, Chiribiri A. Journal of Cardiovascular Magnetic Resonance 2012 14(Suppl 1):P16.

- Sensitivity of quantification methods to tracer arrival time for myocardial perfusion estimation in DCE-MRI . **Zarinabad N**, Chiribiri A, Hautvast G , Breeuwer M, Nagel E. European heat journal for ESC Munich Aug 2012

- A novel method for assessing diseased myocardium: tracer arrival time evaluation. **Zarinabad N**, Chiribiri A, Hautvast G , Breeuwer M, Nagel E. European heat journal for ESC Munich Aug 2012
- Modified ARMA approach for assessment of Myocardial blood flow from DCE-MRI data. **Zarinabad N**, Hautvast G , Chiribiri A, Breeuwer M, Nagel E. Bioengineering12, oxford.UK.

- First pass vasodilator-stress myocardial perfusion CMR in mice on a whole-body 3Tesla scanner: validation against microspheres. Jogiya R, Makowski M, Phinikaridou A, Jansen

A, **Zarinabad N**, Chiribiri A, Botnar M, Nagel E, Kozerke S, Plein S. J Cardiovasc Magn Reson 14 Suppl 1:P61 (2012) PMID 22376451.

- Quantitative assessment of myocardial perfusion by magnetic resonance imaging in the isolated porcine heart. Schuster A, Chiribiri A**,** Ishida M**,** Paul M**,** Hussain S**,** **Zarinabad N,** Morton G, Jogiya R, Perera D**,** Schaeffter T**,** Plein S, Nagel E. J Cardiovasc Magn Reson. 2011; 13(Suppl 1): P55.Published online 2011 February 2.

- Dynamic simulation of first pass myocardial perfusion MR with a novel perfusion phantom. Chiribiri A**,** Schuster A**,** Ishida M**,** Hautvast G**,** **Zarinabad N,** Paul M**,** Hussain **S,** Batchelor P**,** Breeuwer M**,** Schaeffter T**,** Nagel E **.** J Cardiovasc Magn Reson 2011;13:46.

- The relationship between spatial resolution levels and quantitative myocardial perfusion. **Zarinabad N**, Chiribiri A, Hautvast G , Breeuwer M, Nagel E. 16th annual meeting of society of Cardiovascular Magnetic Resonance. February 2013.

- Improved accuracy of myocardial blood flow quantification by first pass perfusion MR when corrected for steady state T1 relaxation. **Zarinabad N**, Sammut E, Voigt T, Hautvast G, Breeuwer M, Razavi R, Nagel E, Puntmann V, Chiribiri A, 16th annual meeting of society of Cardiovascular Magnetic Resonance. February 2013.